ASSESSING THE RESPONSE OF PLANT AND ALGAL BIOMARKERS TO HIGH CO_2 LEVELS

by

BRIDGET ALISON WARREN

A thesis submitted to the University of Birmingham for the degree of

DOCTOR OF PHILOSOPHY

Department of Earth Sciences

School of Geography, Earth and Environmental Sciences

College of Life and Environmental Sciences

University of Birmingham

January 2023

ABSTRACT

Biomarker-based reconstruction of climatic and environmental variables can and have provided great insight into the processes of the earth system. However, biomarkers are by definition produced by living organisms via complex processes of biosynthesis, and interpretation of information encoded in biomarkers relies heavily on knowledge of these processes observed in the modern. A robust understanding of the modern mechanisms underpinning biomarker behaviour is essential to accurate interpretations of their trends geologically. In particular, understanding how biomarkers and their source organisms responded to increased levels of CO_2 in the geologic record is of extreme importance for understanding how they will respond to anthropogenic climate change, and how climate mechanisms and feedbacks function in high CO_2 worlds. Since gradients of CO_2 concentration are rare in nature, observing biomarker response to CO_2 requires manipulation of environmental conditions in settings which are limited in size and complexity compared to the real world. This thesis examines the response of leaf wax *n*-alkane biomarkers to elevated CO_2 as part of a Free Air CO_2 Enrichment (FACE) experiment in two species over four years, with the aim of determining how, and why, plant biomarkers respond to CO_2, and what this could mean for their use in reconstructing past environments. In addition, this thesis will reconstruct atmospheric pCO_2 using the alkenone $\delta^{13}C$ proxy in the early Eocene: a time interval noted for its high CO_2 conditions. By examining the performance of the proxy in extreme CO_2 concentrations on geologic timescales, the underlying mechanics of the proxy can be evaluated, and the

circumstances at which our understanding of alkenone biomarker response to pCO_2 breaks down can be examined.

Changes to the distribution and carbon isotopic composition of leaf wax *n*-alkane homologues under elevated CO_2 allow for examination of a plant biomarker's functional response to experimental CO_2 changes. This data shows that production of *n*-alkanes changes under elevated CO_2 in one of the two species studied: the observed changes likely acted to optimise plant response to its environment. This shows that *n*-alkane production can be changeable within a single generation of plants on extremely short timescales geologically, but that response is highly species-specific and cannot necessarily be extrapolated to the scale of entire catchments. It also provides qualitative evidence that some plants may adjust their production of molecules known to reduce water loss under elevated CO_2 in response to water savings made elsewhere in the plant, suggesting a hitherto undescribed feedback mechanism in plant-CO_2 relations, that may have implications for understanding of forest water use under climate change.

This data also shows that biosynthetic processes act to alter the $\delta^{13}C$ of *n*-alkane biomarkers under elevated CO_2 in both studied species. Alongside previously published studies, this data suggests that plants often adjust biosynthesis of *n*-alkanes on short timescales in response to changes in atmospheric CO_2 concentration in ways which influence their $\delta^{13}C$, but do so via multiple mechanisms. This suggests that post-photosynthetic fractionations of $\delta^{13}C$ should be considered when interpreting *n*-alkane $\delta^{13}C$ geologically, as these provide an additional mechanism by which *n*-alkane $\delta^{13}C$ can respond to environment geologically alongside the currently accepted model of plant $\delta^{13}C$ response.

Finally, this thesis examines the response of alkenone biomarkers in a sediment core dating from the hot, high-CO_2 conditions of the early Eocene. The early Eocene environment represents the highest CO_2 and warmest sustained conditions of the last 66 Ma, and existing pCO_2 reconstructions give widely varying results depending on proxy used. The alkenone data presented here represent some of the earliest alkenone $\delta^{13}C$ data ever measured, and thus if the proxy can be successfully applied, the alkenone $\delta^{13}C$-derived pCO_2 record could be extended backward through the early Eocene and could further constrain atmospheric pCO_2 reconstructions for the interval. The data presented here suggests that in these extreme conditions the commonly used assumptions made with algal biology in order to produce quantitative pCO_2 reconstructions may be inaccurate, and alkenone-producing algal biology should be regarded as more changeable on long timescales than is reflected in current data used for calibration. However, although quantitative pCO_2 reconstruction using the alkenone proxy is challenging due to extremely high uncertainty, this data provides a valuable lower constraint on pCO_2 through the interval: even with the combination of input parameters to the model that would produce the lowest pCO_2 estimations, pCO_2 levels remain at or above 1000 ppmv over the interval. This is compatible with the pCO_2 estimations for the interval made using Boron- and phytane-based proxies, but is much higher than the <700 ppmv predictions made using measurements taken from higher plant fossils. Thus, although the alkenone data presented here cannot quantify pCO_2 during this interval, it suggests that Eocene pCO_2 is best reconstructed from non-higher plant sources.

These are the oldest memories on Earth, the time-codes carried in every chromosome and gene… The brief span of an individual life is misleading. Each one of us is as old as the entire biological kingdom, and our bloodstreams are tributaries of the great sea of its total memory.

J. G. Ballard, *The Drowned World*

Acknowledgements

There are many people without whom this thesis would not have been possible. My supervisors: James Bendle, Sarah Greene, Jason Hilton, and Tom Dunkley Jones. Thank you all of you for your support throughout: I have never once doubted that you have had my best interests in mind. Thank you so much for all of the encouragement, the opportunities, and the interesting conversations over the last 4 years. Thank you also to Kweku Afrifa Yamoah and Yvette Eley for the encouragement, the advice, and all the help – this would have been much more difficult without your support. Within Forest Edge, Simon Dixon and Rob Mackenzie have constantly provided support above and beyond anything I would have expected and have been brilliant throughout.

I would like to acknowledge Nick Davison, Gael Denny, and Kweku Afrifa Yamoah for the technical support throughout this project, without which I may have blown up the lab at least once, and certainly couldn't have produced half as good science. Thank you also to Ian Boomer for the lab support and training, and for all the bulk isotope protocols, Osamu Seki for running many samples in Japan for me, and Heiko Moossen for writing this project. Also, Dr Marcus Badger for providing code for Monte Carlo simulations, as well as talking me through how to use it.

I would like to acknowledge funding from the Leverhulme Trust and Forest Edge for this PhD project, as well as funding from NERC for analyses performed at Bristol.

Thank you to everyone in the University of Birmingham and outside it who have supported me throughout, who have kept me somewhat sane and let me ramble about isotopes, leaf wax, and carnivorous plants – Vicki Dutch, Karolin Nubler, Laura James,

Jen Warren, and the PGR community in Birmingham Earth Sciences: Iacopo for the puns specifically, Alice, Luke, Lisa, Soph for one specific chromatography pun, Kate, Alastair, and many others.

Finally, thank you especially to Karolin, Rob Mackenzie, and my mother, for proof-reading when you didn't have to!

Table of Contents

Figures

Tables

Abbreviations

Acetyl-CoA – Acetyl Coenzyme A

ACL – Average Chain Length

BIFoR FACE – Birmingham Institute of Forest Research Free Air CO_2 Enrichment

br- - Branched chain

CAM – Crassulacean Acid Metabolism

CCM – Carbon Concentration Mechanism

CPI – Carbon Preference Index

DCM - Dichloromethane

EA-IRMS – Elemental Analyser/Isotope Ratio Mass Spectrometer

EECO – Early Eocene Climatic Optimum

FAME – Fatty Acid Methyl Ester

GC-FID – Gas Chromatograph/Flame Ionisation Detector

GC-IRMS – Gas Chromatograph/Isotope Ratio Mass Spectrometer

GC-MS – Gas Chromatograph/Mass Spectrometer

GDGT – Glycerol Dialkyl Glycerol Tetraether

g_s – Stomatal conductance

Ma – Million years before present

Malonyl-ACP – Malonyl Acyl Carrier Protein

Malonyl-CoA – Malonyl Coenzyme A

MeOH – Methanol

MEP - Methylerythritol Phosphate

MVA – Mevalonic Acid

n- normal (straight chained)

OTC – Open-top chamber

PO4 – Phosphate ion

RuBisCO – Ribulose Bisphosphate Carboxylase/Oxygenase

SST – Sea Surface Temperature

TEX_{86} – Tetraether Index of tetraethers consisting of 86 carbon atoms

TLE – Total lipid extract

UK'37 – Alkenone unsaturation index

VLCFA – Very long-chained fatty acid

VPD – Vapour pressure deficit

VPDB – Vienna Pee Dee Belemnite

Chapter 1: Background

Response of the terrestrial biosphere to CO_2

Terrestrial plants respond dynamically to changes in CO_2 concentration because, as photoautotrophs, the take-up of CO_2 during photosynthesis is the sole method for incorporating carbon into biomass for the vast majority of plants. Due to this dependence on CO_2, it is unsurprising that plants respond profoundly to CO_2 changes, at spatial scales ranging from biochemical responses within individual plant cells (Gonzalez-Meler et al., 2004; Terashima et al., 2014) to global scale shifts in species diversity and biomass production (Myneni et al., 1997; Zhu et al., 2016) and timescales ranging from near-instantaneous to evolutionary (Franks et al., 2013). Notably, in CO_2 levels higher than current ambient concentration, plants increase water use efficiency (Seibt et al., 2008; Franks and Beerling, 2009; Battipaglia et al., 2013; De Kauwe et al., 2013; Keenan et al., 2013; Adams et al., 2020; Walker et al., 2020). The effects of this are numerous; for example, under elevated atmospheric CO_2 concentrations, plants show a decrease in stomatal conductance and an increase in carbon assimilation (Medlyn et al., 2001; Nowak et al., 2004; Ainsworth and Long, 2005; Haworth et al., 2016).

However, changes observed in experimental setups do not necessarily reflect those seen in the real world. By their nature, experiments which grow plants under elevated CO_2 must raise concentrations quickly, far exceeding the rate of change of the partial pressure of CO_2 in air (pCO_2) forced by anthropogenic emissions, which itself far exceeds the rate of change of pCO_2 forced by natural processes in the geologic record, and which themselves vary hugely in rate as well as magnitude (Zhang et al., 2013; Turner and Ridgwell, 2016). Understanding the differences in response to pCO_2 over these different

timescales is key to understanding both evidence of environmental change detected in plant fossils, and the future response of the terrestrial biosphere to anthropogenic emissions. Furthermore, where predictions of terrestrial biosphere response to anthropogenic CO_2 rely on effects observed in short-term growth chamber experiments, the response of a few, generally small or immature, species grown in artificial conditions for a very small window of time assumes extrapolations of this response, perhaps carried out through ecophysiological modelling, to mature, global-scale terrestrial ecosystems are valid.

The full range of response of terrestrial ecosystems to climate change happens on geologic and evolutionary timescales, and occurs on the scale of the entire planet's climate system. However, increasing size, duration, and complexity of any climate change experiment is costly and time intensive. Shorter-term growth chamber experiments are cheap to perform and reproduce, but any scaling up spatially or temporally increases cost. Spatially, the largest experimental increases in CO_2 concentration occur *in situ*, as Free Air CO_2 Enrichment (FACE), where CO_2 is blown onto outdoor vegetation using tower structures (Figure 1). These experiments are typically on the scale of 10s of metres in diameter, and can run for at least a decade. Unlike smaller-scale experiments, FACE experiments examine the response of plant communities to CO_2 concentrations, and can determine CO_2 response alongside co-occurring weather fluctuations such as drought over multiple years, whilst minimising chamber effects, but are still too short-term and small-scale to examine the impacts of multiple tree generations, including evolutionary responses, or the effects of larger-scale ecological processes such as migration (Luo et al., 2011; Norby and Zak, 2011; Porter et al., 2015; Hart et al., 2019; U.S. Department of Energy, 2020).

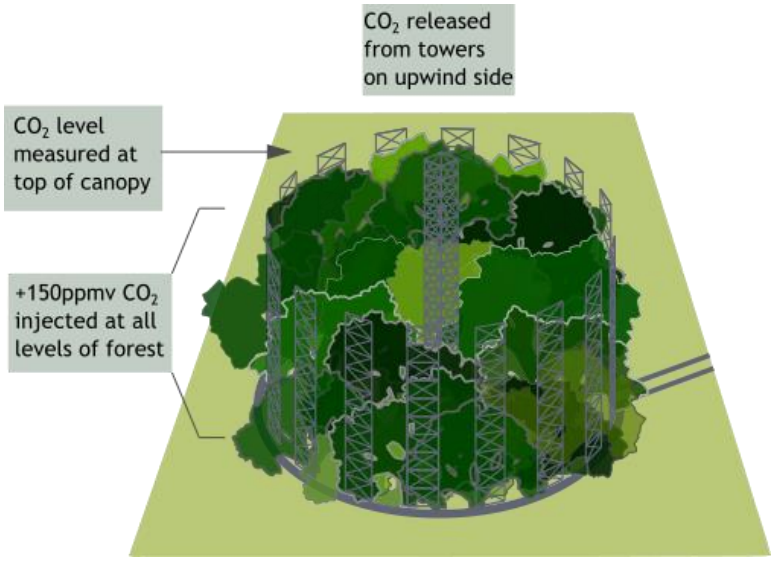

Figure 1: Schematic of a FACE array

More fundamentally, the response of ecosystems to environmental drivers takes place on timescales ranging from seconds (for near-instantaneous biological processes) to hundreds of millions of years, for macroevolutionary trends (Sunday et al., 2014). As a general rule, the longer timescale a method of recording response to CO_2 is, the less data can be collected and the more information is lost: growth chamber and FACE experiments allow in vivo observation of CO_2 response for the duration of their operation, but since technological advances only allow use of techniques after they are invented, the quality and quantity of available data has increased over time and observations taken further before the present are reduced in scope (Figure 2). For example, satellite-derived time series of land surface plant cover only date back to the 1980's (Tucker et al., 1985, 1986). Understanding plant response to CO_2 change on geologic timescales requires interpretation of fossil material, and much information which would have originally been contained within such material is unavoidably lost to diagenesis. Understanding plant response to CO_2 on the longest timescales requires

knowledge of how extinct plant species responded to CO_2, reconstruction of their biology after taphonomic and diagenetic processes alter their remains, and an accurate reconstruction of the CO_2 concentration under which they grew.

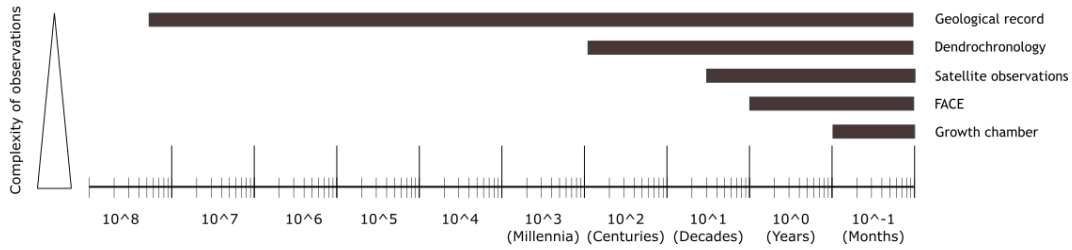

Figure 2: Timescales of archives of information on plant/climate response

Furthermore, the quality of observations of atmospheric CO_2 with which to evaluate plant response also decreases further back in time. Direct continuous measurements of atmospheric CO_2 (Keeling et al., 2001). Prior to this, the concentration of CO_2 contained within bubbles in ice cores can be measured: the oldest recorded ice core CO_2 measurements are around 800,000 years in age (Bereiter et al., 2015). CO_2 concentrations previous to this are reconstructed using a wide array of proxy sources, including the $\delta^{11}B$ of planktic and benthic foraminifera (Rae et al., 2011; Henehan et al., 2013), the $\delta^{13}C$ of organic material produced by photosynthetic algae (Pagani, 2014; Witkowski et al., 2018),the $\delta^{13}C$ of soil carbonate (Breecker, 2013), characteristics of plant stomata and $\delta^{13}C$ (Schubert and Jahren, 2012; Franks et al., 2014; McElwain and Steinthorsdottir, 2017; Konrad et al., 2020), and characteristics of the sodium carbonate mineral nahcolite (Jagniecki et al., 2015).

Each of these proxies has its own limitations, and its own timescale for which it can be observed. In general, as the Earth system becomes less similar to the modern in geologic time, the less reliable proxies become, as most rely on parameters calibrated from the

behaviour of species in the modern (Henehan et al., 2013; Konrad et al., 2020; Zhang et al., 2020), and information on other environmental variables which are needed for proxy calculation become harder to determine.

As with terrestrial ecosystems, CO_2-consuming photoautotrophs constitute the base of almost all marine food webs, meaning increases in CO_2 concentration also influence marine systems. Also similarly to terrestrial systems, the response of marine ecosystems to changes in CO_2 concentration occurs over many different timescales and through a myriad of different processes (Rhein et al., 2013). Unlike land plants, oceanic photosynthesisers do not limit diffusive CO_2 acquisition via stomata: instead, an increase in atmospheric (and therefore dissolved) CO_2 consequently leads to an increase in carbon within the cell (Freeman and Hayes, 1992; Rau et al., 1992; Pagani, 2014). Similar to C_4 photosynthesis in land plants, some marine algae also employ carbon concentration mechanisms to further increase CO_2 flux into the cell (Laws et al., 1997; Iniguez et al., 2020). However, unlike land plants, oceanic ecosystems are often tightly limited by the concentrations of nutrients available for growth, and the increase in dissolved CO_2 available is unlikely to translate into large increases in biomass without a co-occurring increase in nutrient supply to the ocean (Moore et al., 2013).

Changes to CO_2 concentration induce other changes to the physical ocean, which in turn induce other changes on oceanic photosynthesisers and the ecosystems which rely on them. Notably, a rapid increase in dissolved CO_2 decreases the pH of seawater by forming carbonic acid, leading to ocean acidification (Rhein et al., 2013). Many marine organisms form structures out of calcium carbonate that may be vulnerable to the associated decrease in carbonate saturation. However, the timescale at which oceanic

pH changes has a large impact on the biotic response, and organisms may be less susceptible to changes in oceanic carbonate saturation in the geologic record than to that seen in laboratory studies and due to anthropogenic change as evolutionary adaptation could occur (Hönisch et al., 2012; Sunday et al., 2014). In addition, as with terrestrial ecosystems, changes in atmospheric CO_2 outside of a laboratory always induce changes to other aspects of the oceanographic system, including increased temperature and changes to stratification and circulation patterns (Rhein et al., 2013). Therefore, evaluating the impacts of CO_2 on marine primary producers must include some consideration of indirect changes in the environment due to CO_2 (Riebesell and Gattuso, 2015).

Geological biomarkers

The geologic record presents an opportunity to study the effects of changes to pCO_2 and other climatic parameters on timescales where direct observations are not available. However, the full range of information contained within an organism is irreversibly lost after an organism's death, as decomposition destroys or fundamentally alters the material which originally was the organism. Isolated organic compounds which survive this process in some form and retain information on the conditions of their formation are known as geologic biomarkers (Eglinton and Eglinton, 2008).

In order to be defined a geologic biomarker, a molecule must:

1) Be produced by either a single, known clade of organisms, and be specific to it, or be produced by multiple clades which respond similarly to environmental changes as each other. It must be identifiable in the sediment as only being produced by this group.

2) Preserve readily within sediment on geologic timescales, or have a known, reliable decay product which does so.

In order to determine biomarker-based response of plants to their environment, biomarkers for both a) environmental conditions, and b) plant response must be used. It should be noted that the next section is not an exhaustive list of all proposed environmental proxies, nor of plant biomarkers, and non-biomarker-based approaches for environmental reconstruction (e.g. inorganic trace element and/or isotopic ratios in foraminiferal calcite) and plant response to environment (e.g. the morphology of plant macrofossils) are also used (Royer, 2013; Judd et al., 2022).

Biomarker-based reconstruction of pCO_2

The carbon isotopic composition of marine algal biomarkers can be used to reconstruct CO_2, but is limited by understanding of both algal biology and additional environmental conditions, such as temperature and nutrient concentration, which influence it. The $C_{37:2}$ alkenone biomarker is commonly targeted for this method for reconstruction, as it is produced by a small group of haptophyte algae whose biology is well known from modern observations, and uncertainties relating to changes in algal biology can be minimised compared to other biomarkers whose producers may not be as tightly constrained (de Bar et al., 2019).

Mechanically, the proxy uses the $\delta^{13}C$ of algal biomarkers to reconstruct the total $\delta^{13}C$ of algal cells, assuming constant biosynthetic fractionation (Pagani, 2014). The $\delta^{13}C$ of co-occurring planktic foraminifera are used to reconstruct the $\delta^{13}C$ of the CO_2 gas, which is then reconstructed to give the $\delta^{13}C$ of aqueous CO_2 via an empirical equation (Mook et al., 1974). The fractionation between the $\delta^{13}C$ of algal cells and the aqueous CO_2 from

which they grew, or ε_p, is inversely proportional to the concentration of aqueous CO_2: $[CO_2]_{aq}$ is reconstructed from ε_p and empirically derived parameters representing the enzymatic fractionation during photosynthesis (ε_f) and the total of physiological parameters also influencing algal $\delta^{13}C$ (b), including the concentration of phosphate, cell size, and growth rate (Laws et al., 1995, 1997; Bidigare et al., 1997; Henderiks and Pagani, 2007, 2008). Finally, the relationship between $[CO_2]_{(aq)}$ and $[CO_2]_{(g)}$ can be determined via physical principles. Use of the alkenone pCO_2 proxy is complicated during glacial/interglacial periods by potential use of carbon concentration mechanisms (CCMs) but match well with estimates made in higher CO_2 conditions (Stoll et al., 2019; Badger, 2021). Because of the influence of CCMs, decreases in sensitivity of the proxy at high $[CO_2]$, and the absence of $C_{37:2}$ alkenones in sediments earlier than the Eocene, the proxy is most useful at moderate CO_2 concentrations during the Cenozoic. Outside of this time interval, the proxy can be applied qualitatively or quantitatively to more generic algal biomarkers such as phytane (Witkowski et al., 2018) or short-chain *n*-alkanes (Naafs et al., 2016). However, as one of the major sources of uncertainty in the alkenone proxy are biological mechanisms which alter response to CO_2 (Zhang et al., 2020) despite the producers of alkenones being known and their biology well constrained in the modern, use of more generic algal biomarkers risks unconstrained biological errors.

Many mechanistic proxies for CO_2, including both algal biomarker $\delta^{13}C$ and others such as leaf gas exchange, require a reconstruction of temperature for their final calculation, as the physical and physiological processes linking CO_2 to the measured proxy are also temperature controlled (Hayes et al., 1989; Pagani, 2014). With algal $\delta^{13}C$ specifically, an accurate temperature reconstruction is essential to the use of the proxy, as both the magnitude of ε_p and the solubility of CO_2 in water are heavily dependent on it. Two

common methods of reconstruction of sea surface temperature (SST) in order to use as inputs for the determination of pCO_2 from algal $\delta^{13}C$ are discussed below.

Biomarker-based reconstruction of temperature

As changes in temperature fundamentally alter chemistry and response to changes in temperature are key to the survival of many organisms (Arrhenius, 1889), many biomarker-based temperature proxies have been proposed. These often consist of the ratios of multiple forms of a class of molecules, which are adjusted to maintain optimal physical properties for their function under a range of temperatures (Eglinton and Eglinton, 2008). The magnitude of all isotope effects are controlled by temperature, meaning all isotope-based proxies technically respond to temperature, but the magnitude of such effects may be small when compared to the effects of other environmental or biological factors (Bigeleisen and Mayer, 1947; Friedman et al., 1977; Pancost and Boot, 2004).

Alkenones and $U^{K'}_{37}$

Alkenones are a group of long-chained, unsaturated methyl and ethyl ketones that are solely produced by a single, monophyletic group of haptophyte algae (Marlowe et al., 1990). Alkenone-producing algae likely first originated in the Cretaceous, and the $C_{37:2}$ alkenone is first found in sediments dating from the early Eocene (Farrimond et al., 1986; Marlowe et al., 1990; Brassell et al., 2004; Brassell, 2014).

The relative proportions of the C_{37} di- and triunsaturated ketones are used for temperature reconstruction via the alkenone unsaturation index ($U^{K'}_{37}$) defined as

$$UK'_{37} = \frac{C_{37:2}}{C_{37:2}+C_{37:3}}$$

(1)

Since alkenones are produced by a single clade of haptophyte algae through geologic time and temperature reconstructions produced from $U^{K'}_{37}$ broadly match trends observed by other proxies, it is likely that either the relationship between $U^{K'}_{37}$ and temperature persists geologically, or every independent method for determination of palaeotemperature is also consistently wrong (Brassell, 2014). Changes to the processes of alkenone formation may affect the $U^{K'}_{37}$ ratio in ways that may not be detectable, but by using a molecule limited phylogenetically in its production, uncertainties are minimised in alkenones (Tierney and Tingley, 2018). In addition, alkenone-producing haptophytes leave additional fossil traces that can further be used to constrain changes to their biology (McClelland et al., 2017; Wilkes et al., 2018). However, their precise biological purpose and the mechanistic nature of the relationship between alkenone production and temperature is unknown: alkenones themselves are most likely synthesised as a store of energy but the precise reason for their temperature dependence is unclear (Eltgroth et al., 2005; Herbert, 2013). Therefore, the relationship between $U^{K'}_{37}$ and temperature is entirely empirical, and could theoretically shift on long timescales.

(Prahl et al., 1988) where $C_{37:2}$ and $C_{37:3}$ represent the relative concentrations of the di- and triunsaturated ketones respectively. This index correlates empirically with temperature; the most commonly used temperature calibration is

$$T(°C) = \frac{UK\prime_{37} - 0.039}{0.034}$$

(2)

(Prahl et al., 1988). Although the $U^{K'}_{37}$ index correlates with parameters such as light levels and nutrient stress, these influences are considered secondary to temperature dependence (Versteegh et al., 2001; Prahl et al., 2003; Conte et al., 2006)

The linear temperature relationship described by Equation 2 is considered a good approximation of core top determinations of alkenone temperature, but may not fully reflect temperature under specific circumstances (Müller et al., 1998; Conte et al., 2006; Tierney and Tingley, 2018). The relationship is fundamentally limited at its upper and lower ends where the concentration of $C_{37:2}$ for cold or $C_{37:3}$ for warm temperatures becomes very small. The $C_{37:3}$ is entirely absent at very warm temperatures equating to 29°C using the calibration of (Prahl et al., 1988), meaning the proxy cannot provide quantitative temperature information above this point. Below but near this threshold, and equivalently at temperatures <8°C, the proxy may also increase in uncertainty and may not be entirely linear (Sikes et al., 1997). Conte et al. (2006) suggested a third-order polynomial relationship would better reflect very high and very low temperatures, and the relationship becomes less certain as the $C_{37:2}$ approaches saturation. It is debated whether the relationship becomes nonlinear at these temperatures. Pelejero and Grimalt, (1997) and Kienast et al. (2012) suggest the existing linear calibration is accurate, whereas Sonzogni et al. (1997), Müller et al. (1998), Conte et al. (2006) and Tierney and Tingley (2018) argue that temperatures are underestimated by Equation 2 as the proxy approaches saturation.

Physical measurement of the proxy becomes an issue at high saturations, which may further compound this issue. Where the $C_{37:3}$ is only present in very low concentrations, irreversible adsorption to capillary columns during chromatographic analysis can further reduce recorded concentration, leading to a warm bias and increased standard deviation (Villanueva and Grimalt, 1996). It has been suggested that nonlinear temperature calibrations can partially be attributed to column biases rather than an inherent feature of alkenone production (Herbert, 2013), further complicating determination of potential biases at warm temperatures, but the effect can persist even when low concentrations of the $C_{37:3}$ are accounted for (Bentaleb et al., 2002).

GDGTs and TEX_{86}

Isoprenoidal glycerol dialkyl glycerol tetraether lipids (GDGTs) are membrane lipids that are in marine settings primarily produced by Thaumarchaeota (Schouten et al., 2013). Isoprenoidal GDGTs are GDGTs containing two biphytane chains connected to glycerol that contain varying numbers of cyclopentane and cyclohexane rings (Figure 3). They are abundant and ubiquitous in sediment, and resistant to degradation on geologic timescales, allowing their use to as an archive of palaeoclimate information at least into the Mesozoic (Jenkyns et al., 2012).

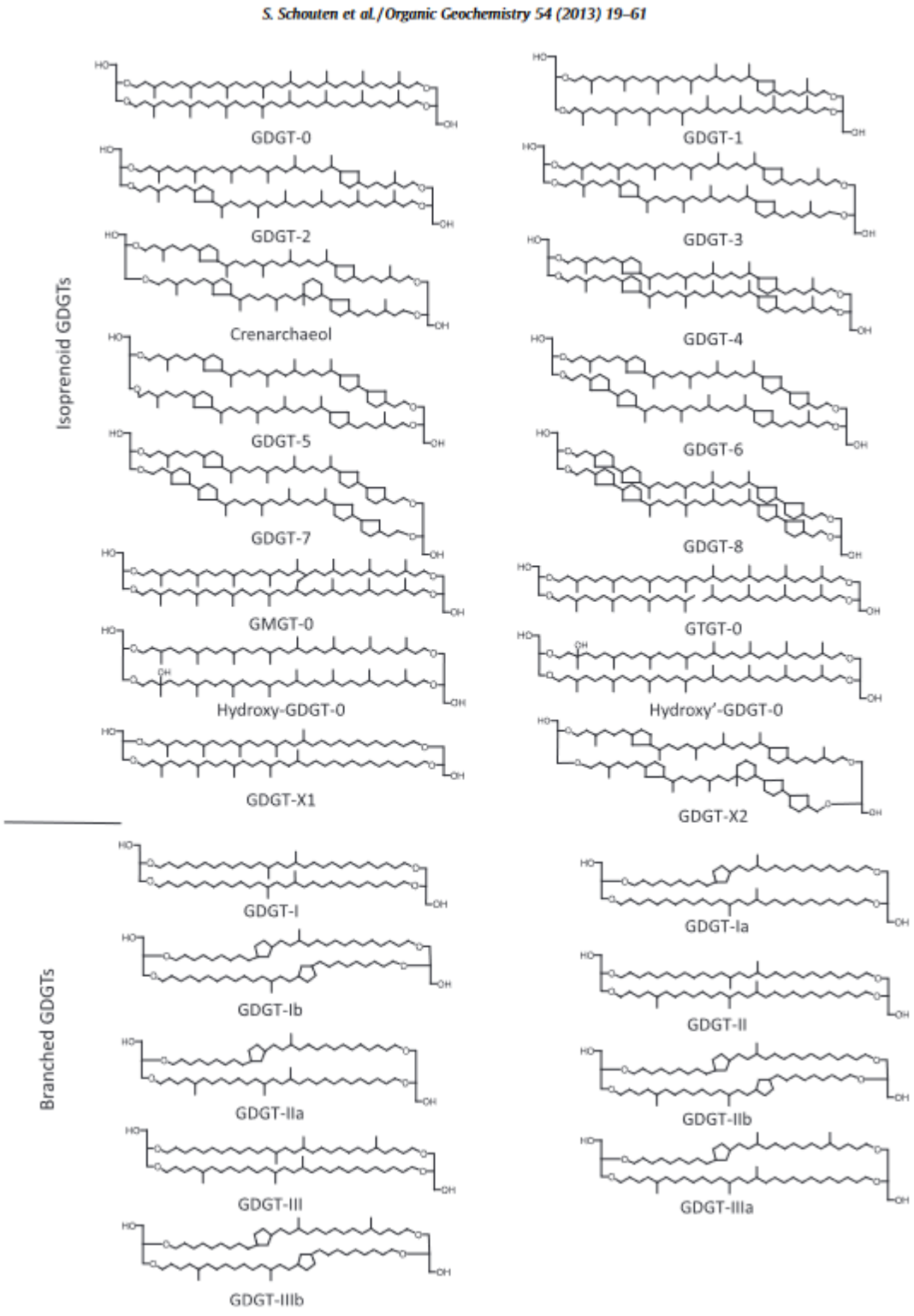

Figure 3: Chemical structure of GDGTs. From Schouten et al. (2013).

The relative abundance of different cyclopentane moieties in isoprenoidal GDGTs correlates with water temperature (Schouten et al., 2002; Kim et al., 2010). This is quantified as tetraether index of tetraethers consisting of 86 carbon atoms (TEX_{86}), which uses the relative abundance of a selection of tetraethers containing 86 carbon atoms, defined as

$$TEX_{86} = \frac{(GDGT-2)+(GDGT-3)+(cren')}{(GDGT-1)+(GDGT-2)+(GDGT-3)+(cren')}$$

(3)

(Schouten et al., 2002) where GDGT-1, -2, and, -3 represent GDGTs with the respective number of cyclopentane rings and cren' is the regio-isomer of crenarchaeol (Figure 3). TEX_{86} linearly correlates with sea surface temperature according to:

$$TEX_{86} = 0.015T + 0.28$$

(4)

where T represents sea surface temperature (SST) in degrees Celsius (Schouten et al., 2002). A more sophisticated approach uses Bayesian analysis to produce a probability distribution of predicted temperatures, and accounts for spatial variation in modern GDGT distributions, while increasing uncertainty in data-poor areas (Tierney and Tingley, 2014).

TEX_{86} temperature reconstructions match calibrations well up to 30°C , while estimates of SST outside this range may be more uncertain as modern oceans rarely reach these temperatures, limiting the possibility for modern calibration of the proxy (Dunkley

Jones et al., 2020). Fundamentally, modern calibrations of the TEX_{86} proxy use the range of SST found in modern oceans, which generally do not exceed 30°C. Culture studies do not include the full range of modern GDGT producers, and often fail to reproduce the same temperature trends as core-top data, meaning their use for calibration of temperature reconstruction above 30°C is questionable. It is suggested that changes to the archaeal community composition may control GDGT distributions, and that the response of GDGTs to temperature may partially be driven by shifts toward communities more suited to different temperatures that also produce different GDGT distributions, rather than, as with alkenones, changes in production of GDGTs within individual species (Elling et al., 2017; Bale et al., 2019).

Since SST in the geologic record can be >30°C and the stability of archaeal community compositions are hard to reconstruct on evolutionary timescales, use in hothouse conditions such as the Eocene requires extrapolating the GDGT-temperature relationship beyond the empirical relationships observed in the modern, and introduces further uncertainties. A machine learning approach to GDGT-based palaeothermometry has attempted to account for this by increasing uncertainty in temperature estimates where GDGT distributions are dissimilar to any observed in the modern, allowing for identification of data and time intervals where temperature reconstructions are most accurate (Dunkley Jones et al., 2020).

Plant wax biomarkers

Land plants produce many molecules that can be used as biomarkers (Freeman and Pancost, 2014). Of these, many are particular to certain plant groups (e.g. di- and triterpenoids for angiosperms and gymnosperms, respectively (Diefendorf et al., 2014)).

Long-chained *n*-alkyl lipids, however, are a class of land plant biomarkers whose origin is largely constrained to this group, but are ubiquitous within it (Busta and Jetter, 2018). Higher plant *n*-alkyl lipids are a suite of molecules found on plant surfaces which are characterised by long (>C_{20}), straight-chained *n*-alkyl tails, and form via the acetogenic pathway of biosynthesis; this long *n*-alkyl tail leads to stability on geologic timescales (Buggle et al., 2010; Diefendorf et al., 2015c). Compound types commonly present include *n*-fatty acids, *n*-alkanols, *n*-aldehydes and *n*-alkanes (Samuels et al., 2008).

n-Alkyl lipids are the dominant constituent of plant waxes, which form a protective layer on the surfaces of plants. As *n*-alkyl tails are extremely hydrophobic, the presumed primary function of plant waxes is to prevent water loss through the plant cuticle as a waterproofing agent (Riederer and Schneider, 1990). As waxes fulfil essential functions in mediating plant interactions with the environment, and are ubiquitous in land plants, they are presumed essential for plants' survival on land (Gülz, 1994; Xue et al., 2017). Although other plant organs are also covered in wax, *n*-alkyl lipid concentration is significantly higher on the leaves, and thus when studied in the modern, the focus is generally on the wax present specifically on leaves (Mueller et al., 2012).

Biosynthesis of n-alkyl lipids

n-Alkyl lipids are synthesised from a substrate of acetyl coenzyme A (acetyl CoA) and elongated by sequential addition of acetyl-CoA derived carbon. Initial elongation up to a C_{18} unit takes place within the stroma of the plastid within epidermal cells using malonyl-CoA derived from acetyl-CoA (Wakil, 1961; Kunst and Samuels, 2003). The molecule is then transported to the endoplasmic reticulum for elongation using malonyl-ACP also derived from acetyl-CoA, forming a final *n*-alkyl-ACP, of 20-34 C in length.

Different *n*-alkyl lipids are then formed via different pathways: *n*-Alkyl-ACP is initially converted to *n*-aldehydes, then either via decarbonylation to *n*-alkanes, secondary alcohols, and *n*-ketones, or via acyl-reduction to primary alcohols and wax esters (Post-Beittenmiller, 1996). As the initial acetyl-CoA and derived moieties used for elongation all contribute 2 carbons to the chain, *n*-alkyl-ACPs generally contain an even number of carbons: a carbon is lost during decarbonylation, meaning *n*-alkanes, secondary alcohols, and *n*-ketones generally have odd numbers of carbons in their skeletons (Busta and Jetter, 2017). Smaller amounts of odd-chained *n*-alkyl-ACP units and resulting even-chained decarbonylation products and odd-chained acyl-reduction products are produced via the same elongation process using an initial unit of propionate (Zhou et al., 2010). The predominance of odd-over-even for products of decarbonylation and even-over-odd for products of acyl reduction persists in *n*-alkyl lipids found in the sedimentary record, and is one of the key indicators that *n*-alkyl lipids found dissociated from their source originated from land plants (Cranwell, 1981).

Long-chain *n*-alkyl lipids exhibiting the same alternating patterns of abundance are found in the protective coatings of insects (Chikaraishi et al., 2013) and fungal spores (Oro et al., 1966) but the contribution of these sources to the geologic record is considered minor compared to the contributions of plants since their biomass is much lower. Although individual locations may show alternating patterns of abundance due to alternate sources of *n*-alkyl compounds to higher plants (Zegouagh et al., 1998), they are generally considered diagnostic of this source (Freeman and Pancost, 2014).

n-*Alkanes*

The *n*-alkane component is the most stable geologically due to the lack of functional groups (Cranwell, 1981). Due to this, the relative abundance of alkanes within leaf wax, and to the ease of their extraction, *n*-alkanes are the most commonly used *n*-alkyl lipid biomarker (Pancost and Boot, 2004; Jetter et al., 2006). Leaf wax *n*-alkanes have been reported to contain chains of 21 to 37 carbons in length, but which homologues are present within this range, and at what relative proportions, varies widely between plants. In general, plant wax *n*-alkane distributions are characterised by homologues ranging from C_{25}-C_{33}, with the highest abundance homologue between C_{27} and C_{31} (Bush and McInerney, 2013).

Plant wax *n*-alkane homologue variability and associated proxies

It was initially suggested that *n*-alkane chain length distributions could be used for chemotaxonomic purposes, where chain length distributions characteristic of species could be used to infer their presence in the geologic record (Eglinton et al., 1962). Subsequent research has found, however, that the relatively small number of homologues and wide variability within plant groups mean that, although individual plant *n*-alkane distributions may differ substantially, few trends are strong and consistent enough to allow attribution to specific plant groups in the geologic record (Bush and McInerney, 2013). The distribution patterns of *n*-alkanes vary widely between species at individual study sites, indicating species specificity, and are partially phylogenetically controlled (Maffei et al., 2004; Rommerskirchen et al., 2006; Diefendorf et al., 2015b) but outside of specific contexts, the overlap between different clades or functional groups precludes the use of *n*-alkane distributions to determine species

composition in the geologic record (Bush and McInerney, 2013). Modern use of *n*-alkane homologue distributions to determine palaeoclimate and palaeoenvironmental conditions has focussed on changes in different metrics of *n*-alkane distributions, and interprets these in the context of both plant clades and environmental conditions that may influence the relative proportions of homologues present.

Average Chain Length

Average Chain Length (ACL) represents the weighted mean average carbon chain length of all homologues of *n*-alkanes present within a sample, and is defined as

$$ACL_{21-35} = \sum_{n=21}^{35} \frac{n[C_n]}{[C_n]}$$

(5)

(Poynter et al., 1989) where each C_n represents the concentration of each *n*-alkane homologue, and *n* represents the number of carbons of the *nth* homologue. The range of homologues used to calculate ACL are variable; in its standard form, all homologues present are used to calculate ACL. In sediment samples where shorter homologues ($<C_{25}$) typical of algal or macrophyte inputs are abundant, ACL can be calculated using a narrower range of homologues more typical of higher plants (Poynter and Eglinton, 1990).

Along environmental gradients and in modern plants, ACL has been shown to correlate positively with temperature and aridity (Dodd et al., 1998; Bendle et al., 2007; Sachse et al., 2010; Leider et al., 2013; Tipple and Pagani, 2013; Carr et al., 2014; Badewien et al., 2015; Bush and McInerney, 2015; Eley and Hren, 2018; Wang et al., 2018b; Andrae et al., 2019; Teunissen van Manen et al., 2019; Lu et al., 2020). However, neither two-way

relationship is conclusive on its own. When correlations are present, they tend to show large residuals and reflect different aspects of environmental conditions (e.g. mean annual temperature vs summer temperature (Wang et al., 2018a)), several studies fail to detect a measurable correlation with environment in ACL at all (Carr et al., 2014; Schwab et al., 2015), and several found some species correlated with temperature/precipitation and some did not along the same gradient (Hoffmann et al., 2013; Cerda-Peña et al., 2020). A global compilation of ACL vs temperature data failed to detect a measurable correlation, suggesting such trends are limited to specific regions (Diefendorf and Freimuth, 2017). Aridity data is less often reported and often difficult to deconvolve from temperature effects, but also appears to covary inconsistently with ACL (Hoffmann et al., 2013; Bush and McInerney, 2015).

Sedimentary *n*-alkanes represent an integrated signal of *n*-alkane contribution to the sediment record, which reduces the range of ACL observed from that of many individual plants into one average. This may act to average the effects of individual species on ACL, leaving a common climate signal: for example, soil *n*-alkane ACL has been suggested as a quantitative proxy for Vapour Pressure Deficit (VPD) but residuals remain large even with this averaging (Eley and Hren, 2018). However, questions remain over the processes controlling *n*-alkane integration to soil, lake and marine sediment archives (Diefendorf and Freimuth, 2017). Furthermore, in the geologic record, since species composition contributing to a sample is not known and often cannot be estimated, changes in ACL with environment must be deconvolved from potentially much larger shifts in ACL associated with changes in species composition, while species composition is also potentially changing due to shifts in the climate (Schouten et al., 2007; Smith et al., 2007). ACL is often reported in a palaeoclimatological context, but although

relationships between ACL and environment are suspected, they are often difficult to prove, and ACL is rarely used as an indicator of a specific environmental shift in isolation. It is instead used as a combined metric of environment and plant community: a change in ACL can be used alongside other proxies to support the overall interpretation of a record.

Carbon Preference Index

Carbon Preference Index (CPI) represents the proportion of odd to even chained *n*-alkanes present in a sample. It is defined as:

$$CPI = \frac{[\sum C_{odd(C21-33)} + \sum C_{odd(C23-33)}]}{2 \sum C_{even(C22-32)})}$$

(6)

(Bray and Evans, 1961; Marzi et al., 1993). Almost all analysed land plants have a CPI>1, as is expected given their biosynthesis (Reddy et al., 2000; Zhou et al., 2010; Bush and McInerney, 2013). CPI is most often used as a metric applied to sedimentary *n*-alkanes to determine whether the original *n*-alkane signal may have been overprinted (Castañeda et al., 2009). In land plants themselves, CPI has a huge range: the average CPI recorded in the dataset of (Bush and McInerney, 2013) is 11.6 (meaning odd-chained homologues are 11.6 times more abundant than even) and 90% of recorded leaves have CPI<25.

CPI of plants themselves are rarely used as a potential palaeoclimate proxy, and few trends of CPI with environment or plant type have been noted. Gymnosperms tend to have a lower CPI than angiosperms, and CPI appears to be somewhat controlled by phylogeny (Diefendorf et al., 2015b). Unlike ACL, CPI has not shown a relationship with

temperature or aridity on a regional scale (Carr et al., 2014; Bush and McInerney, 2015; Wang et al., 2018a)

An extremely small increase in the recorded abundance of low concentration, even-chained homologues can dramatically alter CPI. If an *n*-alkane sample is measured at extremely low concentration and no even-chained homologues are detected, CPI tends to infinity. If the same sample was run at higher concentration and it were determined that even-chained alkanes were 100 times less abundant than odd, CPI would be recorded as ~100: still extremely high, but very different from the initial result. Therefore, measurement of CPI requires careful determination of the difference between low concentration and no concentration of even-chained homologues, and care must be taken to run samples at a high enough concentration to detect these differences.

Because of the wide range in *n*-alkane CPI present within plants, the use of CPI as a measure of fidelity to higher plant source is not generally quantitative. It is most often used as a threshold, where CPI<1 indicates samples should be considered potentially altered diagenetically. Alternatively, a low CPI may indicate substantial contribution of altered *n*-alkanes below a certain chain length, but defining CPI to include only longer chain lengths may still show substantial odd-over-even preference: in these cases, shorter homologues should be excluded when calculating ACL or $\delta^{13}C$ of higher plant *n*-alkanes in a sample (Bendle et al., 2007).

Concentration

The total concentration of *n*-alkanes per dry weight of leaf varies hugely, both within and between species, and has been detected in a range from <1 to >5000 μg/g (Bush and McInerney, 2013). In modern plants it is typically measured as *n*-alkanes per gram of

dried leaf material, but is sometimes reported as *n*-alkanes per leaf area. Since leaf density is not constant and area divided by weight is a proxy for plant growth rate (Poorter et al., 2009), this is a potentially important distinction, but due to the difficulty in recording leaf area as opposed to weight, it is less often reported and the two should broadly correlate on a regional scale.

n-Alkane concentration in the sedimentary record is rarely comparable to *n*-alkane calculated directly from modern plants by dry weight, as *n*-alkanes are dissociated from source material and the original dry leaf weight is lost. Furthermore, *n*-alkanes are potentially transported thousands of kilometres through both riverine and aeolian transport mechanisms, and the precise size of the catchment the *n*-alkanes originated from is generally unknown, let alone the original volume of vegetation present (Vogts et al., 2012; Yang et al., 2021).

Knowledge of specific plant groups' patterns in *n*-alkane concentration can however be useful in interpretation of other *n*-alkane data. For example, succulents in South Africa have much higher *n*-alkane concentration than co-occurring vegetation, meaning they may give an outsize contribution to *n*-alkane sedimentary records in this area. Since succulents commonly use the Crassulacean Acid Metabolism (CAM) photosynthetic pathway, and CAM plants have a differing $\delta^{13}C$ signature to both C_3 and C_4 plants, this may bias a *n*-alkane $\delta^{13}C$ record produced in the region (Carr et al., 2014). Similarly, gymnosperms produce lower concentrations of wax than angiosperms (Bush and McInerney, 2013), although it has been suggested that this may be limited to northern hemisphere taxa (Diefendorf et al., 2015b): therefore, where *n*-alkane records are used

in regions containing both clades, knowledge of *n*-alkane concentrations may suggest that the record is biased toward angiosperms (Diefendorf et al., 2011).

Plant wax *n*-alkane isotopes

Plant wax *n*-alkanes contain both carbon and hydrogen atoms, the isotopic composition of which are a powerful tool in interpretation of both the environments in which their progenitor plants grew, and their response to said environment. In general, the $\delta^{13}C$ of *n*-alkanes are interpreted as representing the relative proportions of photosynthetic mode of the plants which contributed to a sample (O'Leary, 1988; Cerling et al., 1997; Tipple and Pagani, 2010) or, in the absence of C_4 plants, species community composition and response to changes in water availability (Schouten et al., 2007; Tipple et al., 2011; Schlanser et al., 2020). Hydrogen isotopes are generally interpreted in terms of the source δD of precipitation and, potentially, evapotranspiration (Sachse et al., 2012; Kahmen et al., 2013).

$\delta^{13}C$

The main factors influencing the $\delta^{13}C$ of *n*-alkanes can be summarised as the $\delta^{13}C$ of atmospheric CO_2, fractionations during the photosynthetic fixation of CO_2 into glucose, and post-photosynthetic fractionation during *n*-alkane biosynthesis (Figure 4). The $\delta^{13}C$ of plant tissue is heavily influenced by the photosynthetic mode of the plant: the average C_3 plant $\delta^{13}C$ is around -28.5‰, whereas the average C_4 plant $\delta^{13}C$ is around -12‰ (Cerling and Harris, 1999; Kohn, 2010). CAM photosynthesis produces a broader range of isotopic compositions and, for plants which display facultative CAM, switches between photosynthetic mode based on environment can further alter $\delta^{13}C$ (Osmond et al., 1975; Mooney et al., 1977). In aquatic plants, further $\delta^{13}C$ shifts can be caused due to

adaptations to low dissolved CO_2 levels: use of bicarbonate as well as dissolved CO_2 leads to an increase in $\delta^{13}C$, and it is possible that the aquatic carnivorous plant genus *Utricularia* may have anomalously depleted $\delta^{13}C$ in some cases, due to incorporation of carbon from their prey (Mendonça et al., 2013; Warren et al., 2021). This thesis will focus on C_3 photosynthesis only, as a) the majority of modern plants use this mode, including all of those studied here, and b) it is assumed that all plants prior to the evolution of C_4 plants at some point in the Cenozoic used this mode (Tipple and Pagani, 2007).

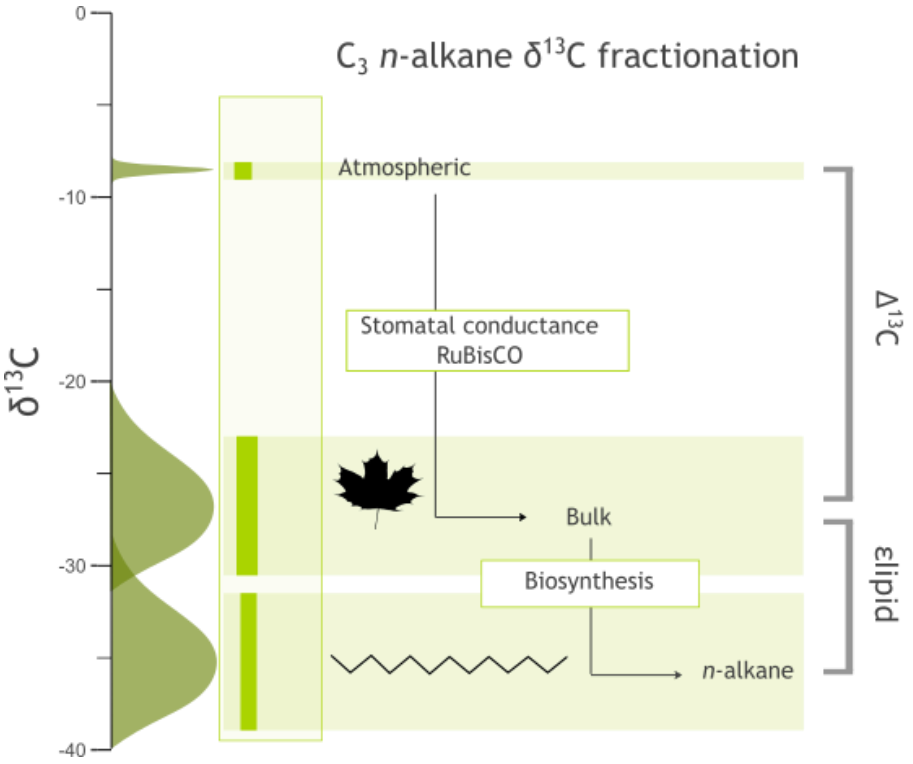

Figure 4: Average $\delta^{13}C$ of atmospheric CO_2, bulk $\delta^{13}C$, and *n*-alkane $\delta^{13}C$ in C_3 plants (data from Cerling and Harris (1999), Keeling et al. (2001); and Tipple and Pagani, (2010))

$\delta^{13}C$ of atmospheric CO_2

On a regional scale, the $\delta^{13}C$ of atmospheric CO_2 is generally consistent spatially (Keeling et al., 2005b). It is, however, currently decreasing at a geologically unprecedented rate due to anthropogenic climate change, as the $\delta^{13}C$ of fossil fuels is extremely isotopically light (Andres et al., 2000; Saurer et al., 2004). On geologic timescales, atmospheric $\delta^{13}C$ is also variable: over the course of the Cenozoic it has varied by around 2‰ (Tipple et al., 2010). Atmospheric $\delta^{13}C$ is ultimately controlled by carbon cycle dynamics, and can be reconstructed on geologic timescales from the carbon isotopic composition of CO_2 bubbles in ice cores and the $\delta^{13}C$ of planktic foraminiferal tests (Francey et al., 1999; Tipple et al., 2010). Generally, the $\delta^{13}C$ of atmospheric CO_2 is well constrained in comparison to the fractionations applied by biological processes within plants (Diefendorf et al., 2015a). A signal of atmospheric $\delta^{13}C$ is observed in the $\delta^{13}C$ of C_3 plants through the phanerozoic, but fractionations during and after photosynthesis due to other biological and environmental factors mean use of C_3 plant material as a tracer of atmospheric $\delta^{13}C$ is not practical, partially due to the presence of other, better constrained methodologies (Arens et al., 2006; Lomax et al., 2012).

It should be noted that the direct impacts of atmospheric $\delta^{13}C$ on photosynthetic and post-photosynthetic fractionations are unknown. This is of relevance as experimental studies examining the impact of pCO_2 on plant $\delta^{13}C$ generally use CO_2 gas which is far more depleted in ^{13}C than atmospheric CO_2. Thus, it is possible that in these studies, including those presented later in this thesis, effects on carbon isotope fractionation and plant biology in general attributed to CO_2 changes may be due to co-occurring changes in atmospheric $\delta^{13}C$ (H. Zhang et al., 2019; Lomax et al., 2019). There is currently no known

mechanism by which this would substantially occur, and no direct evidence it is the case, but the potential for an effect should not be discounted.

Carbon isotope fractionations during photosynthesis

Ultimately, the source of carbon for photosynthesis is CO_2. In C_3 plants, this imparts a large isotopic fractionation: the current $\delta^{13}C$ of the atmosphere is ~-8.7‰, whereas the average $\delta^{13}C$ of C_3 plant tissue is between -23 and -31.5‰ (Kohn, 2010).

The difference in $\delta^{13}C$ between atmospheric and bulk plant tissue in C_3 plants is expressed in terms of carbon isotope discrimination, $\Delta^{13}C$, according to:

$$\Delta^{13}C = \frac{\delta_{atmo} - \delta_{plant}}{1 + \delta_{plant}}$$

(7)

(Farquhar et al., 1989) where δ_{atmo} and δ_{plant} represent the $\delta^{13}C$ of atmospheric and plant photosynthate respectively. $\Delta^{13}C$ is controlled according to:

$$\Delta^{13}C = a + (b - a)\frac{C_i}{C_a}$$

(8)

(Farquhar et al., 1989) where *a* represents fractionation due to diffusion of CO_2 in air, and is approximately 4.4‰ (Craig, 1953; Cerling et al., 1991), *b* is fractionation due to carboxylation, and is mainly caused by enzymatic fractionation of ribulose-1,5-bisphosphate carboxylase-oxygenase (Rubisco), approximately 29‰ (Roeske and O'Leary, 1984), and C_i and C_a are the partial pressures of CO_2 in the intercellular space and atmosphere respectively. Equation 8 can be further extended to allow for biological effects such as mesophyll conductance and photorespiration and environmental effects

such as boundary layer diffusion, but in practice, the simplified form is sufficient given other uncertainties when using $\Delta^{13}C$ in the geologic record (Tipple and Pagani, 2007; Franks et al., 2014).

In general, bulk (or average) photosynthetic plant tissue (i.e. tissue taken from leaves rather than wood or roots) is assumed to represent the average $\delta^{13}C$ of carbon fixed by photosynthesis; assuming that no C is lost after photosynthetic incorporation, bulk $\delta^{13}C$ must represent the initial photosynthetic carbon pool. This assumption is not strictly correct as photorespiration releases CO_2, changing the mass balance, but the broad relationship between bulk plant tissue carbon and photosynthetically incorporated carbon is unchanged (Cernusak, 2018).

The relationships between environment, C_i/C_a, and $\Delta^{13}C$ have been extensively studied experimentally (Beerling and Woodward, 1995; Ehleringer and Cerling, 1995; Scheidegger et al., 2000; Saurer et al., 2004; Lomax et al., 2019). C_i is actively controlled by plant physiological processes, and can be actively controlled by altering stomatal conductance (g_s).

Stomatal conductance is the rate of movement of gases into and out of a leaf. It is controlled by stomata; pores on the surface of leaves surrounded by two stomatal guard cells, which increase or decrease turgor pressure to change the size of the pore. A higher stomatal conductance allows CO_2 to enter the plant at a greater rate, but allows a proportionate amount of water vapour to leave through the same opening. Stomatal movements are highly dynamic and respond rapidly to water stress by opening and closing, which decreases C_i if C_a remains constant (Drake et al., 2013; Gardner et al., 2022).

$\Delta^{13}C$ is often reformulated as the intrinsic water-use efficiency of a plant, or the ratio of carbon assimilation to water loss (A/E). A and E both increase with stomatal conductance (g_s) nonlinearly, such that the water use efficiency decreases with g_s. With a constant C_a, this results in a tradeoff whereby opening stomata more widely allows more CO_2 to enter the leaf, but decreases the water use efficiency (Cowan, 1978; Farquhar et al., 1989; Cernusak, 2018). In water-limiting environments this tradeoff becomes critical to plant survival, and plants decrease g_s to maximise the amount of CO_2 takeup per unit water loss. In environments where water is not limited, g_s increases. As g_s increases with C_i/C_a, this means that, in C_3 plants, assuming stomatal response is optimised to environment, $\Delta^{13}C$ increases in wetter environments and increases in more arid ones. Globally, $\Delta^{13}C$ correlates to mean annual precipitation and this relationship is presumed to hold in the geologic record (Diefendorf et al., 2010; Kohn, 2010; Reichgelt et al., 2020).

The response of $\Delta^{13}C$ to changes in pCO_2 are less clear. In the absence of an adjustment to carbon assimilation rate or g_s, elevated pCO_2 will raise C_i/C_a (Scheidegger et al., 2000). However, plants actively respond to CO_2 by decreasing g_s, which acts to reverse the increases in C_i/C_a: depending on the magnitude of response, C_i/C_a can increase, decrease, or remain constant (Saurer et al., 2004). It is debated conceptually, and sometimes assumed geologically, that plants actively maintain a constant C_i/C_a with CO_2 concentration as a set point, and only vary it with water (Ehleringer and Cerling, 1995; Smith et al., 2007).

The measured response of $\Delta^{13}C$ to pCO_2 varies between studies and appears heavily dependent on the timescales on which pCO_2 is altered: growth chamber studies, which

are generally run for timescales ranging from weeks to months, report increases in $\Delta^{13}C$ with pCO_2 (Schubert and Jahren, 2012; Lomax et al., 2019), whereas FACE experiments, which tend to run for up to 10 years, report a slight decrease in $\Delta^{13}C$ with CO_2 (Ainsworth and Long, 2005; Battipaglia et al., 2013). Studies of $\Delta^{13}C$ in tree ring cellulose from pre-industrial to modern CO_2 concentrations show that C_i/C_a is constant (Saurer et al., 2004) or has decreased (Gagen et al., 2011; Gomez-Guerrero et al., 2013); it has been observed that the response of C_i/C_a to pCO_2 may have shifted from constant to a decrease in the latter half of the 20th century, as both the total concentration and the rate of change of CO_2 concentration in the atmosphere have increased (Gagen et al., 2011; Weiwei et al., 2018). However, since C_i/C_a also responds to changes in water supply, deconvolving the effects of CO_2 from co-occurring droughts is challenging. On geologic timescales, C_i/C_a must not strongly respond to pCO_2, as carbon isotopes recorded during high-CO_2 periods such as the Eocene are similar to modern values (Diefendorf et al., 2015a; Kohn, 2016). A slight negative relationship between $\Delta^{13}C$ and CO_2, representing a slight decrease in C_i/C_a was suggested in (Schlanser et al., 2020), but on geologic timescales, it is difficult to deconvolve the impacts of changes in CO_2, co-occurring changes in hydrology, and changes in plant biology, considering how the uncertainties of all increase moving back in time.

Post-photosynthetic carbon isotope fractionation in n-alkanes

The difference between bulk plant and *n*-alkane $\delta^{13}C$ is defined using epsilon notation as:

$$\varepsilon_{lipid} = \left[\left(\frac{\delta_{lipid}+1000}{\delta_{leaf}+1000}\right) - 1\right] \times 1000 \approx \delta_{lipid} - \delta_{leaf}$$

(9)

(Hayes, 2001). Generally speaking, epsilon notation of isotope effects reflects the difference in composition applied during a single reaction, which is not the case for the complex series of biochemical reactions which collectively synthesise *n*-alkanes from photosynthetic carbon pools, but the mathematical relationship between the two follows Equation 9. Similarly, epsilon notation can be used as a measure of the difference in isotopic composition between two related compounds, even if one is not a direct precursor of the other. It should further be noted that although Equation 9 approximates the fractionation occurring between the photosynthetic carbon pool and *n*-alkanes synthesised from it, bulk plant tissue may not perfectly represent the photosynthetic carbon pool used for *n*-alkane synthesis (Diefendorf et al., 2021).

In C_3 plants, lipids are 3-5‰ depleted in ^{13}C relative to bulk plant material (Park and Epstein, 1961; Hobbie and Werner, 2004; Bowling et al., 2008). *n*-Alkanes are further depleted in ^{13}C relative to bulk (Collister et al., 1994). Cumulatively, this implies post-photosynthetic isotopic fractionation occurs at multiple points during the biosynthesis of *n*-alkanes. Relative to bulk, lipids are depleted in ^{13}C largely due to a kinetic isotope fractionation applied during the carboxylation of pyruvate to form acetyl CoA (DeNiro and Epstein, 1977) but details of the magnitude of isotope effects downstream of this are unclear. $\delta^{13}C$ is more variable in lipids produced via the acetogenic pathway than lipids produced via the mevalonic acid (MVA) pathway (including sterols) or the 2-C-methyl-d-erythritol-4-phosphate (MEP) pathway (including phytol). This was attributed to the large range of biomolecules resulting from acetogenesis, implying many different

opportunities for branching (Chikaraishi et al., 2004a, b) which therefore implies isotope effects during the transformation of *n*-alkyl-ACP to final *n*-alkyl lipids can have a significant effect. *n*-Alkanes are systematically enriched in ^{13}C compared to *n*-alkanols and *n*-fatty acids (Chikaraishi and Naraoka, 2007). This is probably partially because during decarbonylation of *n*-alkyl-ACP, one carbon is removed. The initial acetyl-CoA units' isotopic composition is position-specific and the final carbon (equivalent to the carboxyl carbon on the initial acetyl-CoA unit) is depleted in ^{13}C compared to the methyl position (DeNiro and Epstein, 1977). However, the magnitude of depletion of the carboxyl carbon necessary to account for the difference is unrealistically large and further causes of this enrichment are unknown (Chikaraishi and Naraoka, 2007).

The effect of environment on εlipid is not extensively documented. It is known to vary between species with some phylogenetic control – for example, εlipid is smaller in gymnosperms than angiosperms, and may be lower in C_3 plants than C_4 (Tipple and Pagani, 2010; Diefendorf et al., 2011). Changes with environment are less clear: Diefendorf et al. (2021) found an increase in magnitude of εlipid in *Juniperus monosperma* grown under drought conditions for four years, but no effect of temperature. Huang et al. (1999), Schubert and Jahren (2012) and Zhang et al. (2019) all either studied or reported data on εlipid in differing CO_2 concentrations. Schubert and Jahren (2012) and Zhang et al. (2019) both found εlipid decreased in higher CO_2, whereas Huang et al. (1999) found no effect. All of these studies were short-term and the influence of CO_2 does not appear to be consistent between the species studied. Finally, a systematic review of published εlipid data (Basu et al., 2021) found few consistent trends: εlipid appeared to decrease with increasing temperature and precipitation in angiosperm trees but in no other groups, and CO_2 had a weak effect only

in deciduous herbs. However, the full dataset used was not phylogenetically controlled, and although it contained many data points, there were relatively few studies contained within, meaning influence of the specific species and study conditions could obscure trends. Furthermore, for CO_2, there are no spatial gradients in the modern to measure response of εlipid over globally; response to CO_2 was determined using CO_2 values reconstructed from atmospheric values in the year of sample collection, and from calculation of concentration with altitude. The range of atmospheric CO_2 concentrations in the atmosphere only varied over ~40 ppmv during the interval for which εlipid could be calculated, and considering altitude corrections only increases to 90 ppmv. It is also questionable whether all CO_2 effects would be accounted for by using altitude-based corrections for CO_2 partial pressure, or whether εlipid could be separately driven by altitude-independent changes such as the CO_2:O_2 ratio.

Further research is necessary to determine:

a) How εlipid varies with environment, be it linearly or with some other relationship,

b) Whether it varies systematically, and if factors such as phylogeny and growth form influence its response,

c) Whether timescale of exposure to changes in environmental conditions influence response, and finally,

d) How these changes can be studied and accounted for in the geologic record.

Aims and objectives for this thesis

The aim of this thesis is to investigate the impact of high CO_2 climate states on two of the most commonly used biomarkers for environmental reconstruction. Both *n*-alkanes and alkenones are produced by autotrophs which rely on CO_2 uptake to produce biomass:

for this reason, their biology is profoundly affected by its concentration. Yet, in both instances, neither direct responses nor indirect consequences of higher than ambient CO_2 concentrations on either group are fully understood, with implications for the interpretation of the behaviour of both biomarkers geologically. In particular, examining and understanding biomarker – and thus biological – response to CO_2 in laboratory conditions and theoretical models inevitably simplifies both the organism and the environment in which it lives. In order to truly understand biomarker response to CO_2, it cannot be changed in isolation as CO_2 does not change in isolation naturally, and the interplay between CO_2 concentration, other environmental conditions such as temperature and seasonal cycles, and changes to the way organisms respond to their environments physiologically, biochemically, and phenologically will be examined.

This thesis aims to examine the behaviour of three commonly used metrics by which alkenones and *n*-alkanes are determined – *n*-alkane chain length distributions and carbon isotopic composition, and alkenone carbon isotopic composition – under high CO_2 conditions, both in modern experiments and in the geologic record. In particular, it aims to examine CO_2-biomarker relationships in the context of the changes in biology driving biomarker responses to CO_2, and dissect the assumptions used when interpreting these relationships geologically.

In order to achieve this, the following research questions are addressed:

Research question 1: How does increasing atmospheric CO_2 concentration influence the chemical and isotopic composition of *n*-alkane biomarkers? What environmental and/or biological processes control any CO_2 response? Are any mechanisms implicated in *n*-alkane response to CO_2 likely to persist on geologic

timescales? Chapter 3 aims to examine whether changes to the distribution patterns of *n*-alkane homologues are altered by CO_2, and whether *n*-alkane production changes under elevated CO_2 due to changes in plant-water relationships. Chapter 4 examines the carbon isotopic change induced during post-photosynthetic processes under elevated CO_2, and examines both environmental and biological mechanisms that may drive such trends.

Research question 2: Is plant *n*-alkane response to CO_2 specific to species, growth season timing, or specific *n*-alkane homologues? What are the implications for differences in CO_2 response for interpretation of *n*-alkanes in the geologic record? Chapter three discusses the timescale needed for *n*-alkanes to respond to both pCO_2 and a co-occurring drought, and Chapter four examines whether changes to εlipid can be induced by changes in the ontogeny of leaf wax production under elevated CO_2, and whether CO_2- induced changes to alkane $\delta^{13}C$ are expressed evenly across different alkane homologues, and in branched as well as *n*-alkanes. Both chapters also contrast the response of the two study species throughout the study.

Research question 3: How do extremely high temperatures and CO_2 concentrations in the early Eocene affect the alkenone $\delta^{13}C$ proxy for atmospheric pCO_2? Does the diffusive model for pCO_2 give realistic results for this time interval, and what biological and environmental parameters influence its predictions the most? Can alkenone $\delta^{13}C$ values be used quantitative under early Eocene oceanographic conditions, and, if not, what can qualitative interpretation of trends in pCO_2 reconstruction say about both the Eocene environment and how alkenone producers responded to it? Chapter five examines an alkenone pCO_2 reconstruction for the early Eocene under

several different scenarios for biological and oceanographic constants, and evaluates their impact for the sensitivity of the proxy. It also compares reconstructed values with existing pCO_2 reconstructions from alternate proxies in the early Eocene, in order to move toward a consensus pCO_2 value for the interval.

Chapter 2: Methods

Leaf samples

BIFoR FACE

All leaf samples were obtained from the Birmingham Institute of Forest Research's Free AIR CO_2 Enrichment experiment (BIFoR FACE). The site is located within a 19.1 ha temperature deciduous forest: the canopy is dominated by *Quercus robur* (pedunculate oak). The forest understorey contains coppiced *C. avellana* (common hazel), *A. pseudoplatanus* (European sycamore), *Crataegus monogyna* (common hawthorn), and *Ilex aquifolium* (common holly).

The site consists of six roughly circular arrays of around 30 m diameter located in Staffordshire, UK (52.801°N, 2.301°W) surrounded by steel towers used to fumigate the forest with +150 ppmv CO_2 from levels measured above the canopy in control arrays (aCO_2). CO_2 is injected into fumigated (eCO_2) arrays via vents within the towers at all levels of the forest. Three arrays (1, 4, and 6) are used for CO_2 fumigation, and three (2, 3, and 5) are left at ambient CO_2 concentrations as a control.

CO_2 fumigation began on 1st April 2017 and has continued through the growth season up until the present. Fumigation takes place from 1st April to 31st October each year during daylight hours, in order to target CO_2 release to times where photosynthesis occurs. Fumigation is halted when air temperature is <4°C as photosynthetic carbon uptake below this temperature is considered negligible. It is also stopped during periods of high wind (15 mins with average wind speed>8ms^{-1}) as under these conditions, constant CO_2 enrichment cannot be maintained without wasting large quantities of gas. CO_2 concentration was maintained within ± 20% of its target value for 97% of operation

time as of 2019. Cross contamination of CO_2 from fumigated to control arrays is possible with strong cross winds, but has an extremely minor impact on CO_2 concentration in ambient arrays (Hart et al., 2019).

Weather data

Weather data between 2017 and 2022 was taken from the nearby Shawbury weather station (52.795°N, 2.663°W). Monthly average temperature and precipitation data were obtained from the Met Office, and can be retrieved at https://www.metoffice.gov.uk/pub/data/weather/uk/climate/stationdata/shawburydata.txt

Leaf collection

Leaves were collected from approximately head height from specimens of *A. pseudoplatanus* and *C. avellana*. One sample of each species was taken per ambient and enhanced array (6 total per month). Samples were picked and immediately wrapped in aluminium foil. On collection, leaves were immediately frozen at -20°C and transported to the University of Birmingham. Samples were then split in two down the central vein for a) bulk isotope, and b) lipid analysis. Stems of *A. pseudoplatanus* were discarded; stems of *C. avellana* were smaller and were not removed.

Of all species present at BIFoR FACE, *A. pseudoplatanus* and *C. avellana* were used in order to compare the differing responses of two species. Of the four species which had at least one specimen present in every array from the beginning of the experiment (*A. pseudoplatanus*, *C. avellana*, *Ilex aquifolium* and *Quercus robur*), *I. aquifolum* was excluded because, as an evergreen study, it could not be confirmed that all leaf biomass accumulation took place under the elevated CO_2 treatment conditions, from April to

October. For the remaining three species, CO_2 switch-on occurred after leaf flush, and was switched off after senescence. Leaves were also not collected from *Q. robur* as they were not accessible from ground level, limiting the volume of sample available and the number of replicates that could be analysed. For *A. pseudoplatanus* and *C. avellana*, sampling took place at head height in order to minimise isotopic variability due to tree height (Martinelli et al., 1998).

Leaves were collected approximately monthly from the BIFoR FACE facility, throughout the growth season from 2018 until 2021. Samples of up to 6 leaves were taken. To increase the number of replicates, a further set of samples of *C. avellana* were taken on a single date in July 2022 consisting of 16 eCO_2 and 13 aCO_2 samples from 14 and 12 trees respectively.

Initial processing

Leaves were processed and waxes were extracted at the University of Birmingham. The majority of leaves were split in two (Figure 1), with one half used for wax extraction and one homogenised for bulk analysis.

A subset of leaves were not divided in two. When this occurred, one point per leaf was removed using a scalpel, dried, and stored separately for bulk isotope analysis without homogenisation. These points were placed approximately in the positions indicated in Figure 1, between major veins, to minimise intra-leaf variability. Samples which were homogenised vs samples were a subsample was taken for bulks are indicated in Table A2. The difference between samples homogenised and not homogenised was determined to be minimal (Figure 2).

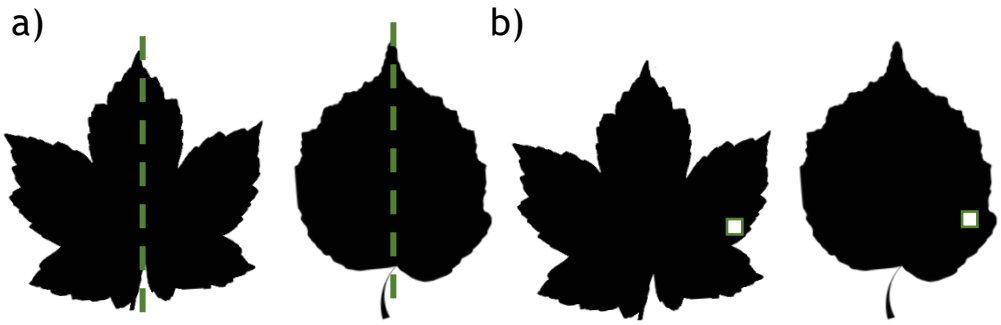

Figure 1: Division of leaves for bulk isotopic and *n*-alkane analysis for a) homogenised samples, and b) non-homogenised samples

Leaf bulk $\delta^{13}C$ analyses

Homogenisation

Where homogenised, all leaves were placed into a plastic sample tube together with two stainless steel beads, which were cleaned in acetone and deionized water between use. Leaves were then ground for 240 seconds in a SPEX™ 1600 MiniG. Samples were then examined and crushed a second time if not fully homogenised. Approximately 3.5 mg of powdered leaf was weighed into tin cups for bulk isotope analysis in Birmingham, and approximately 0.25 was weighed for analysis at the Institute of Low Temperature Science, Hokkaido University, Japan. Where samples were not homogenised, a small piece of each leaf within the sample were combined, so that the average of all leaves within the sample was measured.

EA-IRMS

Leaf samples were analysed for bulk $\delta^{13}C$ at the University of Birmingham and Hokkaido University. A list of samples and their analysis site are in Table A2. 25 samples were analysed in both Birmingham and Hokkaido to allow for comparison of the two.

At Hokkaido University, samples were analysed for $\delta^{13}C$ using an Elementar© Vario ISOTOPE coupled to an IsoPrime vision isotope ratio mass spectrometer. An acetalinide

standard of known isotopic composition was used to calibrate $\delta^{13}C$ relative to the PDB isotope reference. Three replicates were run of all samples. Long-term analytical precision for samples run in Hokkaido was within 0.2‰.

At the University of Birmingham, samples were analysed for stable-isotope and elemental composition using an Elementar© Vario Pyrocube elemental analyser (EA) coupled to an Isoprime-20© isotope-ratio mass-spectrometer (IRMS). More details on the EA can be found here (https://www.elementar.com/en-gb/products/stable-isotope-analyzers/ea-inlets/vario-pyro-cube).

$\delta^{13}C$ and $\delta^{15}N$ analyses were run sequentially on the same sample but due to the high CN ratio, an in-line diluter was used to reduce the size of the carbon peak. Data was calibrated using a range of commercial isotopic and elemental standards, all of which were traceable back to IAEA standards. Long-term analytical precision of samples run in Birmingham was within 0.1‰.

No systematic difference was detected between homogenised and non-homogenised samples run in Birmingham (Figure 2b, t-test, p=0.6). No samples run in Hokkaido were homogenised.

A systematic offset was detected between bulk isotope samples run in Hokkaido compared to Birmingham (Figure 2a). To account for this, the mean difference between samples where replicates were run in both Birmingham and Hokkaido was calculated (-0.46‰. To account for this, 0.46‰ was added to all raw bulk isotope values generated from Hokkaido to normalise them to Birmingham values. Where samples were measured both in Birmingham and Hokkaido, the Birmingham value was used, as the

majority of samples were run in Birmingham, and the majority of Birmingham samples were homogenised, unlike Hokkaido.

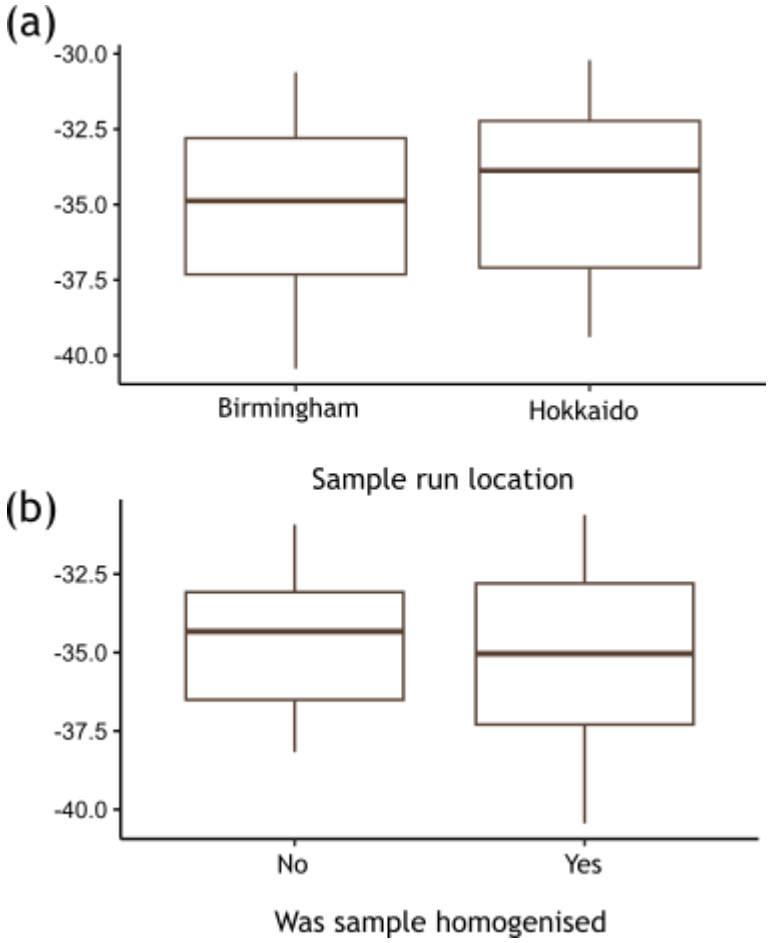

Figure 2: Difference in bulk $\delta^{13}C$ between a) sample run location, and b) whether sample was homogenised

Laboratory

Cleaning

All cleaning procedures were used both for processing of leaf and sediment samples.

Glassware

All glassware was wrapped in aluminium foil and furnaced at 450°C for 8 hours before use. After use, reusable glassware (e.g. test tubes, beakers) were scrubbed with a brush and soaked for 12-24 hours in a bucket containing Lipsol™ detergent and tap water. They were then scrubbed again and moved to a secondary bucket, also containing Lipsol™ and tap water. Finally, they were rinsed thoroughly with tap water and left to drip dry, whereupon they were furnaced as above.

Column consumables

Silica gel was deactivated using 5% back-extracted ultra-pure water, and furnaced at 450°C prior to use for 8 hours.

Leaf samples

Extraction

Both sediment and leaf samples were extracted via ultrasonication. For leaves, approximately 0.5g of dried leaf was weighed and placed in a glass 50ml test tube. Samples were ultrasonicated for 10 minutes in 9:1 DCM:MeOH (HPLC grade dichloromethane: HPLC grade methanol), whereupon solvent was decanted into 500ml test tube, and the sample was re-immersed in solvent. This was repeated three times.

The resulting total lipid extract (TLE) was evaporated at 40°C under a partial vacuum, using a Buchi Syncore connected to a Buchi Vacuum pump V-700. The samples were then filtered into a pre-weighed 8ml vial through a glass Pasteur pipette containing glass wool that had first been rinsed through with DCM to remove any remaining leaf matter. The resulting 8ml vials were covered loosely in tin foil to avoid contamination with dust and air dried. When dried, samples were weighed to obtain the TLE weight.

Columns

Compounds were separated from the total lipid extract via column chromatography. Pasteur pipettes were plugged with glass wool, rinsed through with DCM, and left to dry. 2ml 5% deactivated silica gel was then packed into the column. The sample was then redissolved and eluted through the silica column.

To extract *n*-alkanes from leaf samples, columns were eluted using 1) 5ml hexane, 2) 5ml DCM, and 3) 5ml MeOH to obtain fractions N1-3 respectively. Samples were captured in 8ml glass vials, dried down, and transferred to autosampler vials. Fractions N2 and N3 were archived with no further analysis.

Sediment samples

In addition to leaf samples from BIFoR, a separate set of Eocene sediments were analysed for alkenones. These were taken from Site 16/28-sb01 in the North-east Atlantic (54.0222°N 13.5143°W) and were acquired in 1999 by the *MV Bucentaur,* undertaken by the Rockall Studies Group of the Petroleum Infrastructure Program (PIP) Ireland. Full site details are in Chapter 5.

Samples from Site 16/28-sb01 were extracted at the University of Birmingham by Bethany Chamberlain, supervised by Dr Heiko Moossen. All samples were freeze dried and homogenised using a glass pestle and mortar prior to extraction. 6-16g of sediment was analysed per sample.

Extraction

Samples were extracted using 20 ml DCM:MeOH (3:1, v/v) and vortexed, followed by 20 minutes of sonication, heated to 40°C for one hour, and centrifuged at 1000 reps/min for 3 minutes. Solvent was then decanted into a 100ml test tube. The process was repeated

for a total of four times to produce a total lipid extract (TLE). Sediments were dried and transferred to 8ml vials as with leaf samples.

Columns

Pasteur pipettes were plugged with glass wool, rinsed through with hexane, and left to dry. As with leaves, 2ml 5% deactivated silica gel was then packed into the column. The sample was then redissolved and eluted through the silica column.

To separate sediment samples, the TLE was split into four fractions: 1) 4ml hexane, containing aliphatics, 2) 2ml 2:1 hexane:DCM, containing aromatics, 3) 4ml DCM, containing aldehydes, ketones, and alkenones, and 4) 5ml MeOH, containing polar compounds, including GDGTs. Each fraction was then dried down under nitrogen and transferred into autosampler vials. The N3 fraction was then analysed for alkenones. To filter for GDGTs, the N4 fraction was redissolved in 500 µl 99:1 hexane:isopropanol and passed through a 0.45 µm polytetrafluorethylene filter.

Analytical

GC-FID and GC-MS

Sediment samples were analysed for alkenones (N3 fraction) and leaf samples for *n*-alkanes (N1 fraction) using an Agilent 7890B GC-flame ionisation detector (GC-FID), using a splitless mode Agilent 7693 autosampler at 330°C. A HP1-MS 60m Agilent 19091S-916 column was used, with a 100% dimethylpolysiloxane stationary phase, using compressed air as the carrier gas. The oven temperature program held at 60°C for one minute, before ramping to 150°C at 30°C/minute, then to 320°C at 3°C/minute, for a total runtime of 66 minutes for the N1 fraction, and was held at 320°C for an additional

ten minutes for the N3. The FID was held at 300°C throughout. A hexane blank was run before, every 10 samples, and after each run to check GC-FID performance.

Leaf samples were initially run at 500µl. *n*-Alkanes were identified and quantified using a C10-C40 even numbered *n*-alkane standard (Sigma Aldrich), at 10µg/ml concentration, run at the beginning of each sample run. Sample peaks were quantified using Agilent MS-ChemStation. Where *n*-alkane concentrations <2 µg/ml for the highest concentration homologue, samples were transferred to inset vials and concentrated to 100µl, then rerun and integrated at the higher concentration. Sediment samples were initially run at 100µl, and then 20µl. An example chromatogram for the N1 fraction of leaf sam

A subset of samples were run via GC-MS to confirm identity of alkenones and *n*-alkanes, and identify any further peaks commonly found within them. Samples were introduced to an Agilent 7890B GC- 5977A mass spectrometer using a splitless mode Agilent 7693 autosampler at 280°C. A 60m Agilent DB-5 column was used, with a (5%-Phenyl)-methylpolysiloxane stationary phase, using helium as the carrier gas. The oven temperature program was held at 70 °C for 1 minute, was ramped to 150°C at 30°C/minute, then to 320 °C at 3°C/minute. For leaf samples, it was then held at 320 °C for 15 minutes, and for sediment samples, it was held at 320°C for 25 minutes.

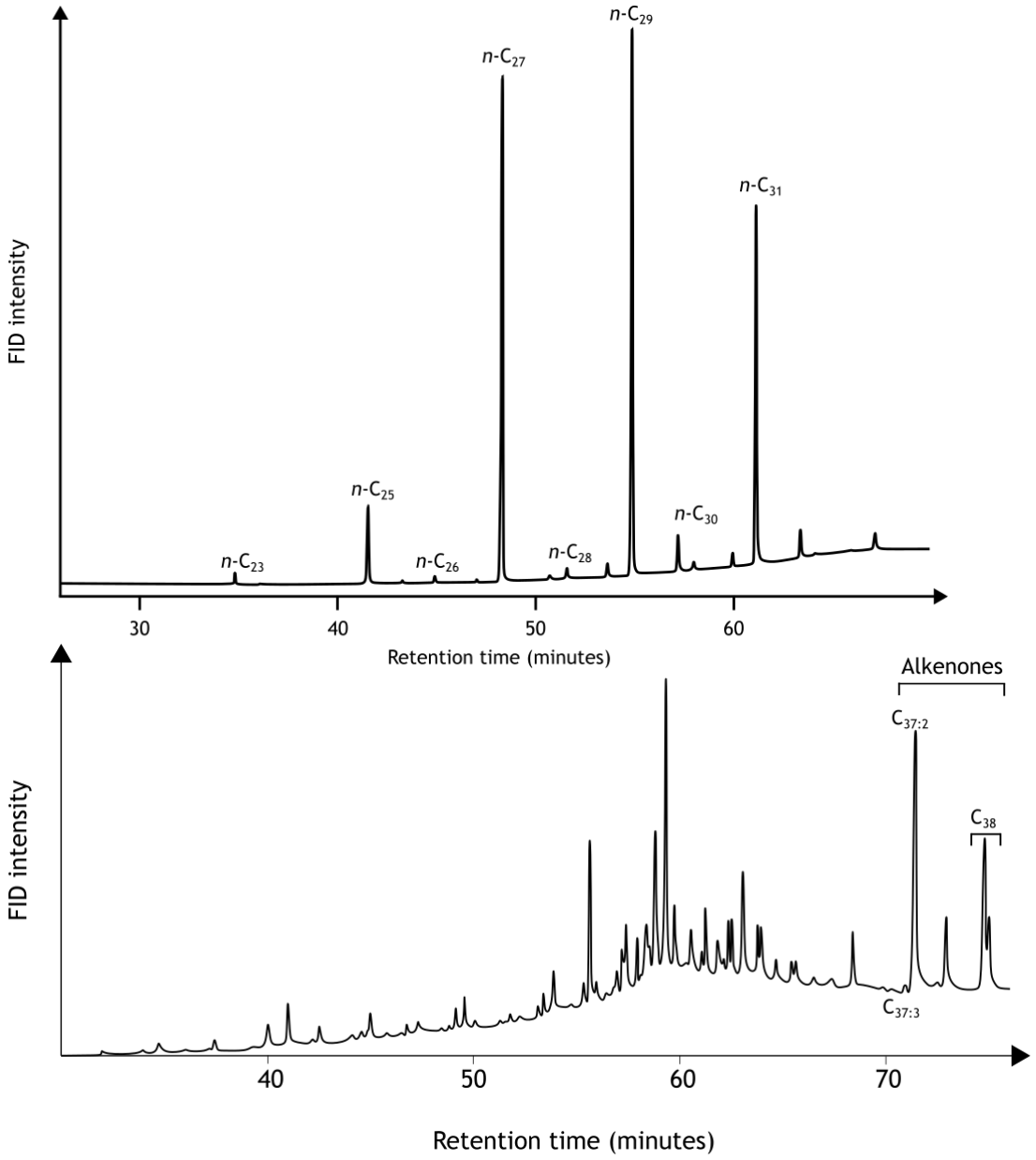

Figure 3: Representative chromatogram for a) N1 of leaf samples, and b) N3 of sediment sample

GC-IRMS

Leaf samples

The compound-specific $\delta^{13}C$ of odd-chained *n*-alkanes between *n*-C_{25} and *n*-C_{33} in length, and the *i*-C_{31} and *ai*-C_{32} branched alkanes, were determined via GC-C-IRMS (gas

chromatography-combustion-isotope ratio mass spectrometry), and were run externally in either the Organic Geochemistry Unit, University of Bristol, or Hokkaido University. Locations of the run for each sample are listed in Table S1.

For samples run at the Organic Geochemistry Unit, Bristol, compound specific $\delta^{13}C$ analyses of alkanes were performed using an Agilent Industries 7890A gas chromatograph coupled to an IsoPrime 100 mass spectrometer. Samples were introduced via a split/splitless injector in splitless mode onto a 50 m × 0.32 mm fused silica capillary column coated with a HP-1 stationary phase (100% dimethylpolysiloxane, Agilent, 0.17 μm). The GC temperature programme was held at 70°C for 3 minutes, increased to 130°C at 20°C/min, and then to 300°C at 4°C/min, then held at 300°C for 5 minutes. Helium was used as a carrier gas and maintained at a constant flow of 2 mL/min. The combustion reactor consisted of a quartz tube filled with copper oxide pellets which was maintained at a temperature of 850°C. Instrument accuracy was determined using an external fatty acid methyl ester (FAME) standard mixture (C_{11}, C_{13}, C_{16}, C_{21} and C_{23}) of known isotopic composition and to calibrate to the PDB isotope reference. Instrument error was ±0.3‰. Data processing was carried out using Ion Vantage software (version 1.6.1.0, IsoPrime).

For samples run at Hokkaido University, compound specific $\delta^{13}C$ analyses of alkanes were performed using a HP 7890 gas chromatograph coupled to an Elementar GC5 combustion interface and an Elementar IsoPrime vision mass spectrometer. Samples were introduced in splitless mode onto a 30m x 0.32 mm fused silica capillary column coated with a DB-5 stationary phase ((5%-Phenyl)-methylpolysiloxane, Agilent, 0.25 μm). The GC temperature program began at 50°C, increased at 30°C/minute to 120°C,

then to 310°C at 5°C/minute. The combustion tube temperature was maintained at 850°C. Instrument accuracy was determined using an Indiana University *n*-alkane isotope standard (A6) and used to calibrate $\delta^{13}C$ values relative to the PDB isotope reference. All samples were run in duplicate, and average standard deviation of samples was 0.16‰.

Sediment samples

Sediment samples were analysed for alkenone $\delta^{13}C$ at the Max Planck Institute for Biogeochemistry, Jena, using an Agilent HP5890 gas chromatograph coupled to a Thermo Fisher Delta + XP ratio mass spectrometer. Samples were introduced via a splitless inlet onto a 50m x 0.32 mm fused silica capillary column coated with an Ultra 2 stationary phase ((5%-phenyl)-methylpolysiloxane, Agilent, 0.25 μm). The GC temperature program was held for 1 minute at 70°C, increased to 120°C at 30°C/minute, increased to 320°C at 3°C/minute, and held at 320°C for 15 minutes. Instrument accuracy was determined using an Indiana University *n*-alkane isotope standard (B4) and used to calibrate $\delta^{13}C$ values relative to the PDB isotope reference. All samples were run in duplicate, and average standard error of the samples was 0.5‰.

Data analysis

Unless otherwise stated, all statistics were performed in R version 4.0.3.

Carbon isotopes were expressed using delta notation throughout

$$\delta^{13}C = \frac{(\frac{^{13}C}{^{12}C})_{sample} - (\frac{^{13}C}{^{12}C})_{PDB}}{(\frac{^{13}C}{^{12}C})_{PDB}} \times 1000 \quad (1)$$

Where the $^{12}C/^{13}C$ ratio in per mille (‰) is expressed in comparison to the standard Vienna Pee Dee Belemnite (VPDB). The difference between substrate and product $\delta^{13}C$ is expressed as the enrichment factor, Ɛ, according to

$$\varepsilon_{product} = \frac{\delta^{13}C_{product}+1}{\delta^{13}C_{substrate}+1} - 1.$$

(2)

Although the enrichment factor is strictly defined as the fractionation between the substrate and product of a single reaction, the formulation expresses the difference in isotopic composition between two substances, regardless of their relationship to each other (Hayes, 2001).

Chapter 3: Impact of elevated CO_2 on the distribution of *n*-alkane homologues in a temperate FACE experiment

Authorship statement

Leaf samples were collected from the Birmingham Institute of Forest Research's Free Air CO_2 Enrichment experiment by on-site technical staff from 2018-2021, according to a protocol initially developed by Dr Heiko Moossen, and expanded on by myself. 2022 leaf samples were collected by myself. All wet lab chemistry, GC-FID and GC-MS analyses were performed by myself.

Abstract

Plant wax *n*-alkanes are both a crucial suite of molecules used by plants to waterproof and protect their outermost surfaces, and a key biomarker targeted by organic geochemists seeking to analyse plant response to palaeoenvironmental change in the geologic record. Theoretically, a change in the amounts of different *n*-alkane homologues would alter plant water loss through the cuticle, and it may be advantageous for plants to do this in certain environments. Modern studies along environmental gradients suggest that temperature and aridity alter metrics of *n*-alkane homologue distribution such as average chain length (ACL), and ACL is often used to track these changes geologically. However, the effect of CO_2 on *n*-alkane homologue distribution has not previously been studied, in part because CO_2 gradients do not occur in nature and any such study must experimentally manipulate CO_2 concentration. Here, I present *n*-alkane chain length distributions from the Birmingham Institute of Forest Research (BIFoR)'s

Free Air CO_2 Enrichment (FACE) experiment. Specimens of *A. pseudoplatanus* and *C. avellana* were exposed to 5-6 years of elevated CO_2. CO_2 induced a decrease in ACL and *n*-alkane concentration, and an increase in the root-mean square of *n*-alkane chain lengths, in *C. avellana* but not *A. pseudoplatanus* from the fourth year of CO_2 enrichment onward. A co-occurring drought in 2022 induced the opposite changes. These shifts in *n*-alkane distributions are consistent with an active response whereby *C. avellana* alters its *n*-alkane chain lengths in order to optimise leaf permeability. *A. pseudoplatanus*, however, did not respond to environment through the study: therefore, *n*-alkane response to environment is likely species-specific. This work suggests that in the sediment record, *n*-alkane chain length distributions may alter with CO_2, but as with temperature and aridity, this response does not occur universally.

Introduction

All known land plants produce a layer of wax over their surface, which forms a protective coating to cover the interior of the plant. This barrier is primarily composed of long chain *n*-alkyl lipids including *n*-alkanes, *n*-fatty acids, *n*-aldehydes et al. (Jetter et al., 2006; Busta and Jetter, 2018). Both the distribution patterns of the different homologues and their isotopic composition form a useful archive of palaeoclimate information due to their ability to record information on their growth conditions, and their relative recalcitrance in sedimentary records (Cranwell, 1981; Freeman and Pancost, 2014). In particular, the *n*-alkane component of plant wax is of note for its utility in palaeoclimate reconstruction: *n*-alkanes are produced as a major component of plant wax in chain lengths from *n*-C_{21} to *n*-C_{35}, (Bush and McInerney, 2013), the relative distributions of which vary significantly within and between plant species, and can

covary with environmental conditions in the geologic record (Pagani et al., 2006; Castañeda and Schouten, 2011). *n*-Alkanes are ubiquitous in land plants (Jetter et al., 2006), when dissociated from their source plant their origin remains identifiable in sediments from the distribution patterns of homologues (Bray and Evans, 1961), and due to their lack of functional groups they are the most stable of the *n*-alkyl lipids on geologic timescales (Cranwell, 1981).

Due to their hydrophobic properties, the *n*-alkyl lipid component of plant waxes are responsible for the prevention of cuticular water loss (Schönherr, 1976; Schreiber et al., 1996; Parsons et al., 2012; Jetter and Riederer, 2016; Seufert et al., 2022). Changes in the distribution patterns of the homologues alter plant cuticular permeability to both water and emitted volatile organic compounds (Cheng et al., 2019; Diarte et al., 2021) as well as the rheological properties of leaves (Lourens and Reynhardt, 1979; Petracek and Bukovac, 1995). Due to their role in the prevention of plant water loss and the potential for optimisation of wax permeability to a given environment, links between the distribution of homologues of leaf wax *n*-alkanes and environmental parameters such as temperature and aridity have been suggested (Bush and McInerney, 2015; Eley and Hren, 2018). However, correlations are not consistently observed and the precise nature of the relationship between plant wax and environment remains unconstrained (Jetter and Riederer, 2016; Seufert et al., 2022).

The role which *n*-alkyl compounds play in preventing desiccation is complex. Due to their apolarity, the chemical properties of the hydrocarbon tails of *n*-alkyl compounds are likely more responsible for creation of an impermeable barrier than their associated functional groups, and the dominant control on total permeability of the cuticular layer

relates to the proportion of regions of crystalline wax which *n*-alkyl tails form within the larger cutin matrix. In this model of cuticular function, cuticular permeability to water depends on 1) the average length of *n*-alkyl carbon chains (defined as average chain length (ACL) the weighted mean average number of carbons in the *n*-alkyl tail) and 2) the range in the distribution of *n*-alkyl chain lengths present (defined as dispersion, the root-mean square of the deviation from the average chain length). A higher ACL and lower (i.e. a narrower range of homologues) dispersion lead to a decrease in permeability of the cuticle as a whole (Riederer and Schneider, 1990; Carr et al., 2014). Conversely, a wider range of distribution of *n*-alkyl chain lengths and a lower average chain length affect the mechanical plasticity of chain lengths and increases the rate at which waxes anneal, healing potential defects and potentially making the cuticle more resistant to disturbance and (Lourens and Reynhardt, 1979). It is therefore theoretically advantageous for plants in environments where saving water is more important for survival (i.e. hot, dry environments) to produce longer chain lengths in a narrower range of homologues, and for the reverse to be true in cooler, wetter environments.

Wax response to environment is somewhat plastic (Samuels et al., 2008). Water and temperature stress have been shown to impact wax-related gene expression (Treviño and O'Connell, 1998; Hooker et al., 2002; Rahman et al., 2021), but whether shifts in gene expression induced in a laboratory setting cause a consistent shift in wax composition is less clear, and few laboratory studies have investigated changes in chain length as opposed to changes in total wax content or the ratio of different chemical constituents of wax. Macková et al. (2013) showed an increase in both longer homologues and a wider range of homologues (implying a decrease in permeability) in seedling plants under simulated drought stress, whereas (Zhang et al., 2021) detected a

decrease in total cuticular permeability with water depravation but variable responses in *n*-alkane and *n*-fatty acid chain length distributions, showing both increases and decreases in ACL and homologue ranges depending on compound, wax location, and germplasm. On longer timescales, both Bai et al. (2019) and Diefendorf et al. (2021) found no significant change in ACL with drought or heat treatment after several years' continuous exposure in experimental plots and open-top chambers respectively, although neither paper reported results for dispersion.

Reported changes in *n*-alkane ACL along environmental transects tend to show an increase in ACL with temperature and aridity (Dodd et al., 1998; Bendle et al., 2007; Sachse et al., 2010; Leider et al., 2013; Tipple and Pagani, 2013; Carr et al., 2014; Badewien et al., 2015; Bush and McInerney, 2015; Eley and Hren, 2018; Wang et al., 2018b; Andrae et al., 2019; Teunissen van Manen et al., 2019; Lu et al., 2020), though patterns are not always seen in both temperature and aridity where both were measured (Carr et al., 2014; Bush and McInerney, 2015; Schwab et al., 2015) and the opposite trend (i.e. ACL decrease in warmer, drier conditions) was also sometimes observed. Since changes in ACL observed in individual species along environmental gradients are often much smaller than the differences between species (Feakins et al., 2016; Wang et al., 2018a), and since temperature and aridity often covary along gradients, deconvolving the effects of the two is challenging.

Alongside changes in temperature and aridity, plant-water relations are strongly influenced by the concentration of atmospheric CO_2 within which they are grown (Seibt et al., 2008). Due to an increase in the water-use efficiency plant gas exchange, increasing CO_2 concentration leads to an increase in available water at the leaf level

(Ainsworth and Long, 2005), although plant-to-ecosystem level feedbacks may, depending on ecosystem, reduce the magnitude of water savings observed (Wullschleger et al., 2002). . In practice, this manifests as a decrease in stomatal conductance seen consistently in elevated CO_2 across FACE experiments (Ainsworth and Long, 2005). Consequently, elevated CO_2, plants save water at the leaf level by decreasing stomatal water loss. It is possible that these water savings would induce a decrease in the need to save water from cuticular water loss, leading to an increase in cuticular permeability: as with a decrease in temperature and aridity, this would lead to decreased ACL and wax concentration, and increased dispersion. Therefore, in elevated CO_2, it is theoretically advantageous for plants to actively adjust these parameters: water savings are made elsewhere, and by making these changes, leaf wax becomes more plastic mechanically.

Unlike temperature or water availability, the effect of atmospheric CO_2 concentration on plant wax has not been extensively investigated. Large-scale spatial CO_2 gradients do not occur in nature, meaning the cline-based approach to looking at the effect of temperature and aridity on *n*-alkane composition is not possible with CO_2. Previous studies have reported qualitative changes to leaf surface epicuticular waxes (Thomas and Harvey, 1983; Prior et al., 1997; Vanhatalo et al., 2001) and changes to total wax concentration (Prugel and Lognay, 1994; Graham and Nobel, 1996; Prior et al., 1997; Paoletti et al., 1998; Percy et al., 2002). However, cuticular permeability is determined neither by epicuticular wax structure (Vogg et al., 2004; Zeisler-Diehl et al., 2018; Seufert et al., 2022) nor total wax concentration (Jetter and Riederer, 2016; Staiger et al., 2019), meaning any CO_2-induced shifts in wax relating to changes in water retention were not recorded.

(Huang et al., 1999) determined that a +250 ppmv CO_2 concentration increase resulted in increased CPI and total *n*-alkane concentration but no change to ACL or dispersion in *Betula pendula* seedlings grown from seed for 6 months. However, the ACL response to other environmental variables such as temperature is species-specific (Hoffmann et al., 2013) and seedlings may require a longer time period of exposure to show results. Furthermore, it is unknown how mature specimens would respond to the same exposure, or response to covarying CO_2 increase and other environmental variables such as temperature. CO_2 concentration is therefore an environmental variable which may induce changes to plant wax *n*-alkane chemistry in a similar manner to other variables such as temperature and aridity, but such an effect may hitherto not have been detected.

Methods

Sample collection

Leaves were collected from the Birmingham Institute of Forest Research (BIFoR) Free Air CO_2 Enrichment experiment (FACE), located in Staffordshire, UK (52.801°N, 2.301°W). BIFoR FACE consists of a mature semi-natural deciduous forest where trees are exposed to levels of +150 ppmv CO_2 (compared to atmospheric). BIFoR FACE utilises three elevated CO_2 arrays and three ambient CO_2 control arrays: arrays 1, 4, and 6 were elevated CO_2 arrays and arrays 2, 3, and 5 were ambient. CO_2 fumigation was initiated in April 2017 and operates during daylight hours through the growth season. Further details on experimental setup are available in Hart et al. (2019).

Leaves of the species *Acer pseudoplatanus* and *Corylus avellana* were used. These species were chosen because there were several specimens present in each array, allowing easy access, and unlike the co-occurring *Quercus robur* leaves were accessible without

needing to climb trees. Additionally, and unlike the co-occurring *Ilex aquifolium*, both are deciduous: as at BIFoR FACE elevated CO_2 conditions were only maintained over the growth season, which in practice began and ended before and after leaf formation and senescence, this means all leaf growth in both species took place under elevated CO_2 conditions. Both species are common European deciduous woodland understory species and are widespread in the UK, and both are generalists, rather than adapted to extremely wet or arid growth conditions (Niinemets and Valladares, 2006; Sterry, 2007). Both are angiosperms but are not otherwise closely related: *Acer pseudoplatanus* is a member of the order Sapindales, and *Corylus avellana* is in Fagales.

Weather data was taken from the nearby Shawbury weather station (52.794°N, -2.663°W). The average growth season temperature (April-September) from 2018 to 2021 ranged from 13.4-14.5°C, and average monthly rainfall ranged from 50.9-72.1 mm. The early growth season in 2021 was notable for its low temperatures, leading to a delayed leaf flush. 2022 was the driest year of the experiment, with 265 mm of rain through April-August, which represents 60% of the average rainfall of the previous five years for the same monthly time period.

Leaves of *Acer pseudoplatanus* (European sycamore) and *Corylus avellana* (common hazel) were sampled from the forest understory at approximately head height. Samples were collected approximately once per month through the growth season from 2018 to 2021 (Figure 1). In order to increase number of replicates, a further 18 ambient and 16 elevated CO_2 samples of *C. avellana* were sampled in July 2022, including three trees where 2 replicate sets of leaves were taken. Of these samples, array 4 (consisting of two

trees were replicate samples were taken) was collected 1 week after the rest of the month's samples.

An average of four *A. pseudoplatanus* and six *C. avellana* leaves were taken per sample. On collection, leaves were wrapped in aluminium foil and stored in Whirl-Pak bags at -20°C prior to processing.

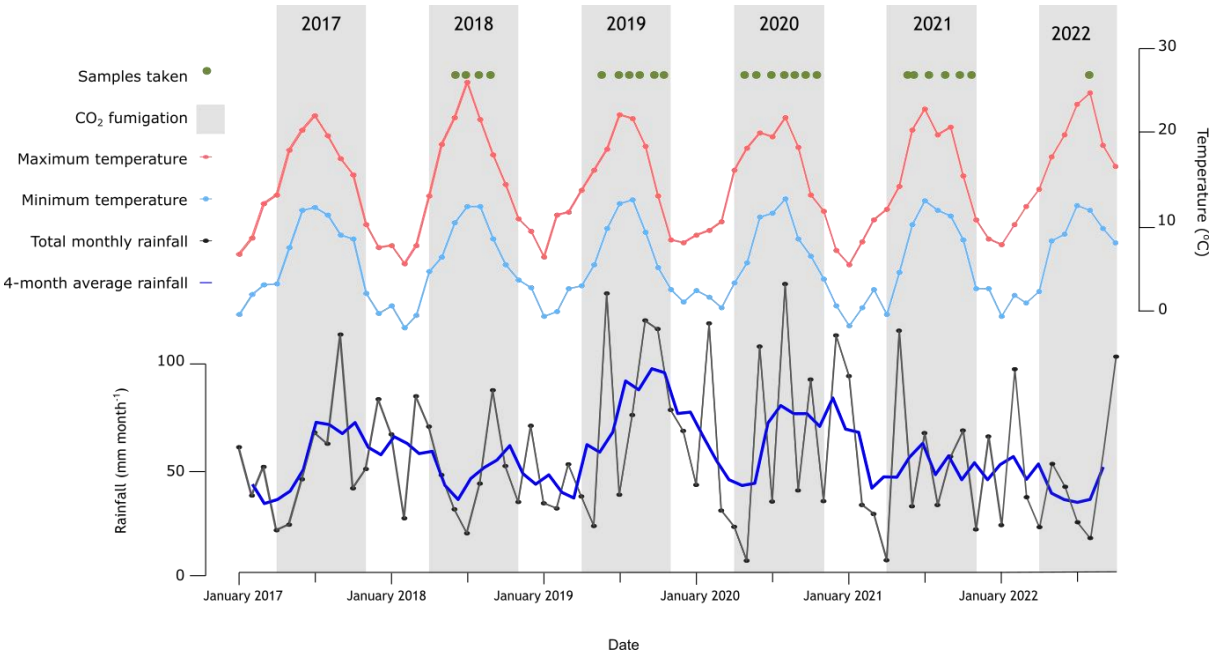

Figure 1: Sampling dates (green), mean daily maximum (red) and minimum (light blue) temperature (°C), total monthly rainfall (black) and 4-month moving average rainfall (dark blue) (mm month^{-1}) from the Shawbury weather station from January 2017 to October 2022. Periods where CO_2 fumigation occurred are marked by the grey bars.

Laboratory

Leaves were divided two along the vein for separate analyses prior to processing. All leaves were oven dried for 48 hours at 55°C. 0.1-1g leaf material was then

ultrasonicated in 9:1 dichloromethane (DCM):methanol (v/v) three times for 10 minutes, and dried down to remove solvent. The resultant total lipid extract was further separated into three fractions using silica gel liquid chromatography. The *n*-alkane fraction was eluted using hexane. Further fractions using DCM and methanol were obtained and archived without further analysis.

The hexane fraction, containing *n*-alkanes, was analysed quantitatively using an Agilent 7890B GC-flame ionization detector (FID), fitted with a HP1-MS 60m Agilent 19091S-916 column. Oven temperature was initially set to 60°C, and ramped at 30 °C/minute to 150°C, then at 3°C /minute to 320°C. *n*-Alkanes were identified and their concentrations quantified using an external *n*-alkane standard mixture (*n*C10-*n*C40, even numbered alkanes only, 10µg/g concentration).

Data analysis

ACL was determined from the weighted average concentrations of C_{21}-C_{35} *n*-alkanes, according to:

$$ACL_{C21-C35} = \sum_{n=C21}^{C35} \frac{n[C_n]}{[C_n]}$$

(10)

(Poynter et al., 1989) where $[C_n]$ is the proportional concentration of an alkane with *n* carbon atoms in its skeleton, normalised to 1

Dispersion was calculated as

$$d = \sum_{C21}^{C35} C_n(n - ACL)^2$$

(11)

(Dodd and Afzal-Rafii, 2000) where ACL is calculated by Equation 1. Dispersion was calculated using both odd-chain only and all homologues present.

Carbon preference index (CPI) was also calculated for all samples, and was defined as:

$$CPI = \frac{[\sum C_{odd(C21-33)} + \sum C_{odd(C23-33)}]}{2\sum C_{even(C22-34)})}$$

(12)

(Marzi et al., 1993).

All statistical analyses were performed in R version 4.0.3. The 2022 *C. avellana n*-alkane ACL and dispersion were tested for normality via a Shapiro-Wilk test, which indicated a normal distribution, therefore, t-tests were used to compute differences in means.

To allow comparison of CO_2 treatment effects in isolation, the variation in each set of replicates between months was detrended or accounted for using two methods. Firstly, the average of each of the three replicates taken for each species, treatment and month were averaged, and the effect of treatment was calculated using a paired student's *t*-test. In this way, the average values for each treatment can be compared directly for each month.

Secondly, the monthly variation was removed from all three replicates of each treatment. This was achieved by taking the average of all six data points, and subtracted from all six points to give the deviation around this point: for example, in a case where

all three ambient arrays had an ACL value of 27 and all three elevated had an ACL of 29, the average of the six would be 28, and the detrended ACL for the ambient and elevated treatments would be -1 and 1 respectively. Where three data points of one treatment but two of the other were present, samples were averaged so that the missing data point was assumed to be the average of the other two for its treatment, e.g. if array 1 (enhanced CO_2) was missing, the average would be taken as (1.5*(array 4,6) + array 2, 3, 5).

Results

Range of *n*-alkanes detected

n-Alkanes were recovered in the range *n*-C_{21} to *n*-C_{35}. All measured samples contained the C_{25}, C_{27}, C_{29} and C_{31} homologues, and >90% contained measurable levels of the C_{25}-C_{33} homologues. 99% of measured samples exhibited CPI>1, as is typical of land plants (Eglinton and Hamilton, 1967; Bush and McInerney, 2013). The three samples with CPI<1 were sampled close to the beginning or end of the growth season (Figure 3), meaning all mature leaves, which had not begun senescence, displayed CPI>1, and of the samples with CPI<1, the even-over-odd preference was recorded solely due to a larger-than-expected C_{28} *n*-alkane.

Table 1: Number of samples and average ACL, CPI, and dispersion for both species and CO_2 treatments in 2018-2021, and 2022 in *C. avellana*. 1x standard deviations are indicated in brackets.

Sample	Samples	ACL	CPI	Dispersion
C. avellana ambient (2018-2021)	69	28.4 (0.70)	7.7 (2.4)	4.88 (1.7)
C. avellana elevated (2018-2021)	67	28.1 (0.95)	7.5 (2.6)	5.42 (1.6)
A. pseudoplatanus ambient	64	28.9 (0.36)	13.2 (4.4)	4.71 (1.6)
A. pseudoplatanus elevated	65	28.9 (0.32)	12.8 (4.6)	4.33 (0.77)
C. avellana ambient (2022)	13	30.6 (0.48)	8.0 (1.0)	5.85 (1.7)
C. avellana elevated (2022)	16	30.0 (1.0)	7.3 (1.5)	4.16 (0.69)

2018-2021: species and seasonality

There were no clear, consistent seasonal trends in ACL in either species. *A. pseudoplatanus* ACL appeared stable throughout the growth season in all years, whereas in *C. avellana*, in years other than 2019, the earliest sampling dates tended to show lower ACL than those taken later (Figure 2c). Similarly, the first samples taken in 2018, 2020 and 2021 in *C. avellana* had a higher dispersion than during the rest of the growth season. Dispersion decreased throughout the growth season in *A. pseudoplatanus* in all

years, however since *C. avellana* showed higher variability between replicates, a small seasonal trend, if present, cannot be identified (Figure 2b). From 2018 to 2021, ACL appeared constant year-on-year in both species.

Between 2018 and 2021, ACL ranged from 28.1 to 31.0 in *A. pseudoplatanus,* and from 24.9 to 29.4 in *C. avellana* (Figure 2c). Dispersion ranged from 2.4 to 14.7 in *A. pseudoplatanus* and 2.1 to 9.1 in *C. avellana* (Figure 2b). On average, *A. pseudoplatanus* had a higher ACL and lower dispersion than *C. avellana* (Table 1). The ACL and dispersion of *A. pseudoplatanus* were less variable than *C. avellana*, both within individual sample dates and over time, although several extremely high and low samples were measured for this species (Figure 2).

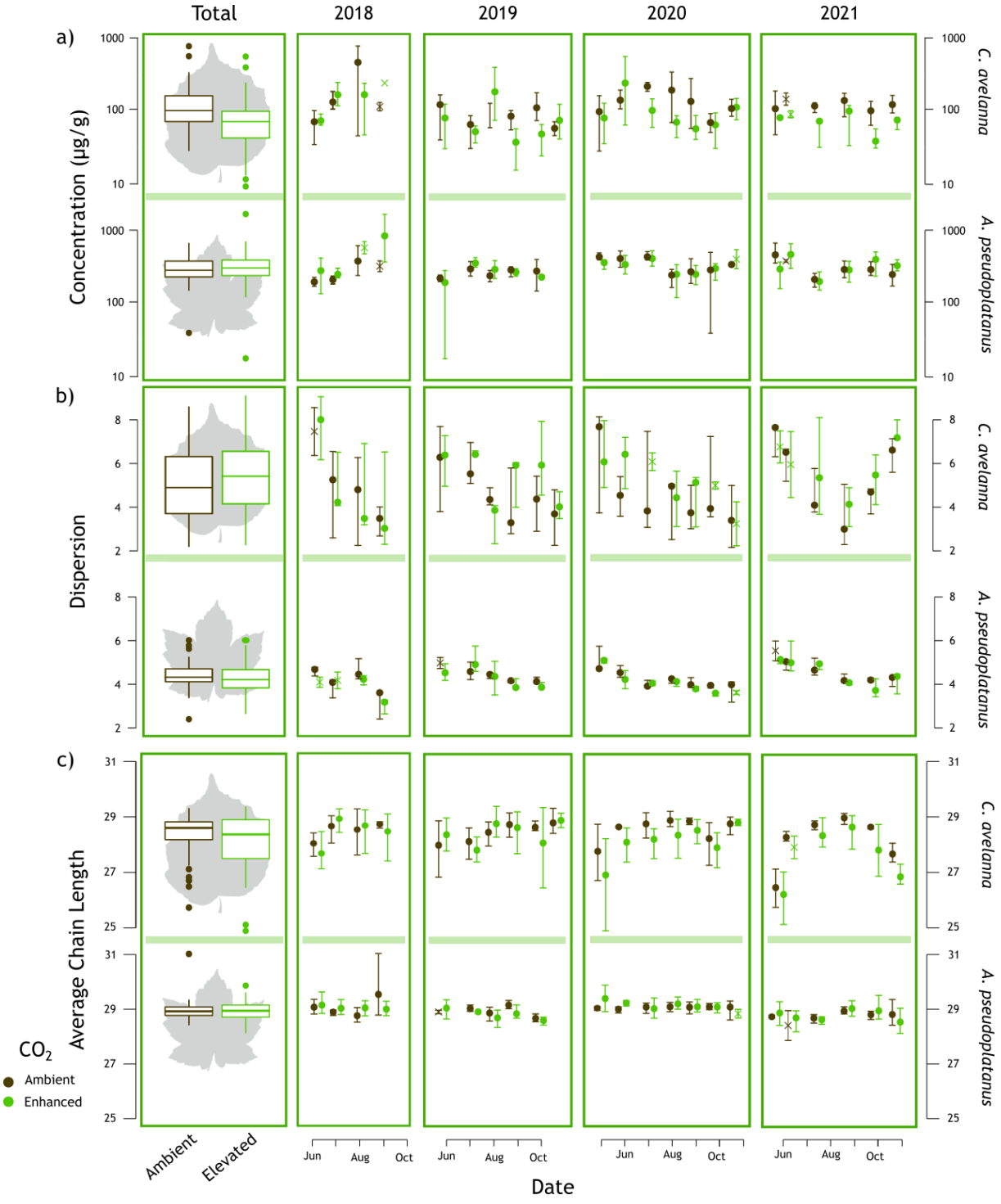

Figure 2: a) Total *n*-alkane concentration, b) Dispersion and c) Average Chain Length for both species, all samples (left panel) and monthly (right four panels), 2018-2021.

Total *n*-alkane concentration was highly variable in both species, ranging from 14 to 760 µg/g dry wt in *C. avellana*, and 16 to 1663 µg/g dry wt in *A. pseudoplatanus* (Figure 2a).

CPI decreased through the growth season in both species. The decrease was more pronounced in *A. pseudoplatanus* than *C. avellana*, and the trend was not affected by CO_2 treatment. In *A. pseudoplatanus*, the concentration of odd homologues stayed constant through the growth season, but the concentration of even-chained homologues increased through the growth season, driving the decrease in CPI. In *C. avellana*, although CPI decreased throughout the growth season, no significant trends were observed in odd- or even-chained concentration ($p>0.1$ both odd and even *n*-alkanes under both CO_2 treatments).

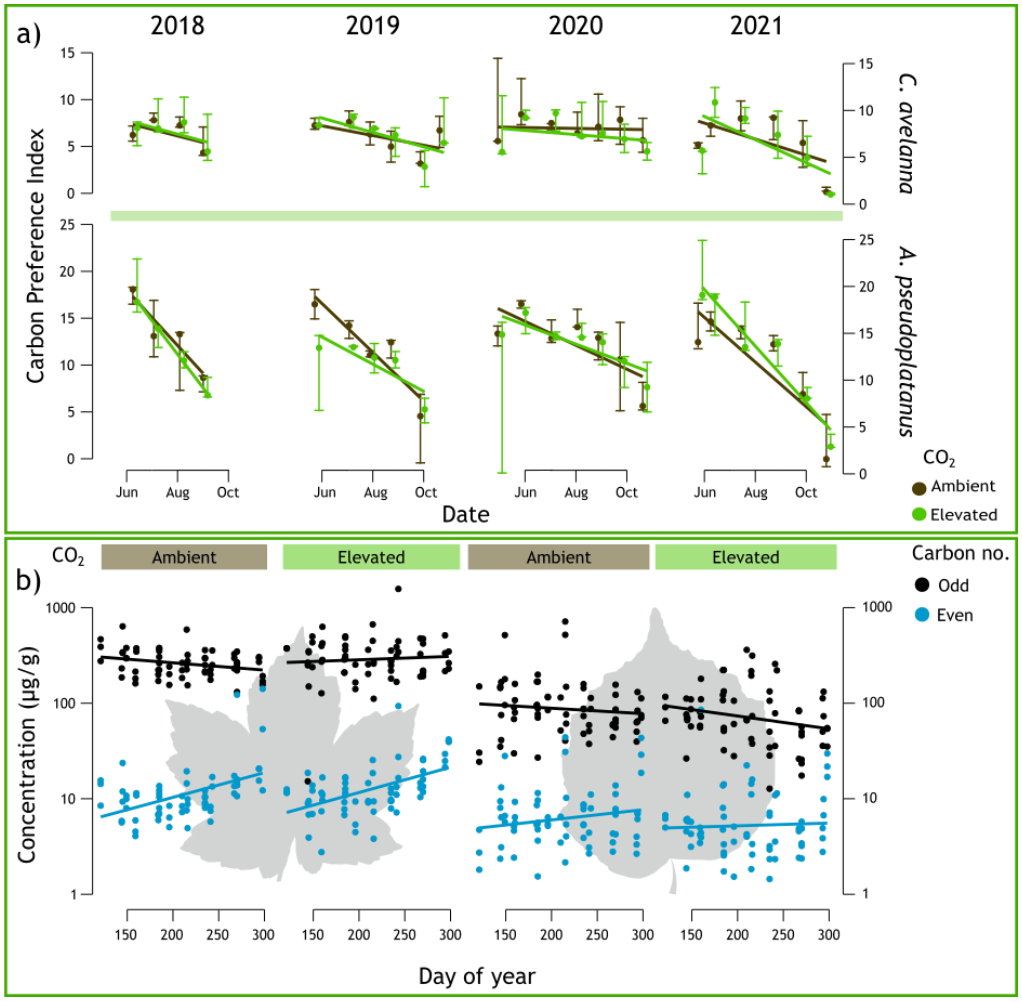

Figure 3: a) Carbon preference index for both species, 2018-2021 b) Total concentration of odd (black) and even (blue) homologues in *A. pseudoplatanus* (left and *C. avellana* (right) over the growth season.

Effect of CO_2 (2018 to 2021)

A. pseudoplatanus ACL and dispersion showed no difference between CO_2 treatments. However, in *C. avellana*, ACL slightly decreased and dispersion slightly increased in elevated CO_2 treatments compared to ambient from 2020 onward: when detrended from monthly variation by normalising each month to zero, elevated CO_2 samples in these years showed a 0.5 decrease in ACL, and a 0.74 increase in dispersion compared to

ambient (Figure 4). The difference in ambient and elevated values for these years in *C. avellana* shows this decrease to be significant (ACL: p=0.0006, dispersion: p=0.01).

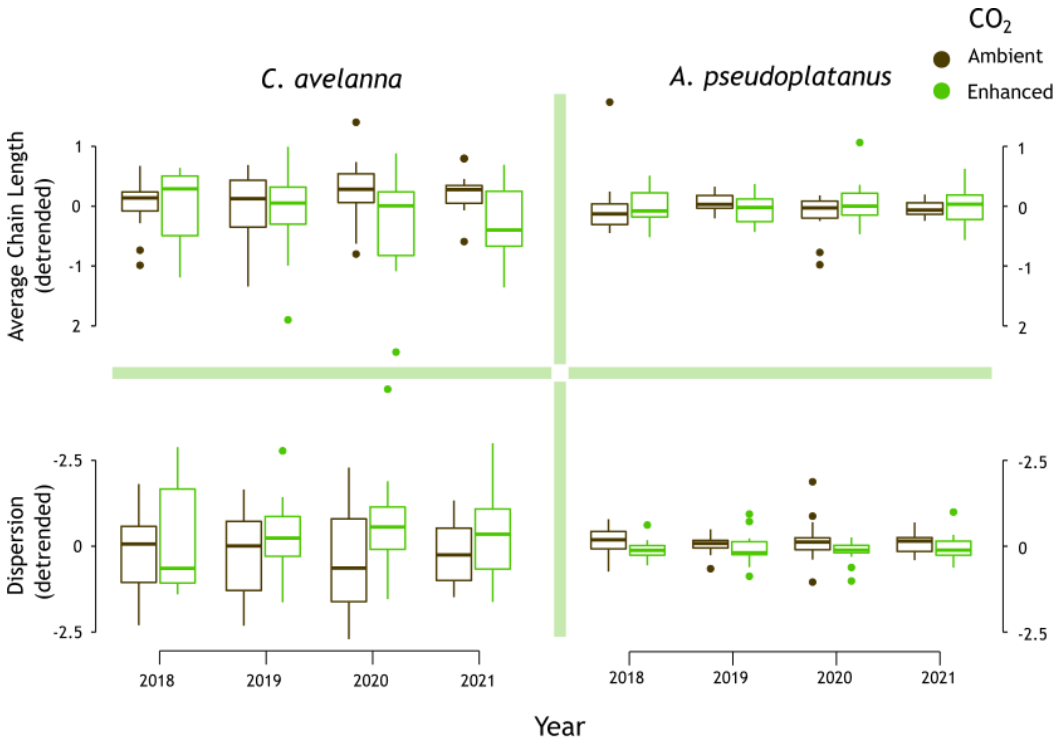

Figure 4: Yearly average ACL and dispersion, detrended from monthly variation.

There was no effect of CO_2 treatment on concentration in *A. pseudoplatanus*, but concentration was lower in *C. avellana* in elevated compared to ambient in every year of the study except 2018 (Figure 2a). Elevated CO_2 samples from 2019-2021 had a 26% lower total concentration of *n*-alkanes to ambient.

2022

Same-tree replicates

Replicates taken from the same tree in 2022 showed an average 0.9 difference in ACL and 0.8 in dispersion. The difference in ACL between replicates was similar to the range seen within the three replicates taken monthly from 2018-2021 (1.1 in *C. avellana*), but less than the range seen for dispersion (1.8).

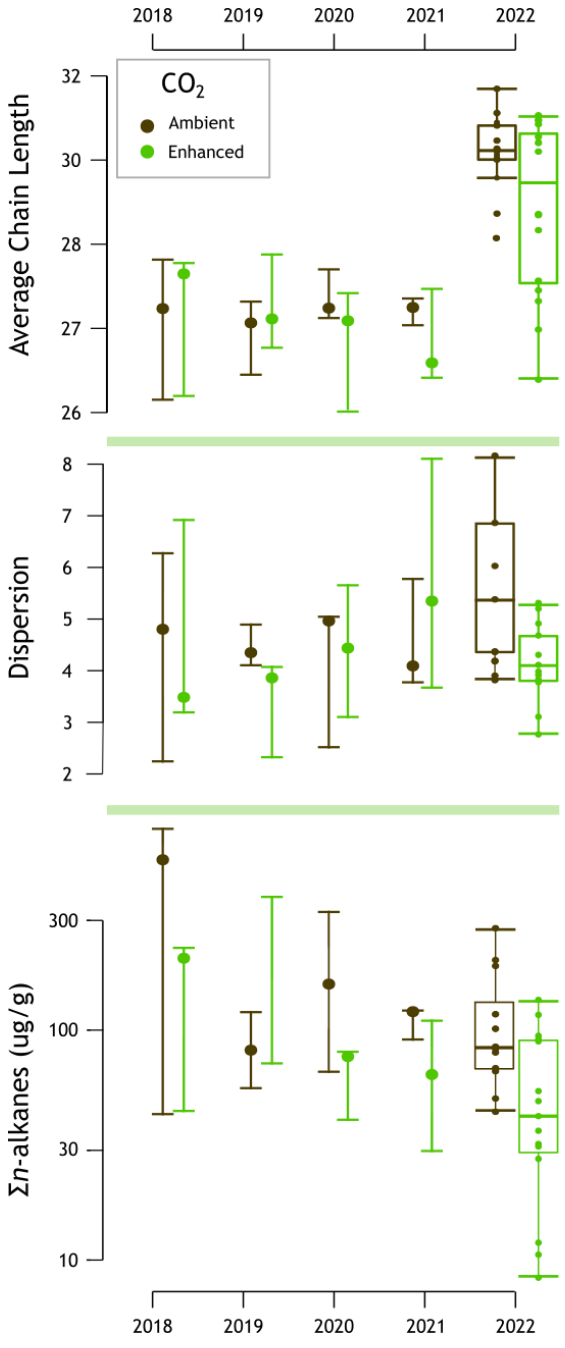

Figure 5: ACL, dispersion, and total *n*-alkane concentration, 2018-2022, in *C. avellana,* in July

All samples

Summary statistics of the ACL, dispersion, and concentration of *n*-alkanes collected in *C. avellana* in 2022 are summarised in Table 1. Large numbers of replicates of *A. pseudoplatanus* were not collected from a single month, meaning the full range of intraspecies variation could not be calculated as the combined data summarised in Table 1 includes seasonal variation.

The 2022 replicates in *C. avellana* show a decrease in ACL, dispersion, and total *n*-alkane concentration in elevated samples compared to ambient (Figure 5). Both of

these differences are significantly different (t-test, ACL: t=2.2 p=0.04, dispersion: t=3.3 p=0.005, $\log_{10}$(concentration): 0.005). ACL was 7% higher in ambient samples than in the average of the previous four July samples, and 5% higher in the elevated samples. Dispersion and concentration, however, were within the range of the previous four years.

Of the 34 samples taken in 2022, the four (consisting of two sets of replicates) from array 4 (eCO_2) were collected 1 week after the main sampling collection. These four samples exhibited significantly lower ACL and concentration, and higher dispersion, than the other two elevated CO_2 arrays (p=0.01, 0.01 and 0.0007 respectively). In particular, the concentration of *n*-alkanes (average 15 μg g^{-1}) in this array were exceptionally low: lower than any value recorded in July in this species (minimum 29 μg g^{-1}) and lower than all but one other concentration recorded in *C. avellana* over the entire study. Without the addition of array 4, the difference in ACL between CO_2 treatments is not present (p=0.4), though concentration may still be lower in eCO_2 (p=0.08).

Discussion

Intra-species variation in *n*-alkane distribution

Although many studies have investigated the range of plant wax *n*-alkanes recovered from different species at a single site (Ficken et al., 2000; Diefendorf et al., 2015b) or the same species over different environmental conditions (Dodd et al., 1998; Hoffmann et al., 2013), this dataset represents the largest number of replicates compiled of a single plant species in a single location.

The three sets of 2 replicate samples taken from the same *C. avellana* specimen in 2022 showed large variability in ACL similar to the range observed in replicates taken from separate specimens. Given that each sample consisted of 6 leaves, the inter-leaf variability is likely much larger than the average presented in each sample. The range of dispersion present was smaller. The similar variability in ACL between same-tree replicates and different trees suggests that although many leaves may be necessary to measure a reproduceable ACL value, these leaves could potentially be taken from the same specimen. However, only 2 replicates from three trees were taken, meaning further data is necessary to determine the range of *n*-alkane homologues present between individual leaves and individual trees of the same species.

The studies ofDiefendorf et al. (2011), Bush and McInerney (2013) and Diefendorf, Leslie and Wing (2015) all took many (53, 44 and 34 respectively) samples for leaf wax chain length analyses from a single location, examining the chain lengths of multiple species. The standard deviation of ACL, CPI and odd-chained dispersion were all lower in both species in this study, across both treatments, than was recorded between multiple species at the same site (Table 3), suggesting some genetic control on all three parameters. In combination with the replicate samples from single trees, this implies that the majority of difference between wax homologue proportions can be attributed to differences between leaves on trees of the same species, and the difference between species, rather than the difference between specimens of the same species. Therefore, in order to characterise the *n*-alkane chain length distributions of a single location, multiple samples should be taken from each species, but it is less important that those samples be taken from different specimens of the same species.

Table 3: Standard deviations of ACL, CPI and odd-chained dispersion from selected studies compared to 2018-2021 values for *Acer pseudoplatanus* and *Corylus avellana* in ambient and elevated CO_2.

Study	Study details	ACL	CPI	Dispersion
Bush and McInerney, 2013	Grown outdoors in Chicago Botanic Garden	1.6	7.0	2.9
Diefendorf et al., 2011	Grown outdoors at the Pennsylvania State University	1.6	15.5	1.8
Diefendorf et al., 2015	Grown outdoors at the University of California Botanical Garden at Berkeley	2.3	6.2	3.4
C. avellana ambient	See Chapter 2	0.70	2.4	1.7
C. avellana elevated	See Chapter 2	0.95	2.6	1.6
A. pseudoplatanus ambient	See Chapter 2	0.36	4.4	1.6
A. pseudoplatanus elevated	See Chapter 2	0.32	4.6	0.77

Seasonality

Average chain length showed little consistent change seasonally throughout the study period in either species. Individual years show trends – for example, 2022 in *C. avellana* shows a decrease following the very low first sample of the year – but no trends repeat over all four years. *A. pseudoplatanus* ACL appeared stable through the growth season,

with low variability, aside from a few individually high or low samples. Dispersion, by contrast, showed a decreasing trend in *A. pseudoplatanus* in every year. This trend may also be present in *C. avellana* in 2018-2020, but due to high variability between samples cannot be identified.

The first sample collected in 2018, 2020 and 2021 in *C. avellana* all showed decreased ACL compared to the rest of the year. This is similar to trends observed in (Tipple and Pagani, 2013; Sachse et al., 2015; Huang et al., 2018), which detected an increased proportion of lower chain lengths in very young leaves immediately following leaf formation, coincident with enhanced wax synthesis. This period of lowered ACL was not detected in 2019 or at all in in *A. pseudoplatanus*: it is possible that this period occurred prior to the beginning of sampling in this species and year and was therefore not detected. The total concentration of *n*-alkanes was highly variable, but was also slightly lower in the first samples of 2018, 2020, and 2021 compared to the next month, suggesting this is a signal of early leaf ontogeny.

ACL remained relatively stable through the growth season after leaves reached maturity. The total concentration of leaf wax present also generally remained constant, albeit with extremely high variability, and the lack of change in both ACL and dispersion implies that the ratio of homologues remained mostly unchanged after leaf maturity. As noted in (Newberry et al., 2015; Sachse et al., 2015; Huang et al., 2018), stable ACL does not necessarily imply a lack of change in leaf wax present, as wax removed by wind abrasion can be replaced with newly synthesised wax of the same homologues. It does, however, imply, that even if wax is replaced, in these two species, ACL is not highly dynamic to environmental conditions on seasonal timescales.

CPI decreased throughout the growth season in both species, although the magnitude of decrease was much greater in *A. pseudoplatanus* than *C. avellana*. In *A. pseudoplatanus*, the decrease in CPI was attributable to an increase in the concentration of even-chained *n*-alkanes, rather than a decrease in concentration of odd, which showed no trend (Figure 3), whereas in *C. avellana*, slight, non-significant increases in even-chain concentration may have combined with slight, non-significant decreases in even-chain concentration to produce a more consistent effect. A similar trend of decrease in CPI through the growth season was observed in (Huang et al., 2018), but no mechanism to explain this decrease has hitherto been suggested. Although the biosynthetic pathway by which even-chained alkanes are produced is known, the genetic factors controlling their expression are not, meaning the biological, ontogenetic, and environmental factors governing CPI are unknown.

Although isotopic measurements are needed to confirm *n*-alkane synthesis in mature leaves as synthesis can be balanced by wax removal (Baker and Hunt, 1986; Newberry et al., 2015), changes in CPI are suggestive of continuing synthesis throughout, as mechanical removal of *n*-alkanes would not alter CPI (Buggle et al., 2010; Wang et al., 2014; Huang et al., 2018).

Drought in 2022

The growth season in 2022 included a severe drought through July and August, and an extreme, record-breaking heatwave which took place the week before sampling occurred (Kendon, 2022; Toreti et al., 2022a, b), leading to maximum temperatures of 36°C regionally (Kendon, 2022). Accordingly, the decrease in available water from rainfall and increase in evaporative heating implies that a decrease in permeability to

preserve water would be advantageous. The average of 7% increase in ACL observed in *C. avellana* compared to the previous four Julys (Figure 1) is likely due to this effect, and indirectly demonstrates an active response to the season's weather conditions in leaf cuticular permeability. Dispersion and *n*-alkane concentration showed no change from the previous years. ACL and dispersion covary in *C. avellana*, but the 2022 samples do not follow the trend of the previous four years. This suggests that, although linked, a change in ACL does not necessarily imply a change in dispersion, and the two may change on different timescales in response to water availability.

As array 4 was collected slightly after the other 30 samples in 2022, it is possible that some of the anomalous trends it exhibited related to sampling date rather than CO_2 treatment. In this case, the lower ACL and concentration, and higher dispersion, may represent a rapid return to more normal conditions after an equally rapid change at the onset of the drought. In particular, the extremely low concentrations of *n*-alkanes measured in this array could suggest a rapid removal of *n*-alkanes as the heatwave concluded. However, it should be noted that these are only four samples from two trees, so wider trends cannot be inferred. It is therefore possible that the drought effects in 2022 removed differences between the CO_2 treatments, and that rapid return to or beyond pre-drought *n*-alkane homologue distributions in array 4 are responsible for all the CO_2 effects observed in this year, or that the extra week between sampling dates made little difference to array 4's *n*-alkane distribution and the effects observed in Figure 5 represent CO_2 effects.

It is unclear how quickly wax would return to its previous state, if at all, post an extreme heat/drought event such as that observed here. It is also noteworthy that although the

extreme heat event lasted <1 week, the drought persisted after the collection of all samples. Gao, Burnier and Huang (2012) reported regrowth of wax post mechanical removal on a timescale of hours, but ACL stayed largely constant through this process, and a rapid addition of wax would increase, rather than decrease the concentration compared to during the drought, and all studies of ACL over the growth season tend to show it remains stable or changes slowly in mature leaves (Tipple et al., 2013; Newberry et al., 2015; Sachse et al., 2015; Huang et al., 2018). Therefore, although it is possible that the delay of 1 week affected array 4's *n*-alkane distribution, and subsequently biased the comparison of elevated and enhanced CO_2 in this year, the most likely explanation remains that CO_2 influenced the composition of this array. However, further study is needed to investigate the impact of transient temperature changes on ACL and other wax *n*-alkane parameters, as well as longer-term studies.

Eley and Hren (2018) suggest that under higher temperatures, ACL may increase due to direct evaporation of shorter homologues, rather than active changes to synthesis of homologues. This explanation cannot explain the observed data, since the concentrations of the C_{33} and C_{35} homologues increased in 2022, alongside a decrease in concentration of homologues C_{29} and below: if preferential removal of shorter-chain homologues were the sole driver of the observed trend, total concentration in 2022 would decrease and only decreases in concentration in the shorter homologues would be observed.

No change in *n*-alkane ACL was found in the drought or heat treatment in Diefendorf et al. (2021) or heat treatment in Bai et al. (2019). Neither study reported values for dispersion. It was additionally suggested in Diefendorf et al. (2021) that the species

studied, *Juniper monosperma*, was drought and heat tolerant prior to the start of the experiment, and could not further increase its ACL from an already high starting point. Neither *C. avellana* nor *A. pseudoplatanus* are notably drought and or/waterlogging tolerant or associated with especially arid or wet environments (Niinemets and Valladares, 2006; Sterry, 2007), and their ACL values were within the normal range for deciduous trees (Bush and McInerney, 2013), suggesting that this is not the case with either species studied here. This further indicates species-specificity in *n*-alkane response to environmental change.

Bai et al. (2019) suggested that, although partially controlled by temperature, the average ACL change due to temperature was only around 0.3 carbon units per 4°C, across different temperature gradient studies and plant type. This study showed an increase in ACL of 1.6 units in 2022 compared to the average from the previous four Julys. Although the increase in temperature is difficult to quantify as it is unclear to what point in the growth season ACL responds, it is clear that 2022 temperatures were not ~20°C higher than previous years at any point. The 2022 growth season was characterised by drought as well as high temperatures, meaning the enhanced effect can potentially be attributed to decreased water availability alongside increased temperature. Temperature and water availability often covary, and metrics such as vapour pressure deficit, which are controlled both by temperature and water present in the environment may themselves control ACL (Eley and Hren, 2018), but without high-resolution measurements of air and soil moisture taken onsite through the study period, the increase in ACL cannot be attributed to a specific combination of the increased temperature and aridity.

Effect of CO_2 on leaf wax *n*-alkane chemistry

The decrease in ACL, increase in dispersion and increase in total *n*-alkane concentration detected in *C. avellana* in this study indicate an increase in permeability under elevated CO_2 after several years' continuous exposure. The observed changes are consistent with the hypothesis that under elevated CO_2, *C. avellana* wax becomes more permeable but less brittle. This response suggests that wax *n*-alkane chemistry can respond to elevated CO_2-derived water savings to optimise its composition. These changes indicate an increase in water loss at the leaf level which would partially counteract water use savings caused by stomatal closure under elevated CO_2 (Norby and Zak, 2011) but the magnitude of such water loss is unknown. Further research is necessary to quantify changes in cuticular permeability as a whole under elevated CO_2, which could have implications for plant-water relations under climate change.

It should be noted that from 2018-2021, a total of three replicates for each species, treatment, and sample date were taken. This implies it is possible that trends observed in this time interval are influenced by low sample size. Array-by-array, data suggests that the decrease in ACL in elevated CO_2 in 2020 and 2021 consistently occurred the most strongly in array 1, but that this array was similar in ACL to the other five arrays in the previous years, suggesting a CO_2 effect on this individual, but that the effect may not have consistently affected the entire species. With dispersion and concentration, the observed CO_2 effect appeared to represent a more even change across all elevated arrays compared to ambient. Replicates were taken in 2022 to try to determine if these trends persisted with a larger sample size: although the co-occurring drought potentially complicated interpretation, it appears the effect of CO_2 on ACL and total *n*-alkane

concentration in this species persist. Dispersion in 2022 showed the opposite trend with CO_2 to the previous three years, meaning, the relationship between CO_2 concentration and dispersion should be further verified with additional replicates in samples not grown in drought conditions. Further samples of additional species should also be taken: although *A. pseudoplatanus* showed no influence of elevated CO_2 on its *n*-alkane chemistry, further replicates may help to identify a small but persistent effect.

The observed response in *C. avellana* was only seen from the third year of CO_2 exposure. 2020 and 2021 were comparable in weather conditions to the previous three years (Figure 1) and no changes in experimental design occurred between 2019 and 2020 that could otherwise account for this trend. It is therefore likely that, in *C. avellana*, *n*-alkane homologue distribution requires several years' continuous CO_2 exposure for effects to emerge. A similar response was not observed in *A. pseudoplatanus*. This suggests either that its wax does not respond to CO_2 within a single individual exposed to changing conditions and multiple generations or evolutionary influences are necessary to influence *n*-alkane distribution, or that a longer acclimation to elevated CO_2 is required to observe an effect. Given that many studies experimentally manipulating environmental conditions to detect impacts on wax chemistry operate on timescales of a year or less (Huang et al., 1999; Kosma et al., 2009; Macková et al., 2013), this data suggests that the timeframe of experiments examining leaf wax response to environment should be increased to allow for potential effects to become apparent, and is potentially species-specific. It is also unclear how the magnitude of CO_2 change could affect *n*-alkane wax chemistry, whether changing the magnitude of CO_2 concentration would affect the rate of response to CO_2, and whether decreases in CO_2 (implying an

increase in required water) would have the opposite effect to the changes observed here.

Decreased ACL and total *n*-alkane concentration in elevated compared to ambient samples persisted in 2022, alongside the influence of the covarying changes in weather. However, the observed trend in dispersion was reversed in 2022: elevated CO_2 samples showed increased dispersion compared to ambient. It is unclear why this effect occurred: it is possible that increases to permeability induced by the elevated CO_2 treatment left *C. avellana* more vulnerable to drought stress long-term, but there is no further evidence to support this hypothesis. It is also noteworthy that dispersion calculated with all homologues rather than just odd-chained homologues shows no change under elevated CO_2 compared to ambient in this year, although CPI also showed no significant change.

Therefore, this data supports the hypothesis that in *C. avellana* but not *A. pseudoplatanus*, elevated CO_2 treatment caused a decrease in ACL and *n*-alkane concentration compared to ambient conditions. A potential increase in dispersion was also identified, but could not be verified due to the impacts of a co-occurring drought. The effect was only present from the third year of CO_2 treatment onwards but the 2022 drought caused much faster and more pronounced changes to *n*-alkane ACL: therefore, in *C. avellana*, leaf wax *n*-alkane chemistry can adjust to environmental conditions on short timescales, but required several years of continual CO_2 exposure to show an effect.

Implications for palaeoenvironmental reconstruction

CPI is often used as a measure of degradation in geologic samples of *n*-alkanes, as diagenetic processes can remove the odd-over-even preference that is characteristic of

n-alkanes produced via acetogenic biosynthesis (Tegelaar et al., 1989). However, this study identifies large changes in CPI – though CPI itself remained positive throughout – within a plant through the growth season, driven by an increase in the concentration of even-chained homologues (Figure 3). Outside of three anomalous samples, however, CPI remained greater than 1 throughout. CPI being changeable on short timescales may have implications for its use as a degradation indicator, as this data suggests a decrease in CPI may represent a change in when in the growth season the *n*-alkanes present in a sample were synthesised. However, CPI is already extremely variable in modern plants: in the dataset of Bush and McInerney (2013), which contains over 2,000 recorded CPI values from the literature, its standard deviation is 10 and ranges from 0 to infinite (i.e. no even-chained homologues were detected), with a maximum non-infinite recorded value of 99: with this range, a large change in CPI that remains >1 in a geologic sample may as easily represent a change in plant community as a change in diagenetic alteration and degradation. Therefore, this data further suggests, as in Bush and McInerney (2013), that CPI should not be used as a quantitative measure of degradation, as plant CPI itself is extremely variable.

Although ACL is rarely used as a palaeoclimate indicator directly, it is used as corroborating evidence for changes in temperature and precipitation alongside changes in species composition (Pearson et al., 2007; Smith et al., 2007; Castañeda and Schouten, 2011; Tipple et al., 2011). Any potential influences of elevated CO_2 on ACL in the geologic record have hitherto not been considered. Since on geologic timescales changes in atmospheric CO_2 concentration are directly linked to increases in temperature (Rohling et al., 2012), it is possible that changes in ACL that covary with temperature in the geologic record were partially responding to changes in atmospheric CO_2.

This may present a potential explanation for the inconsistency of trends between environmental data and ACL: although wax properties shift with environment, changes in wax properties are primarily conveyed via changes in dispersion rather than ACL. However, dispersion did not respond to the 2022 drought as ACL did, suggesting that the balance of the two may change based on timescale, species, and environmental changes.

The observed changes to *n*-alkane distribution with CO_2 are small and species-specific, and are obscured by seasonal variability and other environmental effects even in samples taken from trees of one species in one location. A trend with CO_2 of the magnitude observed in *C. avellana* would be obscured by shifts in vegetation composition if the effect persists similarly to that seen here (Bai et al., 2019), even if the majority of species showed this response. The seasonal changes in *n*-alkane ACL and dispersion which partially obscure trends may be averaged away in the geologic record, since early growth-season samples with lower ACL have a lower concentration of *n*-alkanes both in this study and others, and the majority of *n*-alkanes which enter the geologic record would be from mature leaves (Tipple et al., 2013; Newberry et al., 2015; Sachse et al., 2015; Huang et al., 2018). However, the large variability seen in mature leaves, although not showing a consistent seasonal trend, could be enough to obscure a weak CO_2 effect.

When *n*-alkanes are incorporated into soil or lake records, the ACL recorded can remove some noise as differences between species are averaged (Eley and Hren, 2018), making it more likely that if the small change in ACL detected in *C. avellana* is a more common response to CO_2 than the lack of response seen in *A. pseudoplatanus*, a small change in

ACL may be more detectable in these archives than in the original plant. However, although the change in dispersion identified in this study was larger in magnitude than ACL, as it is itself a measure of variability, dispersion in a geologic sample would likely be overprinted by the inherent variability in chain length distribution between species. Therefore, a small CO_2 effect may be apparent geologically in ACL, even where the effect is difficult to detect looking at individual leaves, but this is not likely to be the case for dispersion even if the effect at the leaf level is larger.

Furthermore, since *n*-alkane homologue distribution is partially phylogenetically controlled (Diefendorf et al., 2015b), it is likely that evolutionary-scale effects influence *n*-alkanes such that the magnitude of changes identified in any experimental study would not reflect those seen over geologic time. It is therefore unlikely that ACL or other wax *n*-alkane parameters will reflect atmospheric CO_2 concentration in the geologic record in a manner that is consistent or quantifiable. However, as with temperature, changes in ACL may qualitatively reflect changes in CO_2 concentration in specific contexts, and could be used as a corroborating argument alongside proxy CO_2 reconstructions.

Chapter 4: Impact of elevated CO_2 on the $\delta^{13}C$ of *n*-alkane biomarkers

Authorship statement

Samples used in this chapter were collected as described in the authorship statement for Chapter 3. Bulk $\delta^{13}C$ was produced at the University of Birmingham by myself and Dr Ian Boomer, and at the University of Hokkaido by Dr Osamu Seki. All data analysis and interpretation were performed by myself. Compound-specific $\delta^{13}C$ was produced by Dr Osamu Seki at the University of Hokkaido, and at the Organic Geochemistry Unit at the University of Bristol, funded by a NERC NEIF grant, by myself under the guidance of Dr Helen Whelton. All data analysis and interpretation were performed by myself.

Abstract

The stable carbon isotopic composition of *n*-alkane biomarkers are a commonly used proxy for studying plant response to palaeohydrology in the geologic record. However, interpretation *n*-alkane $\delta^{13}C$ tends to assume that all variation is due to changes in bulk plant $\delta^{13}C$, reflecting a signal of fractionation due to photosynthesis, and that the biosynthetic fractionations which occur after photosynthesis (εlipid) are constant. However, this assumption has not been tested: if εlipid covaries with environment, this could provide an alternate explanation for previously reported trends in *n*-alkane $\delta^{13}C$, as well as potentially allow the reconstruction of plant biochemistry in the geologic record. Here, I use the Birmingham Institute of Forest Research (BIFoR)'s Free Air CO_2 Environment experiment (FACE) to test the response of εlipid to elevated CO_2 concentrations. To do this, I measure $\delta^{13}C$ of both bulk and *n*-alkanes in *A.*

pseudoplatanus and *C. avellana* over four years. Both species' εlipid increases under elevated CO_2 compared to ambient, but the seasonal change in εlipid suggests that this increase occurs due to different mechanisms. In *A. pseudoplatanus*, this increase occurs consistently throughout the growth season, suggesting a change in carbon allocation to different tissue types within the plant is responsible. Conversely, in *C. avellana*, the effect becomes more pronounced as the growth season progresses, suggesting a change in the timing of *n*-alkane synthesis under elevated CO_2 may induce a change in εlipid. Collectively, this suggests that εlipid cannot be assumed to be constant in the geologic record, and highlights that biosynthetic processes should be considered when interpreting compound-specific isotopes.

Introduction

The $\delta^{13}C$ of *n*-alkane biomarkers is controlled by the sum of all carbon isotopic fractionations which occur during their formation, including those which control source atmospheric $\delta^{13}C$ (Ciais et al., 1995; Francey et al., 1999; Lomax et al., 2012), fractionations which occur during carbon fixation (Farquhar et al., 1989; Collister et al., 1994; Diefendorf et al., 2011), and the sum of biosynthetic fractionations during the synthesis of *n*-alkanes (Monson and Hayes, 1980; Chikaraishi et al., 2004a; Hobbie and Werner, 2004). These processes all potentially vary on geologic timescales, and can be affected by environmental conditions as well as, for the latter two, changes to biological mechanisms in response to environmental change (Huang et al., 1995; Tipple et al., 2010; Diefendorf et al., 2011; Franks et al., 2013).

In the geologic record, plant wax *n*-alkane $\delta^{13}C$ is commonly used to determine the relative contributions of C_3 and C_4 plants to a sample (Tipple and Pagani, 2010; Magill et al., 2013a) and, in environments where no C_4 plants are present, to reconstruct plant water-use efficiency (Schouten et al., 2007; Diefendorf et al., 2015b; Schlanser et al., 2020). Both of these interpretations correlate *n*-alkane $\delta^{13}C$ to the fractionations which occur during photosynthetic carbon fixation. In order to use *n*-alkane $\delta^{13}C$ to reconstruct both C_3/C_4 abundances and C_3 water use efficiency, it is therefore necessary to account for both changes in atmospheric $\delta^{13}C$ and the magnitude of post-photosynthetic fractionations. Although information on the former can often be determined from additional proxy organisms and is generally well constrained for the Cenozoic (Tipple et al., 2010), the magnitude of biosynthetic fractionation is specific to the plants which produced them (Diefendorf et al., 2015b), and is difficult to determine solely from isolated *n*-alkanes found in the sediment record. It must therefore be accounted for based on study of its magnitude in modern plants (Tipple and Pagani, 2010; Magill et al., 2013a).

Biosynthetic processes collectively cause a large decrease in $\delta^{13}C$ between bulk (or average plant tissue) and *n*-alkanes, equal in to roughly half again the magnitude of the fractionation between bulk and atmospheric $\delta^{13}C$ (Basu et al., 2021). This shift in isotopic composition is the sum total of many different fractionations which occur during *n*-alkane biosynthesis. An initial decrease in proportion of ^{13}C is induced during the formation of acetyl CoA from pyruvate (Monson and Hayes, 1982); further fractionations applied at later stages of *n*-alkane biosynthesis result in differences of $\delta^{13}C$ within lipid species (Chikaraishi et al., 2004a, b; Zhou et al., 2015). The sum total isotopic effect of these individual reactions is defined as

$$\varepsilon_{lipid} = \left[\left(\frac{\delta_{lipid}+1000}{\delta_{leaf}+1000}\right) - 1\right] \times 1000$$

(13)

(Hayes, 2001) representing the difference in isotopic composition between the total leaf (or bulk) $\delta^{13}C$ and lipid species (for example *n*-alkanes) within it. Since lipids are typically depleted in ^{13}C compared to bulk, a larger difference between the two usually results in a more negative value.

εlipid is influenced both by phylogeny and growth form, and can be highly variable: for example, it is more negative in shrubs and forbs than in angiosperm and gymnosperm trees (Diefendorf and Freimuth, 2017), but the values heavily overlap within these groups (Diefendorf et al., 2015b). Furthermore, although the impact of plant biology on εlipid has been investigated previously, the influence of environmental conditions remains largely unstudied.

Several mechanisms exist which have the potential to influence εlipid. The two most likely to invoke changes in εlipid with environment are a) a change in the allocation of C to synthesis of *n*-alkanes or any precursor molecule, and b) a change in the seasonal timings by which *n*-alkanes are synthesised relative to bulk.

Although the fractionations associated with the activity of individual enzymes in each step of *n*-alkane synthesis are likely constant on non-evolutionary timescales, changes to εlipid can occur through alteration of the flux of carbon through biosynthetic processes. The difference in the isotopic composition of biosynthetic products is set by both the magnitude of enzymatic fractionation at branch points during biosynthesis, and the allocation of carbon between them. In this case, the overall $\delta^{13}C$ would remain the same,

as no carbon is gained or lost from the system, but the $\delta^{13}C$ of individual molecules would differ. Therefore, any changes to the flux of carbon to different biosynthetic product induced by environmental change could result in an influence of environment on εlipid without causing a change in bulk $\delta^{13}C$ (Collister et al., 1994; Hayes, 2001; Hobbie and Werner, 2004; Dungait et al., 2011).

Alternatively, a change in εlipid with environment can also be induced by changes to the timing of *n*-alkane production seasonally. Bulk tissue and *n*-alkanes are synthesised using the photosynthetic carbon pool present at the time of their synthesis, but the $\delta^{13}C$ of the photosynthetic carbon pool itself is not constant throughout the growth season as a) atmospheric $\delta^{13}C$ differs seasonally, and weighting toward a different time in the year for synthesis alters the atmospheric $\delta^{13}C$ from which photosynthetic carbon is fractionated (Keeling et al., 2001), b) the magnitude of photosynthetic carbon fractionation also varies through the growth season, as plants decrease Ci/Ca during times of water stress (Seibt et al., 2008), and c) plant tissue can be synthesised using carbon stored from the previous growth season, which is enriched in ^{13}C (Terwilliger and Huang, 1996; Tipple and Ehleringer, 2018). If changes to environment induce a change in the seasonal timings of *n*-alkane synthesis relative to bulk tissue, then *n*-alkanes would be synthesised from a photosynthetic carbon pool that was systematically offset from that of bulk tissue, leading to an apparent environmental effect on εlipid.

Since an increase in pCO_2 provides additional substrate to plants for use in biosynthesis (Poorter and Navas, 2003), it is possible that elevated CO_2 could cause a shift in carbon allocation patterns compared to ambient, effecting a change in *n*-alkane $\delta^{13}C$ but not

bulk. An increase in CO_2 concentration is associated with an increase in the proportion of carbohydrates within plants (Ainsworth and Long, 2005) and a proportional decrease in other components (Poorter et al., 1997). A decrease in the supply of C to lipid synthesis due to decreased proportional allocation to the lipid component of the plant would cause an increase in ^{13}C within lipids, and all other plant components, relative to carbohydrates. As lipids comprise only ~2% of plant mass, a small change in the total amount of carbon supplied to their synthesis would be a large proportional change but extremely small in terms of the absolute change in mass, and its effects may therefore be detectable isotopically but not in changes in lipid concentration directly (Hobbie and Werner, 2004; Dungait et al., 2011).

Elevated CO_2 also induces a large number of changes in proportions of many individual compounds within plants but, as with many of the downstream effects of elevated CO_2 on plant metabolism, effects remain poorly studied, are probably species specific, and change based on covarying environmental conditions such as drought stress (Kanani et al., 2010; Creydt et al., 2019; Avila et al., 2020; Geddes-McAlister et al., 2020; Rodrigues et al., 2021). Isotopic changes could be induced by altering allocation at any branch point leading to *n*-alkane synthesis, meaning a shift in isotopic composition could indicate a large-scale shift of plant tissue types, a much smaller-scale change to different compound classes within lipids, or a combination of the two.

(Zhou et al., 2015) suggests that changes to carbon allocation in *n*-alkyl lipids specifically are responsible for variations in isotopic composition within lipids, as concentration of *n*-alkyl lipids are associated with responses to environment to induce water savings but other lipid classes are more constant as their functions within plants require more

stable concentrations. However, changes in concentrations of other lipid components may be expected due to changes to plant metabolism under elevated CO_2 (Scotti-Campos et al., 2019). Therefore, although any changes in *n*-alkane concentration under elevated CO_2 would induce an isotopic shift by changing allocation patterns, changes to the proportion of other molecules may also induce an isotopic change in *n*-alkanes independent of their concentration, and a change in *n*-alkane εlipid in isolation does not identify which branch points may have been affected.

Elevated CO_2 could induce an effect on εlipid due to both changes in carbon allocation and changes in seasonal *n*-alkane production, as changes in CO_2 concentration alter plant-water relations (Seibt et al., 2008). Since a key function of *n*-alkyl lipids within plants is waterproofing and an increase in CO_2 concentration reduces stomatal water loss, a lower concentration of *n*-alkanes may be synthesised under elevated CO_2 as saving water becomes less important for plant survival. Increases in *n*-alkane concentration are often but not always reported as a result of heat/drought stress, implying the trait is somewhat plastic (Kosma et al., 2009; Macková et al., 2013; Diefendorf et al., 2021). Interestingly, (Huang et al., 1999) reported an increase in *n*-alkane concentration in elevated CO_2, but a decrease in *n*-alkanol concentrations: this implies that changes to total *n*-alkyl lipid production are not always reflected in *n*-alkane synthesis specifically. Similarly, water savings under elevated CO_2 may alter the phenology of *n*-alkane production by altering plant water requirements early in the growth season, when *n*-alkane synthesis is often highest (Gao et al., 2012).

Few previous studies have experimentally determined the impact of environment on εlipid. Diefendorf et al. (2021) found that both heat and drought led to a decrease in

εlipid in *Juniperus monosperma* in an open-top chamber experiment, suggesting environmental variables can alter εlipid within a single species on short timescales, but as only a single species was studied, its impact on other species remains unknown. With regards to changes in atmospheric CO_2 concentration, (Huang et al., 1999) found that an increase in CO_2 concentration from 350 to 600 ppmv caused no change in εlipid in *Betula pendula* seedlings grown in pots after one growth season, whereas (H. Zhang et al., 2019) found a decrease in CO_2 concentration led to a decrease in εlipid. Diefendorf et al. (2021) attributed their detected decrease in εlipid in the hotter, drier study groups to shifts in the seasonal timings of *n*-alkane synthesis rather than a direct change to biosynthetic fractionation itself. Effects of this sort may not have occurred in the studies of (Huang et al., 1999) and (H. Zhang et al., 2019), as both were grown indoors or within closed domes (Cotrufo et al., 1994): therefore, changes to the seasonal growth of plants are likely not the only mechanism by which εlipid can vary with environment.

It is therefore possible for εlipid to vary with environmental change, but it does not occur in all experimental setups. It is unknown whether the difference in observed response were due to differences in experimental design or the different species used, or whether the response of εlipid to environment is variable over time. Furthermore, other than Diefendorf et al. (2021), all prior investigations of the response of εlipid to environment have only taken place in extremely short duration growth chamber experiments, meaning any potential changes to εlipid with environment induced on longer timescales, by exposure to co-occurring weather and seasonal changes, or in non-juvenile perennial plants, may not have been seen.

Atmospheric CO_2 concentration has changed profoundly through geologic time (Royer, 2013), and understanding how plant biomarkers are influenced by CO_2 would constrain our understanding of plant response as a whole to CO_2 concentrations on these timescales. Specifically, our current interpretation of *n*-alkane $\delta^{13}C$ attributes all shifts in *n*-alkane $\delta^{13}C$ to changes to the $\delta^{13}C$ of bulk plant tissue (Tipple and Pagani, 2007; Magill et al., 2013b; Schlanser et al., 2020) and does not tend to consider changes in post-photosynthetic fractionation as a potential causal mechanism. Furthermore, if εlipid could be shown to vary consistently with environment, understanding it give rise to additional interpretations of *n*-alkane $\delta^{13}C$ through geologic time.

This study aims to characterise the influence of an increase in CO_2 concentration on leaf wax *n*-alkane εlipid in two species over four years of CO_2 treatment in the BIFoR FACE experiment. The four years of εlipid data from across the growth season presented here will allow attribution of any changes in εlipid to changes in seasonality, and show whether εlipid can be influenced by CO_2 in a longer-term experiment taking place in a natural ecosystem. Specifically, this study will examine whether εlipid is influenced by CO_2, whether this influence is consistent across the study period and through the growth season, if both species respond to CO_2 similarly, and what biological and environmental processes can explain any observed trends in εlipid.

Methods

Preliminary data for the $\delta^{13}C$ of atmospheric CO_2 was obtained from Ullah, 2021 (pers. Comms). These were taken on a single occasion in 2021.

Leaf samples were taken from the Birmingham Institute of Forest Research and processed for bulk and *n*-alkane $\delta^{13}C$ as described in Chapter 2. In brief, samples of

approximately 4 leaves of *A. pseudoplatanus* and six leaves of *C. avellana* were collected from the three ambient CO_2 and three elevated CO_2 arrays at BIFoR FACE each month through the growth season from 2018-2021 to give a total of 6 samples per species collected on each sampling date. Samples were collected from head height, frozen at 20°C and transported back to the University of Birmingham, where they were processed as described in Chapter 2 to determine their bulk and *n*-alkane $\delta^{13}C$.

εlipid was calculated for each sample using Equation 1. The weighted mean average *n*-alkane $\delta^{13}C$ was used to produce εlipid, unless otherwise specified. The CO_2 effect on εlipid was detrended from seasonal variation by calculating the deviation of each sample from the mean of all the samples for its given species and date. The full details of this detrending are explained in Chapter 3.

Results

Bulk $\delta^{13}C$ ranged from -30.5 to -36.3 in the ambient treatment, and -33.0 to -41.0 in the elevated (Figure 1b). Both ambient and elevated values stayed similar over the four years of the experiment, and between the two species (Figure 1b). Weighted mean *n*-alkane $\delta^{13}C$ was generally lighter than bulk $\delta^{13}C$, and similar between both species (Figure 1a). It ranged from -35.1 to -42.4‰ in ambient CO_2, and -32.3 to -46.3‰ in elevated CO_2. *n*-Alkane $\delta^{13}C$ showed more considerable overlap between CO_2 treatments than bulk $\delta^{13}C$.

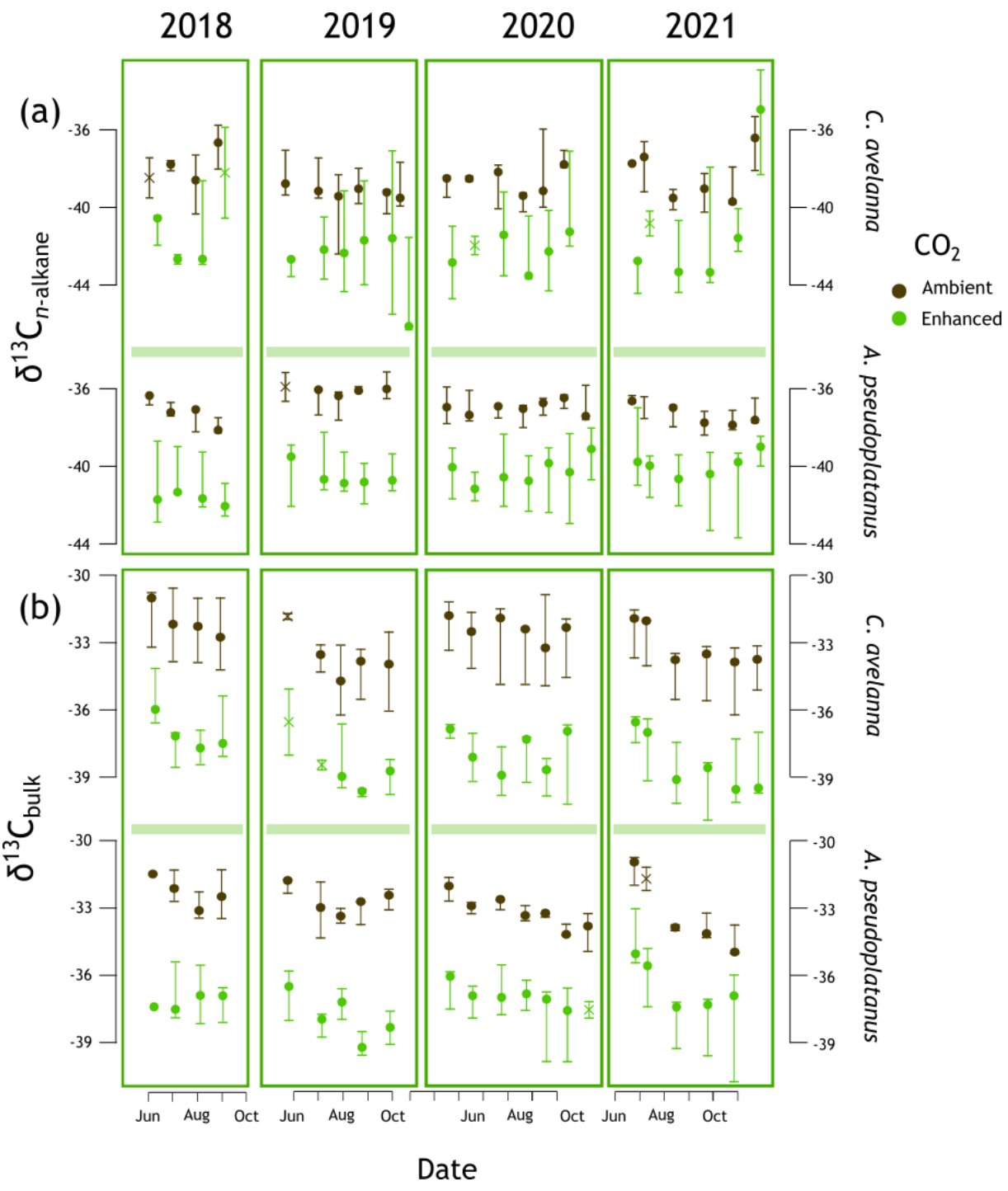

Figure 1: (a) *n*-alkane and (b) bulk plant $\delta^{13}C$ over the 2018-2021 growing seasons. Error bars represent the maximum, minimum, and median of the three measurements made per species and CO_2 treatment for each month. Where only 2 measurements were available, the median of the two measurements is marked with an x.

εlipid was more variable in *C. avellana* than *A. pseudoplatanus* throughout the experiment (Figure 2). Although somewhat obscured by monthly variability, εlipid was consistently higher in elevated than ambient pCO_2 samples in both species. The difference between CO_2 treatments was significant in both species both with and without detrending from monthly variability, but was larger in magnitude in *C. avellana* (average 1.9‰, detrended from monthly variability) than *A. pseudoplatanus* (average 0.63‰).

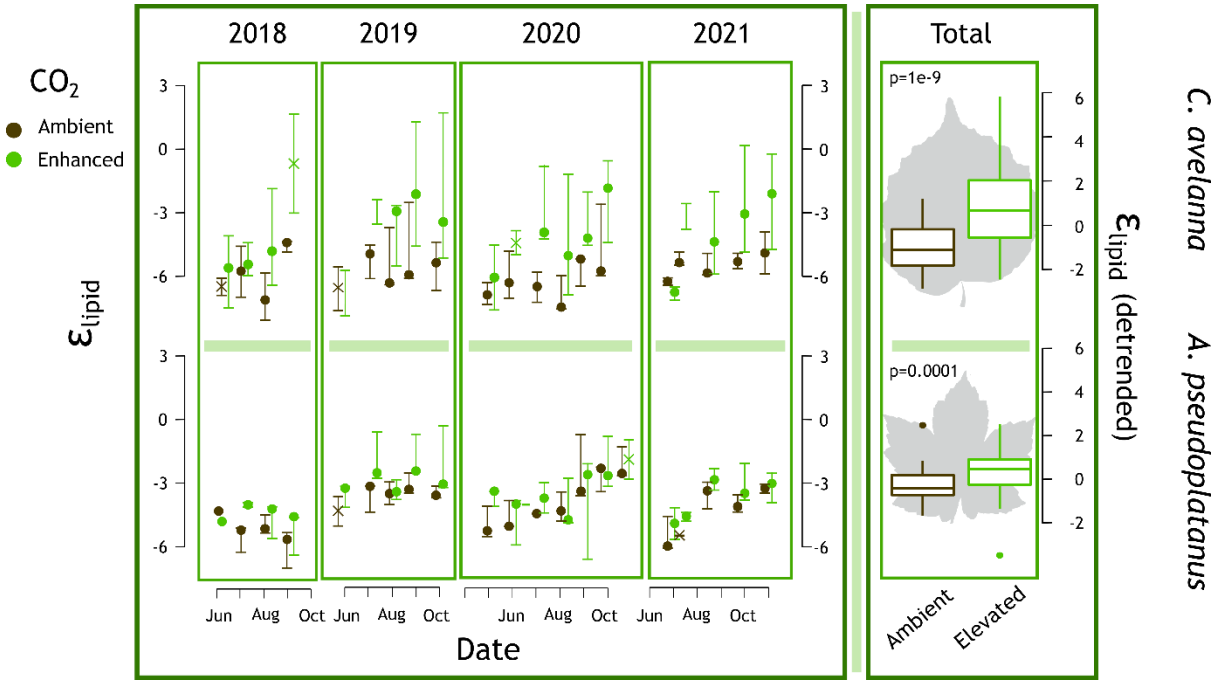

Figure 2: Weighted mean average εlipid over the 4 years of the study (left) and combined and detrended from monthly variation (right).

On average, bulk $\delta^{13}C$ decreased throughout the growth season in both species and treatments (Figure 3a). This decrease occurred at a roughly constant rate of -0.01‰ per day. *n*-Alkane $\delta^{13}C$ was constant through the growth season in *A. pseudoplatanus*, and in

C. avellana ambient CO_2 samples, but increased slightly in elevated CO_2 samples (Figure 3b).

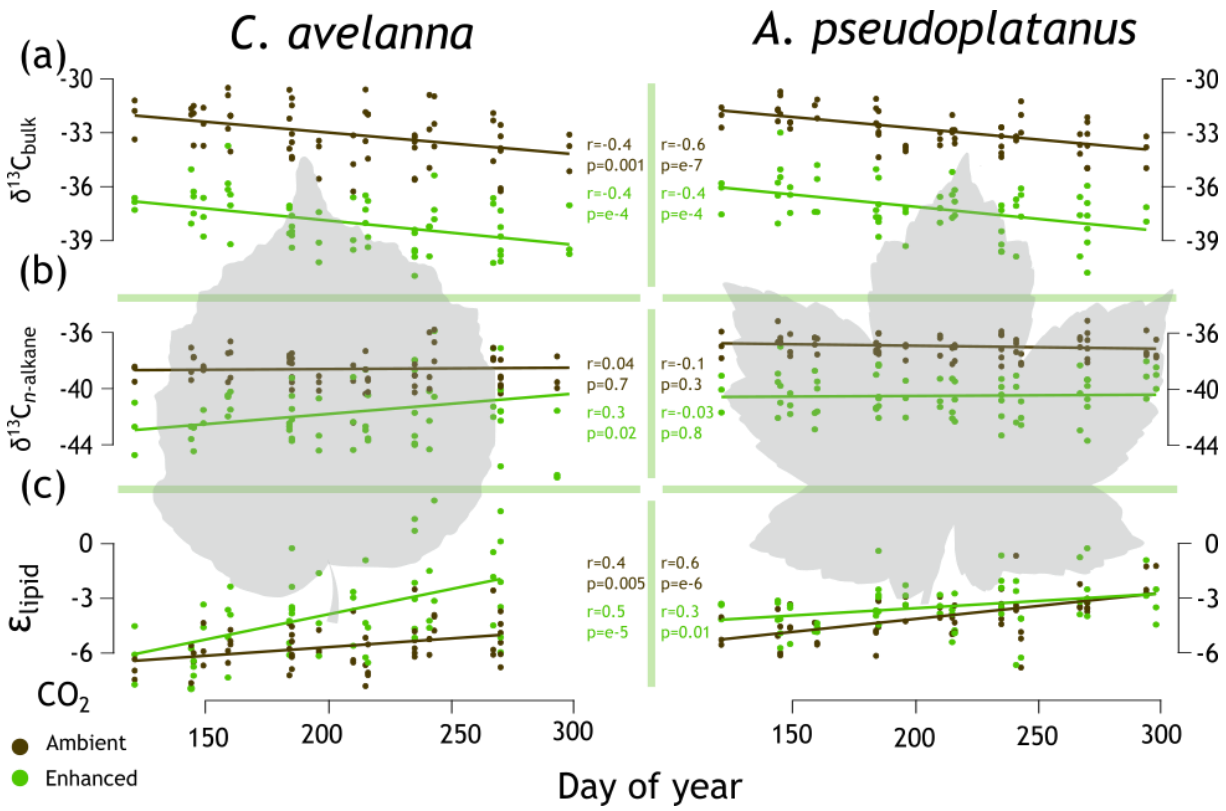

Figure 3: (a) bulk and (b) *n*-alkane $\delta^{13}C$, and (c) εlipid in all four years, compared to the day of year of sample collection

εlipid increased seasonally in both species and CO_2 treatments (Figure 3c). As εlipid is calculated from bulk and *n*-alkane $\delta^{13}C$, this trend originates from the decrease in bulk $\delta^{13}C$ through the growth season, whilst *n*-alkane $\delta^{13}C$ remained constant. The rate of increase of εlipid with day of year in *A. pseudoplatanus* was constant between the two treatments, though, as εlipid was consistently higher, the intercept was also higher. However, in *C. avellana*, the elevated treatment samples increased at roughly 2.5x the rate of the ambient (Table 1): at the beginning of the growth season, *C. avellana* showed

little difference between treatments, whereas by the end, a difference of around 3‰ was observed.

Table 1: Linear regression between εlipid and year for each species and treatment

Species/treatment	Intercept	Slope
C. avellana ambient	-7.78476	0.01057
C. avellana elevated	-9.0477	0.0267
A. pseudoplatanus ambient	-7.07027	0.01479
A. pseudoplatanus elevated	-5.60943	0.01072

The seasonal changes in εlipid were larger in magnitude than any changes between years. In 2018 in *A. pseudoplatanus*, εlipid was significantly lower than the following three years. εlipid also did not increase through the growth season in this species and year, weakening the trend seen in Figure 3c. Other than *A. pseudoplatanus* in 2018, εlipid increased at least moderately as the growth season progressed in both species and CO_2 treatments, and there were no major differences in average εlipid year-on-year.

εlipid of individual homologues

The relationship between εlipid and homologue differed between the two species. In *C. avellana*, the shortest homologues (C_{25} and C_{27}) were more enriched in ^{13}C than the longer homologues (C_{29}+), whereas in *A. pseudoplatanus*, the most enriched homologues were C_{25}, C_{27}, and C_{33} (Figure 4a). All homologues in both species showed a significant increase in εlipid in the higher CO_2 treatment (Figure 4b). Of these, the C_{25} showed the

largest difference in εlipid with CO_2 in *A. pseudoplatanus*, and the C_{25} and C_{27} showed the largest difference in *C. avellana* (Figure 4c).

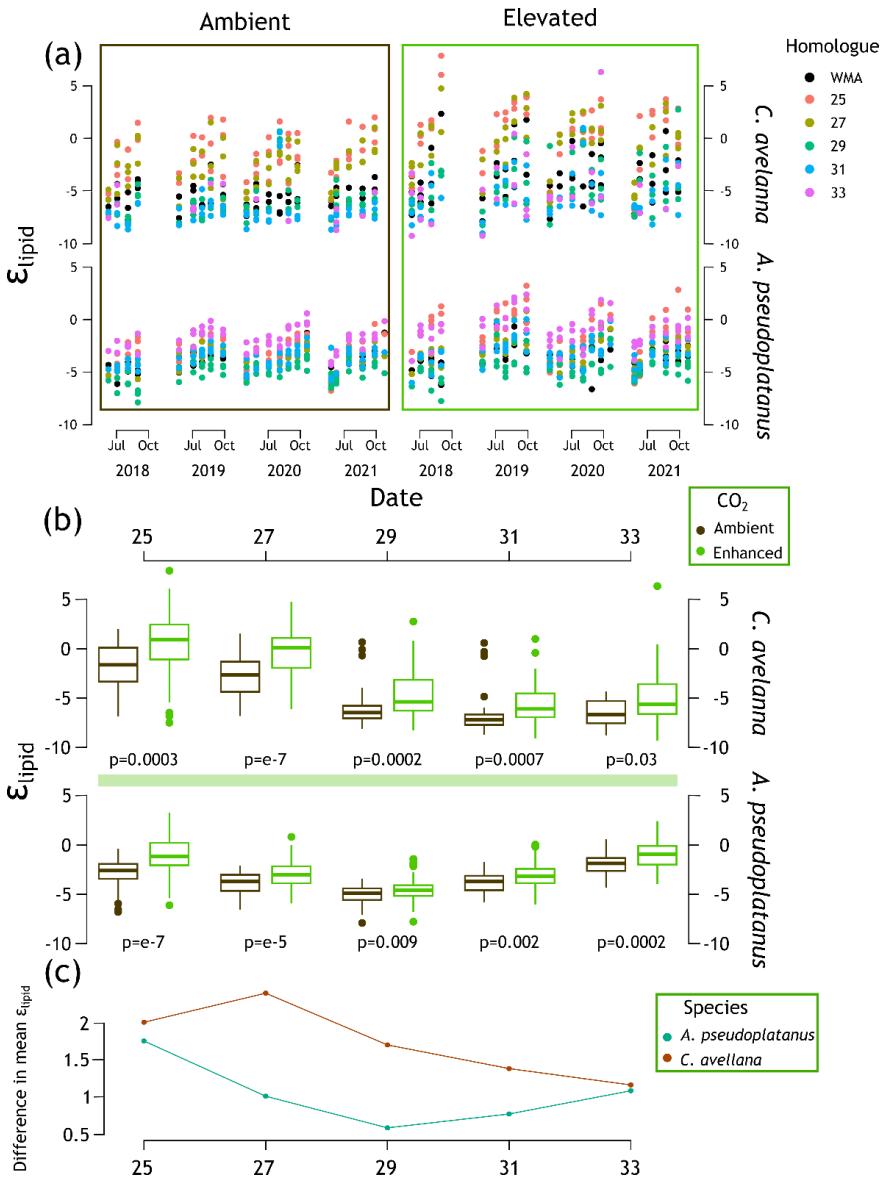

Figure 4: εlipid in the *n*-alkane homologues C_{25} to C_{33} for each species and CO_2 treatment, a) through the growth season, b) aggregated through the entire experiment, and c) difference between mean elevated and ambient εlipid for each homologue when detrended from seasonal variation. P-values indicate student's *t*-test between elevated and ambient samples for each homologue and species.

Branched alkanes

Branched alkanes eluted before the normal alkane of the same chain length: first the *iso*-alkane, then *anteiso*, followed by the normal (Figure 5). *Iso*-alkanes tended to display an odd-over-even preference, and *anteiso*-alkanes an even-over-odd preference.

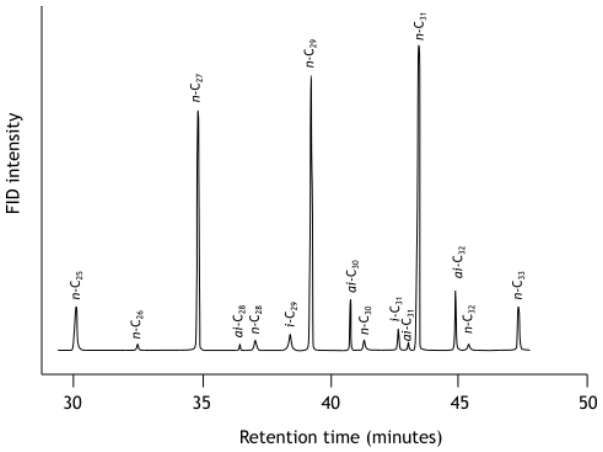

Figure 5: chromatogram showing elution times of branched and *n*-alkanes.

Isotopic composition was measured for the *i*-C_{31} and *ai*-C_{32} alkanes. Of samples where *n*-alkane isotopes were measured, 92% contained measurable levels of the *ai*-C_{32} and 82% contained measurable levels of the *i*-C_{31}.

Branched alkanes' εlipid ranged from -6‰ to +6‰ (Figure 6). The *ai*-C_{32} branched alkane was, on average, more enriched in ^{13}C than the *i*-C_{31} by 0.88 ± 0.76‰, and the C_{31} *n*-alkane by 2.5 ± 1.2‰. The εlipid of the branched alkanes were tightly correlated with each other (Figure 6a) and less tightly correlated with that of the weighted mean average (WMA) *n*-alkane εlipid (Figure 6b).

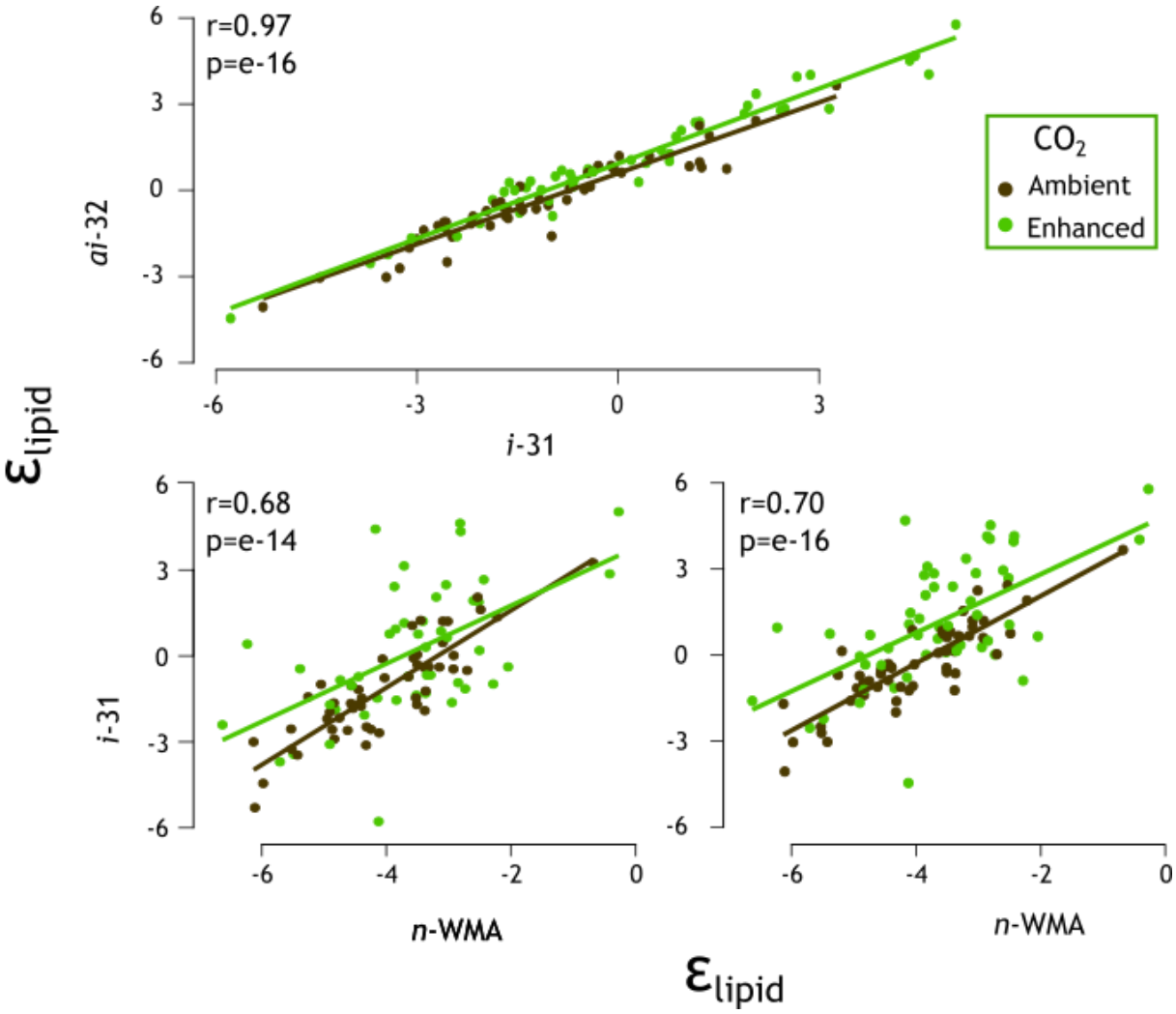

Figure 6: Crossplot of (a) *i*-C_{31} and *ai*-C_{32} branched alkane εlipid and (b) branched and weighted mean average *n*-alkane εlipid (relative to bulk)

Branched alkane εlipid was higher in elevated samples compared to ambient in the first two years of the study; this difference was weaker or absent in 2020 and 2021 (in 2018-19 p=e-5 and e-7 for the *i*-C_{31} and *ai*-C_{32} respectively, in 2020-21 p=0.4 and 0.1). On average over the four years, the difference in εlipid in elevated CO_2 compared to ambient is greater in both branched alkanes than that seen in *A. pseudoplatanus n*-alkanes (average 0.5 increase in *n*-alkanes, and 1.3 and 1.5 for the *i*-C_{31} and *ai*-C_{32} respectively, Figure 7). A further CO_2 effect can be observed in the difference between branched and

n-alkane $\delta^{13}C$ that is expressed more weakly in the later two years of the experiment (Figure 7): there is a strong difference between treatments in the *i*-C_{31} from 2018-19 that is more weakly observed in 2020-2021 (p=e-5 2018-2019 and 0.1 2020-2021), and 2018-2020 but not 2021 in the *ai*-C_{32} (p=e-8 2018-2020, p=0.8 2021).

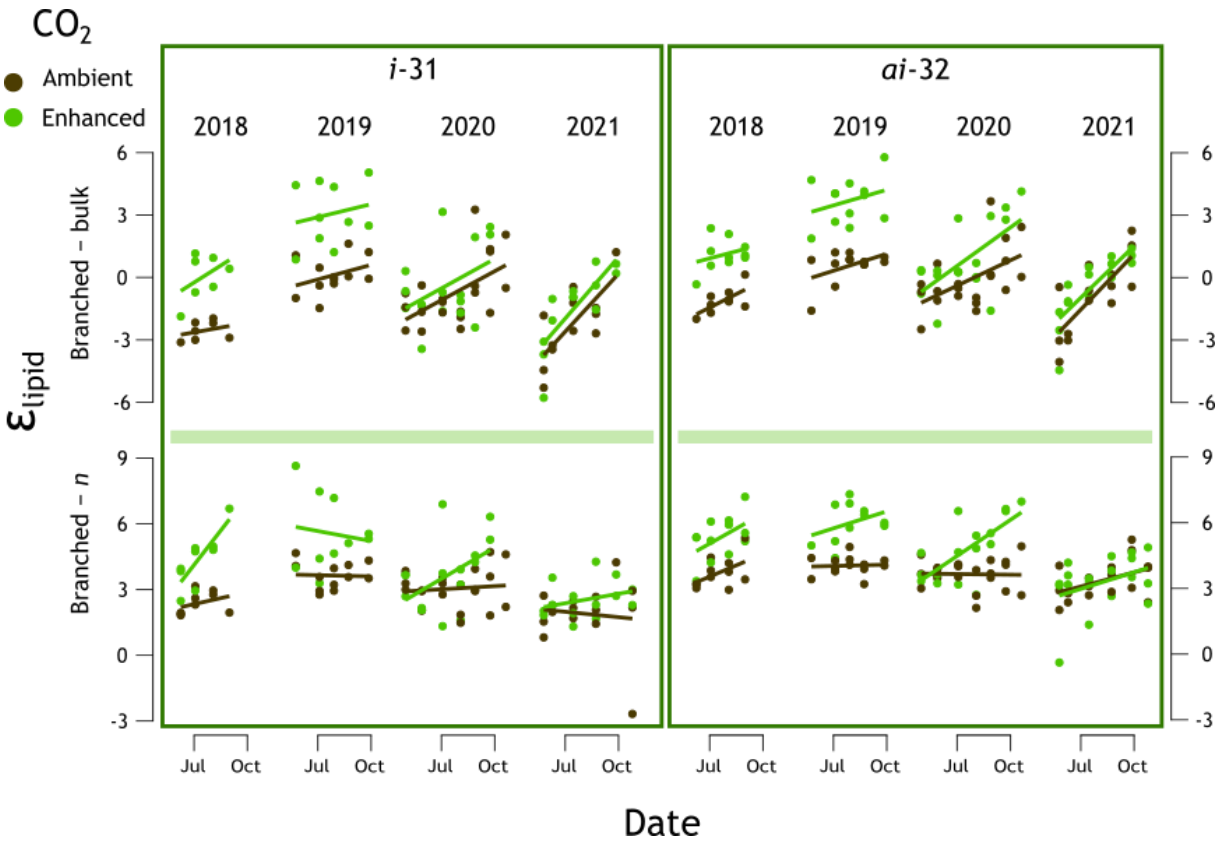

Figure 7: Branched alkane εlipid in *A. pseudoplatanus* for the *i*-C_{31} (left) and *ai*-C_{32} (right) branched alkanes. Top panels are the εlipid between branched and bulk, bottom are the εlipid between branched and weighted mean average *n*-alkane.

As with the *n*-alkanes, branched εlipid compared to bulk increased through the growth season in both homologues (p=e-5 and e-6 in the *i*-C_{31} and *ai*-C_{32} respectively, Figure 7). Unlike with *n*-alkanes, the εlipid of branched alkanes differed between the four years of the study: for example, εlipid of both the *i*-C_{31} and *ai*-C_{32} in both CO_2 treatments were higher in 2019 than the other three years of the study (p<0.0007 in both homologues

and CO_2 treatments). There was no consistent seasonal trend in the offset between branched and *n*-alkane $\delta^{13}C$ (Figure 7).

εlipid and *n*-alkane concentration

Weighted mean average εlipid weakly covaried with $\log_{10}$ total *n*-alkane concentration in *C. avellana* (r=-0.4 p=e-6). This correlation may have also been present in *A. pseudoplatanus*, but was extremely weak (r=-0.2 p=0.06). When the concentration and εlipid of all homologues were compared separately, these trends strengthened in *A. pseudoplatanus* (Figure 8). Trends in *A. pseudoplatanus* were similar with and without the inclusion of the *i*-C_{31} *ai*-C_{32} branched alkanes: although consistently higher in ^{13}C than the *n*-alkanes, the branched alkanes were also consistently lower concentration. The relationship between εlipid and concentration was not present within individual homologues, i.e. low concentration homologues tended to have higher εlipid, but a highly concentrated *n*-C_{25} sample did not necessarily have a lower εlipid than a low concentration sample (Figure 8b).

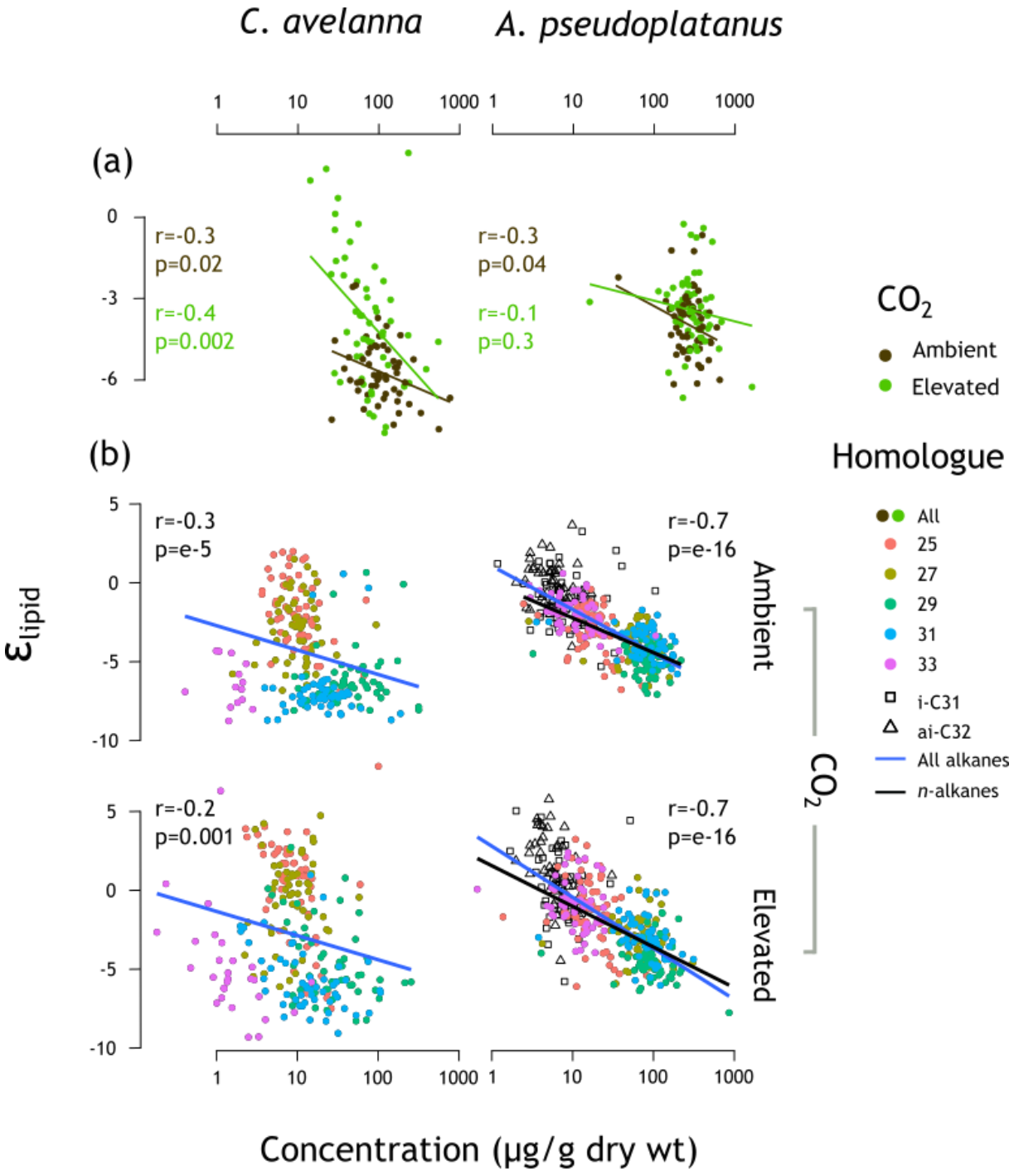

Figure 8: Relationship between $\log_{10}$(concentration) and εlipid of all *n*-alkanes and each alkane homologue. a) weighted average εlipid vs sum concentration of all homologues. b) $\log_{10}$(concentration) and εlipid of each individual alkane homologue.

Discussion

Bulk $\delta^{13}C$

Elevated CO_2 treatment resulted in a clear decrease in bulk $\delta^{13}C$ compared to ambient (Figure 1). This can be directly attributed to the additional CO_2 pumped in to the elevated CO_2 plots, which was significantly lighter than the $\delta^{13}C$ of atmospheric CO_2. This is often the case in elevated CO_2 experiments (Lomax et al., 2019): $\delta^{13}C$ in BIFoR and other experiments was derived from natural gas, which is strongly depleted in ^{13}C compared to atmospheric (Andres et al., 2000). Measured source gas for BIFoR was -36 ± 0.14‰ on one occasion in July 2020 (Ullah, 2021, pers. Comms)

CO_2 supplier to the site was variable and large changes in $\delta^{13}C$ between shipments could not be ruled out. Therefore, the $\delta^{13}C$ of BIFoR's source gas was not considered adequately constrained to the level necessary to quantify changes in photosynthetic fractionation within this dataset.

The plants grown under ambient CO_2, although isotopically heavier than the elevated CO_2 plants, also showed extremely depleted $\delta^{13}C$ compared to expected values for C_3 plants: any plant shown to have lower $\delta^{13}C$ than -31.5‰ is considered to be affected by the canopy effect (Kohn, 2010). 87% of ambient samples in this study are more depleted than this cutoff (Figure 1).

The canopy effect is generally associated with closed-canopy tropical rainforests, and causes a decrease in the $\delta^{13}C$ of plants via several concurrent processes. High temperatures cause large amounts of soil respiration, which releases isotopically light CO_2, which can then be incorporated alongside atmospheric $\delta^{13}C$ into plant tissue. The

closed canopy minimises turbulent mixing of the atmosphere and allows CO_2 to build up in the understorey without removal, compounding the process (Farquhar et al., 1989; van der Merwe and Medina, 1991). This effect is generally seen in tropical rainforests, but can occur in any closed-canopy forest (Bonafini et al., 2013).

It is likely that these effects are responsible for the low bulk $\delta^{13}C$ at BIFoR. $\delta^{13}C$ of canopy oak leaves also taken at BIFoR fall within the normal range for C_3 plants (Table A4), suggesting the depleted $\delta^{13}C$ detected was limited in scope to the understorey. Therefore, this effect is likely not due to cross contamination of CO_2 from enhanced CO_2 arrays into ambient, as this would be seen at all levels of the forest. $\delta^{13}C$ of CO_2 measured in the understorey was measured at between 9 and 11‰ (Ullah, 2021, pers. Comms); significantly more depleted than the global atmospheric average of ~-8.7‰ (Keeling et al., 2001), and a change on a similar order of magnitude to the change in photosynthetic discrimination expected due to changes in CO_2 concentration (Saurer et al., 2003). This implies that CO_2 originating from soil respiration significantly depleted the ^{13}C in source gas for photosynthesis in the studied trees. Since photosynthetic discrimination cannot be determined without highly constrained atmospheric $\delta^{13}C$ or gas exchange data, the effects of this cannot be quantified. It is therefore unknown whether water use efficiency increased in the measured species.

In addition to a decrease in $\delta^{13}C$, the canopy effect implies an increase in atmospheric pCO_2 in the understorey of the forest, due to additionally released respired CO_2 (Flanagan et al., 1996). The absolute CO_2 concentration over the study therefore cannot be assumed. However, as an additional +150 ppmv CO_2 was added at all levels of the canopy, elevated CO_2 arrays still represent an increase in CO_2 concentration compared

to ambient, and although this limits the potential for quantifying CO_2 effects, observed changes in response to the additional +150 ppmv CO_2 in this study can still be attributed to such.

εlipid

The observed increase in *n*-alkane εlipid with CO_2 concentration corresponds to a decrease in the magnitude of biosynthetic fractionation under elevated CO_2. This effect is small and its magnitude is species-specific, but consistent across all four years of the study (Figure 2). This is consistent with the findings of Schubert and Jahren (2012) and Zhang et al. (2019) who also detected an increase in εlipid with increasing CO_2 concentration, which varied in magnitude between their studies (and therefore their study species), but is counter to the study of (Huang et al., 1999), which found no effect of a CO_2 increase on εlipid. As this study found inconsistent changes to εlipid between the two species, it is likely that the differences in εlipid detected in the above study can be attributed at least partially to differing responses between species, rather than solely due to differences in experimental design.

Influence of seasonality on εlipid and CO_2 response

The difference in εlipid between CO_2 treatments increased with day of year in *C. avellana* but not in *A. pseudoplatanus* (Figure 3). This suggests that the CO_2 effect on εlipid in *C. avellana* compounded through the growth season, and is evidence that seasonal changes in *n*-alkane production influenced εlipid in this species.

In *C. avellana*, the difference between treatments was minimal in the earliest samples taken in the season (Figure 3c), suggesting that at the beginning of the growth season, differences in εlipid between treatments were small or absent. Elevated CO_2 treated

samples of this species were the only ones to show a trend in *n*-alkane $\delta^{13}C$ through the growth season: in ambient *C. avellana* and both treatments of *A. pseudoplatanus*, *n*-alkane $\delta^{13}C$ remained constant (Figure 3b).

The seasonal change in isotopic composition of *n*-alkanes can indicate the time in the growth season at which they are synthesised. Any change in $\delta^{13}C$ in bulk or *n*-alkane tissue throughout the growth season indicates production of bulk or *n*-alkane tissue has continued throughout, although constant $\delta^{13}C$ could also be produced if both the substrate and magnitude of fractionations during formation of tissue remain constant seasonally. The $\delta^{13}C$ of both atmospheric CO_2 (Keeling et al., 2005a) and bulk plant $\delta^{13}C$ (Newberry et al., 2015; Tipple and Ehleringer, 2018) vary seasonally depending on use of autotrophic versus stored carbon, explaining the decrease in bulk $\delta^{13}C$ through the growth season observed here (Figure 3a). *n*-Alkane $\delta^{13}C$ in *A. pseudoplatanus* and ambient *C. avellana*, however, remained constant throughout the growth season. This implies *n*-alkanes were produced largely at the beginning of the growth season, or their $\delta^{13}C$ would mirror bulk tissue (Tipple et al., 2013). The apparent increase in ε_{lipid} through the growth season was driven entirely by the decrease in bulk $\delta^{13}C$. This suggests that, for samples taken later in the growth season, bulk $\delta^{13}C$ does not well approximate the photosynthetic carbon pool used for *n*-alkane synthesis, and if ε_{lipid} is to be used to quantitatively trace changes to biosynthetic processes, care must be taken to ensure that both bulk and *n*-alkane $\delta^{13}C$ reflect the same carbon pool temporally. This suggests that in plants where *n*-alkanes are largely synthesised at the beginning of the growth season, calculation of their ε_{lipid} should take place soon after leaf flush, when the carbon pools used for leaf growth and *n*-alkane synthesis are likely more synchronised.

The increase in *n*-alkane $\delta^{13}C$ detected in elevated *C. avellana* but not ambient through the growth season suggests that elevated CO_2 has induced a move from *n*-alkane synthesis only at the beginning of the growth season to some synthesis throughout. Whether *n*-alkanes are synthesised largely at the beginning of the growth season or throughout varies between studies (Sachse et al., 2009, 2010, 2015; Gao et al., 2012; Newberry et al., 2015; Oakes and Hren, 2016; Huang et al., 2018), suggesting it is species- and site-specific. However, as studies tend to investigate changes over the growth season at single locations, changes to the seasonality of *n*-alkane production with environment have not hitherto been studied. This data directly shows that in *C. avellana*, the timing of *n*-alkane synthesis is somewhat plastic to environmental changes. Geologically, understanding the timing of *n*-alkane synthesis throughout the growth season constrains any climate signal that may be recorded, as it is expected that *n*-alkanes would primarily record a signal of the environment at the time they were synthesised. Evidence that *n*-alkane synthesis is changeable on short timescales due to environmental stimuli therefore complicates interpretation of *n*-alkanes geologically (Oakes and Hren, 2016).

In *A. pseudoplatanus,* the difference in εlipid between treatments remained constant through the growth season. Therefore, changes in the timing of *n*-alkane synthesis cannot explain trends in εlipid in this species. This further suggests that the response of *n*-alkane synthesis timings to environment are species-specific, and either suggests that in *A. pseudoplatanus*, the seasonal timing of *n*-alkane production is invariant to environment entirely, or that any covariance requires longer timescales than the duration of this experiment.

Influence of carbon allocation on εlipid and CO_2 response

A. pseudoplatanus, unlike *C. avellana*, showed constantly higher εlipid in elevated CO_2 throughout the growth season (Figure 3c), making it unlikely that seasonal shifts in the production of *n*-alkanes are responsible for the observed effect. This therefore suggests that the change in εlipid is induced by changes in supply and demand of and for carbon within the plant.

Changes in CO_2 concentration profoundly alters leaf chemistry in ways which may induce changes in carbon allocation at branch points during the synthesis of *n*-alkanes (Poorter et al., 1997). If this effect is occurring within this dataset, identifying the precise location of changes in allocation is difficult, and although this dataset contains indications of changes to carbon allocation, the specific reactions involved cannot be determined.

In this study, elevated CO_2 resulted in a decrease in *n*-alkane concentration in *C. avellana* (Chapter 3), indicating a decrease in the proportion of carbon allocated to *n*-alkane synthesis in this species. However, a decrease in the proportion of *n*-alkanes present in elevated CO_2 would lead to a greater isotope fractionation and decreased εlipid, the opposite to what is observed. This data contradicts the hypothesis of (Zhou et al., 2015), which suggested that *n*-alkyl lipid concentration is the dominant control on εlipid, and the two should positively covary. It is possible that, as in (Huang et al., 1999), a decrease in *n*-alkanes detected in elevated CO_2 was accompanied by a greater increase in *n*-alkanol concentration, or that of other *n*-alkyl lipids. As the concentration of all *n*-alkyl lipids was not measured in this study, a decrease in *n*-alkanes cannot necessarily be assumed to represent changes in other *n*-alkyl compounds.

A decrease in concentration of *n*-alkanes under elevated CO_2 functionally corresponds to an increase in leaf permeability, which may be expected under elevated CO_2 (Chapter 3). This would suggest that, under elevated CO_2, εlipid should decrease. However, no study thus far has ever identified a decrease in εlipid with increasing CO_2 concentration, as would be expected if changes in *n*-alkane concentration were the dominant driver of their isotopic response. Moreover, in this study, even when a change in *n*-alkane concentration was identified, the isotopic effect observed was contrary to the expected result.

No change in *n*-alkane total concentration was observed throughout the growth season in *A. pseudoplatanus* (Chapter 3), meaning if any isotope effects were caused by a change in the proportion of *n*-alkanes synthesised, any change must have been small enough to be within the margin of error for *n*-alkane concentration. εlipid and alkane concentration did covary when the concentrations and εlipid of individual *n*-alkane homologues were compared (Figure 8) but, as with *C. avellana*, the relationship was the opposite of what would be expected if εlipid was driven solely by *n*-alkane concentration. It therefore appears that in both species, *n*-alkane concentration and εlipid covary, but in the wrong direction to the assumed mechanism. Unlike with *C. avellana*, however, changes to seasonality cannot explain the observed εlipid in *A. pseudoplatanus*, meaning that it is likely that changes to carbon allocation that do not directly relate to the concentration of *n*-alkanes are responsible.

Branched alkane εlipid

The isotopic composition of a compound is affected by the isotopic composition of its carbon source, the magnitude of instantaneous enzymatic fractionation applied at

branch points during their synthesis, and the proportion of available substrate allocated to the compound at branched points (Hayes, 1993, 2001). Branched alkane $\delta^{13}C$, in tandem with that of *n*-alkanes, provides further information on all of these processes.

Branched alkanes are synthesised using an initial precursor molecule of valine and isoleucine for *iso*- and *anteiso*-alkanes respectively. They are then elongated via sequential additions of acetyl CoA-derived C2 units, as with *n*-alkanes (Kroumova et al., 1994; Busta and Jetter, 2017). Therefore, the $\delta^{13}C$ of branched and *n*-alkanes should be closely related, as the majority of their carbon skeleton comes from the same source, but branched alkanes additionally reflect the $\delta^{13}C$ of their respective amino acids (Figure 6). The pattern of depletion between branched and *n*-alkanes detected in this study (from most to least depleted in ^{13}C; *n*-, *iso*, *anteiso*-) is consistent with previous results for the isotopic composition of these compounds reported in Grice et al., 2008 and Zhou et al. (2010), but not Reddy et al. (2000), which found no systematic difference between the three compounds. The magnitude of these relative depletions is slightly lower but within the error range of (Grice et al., 2008).

Valine is produced from the same chloroplastic pyruvate pool as *n*-alkanes, meaning substrate $\delta^{13}C$ is identical. Therefore, the difference in ^{13}C between *iso*- and *n*-alkanes may relate to a difference in fractionations during its synthesis compared to *n*-alkanes (Grice et al., 2008). Isoleucine, by contrast, is synthesised from oxaloacetate, which is additionally enriched in ^{13}C due to its incorporation of heavier ^{13}C deriving from other sources within the cell (Vollbrecht, 1974; Bryan, 1980; Grice et al., 2008). Therefore, if $\delta^{13}C$ of branched alkanes was only influenced by the $\delta^{13}C$ of their carbon substrate, *iso*-alkane $\delta^{13}C$ would covary more closely with *n*-alkane $\delta^{13}C$ than *anteiso*-alkane $\delta^{13}C$. This

was not the case in this study (Figure 6), which suggests the $\delta^{13}C$ of both branched alkanes were more similar to each other than to *n*-alkanes.

The tight covariance of ε*lipid* between *iso*- and *anteiso*-alkanes suggests that, although their amino acid precursors are different and produced in different parts of the cell, their isotopic composition is linked more closely to each other than to *n*-alkanes. Therefore, the similarity of their composition must be due to differences in a common process to the two branched alkanes, which differs from *n*-alkanes. Changes to carbon allocation at branch points can explain the difference in branched and *n*-alkane $\delta^{13}C$, but does not explain why *iso*- and *anteiso*-alkanes are so similar to each other, as when only comparing the carbon pools used for their synthesis, *iso*-alkanes use entirely the same pool as *n*-alkanes and should more closely follow their trends.

Busta and Jetter (2017) provided genetic evidence that CER2-LIKE proteins, which are partially responsible for the final stages of elongation of VLCFA precursors of *n*-alkanes, do not elongate branched alkanes. The relationship between branched and *n*-alkane $\delta^{13}C$ in (Figure 6) could reflect this, if this group of proteins applies an isotopic fractionation. Although the majority of evidence for ^{13}C depletions in *n*-alkyl lipids focusses on fractionations applied during the biosynthesis of acetyl CoA (DeNiro and Epstein, 1977; Monson and Hayes, 1980, 1982; Blair et al., 1985; Hayes, 1993, 2001; Hobbie and Werner, 2004; Zhou et al., 2015), this data is evidence for an isotope fractionation during the synthesis of *n*-alkanes which occurs downstream of acetyl CoA, and the difference in proteins used for biosynthesis of branched and *n*-alkanes is suggestive of the proteins responsible.

In 2018 and 2019 for both branched alkanes, and 2020 for the *ai*-C_{32}, the difference between branched and *n*-alkane $\delta^{13}C$ was larger in elevated CO_2 samples than ambient (Figure 7). This implies some additional fractionation was induced by elevated CO_2 either during the synthesis of their amino acid precursors, or due to a CO_2 effect on the enzymes used for both branched and *n*-alkane synthesis. Changes to enzyme structure are unlikely, as it would imply genetic changes had occurred after just 2 years of CO_2 exposure in a single generation of plants. This trend is therefore more likely attributable to changes in allocation to existing processes. Elevated CO_2 can decrease protein concentration even while lipid concentration remains constant (Taub et al., 2008; Högy et al., 2013), suggesting that this effect may be a result of CO_2-induced alterations to amino acid synthesis.

Attributing the cause of the increased εlipid in both branched and *n*-alkanes under elevated CO_2 in *A. pseudoplatanus* is therefore challenging. This species shows no change in seasonal production of odd-chained *n*-alkanes under elevated CO_2, and no change to any *n*-alkane chemical parameter (Chapter 3). The only changes with CO_2 detected in this species are the fractionations of branched and *n*-alkanes when compared to bulk $\delta^{13}C$, and the difference in isotopic fractionation between branched and *n*-alkane $\delta^{13}C$. Moreover, trends were not consistent in branched alkanes throughout the study, but were in *n*-alkanes, meaning that there must be some difference in the mechanisms driving branched and *n*-alkane εlipid. Furthermore, difference in $\delta^{13}C$ response to CO_2 between branched and *n*-alkane $\delta^{13}C$ were not constant over time, suggesting a shift in the processes involved during the study. The most likely explanation for the trends seen in *A. pseudoplatanus* is that carbon allocation under elevated CO_2 shifted at several different branch points, but the evidence presented here cannot identify where.

The magnitude of change of εlipid under elevated CO_2 was larger in *C. avellana* than *A. pseudoplatanus* (figure 2), and unlike *A. pseudoplatanus*, wax *n*-alkane chemistry also appeared to respond to CO_2, in ACL, dispersion, and total *n*-alkane concentration (Chapter 3). Furthermore, ACL, dispersion, and εlipid were all more variable in *C. avellana* than *A. pseudoplatanus* (Figure 9). *n*-Alkane concentration was lower in *C. avellana* than *A. pseudoplatanus* (p=e-16), potentially meaning that a smaller change in production of specific *n*-alkanes (e.g. a slight decrease in production of longer chain lengths under elevated CO_2) would be required to induce a measurable effect on *n*-alkane ACL in total. CPI was, however, more variable in *A. pseudoplatanus* than *C. avellana*: this is probably at least partially as a result of the large changes through the growth season observed in *A. pseudoplatanus* but not *C. avellana* (Chapter 3 Figure 3) rather than the difference in CPI between the three replicates taken each month. The influence of CO_2 as well as the larger total range observed in *C. avellana* ACL, dispersion, and εlipid suggests that, potentially, wax response to environment in *C. avellana* is more plastic than *A. pseudoplatanus*. This has implications for future study of leaf wax to environment, as it suggests that if one parameter of *n*-alkanes responds to environment, others may as well.

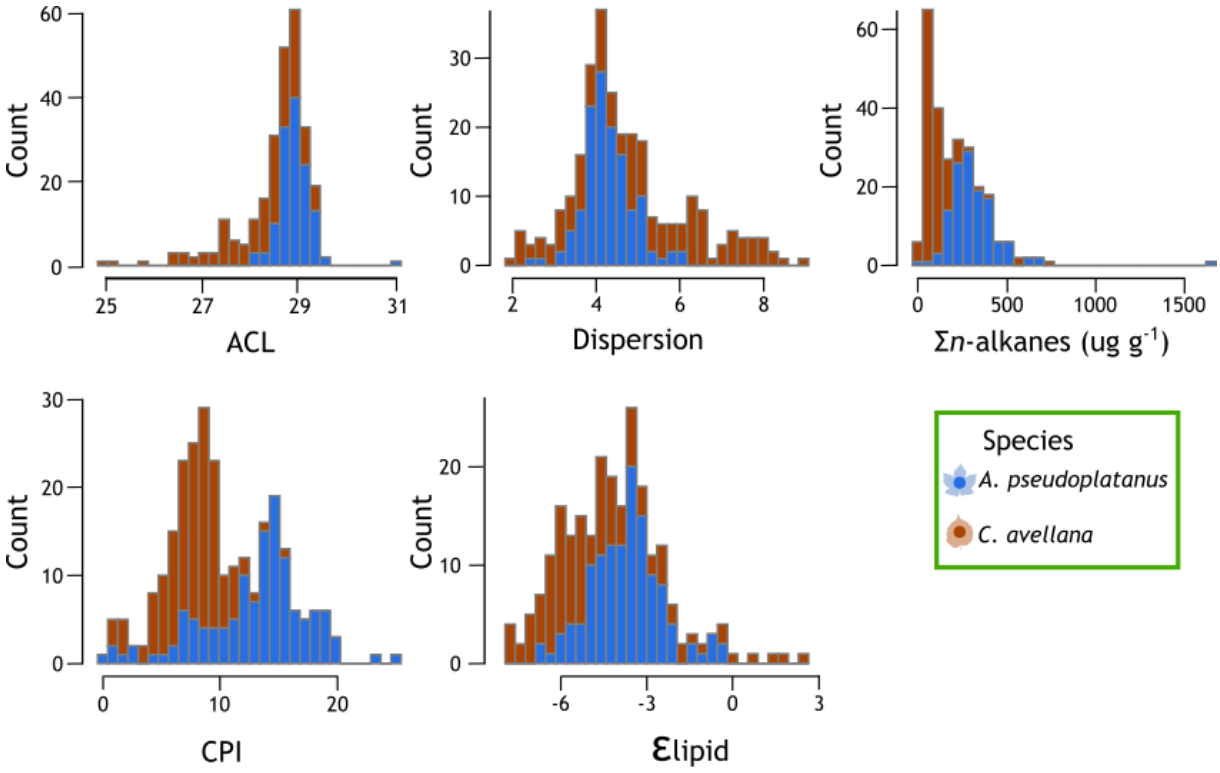

Figure 9: histogram of ACL, dispersion, total *n*-alkane concentration, CPI and εlipid in *A. pseudoplatanus* and *C. avellana* from 2018-2021

Furthermore, although this study only compares two species and the trend therefore cannot be confirmed statistically, it is possible that species with a lower concentration of *n*-alkanes respond more to environment than those with a high concentration. If this is the case, *n*-alkane response to environment in the geologic record may be somewhat muted as species that produce larger concentrations of wax will have an outsize influence on trends recorded at the catchment level (Carr et al., 2014), but an environment containing a greater biomass of species that produce less wax could still show trends. One potential implication of this finding is that environments where wax was predominantly contributed by gymnosperms, which produce less wax than angiosperms (Bush and McInerney, 2013) may respond more strongly to environment

than an equivalent angiosperm-dominated habitat, but as this study did not use gymnosperms, this remains speculative.

Comparison of observed εlipid effect with other published data

This data broadly agrees with the conclusions of Zhang et al. (2019), that higher CO_2 concentrations lead to an increase in εlipid. A re-analysis of bulk and *n*-alkane data presented in Schubert and Jahren (2012) also shows this effect (Figure 10). This is in contrast to the observations of Huang et al. (1999), which observed no change to εlipid under increased CO_2. However, the magnitude of the change in εlipid observed in these studies varied: Zhang et al. (2019) found a ~2‰ difference between 170 and 400 ppmv, whereas Schubert and Jahren (2012) found only a 0.6‰ effect between 400 and 4000 ppmv, with extremely large scatter (Figure 10). When the change in εlipid with CO_2 measured in these studies is normalised to the +150 ppmv used in this study, the observed CO_2 effect ranges from 0 (Huang et al., 1999) to +2.1 (this study in *C. avellana*)

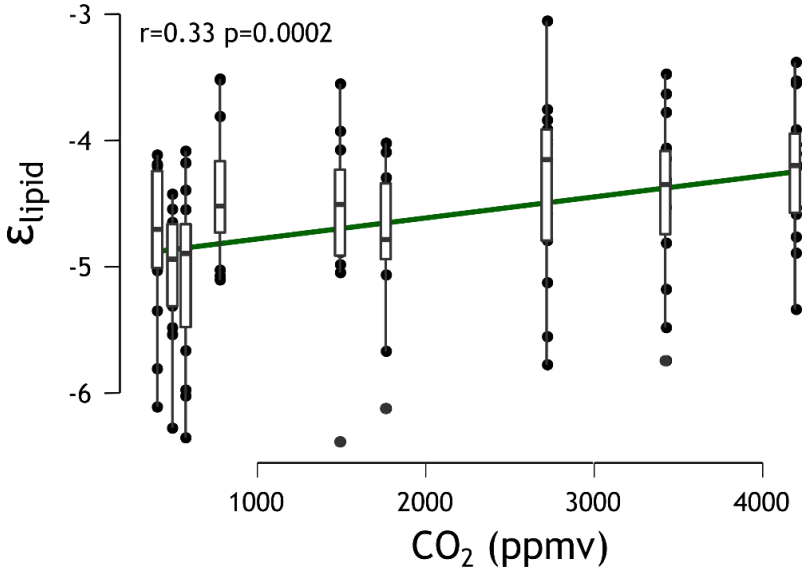

Figure 10: Relationship between [CO_2] and εlipid in the study of Schubert and Jahren (2012).

In both this study and every study of effect of environment on εlipid where both *n*-alkane concentration and εlipid were reported (Huang et al., 1999; H. Zhang et al., 2019; Diefendorf et al., 2021), *n*-alkane concentration negatively covaried with εlipid (as in *C. avellana,* and in Diefendorf et al. (2021) or showed no trend (as with *A. pseudoplatanus*, and in Huang et al., 1999 and Zhang et al. (2019)): the opposite of what is expected if *n*-alkane concentration itself were the only controlling parameter in their isotopic composition. *n*-Alkane concentration was not recorded in the study of Schubert and Jahren, (2012).

Table 2: Change in εlipid in this and other published studies that would be expected under an increase of +150 ppmv, assuming that εlipid varies linearly with CO_2

Source	Predicted increase in εlipid under +150 ppmv CO_2 (‰) (linear model)	CO_2 treatments (ppmv)
This study – *A. pseudoplatanus*	0.63	Ambient atmospheric, +150 to ambient
This study – *C. avellana*	2.1	Ambient atmospheric, +150 to ambient
Zhang et al., 2019	1	170, 280, 400
Schubert and Jahren, 2012	0.0024	407, 497, 576, 780, 1494, 1766, 2723, 3429, 4200
Huang et al., 1999	0	350, 600

Except Schubert and Jahren (2012), all the studies of Table 2, including this one, used too few CO_2 levels to determine whether the observed change in εlipid with CO_2 was linear, and there is no reason to believe this is the case. Zhang et al. (2019), which examined sub-ambient CO_2 concentrations, observed a larger predicted change in εlipid than was seen in *A. pseudoplatanus* in this study. The larger magnitude of εlipid in *C. avellana* was likely due to the effects of changes in the seasonal production of *n*-alkanes, and therefore is not directly comparable to Schubert and Jahren (2012), Zhang et al.

(2019), or other studies using short-term growth chambers. Further data is necessary to quantify the relationship between εlipid and CO_2, and to determine whether, in absence of seasonal effects, the relationship varies linearly.

Summary of CO_2 effect on εlipid

This study detected a sustained increase in εlipid in two species growing within their natural environment under elevated CO_2. This, combined with the work of previous studies (Schubert and Jahren, 2012; H. Zhang et al., 2019; Diefendorf et al., 2021) confirms that changes to εlipid are common in response to short-term changes in environmental conditions. It therefore seems likely that the magnitude of biosynthetic fractionations are somewhat changeable with environment. Since the plants involved in this study were grown in ambient CO_2 prior to the 2017 growth season, it also seems likely that εlipid is responsive to changes in conditions within a single generation.

This data suggests that *C. avellana* εlipid is influenced by seasonality, but *A. pseudoplatanus* is not, meaning an alternate explanation for changes in εlipid to that presented in Diefendorf et al. (2021) is needed. This data could not show whether changes in carbon allocation were directly responsible for observed εlipid shifts, or, if they were the cause of the shifts, which branch points were affected, but also could not rule out the possibility, but the trends seen in branched alkane $\delta^{13}C$ suggest that alterations occurred both in *n*-alkyl lipid and amino acid synthesis. Further study of the isotopic and % composition of other plant components (e.g. carbohydrates, amino acids, lipids synthesised by alternate pathways to the acetogenic, and *n*-alkyl components other than *n*-alkanes) will help to narrow down if, and where, carbon allocation has changed.

Implications for geology

It is difficult to determine the longer-term impact of CO_2 or other environmental conditions on εlipid with the available data. Elevated CO_2 experiments are expensive and are rarely run for >10 years (U.S. Department of Energy, 2020), and CO_2 gradients are rare in nature, meaning that evaluating the longer-term effects of CO_2 levels above ambient concentrations is problematic. This study confirms that changes to εlipid are sustained by the end of the fifth year of CO_2 exposure (Figure 2), but cannot show whether changes are sustained between generations or on evolutionary timescales. As *n*-alkane $\delta^{13}C$ is roughly similar to modern values even at times of extreme CO_2 concentration during the Cenozoic (Diefendorf et al., 2015a), if environment alters εlipid on these timescales, the effect must be small. Furthermore, considering uncertainties in reconstruction of atmospheric CO_2 on geologic timescales, even correlating *n*-alkane $\delta^{13}C$ to CO_2 concentrations is difficult.

Understanding the cause of the εlipid shift would assist in determining whether it would be expected to occur on geologic timescales. If, as was interpreted in Diefendorf et al. (2021), the majority of isotopic effects observed are due to changes in the seasonality of bulk and *n*-alkane production, changes to seasonality itself may also induce an influence on εlipid, independent of changes to pCO_2, temperature, or water availability that may co-occur. The *n*-alkane $\delta^{13}C$ data presented here suggests that in *C. avellana*, elevated CO_2 may have induced *n*-alkane production to increase throughout the growth season where it did not occur previously: the relationship between changes in environment, changes in seasonality of *n*-alkane production, and changes in εlipid require further investigation.

Knowledge of if, and where, changes in carbon allocation may influence *n*-alkane $\delta^{13}C$ would also aid in determination of εlipid in the geologic record. If the same branch points are consistently affected across multiple species, plant functional types, and/or plant clades, this could be taken as evidence that a response in εlipid to CO_2 is conserved, and may occur systematically.

All measured homologues in both species showed an increase in εlipid with CO_2. This increase was largest in the homologues that were, on average, the most enriched in ^{13}C (i.e. the C_{25} and C_{27} in *C. avellana*, and the C_{25} and C_{33} in *A. pseudoplatanus*). These homologues are all often low concentration compared to the more abundant homologues of C_{29} and C_{31} (Figure 4), making their detection geologically more difficult. Furthermore, the C_{25} homologue is produced abundantly by aquatic species and mosses such as *Sphagnum*, making its attribution solely to terrestrial plants in the geological record problematic (Bush and McInerney, 2013). Therefore, although it shows the strongest signal with CO_2 in this data, this may be obscured geologically by its provenance. As all measured homologues show a significant change in εlipid with CO_2 (Figure 4b), use of longer, more abundant homologues that are solely produced by terrestrial plants would show the same signal, albeit more weakly. The C_{33} homologue showed a comparatively strong response in *A. pseudoplatanus* but the weakest response in *C. avellana* (Figure 4c). The response in *C. avellana* is still stronger than all but the C_{25}'s response in *A. pseudoplatanus*, suggesting the longest homologues may be the best target to look for CO_2 effects in εlipid in the geologic record.

(Schlanser et al., 2020) identified a decrease in *n*-alkane $\delta^{13}C$, assuming constant εlipid, with CO_2 on Cenozoic timescales, roughly equivalent to a 4‰ change over the full range

of CO_2. If their CO_2 reconstruction is accurate, this would amount to a 0.6‰ increase over 150 ppmv CO_2 concentration: similar in magnitude to the change observed in *A. pseudoplatanus* in this study, and within an order of magnitude of all detected effects save the larger fractionation in this study in *C. avellana* (Table 2). The analysis of Schlanser et al. (2020) attributed this effect to changes in bulk plant $\delta^{13}C$ due to changes in water-use efficiency induced by CO_2, but this study suggests CO_2-induced alteration to εlipid as an alternate explanation for their data.

This data therefore suggests that caution should be used when applying constant εlipid derived from modern leaves to convert geologic *n*-alkane $\delta^{13}C$ to bulk $\delta^{13}C$. The relationship between bulk $\delta^{13}C$ and CO_2 is contentious (Lomax et al., 2019; Konrad et al., 2020; Basu et al., 2021; Scher et al., 2022), and the link between εlipid and CO_2 identified in this chapter may be enough to affect interpretations. In particular, the CO_2 proxy of Schubert and Jahren (2012) should be applied to *n*-alkane $\delta^{13}C$ with extreme caution, as a consistent change in εlipid with CO_2 has the potential to inflate CO_2 estimates.

Conclusions

This study investigated the influence of elevated CO_2 on the carbon isotopic composition of branched and *n*-alkanes of two common deciduous woodland species over 4 years, within their natural ecological setting. In both species, the difference in bulk $\delta^{13}C$ between the two treatments was greater than the difference in *n*-alkane $\delta^{13}C$, meaning that *n*-Alkane εlipid increased when exposed to +150 ppmv CO_2. This effect was observed consistently across all four years of the study, in all measured *n*-alkane homologues, but the magnitude of the change with CO_2 was inconsistent both between the two species, and between individual *n*-alkane homologues, suggesting the response

of εlipid to CO_2 is species-specific, and CO_2 induces an increase in εlipid via multiple mechanisms. In *C. avellana* but not *A. pseudoplatanus*, the majority of the observed effect can be attributed to changes in the seasonal production of *n*-alkanes: it is most likely that in *A. pseudoplatanus* εlipid instead increased due to changes in carbon allocation under elevated CO_2 to different compounds during biosynthesis. Neither species, however, showed the relationship between εlipid and *n*-alkane concentration expected if changes to the magnitude of *n*-alkane synthesis under elevated CO_2 specifically were responsible for the observed changes in εlipid.

The average εlipid of *n*-alkanes remained relatively constant in both species between the four years of the study. Conversely the εlipid of branched alkanes in *A. pseudoplatanus* were not stable year-on-year: the differences in branched εlipid between CO_2 treatments was large 2018-2019 but absent 2020-2021. This suggests that branched and *n*-alkane synthesis occur by different mechanisms, and that a potential change to the synthesis of amino acids under elevated CO_2 occurred after several years' exposure.

Collectively, this data suggests that εlipid of *n*-alkanes cannot assumed to be constant with environment the geologic record. Therefore, the use of *n*-alkanes as a palaeo-CO_2 proxy as described by Schubert and Jahren (2012) should be undertaken with extreme caution when *n*-alkane $\delta^{13}C$ is not paired with bulk plant $\delta^{13}C$ data, as changing εlipid would induce an effect on *n*-alkane $\delta^{13}C$ similar in magnitude to the changes to bulk $\delta^{13}C$ used by the proxy for CO_2 reconstruction, and may therefore lead to overestimation of palaeo-CO_2. However, if the effects of elevated CO_2 on bulk $\delta^{13}C$ can be adequately deconvolved from that of *n*-alkanes, εlipid in the geologic record may provide information on the biochemical response to past CO_2 concentrations.

Chapter 5: Alkenone-based reconstruction of Eocene pCO_2 from the Rockall Trough, NE Atlantic

Authorship statement

Samples from core 16/28-sb01 were drilled by the *Mv Bucentaur* by the Rockall Studies Group and the British Geological Survey in 1999. Samples were extracted for alkenones by Beth Chamberlain under the guidance of Dr Heiko Moossen. They were initially analysed by GC-FID to confirm the presence of alkenones, and then by GC-C-IRMS to determine their $\delta^{13}C$ by Dr Heiko Moossen. The N4 fraction was analysed for GDGTs using high performance liquid chromatography-atmospheric pressure chemical ionisation-mass spectrometry at the NERC Life Science Mass Spectrometry Facility in Bristol by Hanna Gruszczynska, under the guidance of Dr David Naafs and Dr Ian Bull. Samples were picked for planktic foraminifera these were analysed for their $\delta^{13}C$ by Dr Ulrike Baranowski. Coccolith size was measured by Dr Ulrike Baranowski. I re-analysed the N3 fraction by GC-FID to quantify the concentration of the $C_{37:3}$ and $C_{37:2}$ alkenones for temperature reconstruction, and confirmed their identity using GC-MS. Xiaoqing Liu converted GDGT distributions into sea surface temperature using BAYSPAR, and I converted $U^{K'}_{37}$ to the same using BAYSPLINE. I converted all of the above into a CO_2 reconstruction, using both my own code and, for the monte carlo simulations, code written by Dr Marcus Badger. All analysis and interpretation of CO_2 and temperature data is my own.

Abstract

The alkenone pCO_2 proxy is one of the principal methods by which atmospheric CO_2 concentrations are reconstructed in the Cenozoic. However, its use has previously been limited to the last 45 million years as a) alkenones are rare in the fossil record before this point, and b) the proxy becomes increasingly uncertain in warm, high-CO_2 conditions. As the warmest interval of the last 66 million years, understanding atmospheric pCO_2 concentration during the Early Eocene Climatic Optimum (EECO, 53-49 Ma) is vital to understanding the climate dynamics of so-called greenhouse worlds, but also extremely challenging for alkenone-based pCO_2 reconstructions. This study presents a reconstruction of pCO_2 from 51-49 Ma using alkenones, coccoliths, GDGTs and planktic foraminifera preserved in Core 16/28-sb01, from the Rockall Trough in the Northeast Atlantic. I show that the lack of sensitivity in the proxy at high CO_2 concentrations leads to extremely high CO_2 estimates of over 7000 ppmv under the default input parameters of the proxy. By varying the value of non-CO_2 input parameters to the proxy, CO_2 concentrations decrease, but remain high at >1000 ppmv. The lower range of CO_2 concentrations produce match estimates produced by alternate proxy methods such as the $\delta^{11}B$ of planktic foraminifera in the time interval, but are much higher than estimates produced by analysis of fossil land plant remains. Therefore, this study suggests that lack of constraint on input parameters makes alkenone-based CO_2 reconstruction in the early Eocene challenging, but the proxy qualitatively lends support to the upper range of alternate proxy estimates for CO_2 through the interval.

Introduction

As a major greenhouse gas and driver of long-term climate change through geologic time, understanding both the CO_2 concentration and the climate's response to it is of critical importance in determining Earth's future response to CO_2. In order to determine this, the concentration of CO_2 in earth's atmosphere through time must itself be determined (Royer, 2013; Rae et al., 2021). Many techniques are used to determine past CO_2 concentration, including ice cores, the boron isotopic composition ($\delta^{11}B$) of the shells of planktic foraminifera, precipitation of the mineral nahcolite, and reconstructed gas exchange of fossil plants (Rae et al., 2011, 2021; Royer, 2013; Franks et al., 2014; Jagniecki et al., 2015). In particular, knowledge of the climate dynamics of key intervals in Earth's history can provide insight into the behaviour of the Earth system that allow for best prediction of the future state of the Earth's climate (Gulev et al., 2021).

Improving understanding of CO_2 concentration through the early Eocene would fill a gap in understanding of climate dynamics during a key geologic interval. The Early Eocene Climatic Optimum (EECO) (53.2-49.1 Ma) (Westerhold et al., 2018a) was characterised by the warmest temperatures and highest atmospheric CO_2 concentrations of the Cenozoic (Inglis et al., 2020; Rae et al., 2021), making understanding it a major target for understanding the behaviour of Earth's climate system under high levels of pCO_2 (Gulev et al., 2021). However, quantifying the environmental conditions during this episode has proved challenging: CO_2 estimations over the interval have ranged from values similar to modern ambient concentrations (Cui and Schubert, 2016; Steinthorsdottir et al., 2019) to over 2000 ppmv (Anagnostou et al., 2020).

The alkenone CO_2 proxy is one key method of reconstructing CO_2 on Cenozoic timescales. Alkenones are a class of long-chained unsaturated methyl and ethyl ketone biomarkers, ranging from 35-40 carbons in length, and containing 2-4 unsaturated bonds (Theroux et al., 2010; Brassell, 2014; O'Neil et al., 2021). Of these, the $\delta^{13}C$ of heptatriaconta-15E,22E-trien-2-one ($C_{37:2}$) is commonly used for CO_2 reconstruction, and the relative proportions of it and heptatriaconta-8E,15E,22E-trien-2-one ($C_{37:3}$) are used to reconstruct temperature (Brassell et al., 1986; Prahl and Wakeham, 1987). They are produced by a single group of monophyletic haptophyte algae of the order Isochrysidales which evolved in the Cretaceous; the first $C_{37:2}$ alkenones are found in sediments dating from the early Eocene (Farrimond et al., 1986; Brassell, 2014). Alkenone producing haptophyte algae are well known in the modern: the species *Emiliania huxleyi* is ubiquitous in modern oceans, can make up a large proportion of all plankton in an area (Poulton et al., 2017) and alongside fellow alkenone producer *Gephyrocapsa oceanica* is readily grown in laboratory conditions (Buitenhuis et al., 2008). In the geologic record, evidence of alkenone producers can be determined both from the presence of alkenones and from the presence of fossilised calcium carbonate coccoliths produced to cover the cell surface (Henderiks and Pagani, 2007). As biomarkers, alkenones are of importance as unlike more generic algal biomarkers used for CO_2 reconstruction, their producers are known and have remained specific to Isochrysidales, reducing uncertainty stemming from changes to the makeup of producers, and allowing for additional archives of information present in the geologic record also produced by this group to further inform calibrations (Henderiks and Pagani, 2008; Wilkes et al., 2018). This reduces the likelihood of trends in CO_2 reconstruction being obscured by changes in lipid producer to a very different organism

with very different environmental growth preferences (Herbert, 2013). The pervasive preservation of fossil coccoliths of alkenone-producers alongside alkenone biomarkers allows for a range of biological parameters and growth conditions to be estimated alongside the analysis of biomarkers, including cell size (Henderiks and Pagani, 2007, 2008), carbon limitation (McClelland et al., 2017) and growth rates (Rickaby et al., 2002). However, uncertainties in the alkenone pCO_2 proxy remain, and the proxy is highly dependent on reconstruction of ancient ocean temperatures (Super et al., 2018).

In order to calculate alkenone pCO_2, the temperature at which alkenones were produced is required as an additional input parameter. As alkenone-producing haptophytes are photoautotrophic plankton, this is assumed to be the sea surface temperature. Temperature for use in pCO_2 reconstruction is calculated using a variety of methods, including the ratio of di- to triunsaturated alkenones present within a sample, the relative abundances of C^{86} glycerol dialkyl glycerol tetraethers (GDGTs), and the $\delta^{18}O$ and Mg/Ca of calcite derived from planktic foraminifera (Judd et al., 2022). Notably, in order to accurately reconstruct pCO_2, the temperature reconstruction used must match the precise temperature within which alkenone-producing cells grew, rather than the temperature at a different depth within the water column, and care must be taken to ensure that producers of a given proxy were cohabitating with alkenone producers (Seki and Bendle, 2021).

As the $U^{K'}_{37}$ SST proxy utilises the same alkenones used for pCO_2 reconstruction, these temperature estimates are clearly the most appropriate for alkenone-based CO2 reconstructions. but only within the range of temperatures within which the proxy is applicable. Alkenone-based temperature estimates are reconstructed using the $U^{K'}_{37}$

index, defined as the ratio of the $C_{37:2}$ to the $C_{37:3}$ forms, where a greater relative proportion of the $C_{37:2}$ form is produced at higher growth temperatures. For alkenone CO_2 reconstruction, use of $U^{K'}_{37}$ to reconstruct temperature ensures reconstructed temperatures originate from the same location as the alkenones used to produce $\delta^{13}C$ estimations. However, the $U^{K'}_{37}$ index is only applicable up to an upper temperature threshold, above which the $C_{37:3}$ form does not occur, and becomes increasingly uncertain up to that point (Prahl et al., 1988; Tierney and Tingley, 2018). The linear temperature calibration commonly applied to $U^{K'}_{37}$ devised by Prahl et al. (1988) suggests that $C_{37:3}$ ceases to occur at ~29°C, but various studies suggest that at high temperatures, UK'37's relationship to temperature becomes nonlinear and the $U^{K'}_{37}$ index is <1 at higher temperatures in some locations. Volkman et al. (1995), Sonzogni et al. (1997), Müller et al. (1998), Conte et al. (2006), Richey and Tierney (2016) and Tierney and Tingley (2018) all suggest that at high temperatures, the Prahl et al. (1988) calibration underestimates temperatures above 24°C, though this effect is not seen in all studies, and may be small enough to be within the bounds of error of the linear calibration (Müller et al., 1998; Pelejero and Calvo, 2003; Conte et al., 2006; Kienast et al., 2012; Herbert, 2013). As an alternative to linear calibrations, the Bayesian approach of Tierney and Tingley (2018) suggests a probability distribution of temperatures for any given $U^{K'}_{37}$, where uncertainty increases toward the higher end of the calibration. This does not discount a linear relationship, as the equation of Prahl et al. (1988) lies within the 90% confidence interval throughout, but suggests that it most likely underestimates temperatures close to the threshold, while sensitivity of the proxy decreases overall. In very warm conditions, it may therefore be necessary to use other palaeoclimate archives to generate temperature reconstructions.

The distribution of isoprenoidal GDGTs form an alternate proxy that can be used to generate a temperature record for the reconstruction of CO_2 from alkenone $\delta^{13}C$. Isoprenoidal GDGTs are membrane lipids produced by Thaumarchaeota which are ubiquitous in oceanic sediments (Schouten et al., 2013). They contain a varying number of cyclopentane rings; the weighted average number of rings in a sample closely correlates with temperature in culture and core top studies, and indices of GDGT distributions are regularly used to reconstruct ocean temperatures through the Cenozoic (Kim et al., 2010; Inglis et al., 2015; Judd et al., 2022). Unlike alkenones, the archaeal producers of GDGTs are diverse, changeable both spatially and temporally, and do not necessarily solely occur in the oceanic mixed layer (Sinninghe Damsté et al., 2002; Polik et al., 2018). All of these serve to complicate application of GDGT-derived temperatures to alkenone pCO_2 reconstruction. The wide range of producers of GDGTs may vary both spatially and temporally, and different species may exhibit different relationships with temperature, meaning that fossil GDGTs may not display the same temperature relationship as the modern species used for calibration (Dunkley Jones et al., 2020). It is likely that the GDGT-temperature relationship is partially driven by changes in community composition of GDGT producer as well as a plastic response to temperature within individual lineages, and it is unclear whether changes in community composition in response to temperature would remain consistent through geologic time, even if they correlate spatially in the modern ocean.

Furthermore, the modern ocean GDGT temperature calibration dataset does not exceed 30°C, and the calibration of GDGTs at high temperatures remains debated, and in culture experiments, high-temperature response appears species-specific (Elling et al., 2015; Polik et al., 2018). In the Eocene, GDGT-derived SST reconstructions are often warmer

than foraminiferal calcite-derived proxies (Hollis et al., 2019). GDGT-based temperature reconstructions can be generated by use of a linear or exponential calibration (Kim et al., 2010), or by use of a Bayesian uncertainly model ("BAYSPAR"), which generates a probability distribution of temperatures based on GDGT distributions in the modern. BAYSPAR allows for quantification of uncertainties associated with the modern GDGT calibration, but has been criticised for not increasing uncertainty in situations where GDGT distributions are far from those of modern distributions (Dunkley Jones et al., 2020).

The alkenone pCO_2 proxy

The alkenone pCO_2 proxy quantifies atmospheric CO_2 concentrations by reconstructing the diffusion of dissolved CO_2 into haptophyte algae and its subsequent photosynthetic uptake (Pagani, 2014). Higher dissolved CO_2 levels lead to an increase in the fractionation of ^{13}C between dissolved CO_2 and algal biomass, which correlates with CO_2 concentration. Accounting for algal physiological processes, this can then be quantified to atmospheric CO_2 concentration.

To establish the ^{13}C fractionation between sea water and algal biomass, the $\delta^{13}C$ of dissolved carbon dioxide in seawater is estimated from the $\delta^{13}C$ of planktic foraminiferal calcite. The fractionation of ^{13}C between foraminiferal carbonate and gaseous CO_2 ($\varepsilon_{calcite}$) is controlled by temperature, according to

$$\varepsilon_{calcite} = 11.98 - 0.12T. \quad (1)$$

(Romanek et al., 1992). This calibration was experimentally derived from synthetic calcite. From this, the $\delta^{13}C$ of CO_2 gas can be derived as

$$\delta^{13}C_{CO_{2(g)}} = \frac{\delta^{13}C_{calcite}+1000}{\frac{\varepsilon_{calcite}}{1000}+1} - 1000$$

(2)

The fractionation between dissolved and gaseous CO_2 depends on temperature. The relationship between the two was determined by (Mook et al., 1974) as

$$\varepsilon_{CO_{2(aq)}-CO_{2(g)}}=\frac{-373}{T+273.15}+0.19.$$

(3)

Alkenone $\delta^{13}C$ is first converted to the $\delta^{13}C$ of haptophyte biomass by assuming constant biosynthetic fractionation ($\varepsilon_{alkenone}$) of 4.2‰, as determined from modern chemostat experiments (Popp et al., 1998).

$$\delta^{13}C_{org} = [(\delta^{13}C_{alkenone} + 1000) \times (\frac{\varepsilon_{alkenone}}{1000} + 1)] - 1000$$

(4)

The fractionation of ^{13}C between dissolved CO_2 and haptophyte biomass (Ɛp) can be calculated as

$$\varepsilon_p = (\frac{\delta^{13}C_{CO_{2(aq)}}+1000}{\delta^{13}C_{org}+1000}) \times 1000$$

(5)

(Popp et al., 1989; Freeman and Hayes, 1992). Ɛp is converted into a quantitative reconstruction of aqueous CO_2 concentration according to

$$[CO_2]_{aq} = \frac{b}{\varepsilon_f - \varepsilon_p}$$

(6)

(Rau et al., 1992; Francois et al., 1993; Goericke et al., 1994; Bidigare et al., 1997) where ε_f represents the maximum fractionation induced by carboxylasing enzymes and *b* is a physiological parameter which represents all other biological processes influencing ε_p.

b is calibrated according to its modern and laboratory-derived relationship with $[PO_4]$, and depends on the chosen value of ε_f: linear calibrations for *b* are shown in Table 1 for ε_f = 25 and 28.

Table 1: The linear regressions linking phosphate concentration and *b* under different values of ε_f

ε_f	Intercept	Slope
25	84.07	118.52
28	115.45	135.66

(Bidigare et al., 1997; Eek et al., 1999; Popp et al., 1999; Laws et al., 2001; Pagani, 2014)

To finally produce an estimation of atmospheric CO_2, the atmosphere is presumed to be in equilibrium with ocean surface water. It is calculated using Henry's Law:

$$pCO_2 = \frac{[CO_2]_{aq}}{K_H}$$

(7)

Where K_H is the solubility constant and depends on the temperature and salinity of ocean water.

The value of b used for CO_2 reconstruction can be modified to account for changes in cell geometry through geologic time by measuring mean coccolith size within a sediment sample: coccolith size and cell diameter are linearly correlated according to

$$D_{cell} = 0.55 \times 0.88 L_{coccolith} \quad (8)$$

where both coccolith length and cell diameter are measured in μm (Henderiks and Pagani, 2007). Assuming the cell is a perfect sphere, D_{cell} can be converted to volume:surface area geometrically, equal to:

$$V{:}SA = \frac{D_{cell}}{6} \quad (9)$$

b is then adjusted according to

$$b' = b \times \left(\frac{V{:}SA_{fossil}}{V{:}SA_{E.huxleyi}}\right) \quad (10)$$

(Henderiks and Pagani, 2008) where V:SA represents volume:surface area of the sample coccolithophores and modern *E. huxleyi*, calculated from their diameter. b' is then used in place of the unmodified b in Equation 6. This scaling results in an increase in reconstructed pCO_2 with increasing cell size, as would be expected if CO_2 was transported diffusively, but is reliant on empirical calibration to determine the relationship between cell and coccolith size, and assumes all coccolithophores were perfectly circular. Use of the adjusted b' therefore reduces uncertainty in b by adjusting it to the biology of the fossil specimens which produced the alkenones within a sample.

It does not, however, remove the reliance on an empirical calibration, which may not be consistently valid on geologic timescales, and *b*' still assumes modern growth rates and cell permeabilities determined from *E. huxleyi*.

Both ε_f (i.e. the isotopic fractionation associated with carbon-fixation enzymes) and *b* (the total effect of algal physiological variables) are derived using modern observational and experimental laboratory data (Pagani, 2014). The carbon isotopic fractionation induced by the CO_2-fixing enzyme RuBisCO, which is responsible for the majority of carbon fixation in modern haptophytes (Goericke et al., 1994) is 29‰ (Roeske and O'Leary, 1984) but in modern chemostat experiments this value is around 25‰ (Bidigare et al., 1997). This difference is due either to alternate carbon fixation pathways occurring in tandem with RuBisCO fixation, such as bicarbonate uptake via β-carboxylases such as phosphoenolpyruvate (Freeman and Hayes, 1992; Goericke et al., 1994) or a difference in enzymatic fractionation between the most commonly studied form of RuBisCO (1B) and the form used by haptophyte algae (1D). Form 1B RuBisCO, which is used by terrestrial plants, is the most studied, and ε_f=29‰ is specifically associated with this form: other RuBisCO forms exhibit ε_f as low as 18‰ (Guy et al., 1993; Robinson et al., 2003). Boller et al. (2011) found Form 1D had an ε_f value of ~11‰, but such a low value of ε_f is difficult to reconcile with data from culture experiments (Pagani, 2014). Goericke et al. (1994) estimated ε_f varied from 25-28‰ in algae such as *E. huxleyi*, based on the differing fractionations of different enzymes contributing to carbon fixation, and the lower end of this range is generally suggested from modern calibration data (Laws et al., 1995; Bidigare et al., 1997). For the purposes of pCO2 estimation in the Cenozoic, a constant value of 25‰ is usually used (Pagani et al., 2005; Seki et al., 2010; Badger et al., 2013b; Zhang et al., 2013). It has, however, been

suggested that under high CO_2 conditions with more abundant dissolved CO_2, RuBisCO fixation would be favoured over β-carboxylase leading to higher ε_f values, but this hypothesis has not been tested. In practice, the difference in reconstructed pCO_2 between different values of ε_f is only significant at moderate to high pCO_2, and since many attempts to ground-truth the alkenone pCO_2 proxy have focussed on the low-CO_2 Quaternary Period, changes to ε_f may have been missed (Pagani et al., 2011; Stoll et al., 2019; Y. G. Zhang et al., 2019).

By contrast to ε_f, the value of *b* is often debated (Y. G. Zhang et al., 2019), as it encompasses the effects of physiological processes which partially depend on growth conditions including nutrient supply, growth rate, and light limitation. Deconvolving the impacts of changing biology from the impacts of changing CO_2 and other environmental parameters on long timescales presents a major challenge. Physiologically, *b* depends on cell membrane permeability to CO_2, growth rate, and cell radius (Rau et al., 1996). On geological timescales it is generally assumed that the dominant control on *b* is nutrient supply, which then controls changes to cell physiology (Bidigare et al., 1997), but alterations to cell biology not induced by changes to nutrient supply, or behaving nonlinearly with respect to it, remain a key source of uncertainty in the proxy (Y. G. Zhang et al., 2019; Zhang et al., 2020).

Previous work has not used the alkenone pCO_2 proxy further back than the middle Eocene (Pagani et al., 2005, 2011; Rae et al., 2021) as C_{37} alkenones are not commonly found in sediments until the middle Eocene (Weller and Stein, 2008; Brassell, 2014). The first $C_{37:3}$ alkenones are found in arctic sediments after the EECO and indicate a decrease in temperature through the early and middle Eocene (Weller and Stein, 2008); $C_{37:3}$

alkenones are not found until the middle Eocene at lower latitudes. Palaeogene and Neogene ε_P records indicate a decline in ε_p from the first recorded middle Eocene data through to the quaternary glaciations (Rae et al., 2021, Figure 4): this, when combined with temperature reconstructions, indicates a decrease in atmospheric pCO_2 through this interval, which matches observations made using other palaeo-CO_2 proxies (Pearson and Palmer, 2000; Royer, 2013; Witkowski et al., 2018; Rae et al., 2021).

This study aims to reconstruct CO_2 using the $\delta^{13}C$ of alkenones dating from the early Eocene preserved in Core 16/28-sb01, collected from the Rockall Trough. Extending the alkenone pCO_2 proxy back through the early Eocene will further constrain reconstructions of pCO_2 through this key interval, as well as provide a test of the behaviour of the proxy in extreme CO_2 and temperature conditions.

Methods

Site details

Samples were taken from Site 16/28-sb01, Rockall Trough, NE Atlantic (54.0222°N 13.5143°W (Figure 1). The borehole was drilled in 1999 by the MV *Bucentaur* by the British Geological Survey on behalf of the Rockall Studies Group (Haughton et al., 2005), as part of the Irish PIP (Petroleum Infrastructure Program Ireland). The site was cored to 1465 mbsf, and the modern ocean depth is 1450m (Haughton et al., 2005). Site 16-28-sb01 contains sediments from the Cretaceous, early Eocene, middle Eocene and Plio-Pleistocene, separated by unconformities, dated using calcareous nannoplankton and $\delta^{13}C$ stratigraphy (Baranowski, 2020).

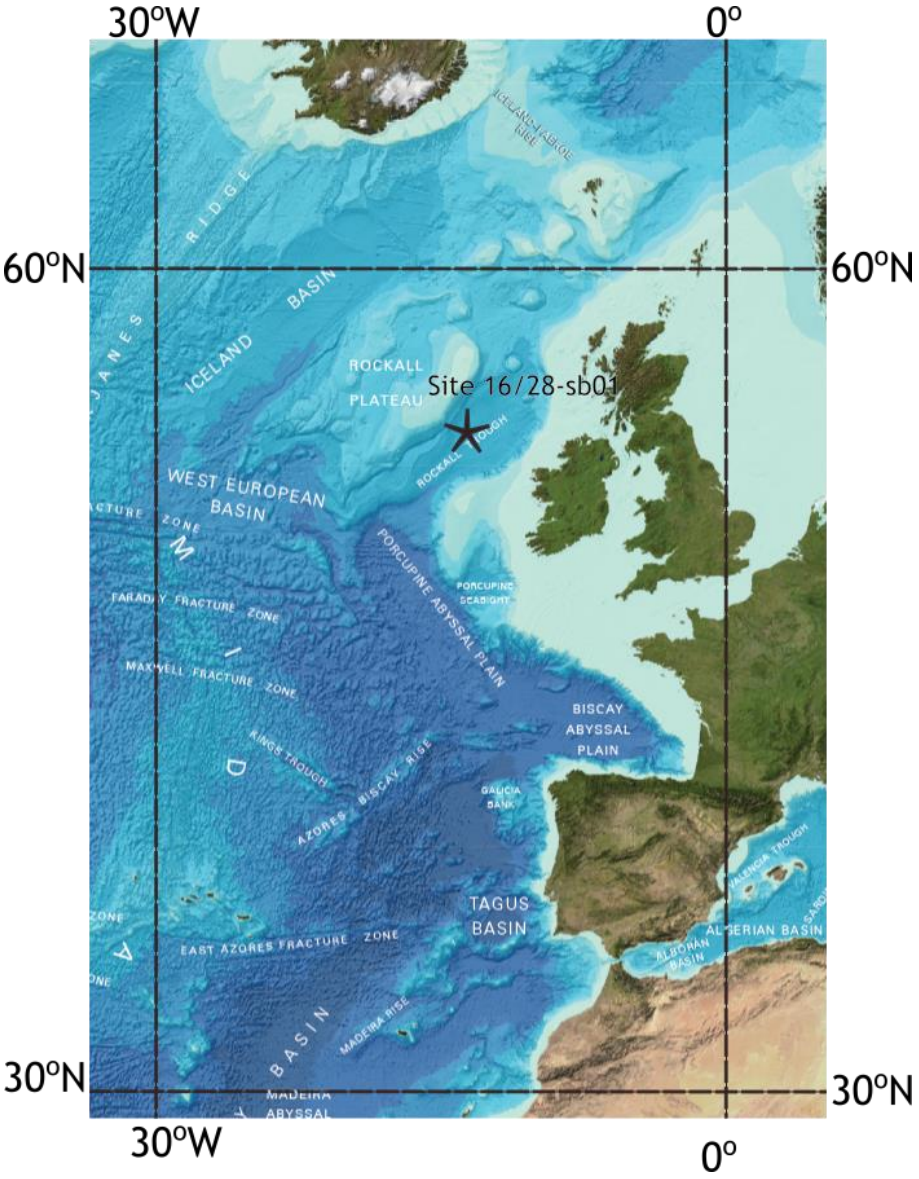

Figure 1: Map showing the modern location of the Rockall Trough and Site 16/28-sb01. Map reproduced from the General Bathymetric Chart of the Oceans World Map 2014, accessed from https://www.gebco.net/data_and_products/printable_maps/gebco_world_map/. (retrieved 30/05/2023)

The core contains Paleogene material from three major lithological units, two of which date to the early Eocene and one to the middle Eocene (Haughton et al., 2005).

Alkenones were present in the second early Eocene section and the middle Eocene section. Eocene sedimentation rates were high (~4cm/kyr (Baranowski, 2020)). The early Eocene section from which alkenones were recovered is characterised by hemi-pelagic clays deposited in a low-energy bathyal slope environment (Haughton et al., 2005). These clays host both well-preserved carbonate microfossils and organic biomarkers. The early Eocene section falls within calcareous nannofossil Zone NP13, and the middle Eocene section falls within Zone NP5c-NP16 (Baranowski, 2020). Isotopic and nannofossil stratigraphy constrains the age of the early Eocene section to 50.65-48.86 Ma (Baranowski, 2020), and the middle Eocene to 44.64-46.11 Ma.

The early Eocene section (146-88 m) consists of marine clays: these are interbedded with mudstones, calcareous limestones and siltstones at the base (146-138m), and transitions to a homogenous succession of clays that form the rest of the early Eocene succession (138-88 m). This is suggestive of a low-energy environment (Haughton et al., 2002, 2005). Dinocysts suggest a fully marine, high-productivity environment, and the pollen and spore assemblage suggests a significant terrestrial input (Harrington, Pers. Comms.). The early Eocene section is interpreted as representing a site within a semi-enclosed basin with water depth ~800m (Maclennan and Jones, 2006).

The middle Eocene section (88 – 41 m) is separated from the early Eocene by an unconformity (Haughton et al., 2005). The section is characterised by calcareous foraminiferal ooze with lower organic biomarker concentrations than the early Eocene succession. Palynomorphs are also absent. This is interpreted as representing a deeper palaeoenvironment with current winnowing as the Rockall Trough became more open to the wider NE Atlantic and potential northern deepwater inflow from across the

Greenland-Scotland Ridge (Harrington et al., 2000). The water depth increased in this succession to around 1km (Maclennan and Jones, 2006).

300 samples, at ~10kyr resolution, were taken for analysis, of which ~50 and ~75 contained enough organic material for GDGT and alkenone-based palaeothermomentry. Of the alkenone samples, a subset of 30 samples were analysed for $\delta^{13}C$ to allow pCO_2 reconstruction.

Laboratory

Details of extraction and analysis of sediment samples for alkenones are described in Chapter 2. In brief, sediments were extracted using 3:1 dichloromethane:methanol via ultrasonication. Alkenones were separated from the resulting total lipid extract via column chromatography, with 5% deactivated silica gel as the stationary phase: alkenones were eluted in the third fraction (N3), using DCM as the mobile phase. The N3 fraction was initially analysed for the presence of alkenones via GC-FID by Dr Heiko Moossen, where they were identified by retention time. Identification was subsequently confirmed by myself using GC-MS. Alkenones were analysed for $\delta^{13}C$ at the Max Planck Institute for Biogeochemistry, Jena, using an Agilent HP5890 gas chromatograph coupled to a Thermo Fisher Delta + XP ratio mass spectrometer.

Specimens of the mixed-layer dwelling planktic foraminifer *Acarinina bullbrooki* were picked and analysed for $\delta^{13}C$, as the best estimate for seawater $\delta^{13}C$ at the depth habitat of alkenone producers (Sexton et al., 2006). Full details of $\delta^{13}C$ analysis are detailed in Baranowski (2020): in brief, $\delta^{13}C$ was measured at the British Geological Survey's Stable Isotope Facility, Keyworth, UK. Samples weighed between 12 and 205 μg, and were analysed using an IsoPrime dual inlet mass spectrometer plus Multiprep device. Samples

were calibrated to VPDB isotope reference using an in-house isotope standard. The calcite-acid fractionation factor applied to the gas values was 1.00798.

As *Acarinina bulbrooki* was not consistently present in all samples that were analysed for alkenones, their $\delta^{13}C$ values were averaged across each stratigraphic unit, and these mean values used when directly paired data was not available.

Table 2: Details of foraminiferal $\delta^{13}C$ analyses from Site 16/28-sb01

Lithological Unit	Depth (m)	Age	Number of core samples analysed	Total number of foraminifera analysed	$\delta^{13}C_{foram}$ (‰ VPBD)	
					Mean	Standard deviation
U2	138.0-88.8	Early Eocene	20	97	3.59	0.59
U3	88.8-40.77	Middle Eocene	5	45	2.50	0.72

Coccolith size – length (long-axis) and width (short-axis) - was measured on at least 200 reticulofenestrid (alkenone-producing) coccoliths per sample. Mean coccolith lengths were then calculated for each sample as the basis to deploy coccolith length-to-cell size relationships noted above.

Alkenones and GDGTs were extracted and analysed from sediment samples taken from core 16/28-sb01 as described in Chapter 2. $C_{37:2}$ and $C_{37:3}$ alkenones were initially identified in the N3 fraction by GC-FID, and their identity was confirmed in a subset of samples via GC-MS by the presence of the presence of the m/z 533, 546 and 548 ions.

GDGTs were analysed via High-Performance Liquid Chromatography/Atmospheric Pressure Chemical Ionisation/Mass Spectrometry at the National Environment Research Council Life Science Mass Spectrometry Facility, at the University of Bristol, using the

method of (Hopmans et al., 2016). GDGT data was previously reported in (Baranowski, 2020), which contains full method details. In brief: analysis was performed using a HPLC-APCI ThermoScientific TSQ Quantum Access triple quadruple MS coupled to an Acela pump and Acela autosampler. Samples were dissolved in 100 µl Hexane: isopropanol (99:1) for analysis. Where concentrations of 100 µl contained insufficient GDGTs for analysis, a repeat injection using 80 µl solvent was performed. Samples were separated using an Aquity UPLC BEH HILIC column (2.1 x 150 mm, 1.7 µm i.d.) at a flow rate of 200 µl minute^{-1}. 15 µl of each sample was injected per run. A gradient elution was applied through the run, with 1) 25 minutes at 82% hexane and 18% isopropanol, 2) 25 minutes changing linearly to 65% hexane and 35% isopropanol, and finally, 3) a linear gradient to 0% hexane, 100% isopropanol. The mass spectrometer was used in selective ion monitoring model (m/z 1302, 1300, 1298, 1296, 1294, 1292, 1050, 1048, 1046, 1036, 1034, 1032, 1022, 1020, 1018, 744, 653). One in-house marine GDGT external standard was run every 7 samples.

Temperature reconstruction

Temperatures were reconstructed using $U^{K'}_{37}$ and TEX_{86} palaeothermometry. Wherever possible, temperature reconstructions used for CO_2 analysis were taken from the same sample as that used for alkenone $\delta^{13}C$. Where alkenones and GDGTs were not present in sufficient concentration, temperatures were interpolated between the two closest points for which an adequate measurement could be made.

Alkenone palaeotemperatures were calculated using the $U^{K'}_{37}$ index, defined as

$$U_{37}^{k\prime} = \frac{C_{37:2}}{C_{37:2}+C_{37:3}}$$

(11)

(Prahl and Wakeham, 1987). Samples fully saturated with $C_{37:2}$ were excluded from analysis for $U^{K'}_{37}$ temperatures, as temperature could not be quantified.

$U^{K'}_{37}$ was converted to sea surface temperature (SST) according firstly to the linear calibration of (Prahl et al., 1988):

$$T(°C) = \frac{U_{37}^{k\prime} - 0.039}{0.034}.$$

(12)

BAYSPLINE (Tierney and Tingley, 2018), which uses Bayesian inference to generate temperature estimates, was also used to produce temperature estimates, as it accounts for high-temperature biases in $U^{K'}_{37}$ with a nonlinear calibration and an incorporation of uncertainty estimates. A prior of 5°C was used, which was large enough it only minorly affected the posterior.

GDGT palaeotemperatures were calculated using the TEX_{86} index, defined as

$$TEX_{86} = \frac{(GDGT-2)+(GDGT-3)+(cren')}{(GDGT-1)+(GDGT-2)+(GDGT-3)+(cren')}$$

(13)

(Schouten et al., 2002). TEX_{86} temperatures were generated using BAYSPAR (Tierney and Tingley, 2014) which uses Bayesian inference to generate temperature reconstructions. The deep-time 'analogue' mode was used, with a prior mean of 20°C.

GDGT distributions were evaluated for terrestrial input using the Branched vs Isoprenoid Tetraether (BIT) index, defined as

$$BIT = \frac{[GDGT - Ia] + [GDGT - IIa] + [GDGT - IIIa]}{[GDGT - Ia] + [GDGT - IIa] + [GDGT - IIIa] + [Crenarchaeol]}$$

(14)

(Kim et al., 2010) where numbers refer to GDGTs as shown in Chapter 1, Figure 3.

CO_2 reconstruction

CO_2 was reconstructed according to Equations 1-10, and included the lith size correction to *b* of Hendricks and Pagani (2007, 2008).

Modern surface phosphate concentrations in the Rockall trench are around 0.4 ± 0.05 μmol kg^{-1}in the mixed layer (Garcia et al., 2018). Pagani et al. (2011) estimated Eocene phosphate levels as slightly higher, at around 0.8 μmol kg^{-1}: pCO_2 reconstructions were calculated for both values.

Multiple CO_2 reconstructions were generated using a range of different parameters: ε_f = 25 and 28 and phosphate levels of 0.4 and 0.8. This was to provide a range of potential pCO_2 and to estimate a lower limit for Eocene CO_2 concentrations.

Monte Carlo Error Propagation

In order to estimate uncertainty for pCO_2 reconstructions, a Monte Carlo uncertainty propagation model following the approach of (Badger et al., 2013b, a) was used (n=10000). Uncertainties of 2.5°C for temperature, 0.4‰ for alkenone $\delta^{13}C$, 0.1‰ for carbonate $\delta^{13}C$, 0.9 μm for coccolith length and 1.5‰ for salinity were used, representing approximately the standard error.

Results and discussion

Sea surface temperature reconstruction

Both BAYSPAR and BAYSPLINE predicted similar temperatures for this interval (average temperature 27.6±3°C and 27.7±2°C respectively, Figure 2). Therefore, both the TEX_{86} and $U^{K'}_{37}$ indices indicate relatively stable, high sea surface temperatures through the early Eocene interval. In the mid-Eocene, the two proxies diverged: BAYSPAR suggested average temperatures of 26±3°C, similar to the early Eocene estimates, whereas BAYSPLINE estimated an average temperature of 17±2°C.

GDGT temperatures were further evaluated using the BIT index. BIT index values were, on average, 0.31 ± 0.13. Of the 7 GDGT samples measured in the middle Eocene, only contained any branched alkanes, leading to a BIT value of 0.06 ± 0.17 and suggesting an almost entirely marine setting. BAYSPAR-derived mean temperature estimates correlate with BIT index weakly (r=-0.29 p=0.02). This data therefore suggests addition of terrestrial organic matter to Site 16/28-sb01 through the early Eocene, and that this terrestrial organic matter input ceased by the middle Eocene as the area deepened. It has been suggested that samples with BIT>0.3, representing some terrestrial input, may exhibit temperature reconstructions biased by terrestrial GDGT input. The BIT index does, therefore, suggest that reconstructed temperatures could be somewhat biased toward terrestrial values, but that such bias should be, on average, <3°C (Weijers et al., 2006). Therefore, it is likely that modifications to temperature with BIT would fall within the 90% uncertainty window defined by BAYSPAR.

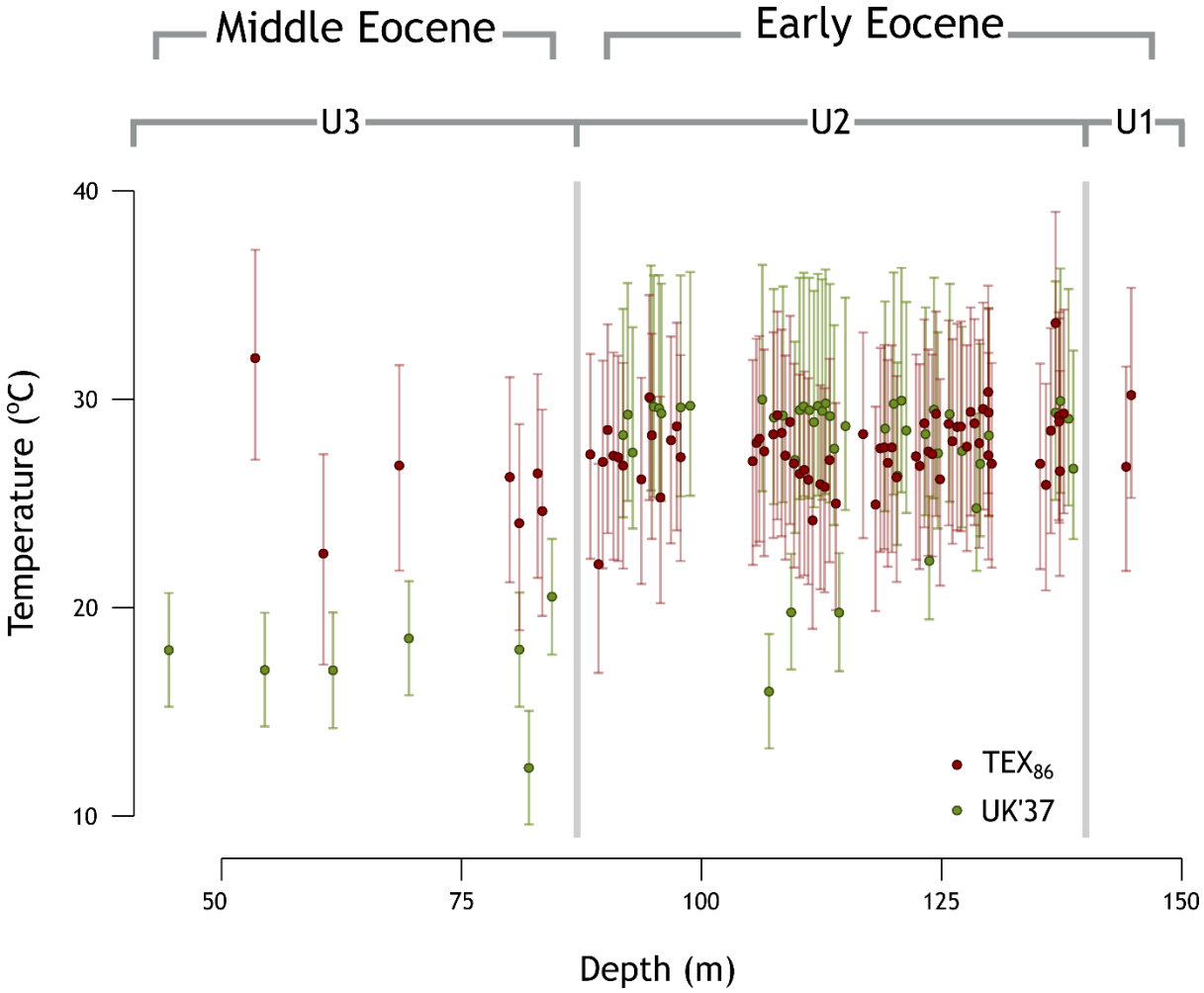

Figure 2: Temperature reconstruction for Site 16/28-sb01. Green points were reconstructed using mean and 90% confidence interval generated using $U^{K'}_{37}$ data via BAYSPLINE, red points are 90% confidence interval generated using TEX_{86} data via BAYSPAR.

Previous results have suggested that TEX_{86} overestimates temperatures compared to other proxies in the Eocene (Hollis et al., 2019; Dunkley Jones et al., 2020) and $U^{K'}_{37}$ underestimates temperatures when toward the top of its temperature (Tierney and Tingley, 2018). In this record, as both proxies broadly agree, temperature reconstructions are likely reasonably accurate. However, both proxies have large uncertainties associated: the average 95% confidence interval size was 5°C and 10°C for

BAYSPAR and BAYSPLINE respectively. This is expected for the $U^{K'}_{37}$ estimates, as the temperatures are at the upper end of the proxy calibration. As, however, temperatures appear stable throughout the interval, assuming that there are no unaccounted-for systematic biases toward hotter or colder temperatures in either proxy, the average temperatures for the interval are likely very close to those recorded. High, stable early Eocene temperatures agree well with global deepwater temperatures calculated from benthic foraminiferal $\delta^{18}O$ (Westerhold et al., 2020) and reconstructions of early Eocene SST from other sites (Inglis et al., 2015; Bornemann et al., 2016; Anagnostou et al., 2020) and suggest that for this interval, temperature is recorded by both GDGTs and $U^{K'}_{37}$, even with potential uncertainties in calibration.

Alternate calibrations for GDGT-derived temperatures – the linear calibration of Schouten et al. (2002) and the exponential calibration TEX_{86}^{H} (Kim et al., 2010) – were not used. Both calibrations diverge from modern observations of extremely high temperatures in the Red Sea, and neither give any error estimation for their estimates beyond instrumental uncertainty. In addition, TEX_{86}^{H} is potentially affected by regression dilution bias, and has been shown to underestimate temperatures in warm tropical regions of the modern ocean (Tierney and Tingley, 2014), which may make it unsuitable for reconstruction of extremely warm Eocene temperatures. Similarly, OPTiMAL's machine learning approach to GDGT temperature calibration was not used, as it relies on matching samples to their nearest closest GDGT distribution in the modern ocean; as these temperatures, and corresponding GDGT distributions, are higher than those seen in modern oceans, OPTiMAL could not resolve palaeo-temperature for the majority of samples (Dunkley Jones et al., 2020).

However, the TEX_{86} and alkenone-based temperature proxies diverge in the middle Eocene part of the record, where $U^{K'}_{37}$ suggests a sharp decrease in temperature while TEX_{86} suggests temperatures remained high. The global benthic oxygen isotope stack of (Westerhold et al., 2020) suggests global deepwater temperatures began to fall at around 49.1 Ma, just after the end of Unit U2, which suggests qualitatively that $U^{K'}_{37}$ is recording temperatures more accurately. However, the changes in oceanographic conditions between the deposition of U2 and U3 decreased the concentration of organics, meaning the middle Eocene is sparsely represented in both the $U^{K'}_{37}$ and TEX_{86} data, and it is possible TEX_{86} could also record a more moderate temperature decrease were more data available.

The mismatch between the GDGT- and alkenone-based reconstructions of temperature in the middle Eocene is difficult to explain. Changes in GDGT temperature can be attributed to changes in depth habitat of the producing archaea, but as alkenone-producing haptophytes are at the top of the water column, for GDGTs to produce higher temperatures than alkenones due to an increase in depth habitat they would be found above the water's surface. It is possible that the early Eocene GDGTs were produced at a lower depth than the alkenones, but that an alteration to GDGT community or behaviour as compared to modern distributions induced a warm bias, cancelling out the two effects, then in the middle Eocene the alteration to GDGT production compared to the modern vanished but the depth of production remained constant, but this explanation is somewhat convoluted.

It should be noted that the concentration of organics decreased dramatically in the middle Eocene section of the core and GDGT levels were only marginally above the

detection limit of the instrument (Baranowski, 2020), which could introduce a preservation bias. The flux of organics to the sediment decreased sharply in the middle Eocene, likely as a result of oceanographic changes: the site deepened (Maclennan and Jones, 2006) and terrestrial input decreased (Haughton et al., 2002), and oxygenation may have increased (Haughton et al., 2005). A decrease in organic transport to the sediment both reduces concentrations directly and increases degradation of what remains (Killops and Killops, 2013). Under oxic conditions, the $C_{37:3}$ alkenone may decompose faster than the $C_{37:2}$, leading to a warm bias, and $U^{K'}_{37}$ may further show a warm bias when run at low concentrations via GC-FID (Villanueva and Grimalt, 1996). However, both of these effects would act to increase $U^{K'}_{37}$ temperatures, but in this instance $U^{K'}_{37}$ temperatures are colder than TEX_{86}. Therefore, changes in oceanographic conditions inducing an increase in alkenone degradation cannot explain the mismatch in temperatures detected in the middle Eocene. Similar GDGT degradation under oxic conditions is also observed, but are lesser to degradation in alkenones under similar conditions (Kim et al., 2009). Oxic degradation of GDGTs is associated with an increase of the BIT index (Huguet et al., 2009): BIT index decreased in the middle Eocene in this data. Therefore, the mismatch in temperatures observed here cannot be explained by a change in oceanographic conditions.

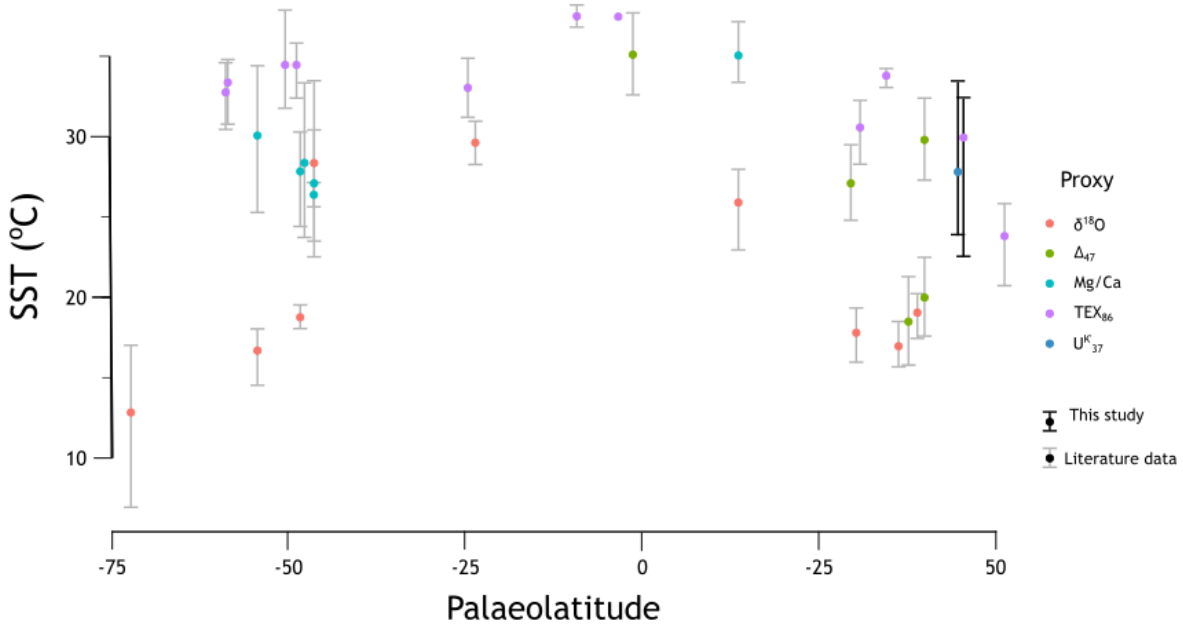

Figure 3: Sea surface temperature estimates from the EECO by latitude recorded in the literature, as compiled by Hollis et al. 2019, compared to this study. Individual data sources are recorded in that paper. Error bars represent 5 and 95% confidence intervals of mean SST for each published SST record in the interval.

Temperature reconstructions using both TEX_{86} and $U^{K'}_{37}$ are broadly within the range seen for other EECO temperatures. The data are warmer than the only EECO temperature reconstruction from higher latitudes than this study Figure 3, data originally reported by Frieling et al. (2014) and re-analysed byHollis et al. (2019)), but this may be expected as a) this data was from further north, and b) the TEX_{86} temperature reconstruction of this data in the EECO ranged from 53.5-51.8 Ma, and showed a warming trend within this interval. The EECO data recorded in this study is younger than that interval, meaning if the increase in temperature measured had continued, the two sites may be in agreement.

The data lie within the range of EECO data measured in midlatitude northern hemisphere sites, though this range is extremely broad and dependent on proxy. Both reconstructions tend toward the higher temperatures seen in TEX_{86} reconstructions, which in the early Eocene often reconstructs temperatures as higher than co-occurring carbonate proxies (Hollis et al., 2019). The agreement with the $U^{K'}_{37}$ reconstruction with TEX_{86}-based estimates rather than carbonates supports the TEX_{86} reconstructions, but, as noted above, $U^{K'}_{37}$ calibration is also uncertain at high temperatures.

Foraminiferal $\delta^{18}O$-based reconstruction of temperature was not used here, although foraminiferal calcite $\delta^{13}C$ was used to reconstruct the $\delta^{13}C$ of seawater for the alkenone pCO_2 proxy. Specimens of *Acarinina* were used to reconstruct the $\delta^{13}C$ of seawater where present, but were absent from much of the record and calcite $\delta^{13}C$ was reconstructed as an average for each unit (Table 2). Measurements were also taken from the planktic foraminifer *Subbotina eocaena*, but, as this species tends to dwell more deeply in the water column than *Acarinina* or alkenone-producing haptophytes (Stott et al., 1990), $\delta^{18}O$-derived temperatures from this species were not used.

For the purposes of CO_2 reconstruction, the TEX_{86} temperature estimates were used, as both temperature records broadly agree but TEX_{86} had lower associated uncertainty. Similar results are obtained using the $U^{K'}_{37}$ estimates for the early Eocene interval. An alternate calculation of the proxy using the $U^{K'}_{37}$ temperature estimation is used for the one middle Eocene sample from which CO_2 was reconstructed.

Ɛp

Compared to later Cenozoic data, Ɛp was extremely high. In the early Eocene interval, average Ɛp was 23.8, and values remained stable throughout the interval. As only two

values for Ɛp were generated for the middle Eocene interval, slight differences between middle and early Eocene Ɛp could not be distinguished, but the average of the two recorded data points (22.7) suggests that if Ɛp decreased by the middle Eocene, the decrease was minor (Figure 4).

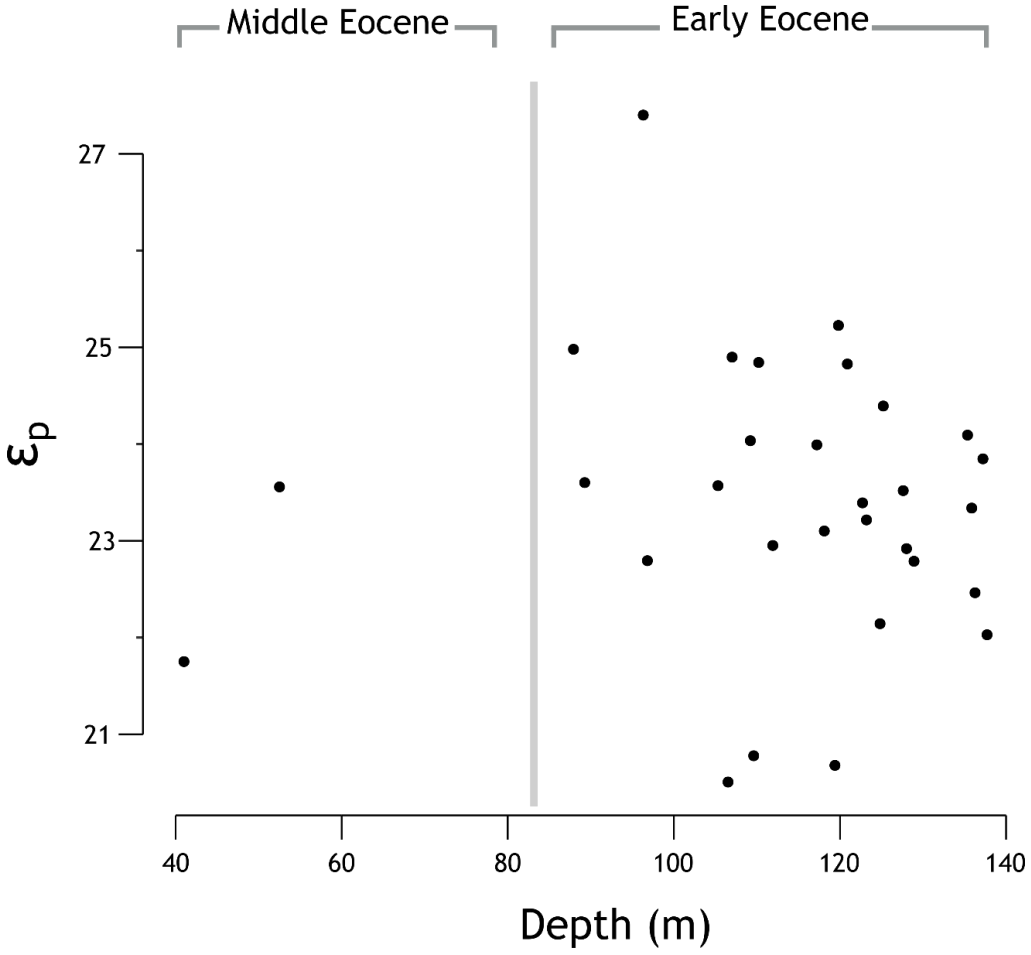

Figure 4: Ɛp reconstructed from alkenone and calcite $\delta^{13}C$ in core 16/28-sb01. Grey bar indicates unconformity between early and middle Eocene samples.

In a broader Cenozoic context, this data extends recorded Ɛp generated from alkenones back to the early Eocene, and fits the broader, long-term decline of Ɛp through this time interval (Figure 5). An Ɛp of 23.8 is the highest average recorded in the Cenozoic, reflecting the shift from a high-CO_2 greenhouse state to a low-CO_2 icehouse (Pagani et al.,

1999, 2005, 2011). Since Ɛp reflects a combined signal of temperature, nutrient supply and pCO_2, this qualitative trend reflects both the temperature and CO_2 decrease through time. This data is slightly higher than the Ɛp calculated by (Witkowski et al., 2018) from phytane for the same interval (Ɛp = 21-22).

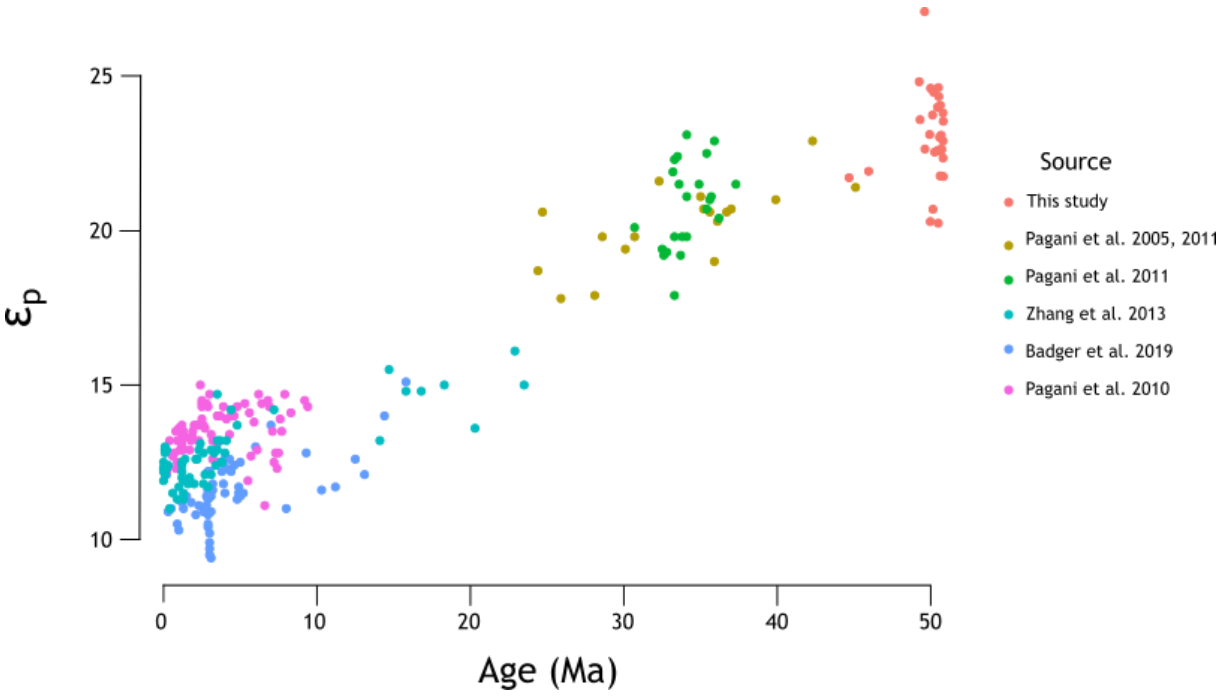

Figure 5: $Ɛ_p$ recorded in this study compared to later Cenozoic $Ɛ_p$ data compiled by Rae et al. 2021

CO_2 reconstruction

As with temperature and Ɛp, all reconstructed CO_2 conditions show CO_2 was variable through the interval but did not increase or decrease consistently throughout. However, the different parameters used in its calculation had a large effect on absolute concentration of CO_2, leading to a mean pCO_2 reconstruction ranging from 1100 ppmv CO_2 (Figure 6c) to >7000ppmv (Figure 6b). The average difference in mean calculated

CO_2 between phosphate levels of 0.4 and 0.8 was around 1400 ppmv, and the difference between ε_f=25 and 28 was around 4700.

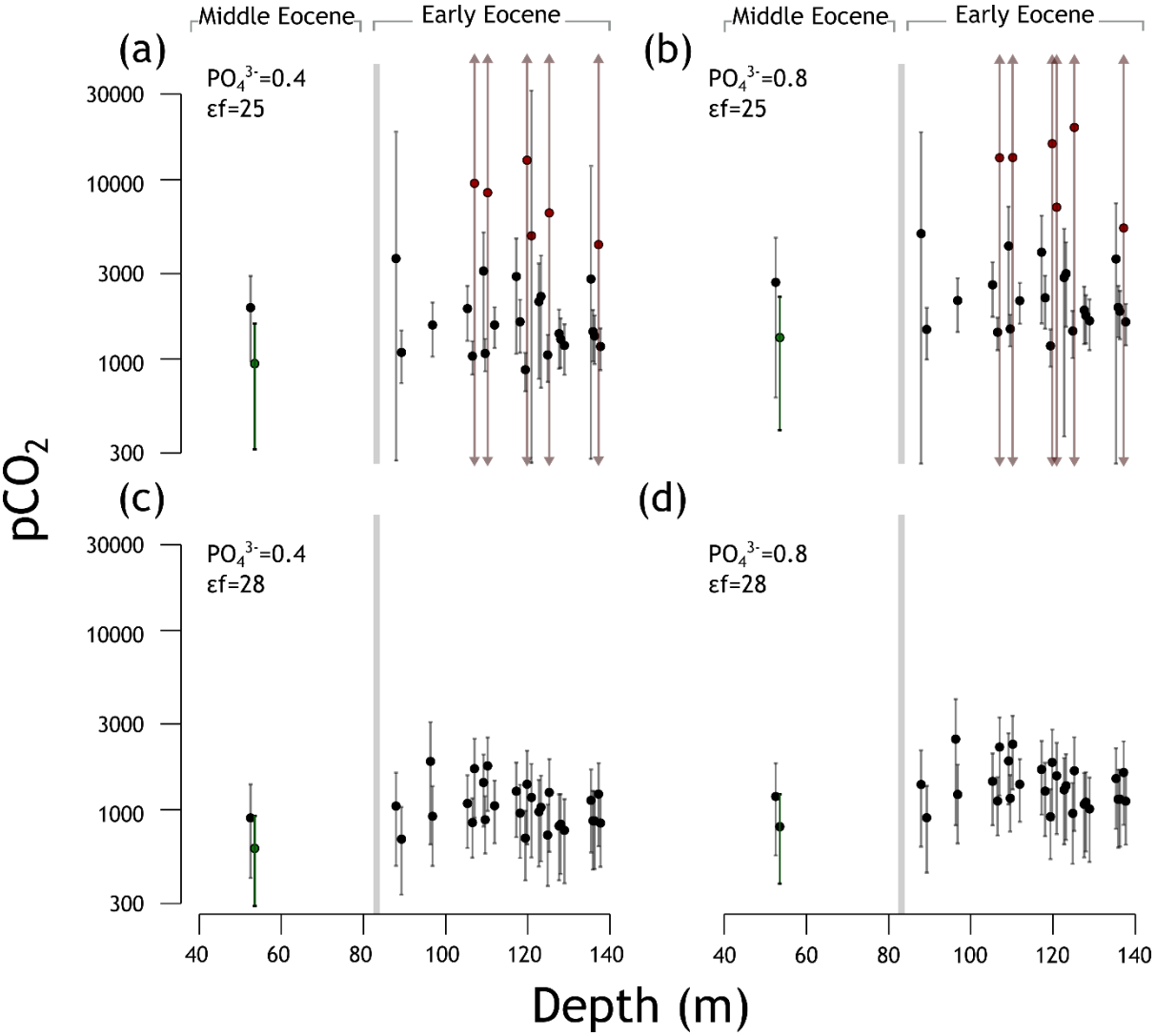

Figure 6: Mean and standard deviation pCO_2 from Monte Carlo simulations of Ɛp and TEX_{86} temperature at site 16/28-sb01. Middle Eocene sample reconstructed using $U^{K'}_{37}$ is marked in green, offset by 1m from the corresponding reconstruction made using TEX_{86}. pCO_2 reconstructions where standard deviation was >100,000 are in red and marked with arrows: in these cases, error bars exceeded the size of the y axis. a) PO_4^{3-}=0.8 ε_f=0.25, b) PO_4^{3-}=0.8, ε_f=0.25, c) PO_4^{3-}=0.4, ε_f=28, d) PO_4^{3-}=0.8, ε_f=28.

This data therefore suggests that although 1400 is a large difference in reconstructed CO_2, compared to the effect of the change to ε_f, phosphate levels are less important in controlling CO_2 reconstruction at this site. This result is partially due to the range of values chosen: if a larger range of phosphate levels had been used, the difference between reconstructions would have been higher, but there is no evidence to suggest phosphate levels were much higher than the upper estimate given here. Conversely, changing from ε_f=25 to ε_f=28 produced a far larger range of CO_2 concentrations, which suggests that at εp values this high, greater constraints on the biology of alkenone-producing algae over long timescales and at high pCO_2 are required.

The alkenone pCO_2 proxy is fundamentally governed by reciprocal functions, and thus sensitivity dramatically decreases at high εp, high temperature, and high phosphate levels (Pagani, 2014). As this dataset reflects a high-CO_2, high temperature environment where phosphate levels cannot be well constrained, sensitivity is extremely low and uncertainties are extremely large. The effects of this decrease in sensitivity are such that the effects of the parameter changes compounds, i.e. the difference in reconstructed CO_2 between the two different ε_f values used is higher in the high phosphate reconstruction than the lower one, and vice versa.

ε_f is potentially the hardest parameter to constrain in the Eocene as direct measurement of 50-million-year-old haptophyte algal biochemistry is impossible. Although (Pagani et al., 2011) suggested that under high-CO_2 conditions the use of enzymes utilising bicarbonate as a carbon source may be suppressed in favour of CO_2-utilising RuBisCO, which would lead to an increase in ε_f, this remains speculative. Further research is needed into different enzyme usage in laboratory conditions to determine whether this

trait may be plastic, but knowing the point to which biological functioning of long-dead organisms can be approximated with their modern relatives is a problem for much of palaeoclimate and palaeobiological reconstructions of ancient conditions and is impossible to determine for certain (Tierney and Tingley, 2018).

The CO_2 reconstructions presented here assume many other biological parameters, such as cell wall permeability and biosynthetic fractionation in the synthesis of alkenones, remained constant through geologic time. There is no accepted method to reconstruct these in the geologic record and both are routinely assumed to be comparable to modern values in CO_2 reconstructions. Early Eocene temperature and CO_2 concentration are more different to modern than any later period in which alkenones are used for reconstruction, meaning that if haptophyte algal biology responds to climate in an unpredicted way or if the proxy behaviour is slightly different than modelled, this reconstruction would be more heavily affected than others from later in the Cenozoic. Furthermore, if haptophyte algal biology has adjusted on evolutionary timescales, the further back in time a sample is taken, the more different it would be to today. Although alkenone production is constrained to a small, monophyletic algal group, reducing this uncertainty, the dominant alkenone producer has changed over time and includes extinct taxa, meaning any evolutionary changes to haptophyte biology compared to the modern would be at a maximum in the oldest samples containing alkenones (including core 16/28-sb01). Unconstrained changes to algal biology in this interval compared to the modern could have a large effect on estimations of *b*, which are impossible to account for here with the data available.

Of the reconstructions shown in Figure 6 the most likely to be closest to the parameters seen in the Eocene is shown in Figure 6b. A variable ε_f, as stated above, cannot be constrained geologically and in modern data is most likely closer to 25 (Figure 6a,b): as such, this value is most often taken for pCO_2 reconstruction and is considered the most likely to be correct (Bidigare et al., 1997; Pagani, 2014). The higher phosphate level suggested in Eocene model simulations by (Pagani et al., 2011) (Figure 6b,d) is likely the more accurate estimation, rather than assuming modern oceanographic conditions apply in a different palaeoclimate and palaeogeographical setting. This is also the highest CO_2 estimate of all 4 combinations of parameters considered, suggesting an average pCO_2 of 7200 ppmv. With ε_f=25 and phosphate=0.4, which also uses the biological terms constrained from modern data, average pCO_2=5000 ppmv: lower, but still extremely high.

Of data compiled by (Hoenisch, 2021), no other CO_2 reconstruction for the Ypresian has suggested CO_2 concentrations >5,000 and only one data point for the interval has suggested CO_2 concentrations >3,500 (Pearson and Palmer, 2000; Hoenisch, 2021). This strongly suggests that assumptions used for the most likely CO_2 reconstruction are erroneous. These assumptions could originate a) in a systematic offset between physical input parameters and the true values for the Eocene (e.g. significantly lowered phosphate or temperature), b) changes to biological assumptions made by the proxy (e.g. a change to biosynthetic fractionation during the synthesis of alkanes, any systematic alteration to which is entirely unconstrained in modern and geologic data), or c) an erroneous assumption made in Equations 1-10 (e.g. CCMs resulting in $\delta^{13}C_{alkenone}$ not following the diffusive model). Increasing ε_f to 28 moves the

reconstructed pCO_2 into the higher end of the range recorded by other proxies over the interval.

It is also noteworthy that in both reconstructions where ε_f=25, some results of the Monte Carlo simulations gave results that were <0, indicating the hyperbolic equations which govern the proxy had broken down entirely. In the case of one sample, ε_p<0 in 64% of simulations. As simulations where ε_f<0 were rejected from calculation of the mean and standard deviation of pCO_2 shown in Figure 6, it is likely that the highest pCO_2 samples are an underestimate of pCO_2 under the governing equations of this proxy, as the mean pCO_2 has, in effect, not been calculated using the full range of parameters suggested by the standard deviations the model was provided.

Due to the low concentrations of organic materials in the middle Eocene portion of the core, only one data point was available for quantitative CO_2 reconstruction from this interval. This single point was lower than the early Eocene CO_2 in $U^{K'}_{37}$-derived CO_2 reconstructions, but comparable in TEX_{86}-derived reconstructions, because $U^{K'}_{37}$ but not TEX_{86} recorded a fall in temperatures during this interval. Therefore, unlike in the early Eocene, there is a large difference in reconstructed pCO_2 between the two temperature proxies of 300-1500 ppmv, depending on ε_f and phosphate used: this represents a decrease in pCO_2 from the early Eocene samples in the $U^{K'}_{37}$-derived reconstruction, whereas the TEX_{86}-derived reconstruction predicts pCO_2 stayed roughly constant. As other temperature and pCO_2 reconstructions for the interval both suggest a decrease in temperature and pCO_2 between the early and middle Eocene (Anagnostou et al., 2016; Westerhold et al., 2018b), the $U^{K'}_{37}$ temperature estimation is more likely more correct for this individual sample.

Assuming the broad assumptions of the diffusive model stand, it is therefore likely that the extreme CO_2 concentrations recorded here are a result of the decrease in sensitivity of the proxy at high Ɛp and temperatures, compounded by potentially unknown changes to algal biology over time. This data therefore suggests that precise, quantitative pCO_2 reconstruction during this interval is not yet possible using the classic alkenone pCO_2 proxy. Estimations may be improved with more precise and accurate understanding of the biological and physical parameters used for CO_2 reconstruction, but as much biological information is irreversibly lost on phytoplankton death and decay, and even the best reconstructions of physical oceanographic conditions cannot perfectly resolve the micro-conditions within which alkenone producers grew, this is challenging on a practical level.

As a more qualitative measure of CO_2, the above data can, however, provide some information, by providing a qualitative estimate to compare to others from the interval. Lower pCO_2 levels are generated in lower phosphate and lower $Ɛ_f$ model runs. The reconstructed pCO_2 of the lowest reconstruction (Figure 6c) is ~1100 ppmv for the interval, suggesting that even when the lower estimates of these parameters are taken, CO_2 was still extremely high during this interval compared to the rest of the Cenozoic: this can be seen qualitatively in Ɛp (Figure 5). Early Eocene CO_2 levels may still be lower than the lowest estimates presented in Figure 6, but this would require the assumptions of the proxy to deviate further from their assumed values: if other proxies, in the future, converge on a highly constrained pCO_2 estimate for the interval that is significantly <1000 ppmv, this can be taken as evidence that the alkenone pCO_2 proxy's assumptions are in some way invalid.

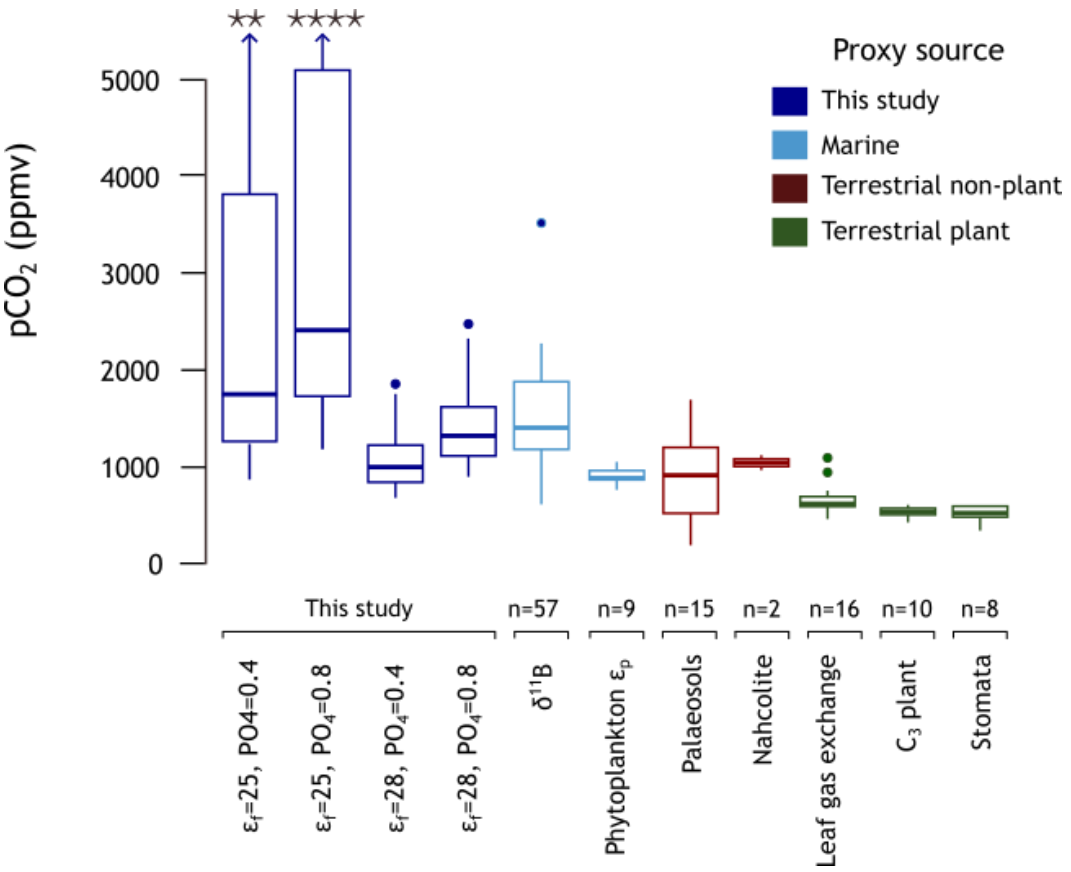

Figure 7: Reported CO_2 concentrations from the literature for the EECO (53.260-49.140 Ma) and this study, below 5000 ppmv to allow viewing of all CO_2 reconstructions on the same scale. No reported literature data is >5000 ppmv. Stars represent individual measurements >5000 ppmv: see Figure 6 for individual points. Top whisker of boxplots are indicated with arrows: values are ε_f =25 PO_4=0.4: 7636, ε_f =25 PO_4=0.8: 10174. Data sources: (Pearson and Palmer, 2000; Greenwood et al., 2003; Smith et al., 2010; Hyland and Sheldon, 2013; Hyland et al., 2013; Franks et al., 2014; Jagniecki et al., 2015; Anagnostou et al., 2016; Cui and Schubert, 2016; Witkowski et al., 2018; Steinthorsdottir et al., 2019). Figure only visualises the mean pCO_2 reconstruction from samples in each study, and does not include uncertainty estimations.

Reported CO_2 concentrations for the early Eocene are variable, and do not currently preclude pCO_2 >1000 ppmv, but do suggest it is lower. Figure 7 shows a compilation of published CO_2 reconstructions from the EECO, a time interval where CO_2 concentrations were likely reasonably stable (Anagnostou et al., 2020; Rae et al., 2021), and that covers all early Eocene CO_2 reconstruction samples reported in this study. Of these, the three higher plant derived proxies (stomatal frequencies, leaf gas exchange and C_3 plant $\delta^{13}C$) all give estimates of CO_2 concentrations of <700 ppmv on average, whereas palaeosol, phytoplankton, and boron-based estimates collectively give average concentrations of >1300 ppmv. Although the nahcolite proxy only consisted of two data points in the interval, it recorded CO_2 within the range of the non-higher plant derived proxies. This data therefore agrees more strongly with the non-higher plant derived proxies, and the lower ε_f=28 estimates of pCO_2 fall within this range.

In summary, depending on input parameters, pCO_2 estimates range from the higher end of normal compared to other proxy reconstructions of the interval, to massively higher than previously reconstructed values (Figure 7). Of the different non-CO_2 and temperature input parameters used for the model in this study, ε_f is responsible for the largest range in pCO_2 reconstructions. A move of ε_f from the most commonly used literature value of 25 to a higher but theoretically plausible value of 28 leads to reconstructions far more in line with both other proxy methods. However, since reconstruction of ε_f with only the information preserved in the geologic record is challenging, these reconstructions cannot be used quantitatively unless a more robust theoretical framework of how ε_f can covary with pCO_2 can be developed and verified experimentally. However, these estimates demonstrate qualitatively that across a range

of different input parameters, pCO_2 remains at or above 1000 ppmv at its highest point in the Eocene.

Conclusions

- Both temperature and CO_2 concentrations were high but relatively stable over the early Eocene in this record

- Quantification of temperature records suggests Bayesian-derived SST estimates from $U^{K'}_{37}$ and TEX_{86} for the early Eocene agree well, despite being at the upper end of the calibration range for both proxies.

- Temperatures derived from $U^{K'}_{37}$ decreased between the early and middle Eocene, but stayed stable when derived from TEX_{86}.

- Ɛp is high in the interval, matching and extending the previously identified trend of a decrease in Ɛp through the Cenozoic

- CO_2 concentrations from Ɛp are massively dependent on small changes in nutrient and biological parameters as they are generated at the extreme end of the proxy's sensitivity range.

- The most likely estimates of biological terms, phosphate, and temperature lead to CO_2 reconstructions much higher than other estimates for the time period, suggesting that an assumption in either the input parameters or the mechanics of the proxy causes generation of unrealistically high CO_2 concentrations when the proxy is itself at low sensitivity. This suggests that at ƐP and temperatures as extreme as those in the Eocene, the alkenone pCO_2 proxy is unlikely to provide well constrained quantified pCO_2 reconstructions, but can still suggest more qualitative trends.

- The collection of parameters that in combination lead to the lowest pCO_2 over the interval still suggest that early Eocene pCO_2 was >1000 ppmv. Either pCO_2 was at least 1000 ppmv in the Eocene, or key assumptions used in the alkenone pCO_2 proxy are incorrect.

- The lower range of pCO_2 estimates produced at site 16/28-sb01 are in broad agreement with previously published marine and non-higher plant terrestrial reconstructions of pCO_2 from the same time interval, but are much higher than pCO_2 reconstructions derived from higher plant remains.

Chapter 6: Conclusions, implications, and further work

Main findings

Collectively, this thesis examines whether the assumptions of the underlying biology behind biomarker-based reconstruction of past environments are correct under CO_2 concentrations higher than those seen at present, through two very different approaches. Chapters 3 and 4 examine whether terrestrial plant biomarkers remain constant under elevated CO_2 induced in a modern experiment, whereas Chapter 5 tests an existing proxy for CO_2 using alkenone biomarkers by looking at its behaviour in a time interval that was radically different environmentally from the present. In both cases, environmental change resulted in hitherto unaccounted-for shifts in biology: *n*-alkanes responded both chemically and isotopically to short-term CO_2 changes, and the CO_2 reconstructions produced from alkenone $\delta^{13}C$ were only realistic if some aspect of alkenone biology had changed over time in ways that are not considered in the mechanics of the proxy.

Chapter 3 evaluated the impact of elevated CO_2 on the chemical composition of leaf wax *n*-alkanes. Leaf wax *n*-alkane chemistry is a trait associated with plant waterproofing and although has been suggested for some time that leaf wax *n*-alkane chemistry adapts to environment, effects are not observed systematically and it has been difficult to identify the precise environmental drivers that lead to a response. This data has identified changes to *n*-alkane chemistry in response to multiple environmental changes within a single generation of trees, proving that *n*-alkane chemistry is, in some species,

responsive to environment on non-evolutionary timescales. An effect of elevated CO_2 on *n*-alkanes was seen in *C. avellana* from the third year of CO_2 exposure onward: the species exhibited decreased ACL, increased dispersion, and a decrease in *n*-alkane concentration, all of which are consistent with an increase in cuticular permeability. It is unknown whether *A. pseudoplatanus* would have exhibited similar trends or if *n*-alkane production is less plastic in this species, or whether the observed trends in *C. avellana* would change further if observed for longer: this question could only be solved by increasing the duration of the experiment to evolutionary timescales. However, the observed increase in ACL during the drought in 2022 suggests that changes to ACL can occur over extremely short timescales.

Chapter 4 evaluated the impact of elevated CO_2 concentration on alkane carbon isotopes and εlipid. Generally speaking, εlipid is treated as constant in the geologic record, despite increasing evidence that it responds dynamically to environment: this thesis adds to and compiles this data with regard to changes in εlipid with CO_2. This chapter shows that εlipid increases with CO_2 concentration across different species and experimental design, and that multiple mechanisms are responsible for this increase. As with *n*-alkane chemistry, this data cannot show whether εlipid is variable on longer timescales, but identification of the trend in the modern suggests that εlipid cannot be assumed to remain constant geologically. Therefore, changes to εlipid with both CO_2 concentration and other environmental drivers such as temperature and precipitation should be considered a potential explanation for trends in *n*-alkane $\delta^{13}C$ in the sediment record. εlipid has often been considered as constant in geologic time, with little evidence given to support this hypothesis: this data can be taken more widely to suggest that biological parameters such as biosynthetic fractionation cannot be taken as constant, no

matter how convenient it is to do so. Evolutionary-scale changes to biological processes will likely only act to increase differences in function compared to the modern, and any evaluation of past environmental change using a data archive derived from something as complex as a living organism should not assume, with limited evidence or knowledge of the mechanisms from which it is derived, that biology is unchanging.

Chapter 5 provides an example of where these assumptions may fundamentally break down. The alkenone pCO_2 proxy is one of the most widely used methods for reconstructing Cenozoic atmospheric CO_2 levels, but is calculated using a complex model that relies on many constants and empirical relationships measured only in modern oceans and laboratories, using modern species. This thesis demonstrates that pCO_2 estimations are more in line with others for the interval when a biological assumption (the value of enzymatic fractionation during carbon isotope assimilation, ε_f) is changed in a past climate state, rather than kept tied to modern values. The proxy's calculation includes assumptions of many other biological constants, which were not varied and are likely impossible to constrain if variable geologically: these include assumptions of the value of post-photosynthetic fractionation during the biosynthesis of alkenones, which Chapter 4 of this thesis demonstrated were not constant in terrestrial plants. Of the time through which alkenones are synthesised, the early Eocene is the most different climatically to the present; it is also the oldest, meaning that alkenone-producing algae themselves may be the most different biologically to those from which the proxy is calibrated. This data does, however, suggest that where biological uncertainties can be quantified, CO_2 estimations can be produced that are in line with alternate methods applied to the early Eocene, and suggests a lower limit of 1000 ppmv CO_2 was likely.

Although imperfect and difficult to quantify precisely, the alkenone pCO_2 proxy therefore still provides useful data in constraining early Eocene CO_2 concentrations.

Future work

Several avenues of future work could expand on research presented in this thesis. In particular, this thesis has noted different areas where biomarkers have altered their composition under changes in CO_2, and has suggested biological processes that may be responsible. Direct measurement of changes in biological processes themselves under elevated CO_2 would help to confirm these associations. Chapter 3 illustrated that under elevated CO_2, one of two species adapted its *n*-alkanes in such a way to potentially decrease cuticular permeability, increasing plant water loss. A direct test of this hypothesis would be to directly measure cuticular permeability under elevated CO_2, across a range of species and timescales, and observe if a) CO_2 affects cuticular permeability directly, and b) if this effect is correlated to *n*-alkane distributions. Chapter 4 suggested several different mechanisms may influence *n*-alkane $\delta^{13}C$ under elevated CO_2, but could not identify the specific pathways that are affected: a more comprehensive survey of different compound-specific $\delta^{13}C$ under changes in CO_2 could provide a more complete picture of carbon allocation-related changes to biomarker $\delta^{13}C$. The changes to branched alkane $\delta^{13}C$ in *A. pseudoplatanus* suggest potential changes to amino acid synthesis on short timescales: this could be directly measured by examining amino acid $\delta^{13}C$. Furthermore, this study only examined *n*- (and branched) alkane $\delta^{13}C$ under elevated CO_2: a complimentary study examining other commonly used plant biomarkers such as di- and triterpenoids could suggest which biomarkers are most likely to be influenced by changes to post-photosynthetic fractionations under elevated

CO_2. If a biomarker is to be used for the C_3 plant proxy, its photosynthetic fractionation must be as close to constant as possible: a comprehensive examination of the $\delta^{13}C$ of different plant biomarkers could identify which compounds are most promising for use in this context, and which should be avoided.

Many of the conclusions drawn in this study are limited by the number of species studied. Differences in *C. avellana* and *A. pseudoplatanus* were observed, but with only two species, broader trends about plant biomarker response to CO_2 are difficult to determine. Therefore, future work should increase the number of plant species studied in lower-cost growth chamber experiments, to confirm whether results seen here can be extrapolated to different plant groups. Both species examined here were deciduous angiosperm trees: a further area for future research would be whether the effect of CO_2 systematically differs by phylogeny or by plant functional type.

Intriguingly, both the variance in and the CO_2 effect on ACL, dispersion, and εlipid were all higher in *C. avellana* than *A. pseudoplatanus*. It was suggested here that this could link to the concentration of *n*-alkanes present, but, with only two species, it is again impossible to prove this link. If future research could establish whether a higher concentration of *n*-alkanes covaries in plants that are more likely to see their *n*-alkanes covary with environment, this could establish a framework that could be used to understand the environments and ecosystems within which the greatest response in *n*-alkanes could be seen geologically.

The alkenone pCO_2 data presented here highlights the biological complexities underlying the proxy. Large changes in reconstructed CO_2 were observed by varying the biological constant ε_f: although ε_f measurements have been made in the modern, their

uncertainty and the values encompass a larger range than the single value often used for reconstructions. For example, recent work suggests that values of ε_f in modern plankton may converge to values around 25, but with uncertainty: measured ε_f in the dinoflagellate species *Alexandrium tamarense* was, on average, 27 (Wilkes et al., 2017). The common ε_f values seen across different phytoplankton and their associated forms of RuBisCO may suggest the mechanism by which ε_f is set is not the action of RuBisCO itself. Understanding ε_f, and if it can be considered constant under different CO_2 concentrations, is essential for understanding the alkenone CO_2 proxy, and should be a key factor in future work. A future approach for this data could also be to further constrain the value of the physiological parameter *b* in deep time, including a comparison of Zhang et al. (2020)'s model for alkenone CO_2 reconstruction using coccolith length to determine the effect of both growth rate and size on ε_p. For both the response of *n*-alkanes and alkenones to CO_2, a further constraint of behaviour of the biology of both could further constrain what would be expected in the geologic record.

This thesis suggested at some of the biological complexities inherent to using biomarker data to reconstruct the Earth system through geologic time. These are inherently difficult to quantify, as although their influence on biomarkers remains, the data used to deconvolve the influences of multiple biological and environmental parameters is often lost geologically. For example, the precise cellular processes which serve to influence *n*-alkane $\delta^{13}C$ are difficult to account for without measurements of the $\delta^{13}C$ of chemical constituents of plants that are not preserved. One solution to further characterise these changes is full use of data sources available in the geologic record; this includes analysis of other plant biomarkers such as sterols and phytol alongside *n*-alkanes (e.g. Schouten et al. (2007), and direct measurement of bulk plant $\delta^{13}C$ from exceptionally preserved

fossil plants as described in (Huang et al., 1995). Clearly, such measurements cannot be taken alongside all analyses of *n*-alkanes, but a greater use of these complimentary data sources would constrain response of plants as a whole on evolutionary timescales. Similarly, use of a fuller range of the fossil remains produced by haptophyte algae alongside alkenones, such as is described in (Wilkes et al., 2018), can be used to further constrain algal biological processes. Understanding the true scope of the behaviour of complex biological organisms through geologic time when organisms have quite literally turned to stone is an immense task where some information is irrevocably and inevitably lost; what we are left with should be used to its fullest extent.

References

Adams M. A., Buckley T. N. and Turnbull T. L. (2020) Diminishing CO_2-driven gains in water-use efficiency of global forests. *Nat. Clim. Change* **10**, 466–471.

Ainsworth E. A. and Long S. P. (2005) What have we learned from 15 years of free-air CO_2 enrichment (FACE)? A meta-analytic review of the responses of photosynthesis, canopy properties and plant production to rising CO_2. *New Phytol.* **165**, 351–372.

Anagnostou E., John E. H., Babila T. L., Sexton P. F., Ridgwell A., Lunt D. J., Pearson P. N., Chalk T. B., Pancost R. D. and Foster G. L. (2020) Proxy evidence for state-dependence of climate sensitivity in the Eocene greenhouse. *Nat. Commun.* **11**.

Anagnostou E., John E. H., Edgar K. M., Foster G. L., Ridgwell A., Inglis G. N., Pancost R. D., Lunt D. J. and Pearson P. N. (2016) Changing atmospheric CO_2 concentration was the primary driver of early Cenozoic climate. *Nature* **533**, 380–384.

Andrae J. W., McInerney F. A., Tibby J., Henderson A. C. G., Hall P. A., Marshall J. C., McGregor G. B., Barr C. and Greenway M. (2019) Variation in leaf wax n-alkane characteristics with climate in the broad-leaved paperbark (Melaleuca quinquenervia). *Org. Geochem.* **130**, 33–42.

Andres R. J., Marland G., Boden T. and Bischof S. (2000) Carbon Dioxide Emissions from Fossil Fuel Consumption and Cement Estimate of Their Isotopic Composition and Latitudinal Distribution. In *The Carbon Cycle* Ca. pp. 54–62.

Arens N. C., Jahren A. H. and Amundson R. (2006) Can C3 plants faithfully record the carbon isotopic composition of atmospheric carbon dioxide? *Paleobiology* **26**, 137–164.

Arrhenius S. (1889) Über die Reaktionsgeschwindigkeit bei der Inversion von Rohrzucker durch Säuren. *Z. Für Phys. Chem.* **4U**, 226–248.

Avila R. T., de Almeida W. L., Costa L. C., Machado K. L. G., Barbosa M. L., de Souza R. P. B., Martino P. B., Juárez M. A. . T., Marçal D. M. S., Martins S. C. V., Ramalho J. D. C. and Damatta F. M. (2020) Elevated air [CO_2] improves photosynthetic performance and alters biomass accumulation and partitioning in drought-stressed coffee plants. *Environ. Exp. Bot.* **177**.

Badewien T., Vogts A. and Rullkötter J. (2015) n-Alkane distribution and carbon stable isotope composition in leaf waxes of C3 and C4 plants from Angola. *Org. Geochem.* **89–90**, 71–79.

Badger M. P. S. (2021) Alkenone isotopes show evidence of active carbon concentrating mechanisms in coccolithophores as aqueous carbon dioxide concentrations fall below 7 μmol L^{-1}. *Biogeosciences* **18**, 1149–1160.

Badger M. P. S., Lear C. H., Pancost R. D., Foster G. L., Bailey T. R., Leng M. J. and Abels H. A. (2013a) CO_2 drawdown following the middle Miocene expansion of the Antarctic Ice Sheet. *Paleoceanography* **28**, 42–53.

Badger M. P. S., Schmidt D. N., Mackensen A. and Pancost R. D. (2013b) High-resolution alkenone palaeobarometry indicates relatively stable pCO_2 during the Pliocene (3.3-2.8 Ma). *Philos. Trans. R. Soc. Math. Phys. Eng. Sci.* **371**.

Bai Y., Azamdzhon M., Wang S., Fang X., Guo H., Zhou P., Chen C., Liu X., Jia S. and Wang Q. (2019) An evaluation of biological and climatic effects on plant n-alkane distributions and δ2Halk in a field experiment conducted in central Tibet. *Org. Geochem.* **135**, 53–63.

Baker E. A. and Hunt G. M. (1986) Erosion of Waxes From Leaf Surfaces By Simulated Rain. *New Phytol.* **102**, 161–173.

Bale N. J., Palatinszky M., Rijpstra W. I. C., Herbold C. W., Wagner M. and Damsté J. S. S. (2019) Membrane lipid composition of the moderately thermophilic ammonia-oxidizing archaeon "Candidatus Nitrosotenuis uzonensis" at different growth temperatures. *Appl. Environ. Microbiol.* **85**.

de Bar M. W., Rampen S. W., Hopmans E. C., Sinninghe Damsté J. S. and Schouten S. (2019) Constraining the applicability of organic paleotemperature proxies for the last 90 Myrs. *Org. Geochem.* **128**, 122–136.

Baranowski U. K. (2020) Greenhouse climate - insights from early and middle Eocene stratigraphic and palaeoclimatic reconstructions of the Rockall Trough, NE Atlantic. University of Birmingham.

Basu S., Ghosh S. and Chattopadhyay D. (2021) Disentangling the abiotic versus biotic controls on C3 plant leaf carbon isotopes: Inferences from a global review. *Earth-Sci. Rev.* **222**.

Battipaglia G., Saurer M., Cherubini P., Calfapietra C., Mccarthy H. R., Norby R. J. and Cotrufo M. F. (2013) Elevated CO_2 increases tree-level intrinsic water use efficiency: Insights from carbon and oxygen isotope analyses in tree rings across three forest FACE sites. *New Phytol.* **197**, 544–554.

Beerling D. J. and Woodward F. I. (1995) Leaf Stable Carbon Isotope Composition Records Increased Water-Use Efficiency of C3 Plants in Response to Atmospheric CO_2 Enrichment. *Funct. Ecol.* **9**, 394–401.

Bendle J. A. P., Kawamura K., Yamazaki K. and Niwai T. (2007) Latitudinal distribution of terrestrial lipid biomarkers and n-alkane compound-specific stable carbon isotope ratios in the atmosphere over the western Pacific and Southern Ocean. *Geochim. Cosmochim. Acta* **71**, 5934–5955.

Bentaleb I., Fontugne M. and Beaufort L. (2002) Long-chain alkenones and UK'37 variability along a south-north transect in the Western Pacific Ocean. *Glob. Planet. Change* **34**, 173–183.

Bereiter B., Eggleston S., Schmitt J., Nehrbass-Ahles C., Stocker T. F., Fischer H., Kipfstuhl S. and Chappellaz J. (2015) Revision of the EPICA Dome C CO_2 record from 800 to 600-kyr before present. *Geophys. Res. Lett.* **42**, 542–549.

Bidigare R. R., Fluegge A., Freeman K. H., Hanson K. L., Hayes J. M., Hollinger D. Y., Jasper J. P., King L. L., Laws E. A., Milder J., Millero F. J., Pancost R. D., Popp B. N., Steinberg P. A. and Wakeham S. G. (1997) Consistent fractionation of 13C in nature and in the laboratory: Growth-rate effects in some haptophyte algae. *Glob. Biogeochem. Cycles* **11**, 279–292.

Bigeleisen J. and Mayer M. G. (1947) Calculation of equilibrium constants for isotopic exchange reactions. *J. Chem. Phys.* **15**, 261–267.

Blair N., Leu A., Munoz E., Olsen J., Kwong E. and Des Marais D. (1985) Carbon isotopic fractionation in heterotrophic microbial metabolism. *Appl. Environ. Microbiol.* **50**, 996–1001.

Boller A. J., Thomas P. J., Cavanaugh C. M. and Scott K. M. (2011) Low stable carbon isotope fractionation by coccolithophore RubisCO. *Geochim. Cosmochim. Acta* **75**, 7200–7207.

Bonafini M., Pellegrini M., Ditchfield P. and Pollard A. M. (2013) Investigation of the "canopy effect" in the isotope ecology of temperate woodlands. *J. Archaeol. Sci.* **40**, 3926–3935.

Bornemann A., D'haenens S., Norris R. D. and Speijer R. P. (2016) The demise of the early Eocene greenhouse – Decoupled deep and surface water cooling in the eastern North Atlantic. *Glob. Planet. Change* **145**, 130–140.

Bowling D. R., Pataki D. E. and Randerson J. T. (2008) Carbon isotopes in terrestrial ecosystem pools and CO_2 fluxes. *New Phytol.* **178**, 24–40.

Brassell S. C. (2014) Climatic influences on the Paleogene evolution of alkenones. *Paleoceanography* **29**, 255–272.

Brassell S. C., Dumitrescu M., Bralower T. J., Premoli-Silva I., Malone M. J., Arthur M. A., Averyt K., Bown P. R., Channell J. E. T., Clarke L. J., Dutton A. L., Eleson J. W., Frank T. D., Gylesjö S., Hancock H., Kano H., Leckie R. M., Marsaglia K. M., McGuire J., Moe K. T., Petrizzo M. R., Robinson S., Röhl U., Sager W. W., Takeda K., Thomas D., Williams T. and Zachos J. C. (2004) Recognition of alkenones in a lower Aptian porcellanite from the west-central Pacific. *Org. Geochem.* **35**, 181–188.

Brassell S. C., Eglinton G., Marlowe I. T., Pflaumann U. and Sarnthein M. (1986) Molecular stratigraphy: a new tool for climatic assessment. *Nature* **320**, 129–133.

Bray E. E. and Evans E. D. (1961) Distribution of n-paraffins as a clue to recognition of source beds. *Geochim. Cosmochim. Acta* **22**, 2–15.

Breecker D. O. (2013) Quantifying and understanding the uncertainty of atmospheric CO_2 concentrations determined from calcic paleosols. *Geochem. Geophys. Geosystems* **14**, 3210–3220.

Bryan J. K. (1980) Synthesis of the Aspartate Family and Branched-Chain Amino Acids. In *Amino Acids and Derivatives* Elsevier. pp. 403–452.

Buggle B., Wiesenberg G. L. B. and Glaser B. (2010) Is there a possibility to correct fossil n-alkane data for postsedimentary alteration effects? *Appl. Geochem.* **25**, 947–957.

Buitenhuis E. T., Pangerc T., Franklin D. J., Quéré C. L. and Malin G. (2008) Growth rates of six coccolithophorid strains as a function of temperature. *Limnol. Oceanogr.* **53**, 1181–1185.

Bush R. T. and McInerney F. A. (2015) Influence of temperature and C4 abundance on n-alkane chain length distributions across the central USA. *Org. Geochem.* **79**, 65–73.

Bush R. T. and McInerney F. A. (2013) Leaf wax n-alkane distributions in and across modern plants: Implications for paleoecology and chemotaxonomy. *Geochim. Cosmochim. Acta* **117**, 161–179.

Busta L. and Jetter R. (2018) Moving beyond the ubiquitous: the diversity and biosynthesis of specialty compounds in plant cuticular waxes. *Phytochem. Rev.* **17**, 1275–1304.

Busta L. and Jetter R. (2017) Structure and biosynthesis of branched wax compounds on wild type and wax biosynthesis mutants of arabidopsis thaliana. *Plant Cell Physiol.* **58**, 1059–1074.

Carr A. S., Boom A., Grimes H. L., Chase B. M., Meadows M. E. and Harris A. (2014) Leaf wax n-alkane distributions in arid zone South African flora: Environmental controls, chemotaxonomy and palaeoecological implications. *Org. Geochem.* **67**, 72–84.

Castañeda I. S. and Schouten S. (2011) A review of molecular organic proxies for examining modern and ancient lacustrine environments. *Quat. Sci. Rev.* **30**, 2851–2891.

Castañeda I. S., Werne J. P., Johnson T. C. and Filley T. R. (2009) Late Quaternary vegetation history of southeast Africa: The molecular isotopic record from Lake Malawi. *Palaeogeogr. Palaeoclimatol. Palaeoecol.* **275**, 100–112.

Cerda-Peña C., Contreras S. and Rau J. R. (2020) Molecular n-alkyl leaf waxes of three dominant plants from the temperate forest in South America. *Org. Geochem.* **149**.

Cerling T. E. and Harris J. M. (1999) Carbon isotope fractionation for ecological mammals and implications for ecological and and paleoecological studies. *Oecologia* **120**, 347–363.

Cerling T. E., Harris J. M., MacFadden B. J., Leakey M. G., Quade J., Eisenmann V. and Ehleringer J. R. (1997) Global vegetation change through the Miocene/Pliocene boundary. *Nature* **389**, 153–158.

Cerling T. E., Solomon D. K., Quade J. and Bowman J. R. (1991) On the isotopic composition of carbon in soil carbon dioxide. *Geochim. Cosmochim. Acta* **55**, 3403–3405.

Cernusak L. A. (2018) Gas exchange and water-use efficiency in plant canopies. *Plant Biol.* **22**, 52–67.

Cheng G., Huang H., Zhou L., He S., Zhang Y. and Cheng X. (2019) Chemical composition and water permeability of the cuticular wax barrier in rose leaf and petal: A comparative investigation. *Plant Physiol. Biochem.* **135**, 404–410.

Chikaraishi Y., Kaneko M. and Ohkouchi N. (2013) Reprint of "Stable hydrogen and carbon isotopic compositions of long-chain (C21-C33) n-alkanes and n-alkenes in insects." *Geochim. Cosmochim. Acta* **111**, 78–87.

Chikaraishi Y. and Naraoka H. (2007) d13C and dD relationships among three n-alkyl compound classes (n-alkanoic acid, n-alkane and n-alkanol) of terrestrial higher plants. *Org. Geochem.* **38**, 198–215.

Chikaraishi Y., Naraoka H. and Poulson S. R. (2004a) Carbon and hydrogen isotopic fractionation during lipid biosynthesis in a higher plant (Cryptomeria japonica). *Phytochemistry* **65**, 323–330.

Chikaraishi Y., Naraoka H. and Poulson S. R. (2004b) Hydrogen and carbon isotopic fractionations of lipid biosynthesis among terrestrial (C3, C4 and CAM) and aquatic plants. *Phytochemistry* **65**, 1369–1381.

Ciais P., Tans P. P., Trolier M., White J. W. C. and Francey R. J. (1995) A Large Northern Hemisphere Terrestrial CO_2 Sink Indicated by the 13C/12C Ratio of Atmospheric CO_2. *Science* **269**, 1098–1103.

Collister J. W., Rieley G., Stern B., Eglinton G. and Fry B. (1994) Compound-specific d13C analyses of leaf lipids from plants with differing carbon dioxide metabolisms. *Org. Geochem.* **21**, 619–627.

Conte M. H., Sicre M. A., Rühlemann C., Weber J. C., Schulte S., Schulz-Bull D. and Blanz T. (2006) Global temperature calibration of the alkenone unsaturation index (UK'37) in surface waters and comparison with surface sediments. *Geochem. Geophys. Geosystems* **7**.

Cotrufo M. F., Ineson P. and Rowland A. P. (1994) Decomposition of tree leaf litters grown under elevated CO_2: Effect of litter quality. *Plant Soil* **163**, 121–130.

Cowan I. R. (1978) Stomatal Behaviour and Environment. *Adv. Bot. Res.* **4**, 117–228.

Craig H. (1953) The geochemistry of the stable carbon isotopes. *Geochim. Cosmochim. Acta* **3**, 53–92.

Cranwell P. A. (1981) Diagenesis of free and bound lipids in terrestrial detritus deposited in a lacustrine sediment. *Org. Geochem.* **3**, 79–89.

Creydt M., Vuralhan-Eckert J., Fromm J. and Fischer M. (2019) Effects of elevated CO_2 concentration on leaves and berries of black elder (Sambucus nigra) using UHPLC-ESI-QTOF-MS/MS and gas exchange measurements. *J. Plant Physiol.* **234–235**, 71–79.

Cui Y. and Schubert B. A. (2016) Quantifying uncertainty of past pCO_2 determined from changes in C3 plant carbon isotope fractionation. *Geochim. Cosmochim. Acta* **172**, 127–138.

De Kauwe M. G., Medlyn B. E., Zaehle S., Walker A. P., Dietze M. C., Hickler T., Jain A. K., Luo Y., Parton Wi. J., Prentice I. C., Smith B., Thornton P. E., Wang S., Wang Y.-P., Warlind D., Weng E., Crous K. Y., Ellsworth D. S., Hanson P. J., Kim H.-S., Warren J. M., Oren R. and Norby R. J. (2013) Forest water use and water use efficiency at elevated CO_2: a model-data intercomparison at two contrasting temperate forest FACE sites. *Glob. Change Biol.* **19**, 1759–1779.

DeNiro M. J. . and Epstein S. (1977) Mechanism of Carbon Isotope Fractionation Associated with Lipid Synthesis. *Science* **197**, 261–263.

Diarte C., Xavier de Souza A., Staiger S., Deininger A. C., Bueno A., Burghardt M., Graell J., Riederer M., Lara I. and Leide J. (2021) Compositional, structural and functional cuticle analysis of Prunus laurocerasus L. sheds light on cuticular barrier plasticity. *Plant Physiol. Biochem.* **158**, 434–445.

Diefendorf A. F., Bickford C. P., Schlanser K. M., Freimuth E. J., Hannon J. S., Grossiord C. and McDowell N. G. (2021) Plant wax and carbon isotope response to heat and drought in the conifer Juniperus monosperma. *Org. Geochem.* **153**, 104197.

Diefendorf A. F., Freeman K. H. and Wing S. L. (2014) A comparison of terpenoid and leaf fossil vegetation proxies in Paleocene and Eocene Bighorn Basin sediments. *Org. Geochem.* **71**, 30–42.

Diefendorf A. F., Freeman K. H., Wing S. L., Currano E. D. and Mueller K. E. (2015a) Paleogene plants fractionated carbon isotopes similar to modern plants. *Earth Planet. Sci. Lett.* **429**, 33–44.

Diefendorf A. F., Freeman K. H., Wing S. L. and Graham H. V. (2011) Production of n-alkyl lipids in living plants and implications for the geologic past. *Geochim. Cosmochim. Acta* **75**, 7472–7485.

Diefendorf A. F. and Freimuth E. J. (2017) Extracting the most from terrestrial plant-derived n-alkyl lipids and their carbon isotopes from the sedimentary record: A review. *Org. Geochem.* **103**, 1–21.

Diefendorf A. F., Leslie A. B. and Wing S. L. (2015b) Leaf wax composition and carbon isotopes vary among major conifer groups. *Geochim. Cosmochim. Acta* **170**, 145–156.

Diefendorf A. F., Mueller K. E., Wing S. L., Koch P. L. and Freeman K. H. (2010) Global patterns in leaf 13C discrimination and implications for studies of past and future climate. *Proc. Natl. Acad. Sci.* **107**, 5738–5743.

Diefendorf A. F., Sberna D. T. and Taylor D. W. (2015c) Effect of thermal maturation on plant-derived terpenoids and leaf wax n-alkyl components. *Org. Geochem.* **89–90**, 61–70.

Dodd R. S. and Afzal-Rafii Z. (2000) Habitat-Related Adaptive Properties of Plant Cuticular Lipids. *Evolution* **54**, 1438–1444.

Dodd R. S., Rafii Z. A. and Power A. B. (1998) Ecotypic adaptation in Austrocedrus chilensis in cuticular hydrocarbon composition. *New Phytol.* **138**, 699–708.

Drake P. L., Froend R. H. and Franks P. J. (2013) Smaller, faster stomata: Scaling of stomatal size, rate of response, and stomatal conductance. *J. Exp. Bot.* **64**, 495–505.

Dungait J. A. J., Docherty G., Straker V. and Evershed R. P. (2011) Variation in bulk tissue, fatty acid and monosaccharide δ13C values between autotrophic and heterotrophic plant organs. *Phytochemistry* **72**, 2130–2138.

Dunkley Jones T., Eley Y. L., Thomson W., Greene S. E., Mandel I., Edgar K. M. and Bendle J. A. P. (2020) OPTiMAL : a new machine learning approach for GDGT-based palaeothermometry. *Clim. Past* **86**, 2599–2617.

Eek M. K., Whiticar M. J., Bishop J. K. B. and Wong C. S. (1999) Influence of nutrients on carbon isotope fractionation by natural populations of Prymnesiophyte algae in NE Pacific. *Deep-Sea Res. Part II Top. Stud. Oceanogr.* **46**, 2863–2876.

Eglinton G., Gonzalez A. G., Hamilton R. J. and Raphael R. A. (1962) Hydrocarbon constituents of the wax coatings of plant leaves: A taxonomic survey. *Phytochemistry* **1**, 89–102.

Eglinton G. and Hamilton R. J. (1967) Leaf epicuticular waxes. *Science* **156**, 1322–1335.

Eglinton T. I. and Eglinton G. (2008) Molecular proxies for paleoclimatology. *Earth Planet. Sci. Lett.* **275**, 1–16.

Ehleringer J. R. and Cerling T. E. (1995) Atmospheric CO_2 and the ratio of intercellular to ambient CO_2 concentrations in plants. *Tree Physiol.* **15**, 105–111.

Eley Y. L. and Hren M. T. (2018) Reconstructing vapor pressure deficit from leaf wax lipid molecular distributions. *Sci. Rep.* **8**.

Elling F. J., Könneke M., Mußmann M., Greve A. and Hinrichs K. U. (2015) Influence of temperature, pH, and salinity on membrane lipid composition and TEX86 of marine planktonic thaumarchaeal isolates. *Geochim. Cosmochim. Acta* **171**, 238–255.

Elling F. J., Könneke M., Nicol G. W., Stieglmeier M., Bayer B., Spieck E., de la Torre J. R., Becker K. W., Thomm M., Prosser J. I., Herndl G. J., Schleper C. and Hinrichs K. U. (2017) Chemotaxonomic characterisation of the thaumarchaeal lipidome. *Environ. Microbiol.* **19**, 2681–2700.

Eltgroth M. L., Watwood R. L. and Wolfe G. V. (2005) Production and cellular localization of neutral long-chain lipids in the haptophyte algae Isochrysis galbana and Emiliania huxleyi. *J. Phycol.* **41**, 1000–1009.

Farquhar G. D., Ehleringer J. R. and Hubick K. T. (1989) Carbon isotope discrimination and photosynthesis. *Annu. Rev. Plant Physiol. Plant Mol. Biol.* **40**, 503–537.

Farrimond P., Eglinton G. and Brassell S. C. (1986) Alkenones in Cretaceous black shales, Blake-Bahama Basin, western North Atlantic. *Org. Geochem.* **10**, 897–903.

Feakins S. J., Peters T., Wu M. S., Shenkin A., Salinas N., Girardin C. A. J., Bentley L. P., Blonder B., Enquist B. J., Martin R. E., Asner G. P. and Malhi Y. (2016) Production of leaf wax n-alkanes across a tropical forest elevation transect. *Org. Geochem.* **100**, 89–100.

Ficken K. J., Li B., Swain D. L. and Eglinton G. (2000) An n-alkane proxy for the sedimentary input of submerged/floating freshwater aquatic macrophytes. *Org. Geochem.* **31**, 745–749.

Flanagan L. B., Brooks J. R., Varney G. T., Berry S. C. and Ehleringer J. R. (1996) Carbon isotope discrimination during photosynthesis and the isotope ratio of respired CO_2 in boreal forest ecosystems. *Glob. Biogeochem. Cycles* **10**, 629–640.

Francey R. J., Allison C. E., Etheridge D. M., Trudinger C. M., Enting I. G., Leuenberger M. C., Langenfelds R. L., Michel E. and Steele L. P. (1999) A 1000-year high precision record of δ13C in atmospheric CO_2. *Tellus B Chem. Phys. Meteorol.* **51**, 170–193.

Francois R., Altabet M. A., Goericke R., McCorkle D. C., Brunet C. and Poisson A. (1993) Changes in the δ13C of surface water particulate organic matter across the

subtropical convergence in the SW Indian Ocean. *Glob. Biogeochem. Cycles* **7**, 627–644.

Franks P. J., Adams M. A., Amthor J. S., Barbour M. M., Berry J. A., Ellsworth D. S., Farquhar G. D., Ghannoum O., Lloyd J., McDowell N., Norby R. J., Tissue D. T. and von Caemmerer S. (2013) Sensitivity of plants to changing atmospheric CO_2 concentration: From the geological past to the next century. *New Phytol.* **197**, 1077–1094.

Franks P. J. and Beerling D. J. (2009) CO_2-forced evolution of plant gas exchange capacity and water-use efficiency over the Phanerozoic. *Geobiology* **7**, 227–236.

Franks P. J., Royer D. L., Beerling D. J., Van De Water P. K. and Cantrill D. J. (2014) New constraints on atmospheric CO_2 concentrations for the Phanerozoic. *Geophys. Res. Lett.* **41**, 4685–4694.

Freeman K. H. and Hayes J. M. (1992) Fractionation of carbon isotopes by phytoplankton and estimates of ancient CO_2 levels. *Glob. Biogeochem. Cycles* **6**, 185–198.

Freeman K. H. and Pancost R. D. (2014) *Biomarkers for Terrestrial Plants and Climate*., Elsevier Ltd.

Friedman I., O'Neil J. R. and Fleischer M. (1977) *Data of Geochemistry*., United States Geological Survey, Washington.

Frieling J., Iakovleva A. I., Reichart G. J., Aleksandrova G. N., Gnibidenko Z. N., Schouten S. and Sluijs A. (2014) Paleocene-Eocene warming and biotic response in the epicontinental West Siberian Sea. *Geology* **42**, 767–770.

Gagen M. H., Finsinger W., Wagner-Cremer F., Mccarroll D., Loader N. J., Robertson I., Jalkanen R., Young G. and Kirchhefer A. (2011) Evidence of changing intrinsic water-use efficiency under rising atmospheric CO_2 concentrations in Boreal Fennoscandia from subfossil leaves and tree ring δ13C ratios. *Glob. Change Biol.* **17**, 1064–1072.

Gao L., Burnier A. and Huang Y. (2012) Quantifying instantaneous regeneration rates of plant leaf waxes using stable hydrogen isotope labeling. *Rapid Commun. Mass Spectrom.* **26**, 115–122.

Garcia H., Weathers K. W., Paver C. R., Smolyar I., Boyer T. P., Locarnini R. A., Zweng M. M., Mishonov A. V., Baranova O. K., Seidov D. and Reagan J. R. (2018) World Ocean Atlas 2018. Volume 4: Dissolved Inorganic Nutrients (phosphate, nitrate and nitrate+nitrite, silicate). *NOAA Atlas NESDIS 84* **84**, 35.

Gardner A., Jiang M., Ellsworth D., MacKenzie A. R., Pritchard J., Bader M. K., Barton C., Bernacchi C., Calfapietra C., Crous K. Y., Dusenge M. E., Gimeno T. E., Hall M., Lamba S., Leuzinger S., Uddling J., Warren J., Wallin G. and Medlyn B. (2022) Optimal stomatal theory predicts CO_2 responses of stomatal conductance in both gymnosperm and angiosperm trees. *New Phytol.*, 1229–1241.

Geddes-McAlister J., Sukumaran A., Patchett A., Hager H. A., Dale J. C. M., Roloson J. L., Prudhomme N., Bolton K., Muselius B., Powers J. and Newman J. A. (2020) Examining the Impacts of CO_2 Concentration and Genetic Compatibility on Perennial Ryegrass — Epichloë festucae var lolii Interactions. *J. Fungi* **6**.

Goericke R., Montoya J. P. and Fry B. (1994) Physiology of isotope fractionation in algae and cyanobacteria. In *Stable isotopes in ecology* pp. 187–221.

Gomez-Guerrero A., Silva L. C. R., Barrera-Reyes M., Kishchuk B., Velázquez-Martínez A., Martinez-Trinidad T., Plascencia-Escalante F. O. and Horwath W. R. (2013) Growth decline and divergent tree ring isotopic composition (δ13C and δ18O) contradict predictions of CO 2 stimulation in high altitudinal forests. *Glob. Change Biol.* **29**.

Gonzalez-Meler M. A., Taneva L. and Trueman R. J. (2004) Plant respiration and elevated atmospheric CO_2 concentration: Cellular responses and global significance. *Ann. Bot.* **94**, 647–656.

Graham E. A. and Nobel P. S. (1996) Long-term effects of a doubled atmospheric CO_2 concentration on the CAM species Agave deserti. *J. Exp. Bot.* **47**, 61–69.

Greenwood D. R., Scarr M. J. and Christophel D. C. (2003) Leaf stomatal frequency in the Australian tropical rainforest tree Neolitsea dealbata (Lauraceae) as a proxy measure of atmospheric pCO_2. *Palaeogeogr. Palaeoclimatol. Palaeoecol.* **196**, 375–393.

Grice K., Lu H., Zhou Y., Stuart-Williams H. and Farquhar G. D. (2008) Biosynthetic and environmental effects on the stable carbon isotopic compositions of anteiso- (3-methyl) and iso- (2-methyl) alkanes in tobacco leaves. *Phytochemistry* **69**, 2807–2814.

Gulev S. K., Thorne P. W., Ahn J., Dentener F. J., Domingues C. M., Gerland S., Gong D., Kaufman D. S., Nnamchi J., Quas J., Rivera J. A., Sathyendranath S., Smith S. L., Trewin B., von Schuckmann K. and Vose R. S. (2021) Changing State of the Climate system. In *Climate change 2021: The physical science basis. Contribution of Working Group 1 to the Sixth Assessment Report of the Intergovernmental Panel on Climate CHange* (eds. V. Masson-Delmotte, P. Zhai, A. Pirani, S. L. Connors, C. Pean, S. Berger, N. Caud, Y. Chen, L. Goldfarb, M. I. Gomis, M. Huang, K. Leitzell, E. Lonnoy, J. B. R. Matthews, T. K. Maycock, T. Waterfield, O. Yelecki, R. Yu, and B. Zhou). Cambridge University Press, Cambridge. pp. 287–422.

Gülz P. G. (1994) Epicuticular Leaf Waxes in the Evolution of the Plant Kingdom. *J. Plant Physiol.* **143**, 453–464.

Guy R. D., Fogel M. L. and Berry J. A. (1993) Photosynthetic fractionation of the stable isotopes of oxygen and carbon. *Plant Physiol.* **101**, 37–47.

Harrington G. J., Higgs K. T. and Zucchi D. (2000) Biostratigraphic report on shallow borehole cores: 11/20-sb01, 16/28-sb01, 82/20-sb1, 83/24-sb01 and 83/24-sb02. In *RSG Project 97/34*

Hart K. M., Curioni G., Blaen P., Harper N. J., Miles P., Lewin K. F., Nagy J., Bannister E. J., Cai X. M., Thomas R. M., Krause S., Tausz M. and MacKenzie A. R. (2019) Characteristics of free air carbon dioxide enrichment of a northern temperate mature forest. *Glob. Change Biol.*, 1–15.

Haughton P., Praeg D., Shannon P., Harrington G. J., Higgs K. T., Amy L., Tyrrell S. and Morrissey T. (2005) First results from shallow stratigraphic boreholes on the eastern flank of the Rockall Basin, offshore western Ireland. In *Petroleum Geology Conference Proceedings* pp. 1077–1094.

Haughton P., Praeg D., Tyrrell S., Morrissey T., Geraghty D. and Lawrence A. (2002) *Integrated sedimentological report on shallow borehole cores: 11/20-sb01, 16/28-sb01, 83/20-sb01, 83/24-sb01, 83/24-sb02*., Rockall Studies Group.

Haworth M., Hoshika Y. and Killi D. (2016) Has the impact of rising CO_2 on plants been exaggerated by meta-analysis of free air CO_2 enrichment studies? *Front. Plant Sci.* **7**, 1–4.

Hayes J. M. (1993) Factors controlling 13C contents of sedimentary organic compounds: Principles and evidence. *Mar. Geol.* **113**, 111–125.

Hayes J. M. (2001) Fractionation of Carbon and Hydrogen Isotopes in Biosynthetic Processes. *Rev. Mineral. Geochem.* **43**, 225–277.

Hayes J. M., Popp B. N., Takigiku R. and Johnson M. W. (1989) An isotopic study of biogeochemical relationships between carbonates and organic carbon in the Greenhorn Formation. *Geochim. Cosmochim. Acta* **53**, 2961–2972.

Henderiks J. and Pagani M. (2008) Coccolithophore cell size and the Paleogene decline in atmospheric CO_2. *Earth Planet. Sci. Lett.* **269**, 576–584.

Henderiks J. and Pagani M. (2007) Refining ancient carbon dioxide estimates: Significance of coccolithophore cell size for alkenone-based pCO_2 records. *Paleoceanography* **22**, 1–12.

Henehan M. J., Rae J. W. B., Foster G. L., Erez J., Prentice K. C., Kucera M., Bostock H. C., Martínez-Botí M. A., Milton J. A., Wilson P. A., Marshall B. J. and Elliott T. (2013) Calibration of the boron isotope proxy in the planktonic foraminifera Globigerinoides ruber for use in palaeo-CO_2 reconstruction. *Earth Planet. Sci. Lett.* **364**, 111–122.

Herbert T. D. (2013) *Alkenone Paleotemperature Determinations*., Elsevier Ltd.

Hobbie E. A. and Werner R. A. (2004) Bulk carbon isotope patterns in C3 and C4 plants : a review and synthesis. *New Phytol.* **161**, 371–385.

Hoenisch B. (2021) Paleo-CO_2 data archive (version 1). , [Data set].

Hoffmann B., Kahmen A., Cernusak L. A., Arndt S. K. and Sachse D. (2013) Abundance and distribution of leaf wax n-alkanes in leaves of acacia and eucalyptus trees along a strong humidity gradient in Northern Australia. *Org. Geochem.* **62**, 62–67.

Högy P., Brunnbauer M., Koehler P., Schwadorf K., Breuer J., Franzaring J., Zhunusbayeva D. and Fangmeier A. (2013) Grain quality characteristics of spring wheat (Triticum aestivum) as affected by free-air CO_2 enrichment. *Environ. Exp. Bot.* **88**, 11–18.

Hollis C. J., Dunkley Jones T., Anagnostou E., Bijl P. K., Cramwinckel M. J., Cui Y., Dickens G. R., Edgar K. M., Eley Y. L., Evans D., Foster G. L., Frieling J., Inglis G. N., Kennedy E. M., Kozdon R., Lauretano V., Lear C. H., Littler K., Lourens L. J., Nele Meckler A., Naafs B. D. A., Pälike H., Pancost R. D., Pearson P. N., Röhl U., Royer D. L., Salzmann U., Schubert B. A., Seebeck H., Sluijs A., Speijer R. P., Stassen P., Tierney J. E., Tripati A., Wade B. S., Westerhold T., Witkowski C. R., Zachos J. C., Zhang Y. G., Huber M. and Lunt D. J. (2019) The DeepMIP contribution to PMIP4: Methodologies for selection, compilation and analysis of latest Paleocene and early Eocene climate proxy data, incorporating version 0.1 of the DeepMIP database. *Geosci. Model Dev.* **12**, 3149–3206.

Hönisch B., Ridgwell A., Schmidt D. N., Thomas E., Gibbs S. J., Sluijs A., Zeebe R. E., Kump L., Martindale R. C., Greene S. E., Kiessling W., Ries J., Zachos J. C., Royer D. L., Barker S., Marchitto T. M., Moyer R., Pelejero C., Ziveri P., Foster G. L. and Williams B. (2012) The Geological record of ocean acidification. *Science* **335**, 1058–1063.

Hooker T. S., Millar A. A. and Kunst L. (2002) Significance of the expression of the CER6 condensing enzyme for cuticular wax production in Arabidopsis. *Plant Physiol.* **129**, 1568–1580.

Hopmans E. C., Schouten S. and Sinninghe Damsté J. S. (2016) The effect of improved chromatography on GDGT-based palaeoproxies. *Org. Geochem.* **93**, 1–6.

Huang X., Zhao B., Wang K., Hu Y. and Meyers P. A. (2018) Seasonal variations of leaf wax n-alkane molecular composition and δD values in two subtropical deciduous tree species: Results from a three-year monitoring program in central China. *Org. Geochem.* **118**, 15–26.

Huang Y., Eglinton G., Ineson P., Bol R. and Harkness D. D. (1999) The effects of nitrogen fertilisation and elevated CO_2 on the lipid biosynthesis and carbon isotopic discrimination in birch seedlings (Betula pendula). *Plant Soil* **216**, 35–45.

Huang Y., Lockheart M. J., Collister J. W. and Eglinton G. (1995) Molecular and isotopic biogeochemistry of the Miocene Clarkia Formation: hydrocarbons and alcohols. *Org. Geochem.* **23**, 785–801.

Huguet C., Kim J. H., de Lange G. J., Sinninghe Damsté J. S. and Schouten S. (2009) Effects of long term oxic degradation on the U37K′, TEX86 and BIT organic proxies. *Org. Geochem.* **40**, 1188–1194.

Hyland E. G. and Sheldon N. D. (2013) Coupled CO_2-climate response during the Early Eocene Climatic Optimum. *Palaeogeogr. Palaeoclimatol. Palaeoecol.* **369**, 125–135.

Hyland E. G., Sheldon N. D. and Fan M. (2013) Terrestrial paleoenvironmental reconstructions indicate transient peak warming during the early Eocene climatic optimum. *Bull. Geol. Soc. Am.* **125**, 1338–1348.

Inglis G. N., Bragg F., Burls N. J., Cramwinckel M. J., Evans D., Foster G. L., Huber M., Lunt D. J., Siler N., Steinig S., Tierney J. E., Wilkinson R., Anagnostou E., de Boer A. M., Dunkley Jones T., Edgar K. M., Hollis C. J., Hutchinson D. K. and Pancost R. D. (2020) Global mean surface temperature and climate sensitivity of the early Eocene Climatic Optimum (EECO), Paleocene-Eocene Thermal Maximum (PETM), and latest Paleocene. *Clim. Past* **16**, 1953–1968.

Inglis G. N., Farnsworth A., Lunt D. J., Foster G. L., Hollis C. J., Pagani M., Jardine P. E., Pearson P. N., Markwick P., Galsworthy A. M. J., Raynham L., Taylor K. W. R. and Pancost R. D. (2015) Descent toward the Icehouse: Eocene sea surface cooling inferred from GDGT distributions. *Paleoceanography* **30**, 1000–1020.

Inglis G. N. and Tierney J. E. (2020) *The TEX 86 Paleotemperature Proxy*., Cambridge University Press, Cambridge.

Iniguez C., Capo-Bauca S., Niinemets Ü., Stoll H. M., Aguilo-Nicolau P. and Galmes J. (2020) Evolutionary trends in RuBisCO kinetics and their co-evolution with CO_2 concentrating mechanisms. *Plant J.* **101**, 897–918.

Jagniecki E. A., Lowenstein T. K., Jenkins D. M. and Demicco R. V. (2015) Eocene atmospheric CO_2 from the nahcolite proxy. *Geology* **43**, 1075–1078.

Jenkyns H. C., Schouten-Huibers L., Schouten S. and Sinninghe Damsté J. S. (2012) Warm Middle Jurassic-Early Cretaceous high-latitude sea-surface temperatures from the Southern Ocean. *Clim. Past* **8**, 215–225.

Jetter R., Kunst L. and Samuels A. L. (2006) *Composition of plant cuticular waxes*., Blackwell, Oxford.

Jetter R. and Riederer M. (2016) Localization of the transpiration barrier in the epi- and intracuticular waxes of eight plant species: Water transport resistances are associated with fatty acyl rather than alicyclic components. *Plant Physiol.* **170**, 921–934.

Judd E. J., Tierney J. E., Huber B. T., Wing S. L., Lunt D. J., Ford H. L., Inglis G. N., Mcclymont E. L., Brien C. L. O., Rattanasriampaipong R., Si W., Staitis M. L., Thirumalai K., Anagnostou E., Cramwinckel M. J., Dawson R. R., Evans D., Gray W. R., Grossman E.

L., Henehan M. J., Hupp B. N., Macleod K. G., Connor L. K. O., Luisa M., Montes S. and Song H. (2022) The PhanSST global database of Phanerozoic sea surface temperature proxy data. *Sci. Data* **9**.

Kahmen A., Hoffmann B., Schefuß E. and Arndt S. K. (2013) Leaf water deuterium enrichment shapes leaf wax n-alkane δD values of angiosperm plants II: Observational evidence and global implications. *Geochim. Cosmochim. Acta* **111**, 50–63.

Kanani H., Dutta B. and Klapa M. I. (2010) Individual vs. combinatorial effect of elevated CO_2 conditions and salinity stress on Arabidopsis thaliana liquid cultures: Comparing the early molecular response using time-series transcriptomic and metabolomic analyses. *BMC Syst. Biol.* **4**.

Keeling C. D., Piper S. C., Bacastow R. B., Wahlen M., Whorf T. P., Heimann M. and Meijer H. A. (2005a) Atmospheric CO_2 and $13CO_2$ Exchange with the Terrestrial Biosphere and Oceans from 1978 to 2000: Observations and Carbon Cycle Implications. *Hist. Atmospheric COsub2sub Its Eff. Plants Anim. Ecosyst.*, 83–113.

Keeling C. D., Piper S. C., Bacastow R. B., Wahlen M., Whorf T. P., Heimann M. and Meijer H. A. (2001) Exchanges of atmospheric CO_2 and $13CO_2$ with the terrestrial biosphere and oceans from 1978 to 2000. In *I. Global aspects, SIO Reference Series, No. 01-06* Scripps Institution of Oceanography, San Diego.

Keeling C. D., Piper S. C., Bacastow R. B., Wahlen M., Whorf T. P., Heimann M. and Meijer H. A. (2005b) Terrestrial Biosphere and Oceans from 1978 to 2000: Observations and Carbon Cycle Implications. In *A History of Atmospheric CO_2 and its effects on Plants, Animals, and Ecosystems* (eds. J. R. Ehleringer, T. E. Cerling, and M. D. Dearing). Springer Verlag, New York.

Keenan T. F., Hollinger D. Y., Bohrer G., Dragoni D., Munger J. W., Schmid H. P. and Richardson A. D. (2013) Increase in forest water-use efficiency as atmospheric carbon dioxide concentrations rise. *Nature* **499**, 324–328.

Kendon M. (2022) *Unprecedented extreme heatwave , July 2022*., Met Office National Climate Information Centre.

Kienast M., MacIntyre G., Dubois N., Higginson S., Normandeau C., Chazen C. and Herbert T. D. (2012) Alkenone unsaturation in surface sediments from the eastern equatorial pacific: Implications for SST reconstructions. *Paleoceanography* **27**, 1–11.

Killops S. and Killops V. (2013) Production, Preservation and Degradation of Organic Matter. In *Introduction to Organic Geochemistry* Blackwell Publishing Ltd., Malden, MA USA. pp. 71–116.

Kim J. H., van der Meer J., Schouten S., Helmke P., Willmott V., Sangiorgi F., Koç N., Hopmans E. C. and Damsté J. S. S. (2010) New indices and calibrations derived from the distribution of crenarchaeal isoprenoid tetraether lipids: Implications

for past sea surface temperature reconstructions. *Geochim. Cosmochim. Acta* **74**, 4639–4654.

Kim J.-H., Huguet C., Zonneveld K. A. F., Versteegh G. J. M., Roeder W., Sinninghe Damsté J. S. and Schouten S. (2009) An experimental field study to test the stability of lipids used for the TEX86 and palaeothermometers. *Geochim. Cosmochim. Acta* **73**, 2888–2898.

Kohn M. J. (2010) Carbon isotope compositions of terrestrial C3 plants as indicators of (paleo)ecology and (paleo)climate. *Proc. Natl. Acad. Sci.* **107**, 19691–19695.

Kohn M. J. (2016) Carbon isotope discrimination in C3 land plants is independent of natural variations in pCO_2. *Geochem. Perspect. Lett.* **2**, 35–43.

Konrad W., Royer D. L., Franks P. J. and Roth-Nebelsick A. (2020) Quantitative critique of leaf-based paleo-CO_2 proxies: Consequences for their reliability and applicability. *Geol. J.*, 1–17.

Kosma D. K., Bourdenx B., Bernard A., Parsons E. P., Lü S., Joubès J. and Jenks M. A. (2009) The impact of water deficiency on leaf cuticle lipids of Arabidopsis. *Plant Physiol.* **151**, 1918–1929.

Kroumova A. B., Xie Z. and Wagner G. J. (1994) A pathway for the biosynthesis of straight and branched , odd- and even-length , medium-chain fatty acids in plants. *Proc. Natl. Acad. Sci.* **91**, 11437–11441.

Kunst L. and Samuels A. L. (2003) Biosynthesis and secretion of plant cuticular wax. *Prog. Lipid Res.* **42**, 51–80.

Laws E. A., Bidigare R. R. and Popp B. N. (1997) Effect of growth rate and CO_2 concentration on carbon isotopic fractionation by the marine diatom Phaeodactylum tricornutum. *Limnol. Oceanogr.* **42**, 1552–1560.

Laws E. A., Popp B. N., Bidigare R. R., Kennicutt M. C. and Macko S. A. (1995) Dependence of phytoplankton carbon isotopic composition on growth rate and $[CO_2]aq$: Theoretical considerations and experimental results. *Geochim. Cosmochim. Acta* **59**, 1131–1138.

Laws E. A., Popp B. N., Bidigare R. R., Riebesell U., Burkhardt S. and Wakeham S. G. (2001) Controls on the molecular distribution and carbon isotopic composition of alkenones in certain haptophyte algae. *Geochem. Geophys. Geosystems* **2**, n/a-n/a.

Leider A., Hinrichs K. U., Schefuß E. and Versteegh G. J. M. (2013) Distribution and stable isotopes of plant wax derived n-alkanes in lacustrine, fluvial and marine surface sediments along an Eastern Italian transect and their potential to reconstruct the hydrological cycle. *Geochim. Cosmochim. Acta* **117**, 16–32.

Lomax B. H., Knight C. A. and Lake J. A. (2012) An experimental evaluation of the use of C3 δ13C plant tissue as a proxy for the paleoatmospheric δ13CO_2 signature of air. *Geochem. Geophys. Geosystems* **13**.

Lomax B. H., Lake J. A., Leng M. J. and Jardine P. E. (2019) An experimental evaluation of the use of Δ13C as a proxy for palaeoatmospheric CO_2. *Geochim. Cosmochim. Acta* **247**, 162–174.

Lourens J. A. J. and Reynhardt E. C. (1979) NMR investigation of Fischer-Tropsch waxes investigation in Fischer-Tropsch waxes. *J. Phys. Appl. Phys.* **12**, 1963–1972.

Lu J., Zang J., Meyers P. A., Huang X., Qiu P., Yu X., Yang H. and Xie S. (2020) Surface soil n-alkane molecular and δD distributions along a precipitation transect in northeastern China. *Org. Geochem.* **144**, 104015.

Luo Y., Melillo J., Niu S., Beier C., Clark J. S., Classen A. T., Davidson E., Dukes J. S., Evans R. D., Field C. B., Czimczik C. I., Keller M., Kimball B. A., Kueppers L. M., Norby R. J., Pelini S. L., Pendall E., Rastetter E., Six J., Smith M., Tjoelker M. G. and Torn M. S. (2011) Coordinated approaches to quantify long-term ecosystem dynamics in response to global change. *Glob. Change Biol.* **17**, 843–854.

Macková J., VaŠková M., Macek P., Hronková M., Schreiber L. and Šantrůček J. (2013) Plant response to drought stress simulated by ABA application: Changes in chemical composition of cuticular waxes. *Environ. Exp. Bot.* **86**, 70–75.

Maclennan J. and Jones S. (2006) Regional uplift, gas hydrate dissociation and the origins of the Paleocene–Eocene Thermal Maximum. *Earth Planet. Sci. Lett.* **245**, 65–80.

Maffei M., Badino S. and Bossi S. (2004) Chemotaxonomic significance of leaf wax n-alkanes in the Pinales (Coniferales). *J. Biol. Res.* **1**, 3–19.

Magill C. R., Ashley G. M. and Freeman K. H. (2013a) Ecosystem variability and early human habitats in eastern Africa. *Proc. Natl. Acad. Sci. U. S. A.* **110**, 1167–1174.

Magill C. R., Ashley G. M. and Freeman K. H. (2013b) Ecosystem variability and early human habitats in eastern Africa. *Proc. Natl. Acad. Sci. U. S. A.* **110**, 1167–1174.

Marlowe I. T., Brassell S. C., Eglinton G. and Green J. C. (1990) Long-chain alkenones and alkyl alkenoates and the fossil coccolith record of marine sediments. *Chem. Geol.* **88**, 349–375.

Martinelli L. A., Moreira M. Z. and Ferreira C. A. C. (1998) Stable carbon isotope ratio of tree leaves, boles and fine litter in a tropical forest in Rondonia, Brazil.

Marzi R., Torkelson B. E. and Olson R. K. (1993) A revised carbon preference index. *Org. Geochem.* **20**, 1303–1306.

McClelland H. L. O., Bruggeman J., Hermoso M. and Rickaby R. E. M. (2017) The origin of carbon isotope vital effects in coccolith calcite. *Nat. Commun.* **8**.

McElwain J. C. and Steinthorsdottir M. (2017) Paleoecology, ploidy, paleoatmospheric composition, and developmental biology: A review of the multiple uses of fossil stomata. *Plant Physiol.* **174**, 650–664.

Medlyn B. E., Barton C. V. M., Broadmeadow M. S. J., Ceulemans R., De Angelis P., Forstreuter M., Freeman M., Jackson S. B., Kellomäki S., Laitat E., Rey A., Roberntz P., Sigurdsson B. D., Strassmeyer J., Wang K., Curtis P. S. and Jarvis P. G. (2001) Stomatal conductance of forest species after long-term exposure to elevated CO_2 concentration: a synthesis. *New Phytol.* **149**, 247–264.

Mendonça R., Kosten S., Lacerot G., Mazzeo N., Roland F., Ometto J. P., Paz E. A., Bove C. P., Bueno A., Gomes J. H. C. and Scheffer M. (2013) Bimodality in stable isotope composition facilitates the tracing of carbon transfer from macrophytes to higher trophic levels. *Hydrobiologia* **710**, 205–218.

van der Merwe N. J. and Medina E. (1991) The canopy effect, carbon isotope ratios and foodwebs in amazonia. *J. Archaeol. Sci.* **18**, 249–259.

Monson K. D. and Hayes J. M. (1980) Biosynthetic control of the natural abundance of carbon 13 at specific positions within fatty acids in Escherichia coli. Evidence regarding the coupling of fatty acid and phospholipid synthesis. *J. Biol. Chem.* **255**, 11435–11441.

Monson K. D. and Hayes J. M. (1982) Carbon isotopic fractionation in the biosynthesis of bacterial fatty acids. Ozonolysis of unsaturated fatty acids as a means of determining the intramolecular distribution of carbon isotopes. *Geochim. Cosmochim. Acta* **46**, 139–149.

Mook W. G., Bommerson J. C. and Staverman W. H. (1974) Carbon isotope fractionation between dissolved bicarbonate and gaseous carbon dioxide. *Earth Planet. Sci. Lett.* **22**, 169–176.

Mooney H. A., Troughton J. H. and Berry J. A. (1977) Carbon isotope ratio measurements of succulent plants in southern Africa. *Oecologia* **30**, 295–305.

Moore C. M., Mills M. M., Arrigo K. R., Berman-Frank I., Bopp L., Boyd P. W., Galbraith E. D., Geider R. J., Guieu C., Jaccard S. L., Jickells T. D., La Roche J., Lenton T. M., Mahowald N. M., Marañón E., Marinov I., Moore J. K., Nakatsuka T., Oschlies A., Saito M. A., Thingstad T. F., Tsuda A. and Ulloa O. (2013) Processes and patterns of oceanic nutrient limitation. *Nat. Geosci.* **6**, 701–710.

Mueller K. E., Polissar P. J., Oleksyn J. and Freeman K. H. (2012) Differentiating temperate tree species and their organs using lipid biomarkers in leaves, roots and soil. *Org. Geochem.* **52**, 130–141.

Müller P. J., Kirst G., Ruhland G., Von Storch I. and Rosell-Melé A. (1998) Calibration of the alkenone paleotemperature index UK'37 based on core-tops from the eastern South Atlantic and the global ocean (60°N-60°S). *Geochim. Cosmochim. Acta* **62**, 1757–1772.

Myneni R. B., Keeling C. D., Tucker C. J., Asrar G. and Nemani R. R. (1997) Increased plant growth in the northern high latitudes from 1981 to 1991. *Nature* **386**, 698–702.

Naafs B. D. A., Castro J. M., De Gea G. A., Quijano M. L., Schmidt D. N. and Pancost R. D. (2016) Gradual and sustained carbon dioxide release during Aptian Oceanic Anoxic Event 1a. *Nat. Geosci.* **9**, 135–139.

Newberry S. L., Kahmen A., Dennis P. and Grant A. (2015) n-Alkane biosynthetic hydrogen isotope fractionation is not constant throughout the growing season in the riparian tree Salix viminalis. *Geochim. Cosmochim. Acta* **165**, 75–85.

Niinemets Ü. and Valladares F. (2006) Tolerance to shade, drought, and waterlogging of temperate northern hemisphere trees and shrubs. *Ecol. Monogr.* **76**, 521–547.

Norby R. J. and Zak D. R. (2011) Ecological Lessons from Free-Air CO_2 Enrichment (FACE) Experiments. *Annu. Rev. Ecol. Evol. Syst.* **42**, 181–203.

Nowak R. S., Ellsworth D. S. and Smith S. D. (2004) Functional responses of plants to elevated atmospheric CO_2 - Do photosynthetic and productivity data from FACE experiments support early predictions? *New Phytol.* **162**, 253–280.

Oakes A. M. and Hren M. T. (2016) Temporal variations in the δD of leaf n-alkanes from four riparian plant species. *Org. Geochem.* **97**, 122–130.

O'Leary M. H. (1988) Carbon Isotopes in Photosynthesis. *BioScience* **38**, 328–336.

O'Neil G. W., Gale A. C., Nelson R. K., Dhaliwal H. K. and Reddy C. M. (2021) Unusual Shorter-Chain C35 and C36 Alkenones from Commercially Grown Isochrysis sp. Microalgae. *J. Am. Oil Chem. Soc.* **98**, 757–768.

Oro J., Laseter J. L. and Weber D. (1966) Alkanes in Fungal Spores. *Science* **154**, 399–400.

Osmond C. B., Ziegler H., Stichler W. and Trimborn P. (1975) Carbon isotope discrimination in alpine succulent plants supposed to be capable of crassulacean acid metabolism (CAM). *Oecologia* **18**, 209–217.

Pagani M. (2014) Biomarker-Based Inferences of Past Climate: The Alkenone pCO_2 Proxy. In *Treatise on Geochemistry: Second Edition* Elsevier Ltd. pp. 361–378.

Pagani M., Arthur M. A. and Freeman K. H. (1999) Miocene evolution of atmospheric carbon dioxide. *Paleoceanography* **14**, 273–292.

Pagani M., Huber M., Liu Z., Bohaty S. M., Henderiks J., Sijp W., Krishnan S. and DeConto R. M. (2011) The role of carbon dioxide during the onset of antarctic glaciation. *Science* **334**, 1261–1264.

Pagani M., Pedentchouk N., Huber M., Sluijs A., Schouten S., Brinkhuis H. and Dickens G. R. (2006) Arctic hydrology during global warming at the Palaeocene/Eocene thermal maximum. *Nature* **442**, 671–675.

Pagani M., Zachos J. C., Freeman K. H., Tipple B. J. and Bohaty S. (2005) Marked decline in atmospheric carbon dioxide concentrations during the Paleogene. *Science* **309**, 600–603.

Pancost R. D. and Boot C. S. (2004) The palaeoclimatic utility of terrestrial biomarkers in marine sediments. *Mar. Chem.* **92**, 239–261.

Paoletti E., Nourrisson G., Garrec J. P. and Raschi A. (1998) Modifications of the leaf surface structures of Quercus ilex L. in open, naturally CO_2-enriched environments. *Plant Cell Environ.* **21**, 1071–1075.

Park R. and Epstein S. (1961) Metabolic fractionation of C13 and C12 in plants. *Plant Physiol.* **36**, 549–557.

Parsons E. P., Popopvsky S., Lohrey G. T., Lu S., Alkalai-Tuvia S., Perzelan Y., Paran I., Fallik E. and Jenks M. A. (2012) Fruit cuticle lipid composition and fruit post-harvest water loss in an advanced backgross generation of pepper (Capsicum sp.). *Physiol. Plant.* **146**, 15–25.

Pearson P. N., van Dongen B. E., Nicholas C. J., Pancost R. D., Schouten S., Singano J. M. and Wade B. S. (2007) Stable warm tropical climate through the Eocene Epoch. *Geology* **35**, 211–214.

Pearson P. N. and Palmer M. R. (2000) Atmospheric carbon dioxide concentrations over the past 60 million years. *Nature* **406**, 695–699.

Pelejero C. and Calvo E. (2003) The upper end of the UK′37 temperature calibration revisited. *Geochem. Geophys. Geosystems* **4**, 1–12.

Pelejero C. and Grimalt J. O. (1997) The correlation between the Uk37 index and sea surface temperatures in the warm boundary: The South China Sea. *Geochim. Cosmochim. Acta* **61**, 4789–4797.

Percy K. E., Awmack C. S., Lindroth R. L., Kubiske M. E., Kopper B. J., Isebrands J. G., Pregitzer K. S., Hendrey G. R., Dickson R. E., Zak D. R., Oksanen E., Sober J., Harrington R. and Karnosky D. F. (2002) Altered performance of forest pests under atmospheres enriched by CO_2 and O3. *Nature* **420**, 403–407.

Petracek P. D. and Bukovac M. J. (1995) Rheological properties of enzymatically isolated tomato fruit cuticle. *Plant Physiol.* **109**, 675–679.

Polik C. A., Elling F. J. and Pearson A. (2018) Impacts of Paleoecology on the TEX 86 Sea Surface Temperature Proxy in the Pliocene-Pleistocene Mediterranean Sea. *Paleoceanogr. Paleoclimatology* **33**, 1472–1489.

Poorter H. and Navas M. L. (2003) Plant growth and competition at elevated CO_2: On winners, losers and functional groups. *New Phytol.* **157**, 175–198.

Poorter H., Niinemets Ü., Poorter L., Wright I. J. and Villar R. (2009) Causes and consequences of variation in leaf mass per area (LMA): A meta-analysis. *New Phytol.* **182**, 565–588.

Poorter H., Van Berkel Y., Baxter R., Den Hertog J., Dijkstra P., Gifford R. M., Griffin K. L., Roumet C., Roy J. and Wong S. C. (1997) The effect of elevated CO_2 on the chemical composition and construction costs of leaves of 27 C3 species. *Plant Cell Environ.* **20**, 472–482.

Popp B. N., Hanson K. L., Dore J. E., Bidigare R. R., Laws E. A. and Wakeham S. G. (1999) Controls on the Carbon Isotopic Composition of Phytoplankton. In *Reconstructing Ocean History* (eds. F. Abrantes and A. C. Mix). Springer US, Boston, MA. pp. 381–398.

Popp B. N., Kenig F., Wakeham S. G., Laws E. A. and Bidigare R. R. (1998) Does growth rate affect ketone unsaturation and intracellular carbon isotopic variability in Emiliania huxleyi? *Paleoceanography* **13**, 35–41.

Popp B. N., Takigiku R., Hayes J. M., Louda J. W. and Baker E. W. (1989) The post-Paleozoic chronology and mechanism of 13C depletion in primary marine organic matter. *Am. J. Sci.* **289**, 436–454.

Porter A. S., Evans-Fitz.Gerald C., McElwain J. C., Yiotis C. and Elliott-Kingston C. (2015) How well do you know your growth chambers? Testing for chamber effect using plant traits. *Plant Methods* **11**, 1–10.

Post-Beittenmiller D. (1996) Biochemistry and molecular biology of wax production in plants. *Annu. Rev. Plant Physiol. Plant Mol. Biol.* **47**, 405–430.

Poulton A. J., Holligan P. M., Charalampopoulou A. and Adey T. R. (2017) Coccolithophore ecology in the tropical and subtropical Atlantic Ocean: New perspectives from the Atlantic meridional transect (AMT) programme. *Prog. Oceanogr.* **158**, 150–170.

Poynter J. G. and Eglinton G. (1990) Molecular composition of three sediments from hole 717C: the Bengal Fan. *Proc Sci. Results ODP Leg 116 Distal Bengal Fan* **116**, 155–161.

Poynter J. G., Farrimond P., Robinson N. and Eglinton G. (1989) Aeolian-derived higher plant lipids in the marine sedimentary record: links with palaeoclimate. In *Paleoclimatology and Paleometeorology: Modern and Past Patterns of Global Atmospheric Transport* (eds. M. Leinen and M. Sarnthein). Springer, Dordrecht. pp. 435–462.

Prahl F. G., Muehlhausen L. A. and Zahnle D. L. (1988) Further evaluation of long-chain alkenones as indicators of paleoceanographic conditions. *Geochim. Cosmochim. Acta* **52**, 2303–2310.

Prahl F. G. and Wakeham S. G. (1987) Calibration of unsaturation patterns in long-chain ketone compositions for palaeotemperature assessment. *Nature* **330**, 367–369.

Prahl F. G., Wolfe G. V. and Sparrow M. A. (2003) Physiological impacts on alkenone paleothermometry. *Paleoceanography* **18**, 1–7.

Prior S. A., Pritchard S. G., Runion G. B., Rogers H. and Mitchell R. J. (1997) Influence of atmospheric CO_2 enrichment, soil N, and water stress on needle surface wax formation in Pinus palustris (Pinaceae). *Am. J. Bot.* **84**, 1070–1077.

Prugel B. and Lognay G. (1994) Preliminary observations on the influence of increasing atmospheric CO_2 levels on cuticular waxes of spruce needles. In *Air pollutants and the leaf cuticle* (eds. K. E. Percy, J. N. Cape, R. Jagels, and C. J. Simpson). Springer, Berlin, Heidelberg.

Rae J. W. B., Foster G. L., Schmidt D. N. and Elliott T. (2011) Boron isotopes and B/Ca in benthic foraminifera: Proxies for the deep ocean carbonate system. *Earth Planet. Sci. Lett.* **302**, 403–413.

Rae J. W. B., Zhang Y. G., Liu X., Foster G. L., Stoll H. M. and Whiteford R. D. M. (2021) Atmospheric CO_2 over the past 66 million years from marine archives. *Annu. Rev. Earth Planet. Sci.* **49**, 609–641.

Rahman T., Shao M., Pahari S., Venglat P., Soolanayakanahally R., Qiu X., Rahman A. and Tanino K. (2021) Dissecting the roles of cuticular wax in plant resistance to shoot dehydration and low-temperature stress in arabidopsis. *Int. J. Mol. Sci.* **22**, 1–21.

Rau G. H., Riebesell U. and Wolf-Gladrow D. (1996) A model of photosynthetic 13C fractionation by marine phytoplankton based on diffusive molecular CO_2 uptake. *Mar. Ecol. Prog. Ser.* **133**, 275–285.

Rau G. H., Takahashi T., Des Marais D. J., Repeta D. J. and Martin J. H. (1992) The relationship between δ13C of organic matter and $[CO_2(aq)]$ in ocean surface water: Data from a JGOFS site in the northeast Atlantic Ocean and a model. *Geochim. Cosmochim. Acta* **56**, 1413–1419.

Reddy C. M., Eglinton T. I., Palić R., Benitez-Nelson B. C., Stojanović G., Palić I., Djordjević S. and Eglinton G. (2000) Even carbon number predominance of plant wax n-alkanes: A correction. *Org. Geochem.* **31**, 331–336.

Reichgelt T., D'Andrea W. J., Valdivia-McCarthy A. D. C., Fox B. R. S., Bannister J. M., Conran J. G., Lee W. G. and Lee D. E. (2020) Elevated CO_2, increased leaf-level productivity, and water-use efficiency during the early Miocene. *Clim. Past* **16**, 1509–1521.

Rhein, M., S.R. Rintoul, S. Aoki, E. Campos, D. Chambers, R.A. Feely, S. Gulev, G.C. Johnson, S.A. Josey, A. Kostianoy, C. Mauritzen, D. Roemmich, L.D. Talley and F. Wang, 2013: Observations: Ocean. In: Climate Change 2013: The Physical Science Basis. Contribution of Working Group I to the Fifth Assessment Report of the Intergovernmental Panel on Climate Change [Stocker, T.F., D. Qin, G.-K. Plattner,

M. Tignor, S.K. Allen, J. Boschung, A. Nauels, Y. Xia, V. Bex and P.M. Midgley (eds.)]. Cambridge University Press, Cambridge, United Kingdom and New York, NY, USA.

Richey J. N. and Tierney J. E. (2016) GDGT and alkenone flux in the northern Gulf of Mexico: Implications for the TEX86 and UK'37 paleothermometers. *Paleoceanography* **31**, 1547–1561.

Rickaby R. E. M., Schrag D. P., Zondervan I. and Riebesell U. (2002) Growth rate dependence of Sr incorporation during calcification of Emiliania huxleyi. *Glob. Biogeochem. Cycles* **16**.

Riebesell U. and Gattuso J.-P. (2015) Lessons learned from ocean acidification research. *Nat. Clim. Change* **5**, 12–14.

Riederer M. and Schneider G. (1990) The effect of the environment on the permeability and composition of Citrus leaf cuticles II. Composition of soluble cuticular lipids and correlation with transport properties. *Planta* **180**, 154–165.

Robinson J. J., Scott K. M., Swanson S. T., O'Leary M. H., Horken K., Tabita F. R. and Cavanaugh C. M. (2003) Kinetic isotope effect and characterization of form II RubisCO from the chemoautotrophic endosymbionts of the hydrothermal vent tubeworm Riftia pachyptila. *Limnol. Oceanogr.* **48**, 48–54.

Rodrigues A. M., Jorge T., Osorio S., Pott D. M., Lidon F. C., Damatta F. M., Marques I., Ribeiro-barros A. I., Ramalho J. D. C. and Antonio C. (2021) Primary Metabolite Profile Changes in Coffea spp. Promoted by Single and Combined Exposure to Drought and Elevated CO_2 Concentration. *Metabolites* **11**.

Roeske C. A. and O'Leary M. H. (1984) Carbon Isotope Effects on the Enzyme-Catalyzed Carboxylation of Ribulose Bisphosphate. *Biochemistry* **23**, 6275–6284.

Rohling E. J., Sluijs A., Dijkstra H. A., Köhler P., Van De Wal R. S. W., Von Der Heydt A. S., Beerling D. J., Berger A., Bijl P. K., Crucifix M., Deconto R. M., Drijfhout S. S., Fedorov A., Foster G. L., Ganopolski A., Hansen J., Hönisch B., Hooghiemstra H., Huber M., Huybers P., Knutti R., Lea D. W., Lourens L. J., Lunt D. J., Masson-Demotte V., Medina-Elizalde M., Otto-Bliesner B., Pagani M., Pälike H., Renssen H., Royer D. L., Siddall M., Valdes P., Zachos J. C. and Zeebe R. E. (2012) Making sense of palaeoclimate sensitivity. *Nature* **491**, 683–691.

Romanek C. S., Grossman E. L. and Morse J. W. (1992) Carbon isotopic fractionation in synthetic aragonite and calcite: Effects of temperature and precipitation rate. *Geochim. Cosmochim. Acta* **56**, 419–430.

Rommerskirchen F., Plader A., Eglinton G., Chikaraishi Y. and Rullkötter J. (2006) Chemotaxonomic significance of distribution and stable carbon isotopic composition of long-chain alkanes and alkan-1-ols in C4 grass waxes. *Org. Geochem.* **37**, 1303–1332.

Royer D. L. (2013) *Atmospheric CO_2 and O2 During the Phanerozoic: Tools, Patterns, and Impacts*., Elsevier Ltd.

Sachse D., Billault I., Bowen G. J., Chikaraishi Y., Dawson T. E., Feakins S. J., Freeman K. H., Magill C. R., McInerney F. A., van der Meer M. T. J., Polissar P., Robins R. J., Sachs J. P., Schmidt H.-L., Sessions A. L., White J. W. C., West J. B. and Kahmen A. (2012) Molecular Paleohydrology: Interpreting the Hydrogen-Isotopic Composition of Lipid Biomarkers from Photosynthesizing Organisms. *Annu. Rev. Earth Planet. Sci.* **40**, 221–249.

Sachse D., Dawson T. E. and Kahmen A. (2015) Seasonal variation of leaf wax n-alkane production and δ2H values from the evergreen oak tree, Quercus agrifolia. *Isotopes Environ. Health Stud.* **51**, 124–142.

Sachse D., Gleixner G., Wilkes H. and Kahmen A. (2010) Leaf wax n-alkane δD values of field-grown barley reflect leaf water δD values at the time of leaf formation. *Geochim. Cosmochim. Acta* **74**, 6741–6750.

Sachse D., Kahmen A. and Gleixner G. (2009) Significant seasonal variation in the hydrogen isotopic composition of leaf-wax lipids for two deciduous tree ecosystems (Fagus sylvativa and Acer pseudoplatanus). *Org. Geochem.* **40**, 732–742.

Samuels A. L., Kunst L. and Jetter R. (2008) Sealing Plant Surfaces: Cuticular Wax Formation by Epidermal Cells. *Annu. Rev. Plant Biol.* **59**, 683–707.

Saurer M., Cherubini P., Bonani G. and Siegwolf R. T. W. (2003) Tracing carbon uptake from a natural CO_2 spring into tree rings: An isotope approach. *Tree Physiol.* **23**, 997–1004.

Saurer M., Siegwolf R. T. W. and Schweingruber F. H. (2004) Carbon isotope discrimination indicates improving water-use efficiency of trees in northern Eurasia over the last 100 years. *Glob. Change Biol.* **10**, 2109–2120.

Scheidegger Y., Saurer M., Bahn M. and Siegwolf R. T. W. (2000) Linking stable oxygen and carbon isotopes with stomatal conductance and photosynthetic capacity: A conceptual model. *Oecologia* **125**, 350–357.

Scher M. A., Barclay R. S., Baczynski A. A., Smith B. A., Sappington J., Bennett L. A., Chakraborty S., Wilson J. P., Megonigal J. P. and Wing S. L. (2022) The effect of CO_2 concentration on carbon isotope discrimination during photosynthesis in Ginkgo biloba: implications for reconstructing atmospheric CO_2 levels in the geologic past. *Geochim. Cosmochim. Acta* **337**, 82–94.

Schlanser K. M., Diefendorf A. F., Greenwood D. R., Mueller K. E., West C. K., Lowe A. J., Basinger J. F., Currano E. D., Flynn A. G., Fricke H. C., Geng J., Meyer H. W. and Peppe D. J. (2020) On geologic timescales, plant carbon isotope fractionation responds to precipitation similarly to modern plants and has a small negative correlation with pCO_2. *Geochim. Cosmochim. Acta* **270**, 264–281.

Schönherr J. (1976) Water permeability of isolated cuticular membranes: The effect of cuticular waxes on diffusion of water. *Planta* **131**, 159–164.

Schouten S., Hopmans E. C., Schefuß E. and Sinninghe Damsté J. S. (2002) Distributional variations in marine crenarchaeotal membrane lipids: a new tool for reconstructing ancient sea water temperatures? *Earth Planet. Sci. Lett.* **204**, 265–274.

Schouten S., Hopmans E. C. and Sinninghe Damsté J. S. (2013) The organic geochemistry of glycerol dialkyl glycerol tetraether lipids: A review. *Org. Geochem.* **54**, 19–61.

Schouten S., Woltering M., Rijpstra W. I. C., Sluijs A., Brinkhuis H. and Sinninghe Damsté J. S. (2007) The Paleocene – Eocene carbon isotope excursion in higher plant organic matter: Differential fractionation of angiosperms and conifers in the Arctic. *Earth Planet. Sci. Lett.* **258**, 581–592.

Schreiber L., Kirsch T. and Riederer M. (1996) Diffusion through cuticles: principles and models. *Soc. Exp. Biol. Annu. Meet.*, 4.5.

Schubert B. A. and Jahren A. H. (2012) The effect of atmospheric CO_2 concentration on carbon isotope fractionation in C3 land plants. *Geochim. Cosmochim. Acta* **96**, 29–43.

Schwab V. F., Garcin Y., Sachse D., Todou G., Séné O., Onana J. M., Achoundong G. and Gleixner G. (2015) Effect of aridity on δ13C and δD values of C3 plant- and C4 graminoid-derived leaf wax lipids from soils along an environmental gradient in Cameroon (Western Central Africa). *Org. Geochem.* **78**, 99–109.

Scotti-Campos P., Pais I. P., Ribeiro-Barros A. I., Martins L. D., Tomaz M. A., Rodrigues W. P., Campostrini E., Semedo J. N., Fortunato A. S., Martins M. Q., Partelli F. L., Lidon F. C., DaMatta F. M. and Ramalho J. C. (2019) Lipid profile adjustments may contribute to warming acclimation and to heat impact mitigation by elevated [CO_2] in Coffea spp. *Environ. Exp. Bot.* **167**, 103856.

Seibt U., Rajabi A., Griffiths H. G. and Berry J. A. (2008) Carbon isotopes and water use efficiency : sense and sensitivity. *Oecologia* **155**, 441–454.

Seki O. and Bendle J. A. P. (2021) Revised alkenone δ13C based CO_2 estimates during the Plio-Pleistocene. *Clim. Past Discuss.*, 1–22.

Seki O., Foster G. L., Schmidt D. N., Mackensen A., Kawamura K. and Pancost R. D. (2010) Alkenone and boron-based Pliocene pCO_2 records. *Earth Planet. Sci. Lett.* **292**, 201–211.

Seufert P., Staiger S., APG IV, Bueno A., Burghardt M. and Riederer M. (2022) Building a Barrier: The Influence of Different Wax Fractions on the Water Transpiration Barrier of Leaf Cuticles. *Front. Plant Sci.* **12**.

Sexton P. F., Wilson P. A. and Pearson P. N. (2006) Palaeoecology of late middle Eocene planktic foraminifera and evolutionary implications. *Mar. Micropaleontol.* **60**, 1–16.

Sikes, E.L. *et al.* (1997) Alkenones and alkenes in surface waters and sediments of the Southern Ocean: Implications for paleotemperature estimation in polar regions. *Geochimica et Cosmochimica Acta*, **61**(7), 1495–1505.

Sinninghe Damsté J. S., Rijpstra W. I. C., Hopmans E. C., Prahl F. G., Wakeham S. G. and Schouten S. (2002) Distribution of membrane lipids of planktonic Crenarchaeota in the Arabian Sea. *Appl. Environ. Microbiol.* **68**, 2997–3002.

Smith F. A., Wing S. L. and Freeman K. H. (2007) Magnitude of the carbon isotope excursion at the Paleocene – Eocene thermal maximum: The role of plant community change. *Earth Planet. Sci. Lett.* **262**, 50–65.

Smith R. Y., Greenwood D. R. and Basinger J. F. (2010) Estimating paleoatmospheric pCO_2 during the Early Eocene Climatic Optimum from stomatal frequency of Ginkgo, Okanagan Highlands, British Columbia, Canada. *Palaeogeogr. Palaeoclimatol. Palaeoecol.* **293**, 120–131.

Sonzogni C., Bard E., Rostek F., Dollfus D., Rosell-Melé A. and Eglinton G. (1997) Temperature and Salinity Effects on Alkenone Ratios Measured in Surface Sediments from the Indian Ocean. *Quat. Res.* **47**, 344–355.

Staiger S., Seufert P., APG IV, Burghardt M., Popp C. and Riederer M. (2019) The permeation barrier of plant cuticles: uptake of active ingredients is limited by very long-chain aliphatic rather than cyclic wax compounds. *Pest Manag. Sci.* **75**, 3405–3412.

Steinthorsdottir M., Vajda V., Pole M. and Holdgate G. (2019) Moderate levels of Eocene pCO_2 indicated by Southern Hemisphere fossil plant stomata. *Geology* **47**, 914–918.

Sterry P. (2007) *Collins complete guide to British trees*., HarperCollins, London.

Stoll H. M., Guitián J., Hernandez-Almeida I., Mejia L. M., Phelps S., Polissar P., Rosenthal Y., Zhang H. and Ziveri P. (2019) Upregulation of phytoplankton carbon concentrating mechanisms during low CO_2 glacial periods and implications for the phytoplankton pCO_2 proxy. *Quat. Sci. Rev.* **208**.

Stott L. D., Kennett J. P., Shackleton N. J. and Corfield R. M. (1990) 48. The evolution of Antarctic surface wters during the Paleogene: inferences from the stable isotopic composition of planktonic foraminifers, ODP leg 113. In *Proceedings of the Ocean Drilling Program, 113 Scientific Reports* (eds. P. E. Barker, J.P. Kennett, and et al.). Proceedings of the Ocean Drilling Program. Ocean Drilling Program.

Sunday J. M., Calosi P., Dupont S., Munday P. L., Stillman J. H. and Reusch T. B. H. (2014) Evolution in an acidifying ocean. *Trends Ecol. Evol.* **29**, 117–125.

Super J. R., Thomas E., Pagani M., Huber M., O'Brien C. and Hull P. M. (2018) North Atlantic temperature and pCO_2 coupling in the early-middle Miocene. *Geology* **46**, 519–522.

Taub D. R., Miller B. and Allen H. (2008) Effects of elevated CO_2 on the protein concentration of food crops: a meta-analysis. *Glob. Change Biol.* **14**, 565–575.

Tegelaar E. W., Matthezing R. M., Jansen J. B. H., Horsfield B. and De Leeuw J. W. (1989) Possible origin of n-alkanes in high-wax crude oils. *Nature* **342**, 529–531.

Terashima I., Yanagisawa S. and Sakakibara H. (2014) Plant responses to CO_2: Background and perspectives. *Plant Cell Physiol.* **55**, 237–240.

Terwilliger V. J. and Huang J. (1996) Heterotrophic whole plant tissues show more 13C enrichment than their carbon sources. *Phytochemistry* **43**, 1183–1188.

Teunissen van Manen M. L., Jansen B., Cuesta F., León-Yánez S. and Gosling W. D. (2019) Leaf wax n-alkane patterns of six tropical montane tree species show species-specific environmental response. *Ecol. Evol.*, ece3.5458.

Theroux S., D'Andrea W. J., Toney J., Amaral-Zettler L. and Huang Y. (2010) Phylogenetic diversity and evolutionary relatedness of alkenone-producing haptophyte algae in lakes: Implications for continental paleotemperature reconstructions. *Earth Planet. Sci. Lett.* **300**, 311–320.

Thomas J. F. and Harvey C. N. (1983) Leaf Anatomy of Four Species Grown Under Continuous CO_2 Enrichment. *Bot. Gaz.* **144**, 303–309.

Tierney J. E. and Tingley M. P. (2014) A Bayesian, spatially-varying calibration model for the TEX86 proxy. *Geochim. Cosmochim. Acta* **127**, 83–106.

Tierney J. E. and Tingley M. P. (2018) BAYSPLINE: A New Calibration for the Alkenone Paleothermometer. *Paleoceanogr. Paleoclimatology* **33**, 281–301.

Tipple B. J., Berke M. A., Doman C. E., Khachaturyan S. and Ehleringer J. R. (2013) Leaf-wax n-alkanes record the plant – water environment at leaf flush. *Proc. Natl. Acad. Sci.* **110**, 2659–2664.

Tipple B. J. and Ehleringer J. R. (2018) Distinctions in heterotrophic and autotrophic-based metabolism as recorded in the hydrogen and carbon isotope ratios of normal alkanes. *Oecologia* **187**, 1053–1075.

Tipple B. J., Meyers S. R. and Pagani M. (2010) Carbon isotope ratio of Cenozoic CO_2: A comparative evaluation of available geochemical proxies. *Paleoceanography* **25**, 1–11.

Tipple B. J. and Pagani M. (2010) A 35 Myr North American leaf-wax compound-specific carbon and hydrogen isotope record: Implications for C4 grasslands and hydrologic cycle dynamics. *Earth Planet. Sci. Lett.* **299**, 250–262.

Tipple B. J. and Pagani M. (2013) Environmental control on eastern broadleaf forest species' leaf wax distributions and d/h ratios. *Geochim. Cosmochim. Acta* **111**, 64–77.

Tipple B. J. and Pagani M. (2007) The Early Origins of Terrestrial C4 Photosynthesis. *Annu. Rev. Earth Planet. Sci.* **35**, 435–461.

Tipple B. J., Pagani M., Krishnan S., Dirghangi S. S., Galeotti S., Agnini C., Giusberti L. and Rio D. (2011) Coupled high-resolution marine and terrestrial records of carbon and hydrologic cycles variations during the Paleocene – Eocene Thermal Maximum (PETM). *Earth Planet. Sci. Lett.* **311**, 82–92.

Toreti A., Bavera D., Acosta Navarro J., Cammalleri C., de Jager A., Di Ciollo C., Hrast Essenfelder A., Maetens W., Magni D., Mazzeschi M. and Spinoni J. (2022a) *Drought in Europe August 2022*., Pblications Office of the European Union, Luxembourg.

Toreti A., Masante D., Acosta Navarro J., Bavera D., Cammalleri C., De Felice M., de Jager A., Di Ciollo C., Hrast Essenfelder A., Maetens W., Magni D., Mazzeschi M. and Spinoni J. (2022b) *Drought in Europe July 2022*., Publications Office of the European Union, Luxembourg.

Treviño M. B. and O'Connell M. A. (1998) Three Drought-Responsive Members of the Nonspecific Lipid-Transfer Protein Gene Family in Lycopersicon pennellii Show Different Developmental Patterns of Expression. *Plant Physiol.* **116**, 1461–1468.

Tucker C. J., Fung I. Y., Keeling C. D. and Gammon R. H. (1986) Relationship between atmospheric CO_2 variations and a satellite-derived vegetation index. *Nature* **319**, 195–199.

Tucker C. J., Townshend J. R. G. and Goff T. E. (1985) African land-cover classification using satellite data. *Science* **227**, 369–375.

Turner S. K. and Ridgwell A. (2016) Development of a novel empirical framework for interpreting geological carbon isotope excursions, with implications for the rate of carbon injection across the PETM. *Earth Planet. Sci. Lett.* **435**, 1–13.

U.S. Department of Energy (2020) *Free-air CO_2 Enrichment Experiments: FACE Results, Lessons and Legacy*.,

Vanhatalo M., Huttunen S. and Bäck J. (2001) Effects of elevated [CO_2] and O3 on stomatal and surface wax characteristics in leaves of pubescent birch grown under field conditions. *Trees - Struct. Funct.* **15**, 304–313.

Versteegh G. J. M., Riegman R., De Leeuw J. W. and Jansen J. H. F. (2001) U37K′ values for Isochrysis galbana as a function of culture temperature, light intensity and nutrient concentrations. *Org. Geochem.* **32**, 785–794.

Villanueva J. and Grimalt J. O. (1996) Pitfalls in the chromatographic determination of the alkenone Uk37 index for paleotemperature estimation. *J. Chromatogr. A* **723**, 285–291.

Vogg G., Fischer S., Leide J., Emmanuel E., Jetter R., Levy A. A. and Riederer M. (2004) Tomato fruit cuticular waxes and their effects on transpiration barrier properties: Functional characterization of a mutant deficient in a very-long-chain fatty acid β-ketoacyl-CoA synthase. *J. Exp. Bot.* **55**, 1401–1410.

Vogts A., Schefuß E., Badewien T. and Rullkötter J. (2012) n-Alkane parameters from a deep sea sediment transect off southwest Africa reflect continental vegetation and climate conditions. *Org. Geochem.* **47**, 109–119.

Volkman J. K., Barrett S. M., Blackburn S. I. and Sikes E. L. (1995) Alkenones in Gephyrocapsa oceanica: Implications for studies of paleoclimate. *Geochim. Cosmochim. Acta* **59**, 513–520.

Vollbrecht D. (1974) Three pathways of isoleucine biosynthesis in mutant strains of Saccharomyces cerevisiae. *Biochim. Biophys. Acta* **362**, 382–389.

Wakil S. J. (1961) Mechanism of fatty acid synthesis. *J. Lipid Res.* **2**, 1–24.

Walker A. P., De Kauwe M. G., Bastos A., Belmecheri S., Georgiou K., Keeling R. F., McMahon S. M., Medlyn B. E., Moore D. J. P., Norby R. J., Zaehle S., Anderson-Teixeira K. J., Battipaglia G., Brienen R. J. W., Cabugao K. G., Cailleret M., Campbell E., Canadell J. G., Ciais P., Craig M. E., Ellsworth D. S., Farquhar G. D., Fatichi S., Fisher J. B., Frank D. C., Graven H., Gu L., Haverd V., Heilman K., Heimann M., Hungate B. A., Iversen C. M., Joos F., Jiang M., Keenan T. F., Knauer J., Körner C., Leshyk V. O., Leuzinger S., Liu Y., MacBean N., Malhi Y., McVicar T. R., Peñuelas J., Pongratz J., Powell A. S., Riutta T., Sabot M. E. B., Schleucher J., Sitch S., Smith W. K., Sulman B., Taylor B., Terrer C., Torn M. S., Treseder K., Trugman A. T., Trumbore S. E., van Mantgem P. J., Voelker S. L., Whelan M. E. and Zuidema P. A. (2020) Integrating the evidence for a terrestrial carbon sink caused by increasing atmospheric CO_2. *New Phytol.*

Wang G., Zhang L., Zhang X., Wang Y. and Xu Y. (2014) Chemical and carbon isotopic dynamics of grass organic matter during litter decompositions: A litterbag experiment. *Org. Geochem.* **69**, 106–113.

Wang J., Axia E., Xu Y., Wang G., Zhou L., Jia Y., Chen Z. and Li J. (2018a) Temperature effect on abundance and distribution of leaf wax n-alkanes across a temperature gradient along the 400 mm isohyet in China. *Org. Geochem.* **120**, 31–41.

Wang J., Xu Y., Zhou L., Shi M., Axia E., Jia Y., Chen Z., Li J. and Wang G. (2018b) Disentangling temperature effects on leaf wax n-alkane traits and carbon isotopic composition from phylogeny and precipitation. *Org. Geochem.* **126**, 13–22.

Warren B. A., Yamoah K. A. and Bendle J. A. P. (2021) Biomarker and isotopic evidence of carnivorous plants in wetland ecosystems. In *British Organic Geochemical Society Conference* Birmingham, UK. p. 43.

Weijers J. W. H., Schouten S., Spaargaren O. C. and Sinninghe Damsté J. S. (2006) Occurrence and distribution of tetraether membrane lipids in soils: Implications for the use of the TEX86 proxy and the BIT index. *Org. Geochem.* **37**, 1680–1693.

Weiwei L. U., Xinxiao Y. U., Guodong J. I. A., Hanzhi L. I. and Ziqiang L. I. U. (2018) Responses of Intrinsic Water-use Efficiency and Tree Growth to Climate Change in Semi-Arid Areas of North China. *Sci. Rep.* **8**.

Weller P. and Stein R. (2008) Paleogene biomarker records from the central Arctic Ocean (Integrated Ocean Drilling Program Expedition 302): Organic carbon sources, anoxia, and sea surface temperature: PALEOGENE CENTRAL ARCTIC OCEAN BIOMARKER. *Paleoceanography* **23**.

Westerhold T., Marwan N., Drury A. J., Liebrand D., Agnini C., Anagnostou E., Barnet J. S. K., Bohaty S. M., De Vleeschouwer D., Florindo F., Frederichs T., Hodell D. A., Holbourn A. E., Kroon D., Lauretano V., Littler K., Lourens L. J., Lyle M., Pälike H., Röhl U., Tian J., Wilkens R. H., Wilson P. A. and Zachos J. C. (2020) An astronomically dated record of Earth's climate and its predictability over the last 66 million years. *Science* **369**, 1383–1388.

Westerhold T., Röhl U., Donner B. and Zachos J. C. (2018a) Global Extent of Early Eocene Hyperthermal Events – a new Pacific Benthic Foraminiferal Isotope Record from Shatsky Rise (ODP Site 1209). *Paleoceanogr. Paleoclimatology* **33**, 626–642.

Westerhold T., Röhl U., Donner B. and Zachos J. C. (2018b) Global Extent of Early Eocene Hyperthermal Events: A New Pacific Benthic Foraminiferal Isotope Record From Shatsky Rise (ODP Site 1209). *Paleoceanogr. Paleoclimatology* **33**, 626–642.

Wilkes E. B., Carter S. J. and Pearson A. (2017) CO_2-dependent carbon isotope fractionation in the dinoflagellate Alexandrium tamarense. *Geochim. Cosmochim. Acta* **212**, 48–61.

Wilkes E. B., Lee R. B. Y., McClelland H. L. O., Rickaby R. E. M. and Pearson A. (2018) Carbon isotope ratios of coccolith–associated polysaccharides of Emiliania huxleyi as a function of growth rate and CO_2 concentration. *Org. Geochem.* **119**, 1–10.

Witkowski C. R., Weijers J. W. H., Blais B., Schouten S. and Sinninghe Damsté J. S. (2018) Molecular fossils from phytoplankton reveal secular PCO_2 trend over the phanerozoic. *Sci. Adv.* **4**, 1–8.

Wullschleger S. D., Tschaplinski T. J. and Norby R. J. (2002) Plant water relations at elevated CO_2 - implications for water-limited environments. *Plant Cell Environ.* **25**, 319–331.

Xue D., Zhang X., Lu X., Chen G. and Chen Z.-H. (2017) Molecular and Evolutionary Mechanisms of Cuticular Wax for Plant Drought Tolerance. *Front. Plant Sci.* **8**.

Yang Y., Bendle J. A. P., Pancost R. D., Yan Y., Ruan X., Warren B. A., Lü X., Yao Y., Huang X., Yang H. and Xie S. (2021) Leaf Wax and Sr-Nd Isotope Evidence for High-Latitude Dust Input to the Central South China Sea and its implication for fertilizaton. *Geophys. Res. Lett.* **48**.

Zegouagh Y., Derenne S. and Largeau C. (1998) Organic matter sources and early diagenetic alterations in Arctic surface sediments (Lena River delta and Laptev Sea , Eastern Siberia), II . Molecular and isotopic studies of hydrocarbons. *Org. Geochem.* **28**, 571–583.

Zeisler-Diehl V., Müller Y. and Schreiber L. (2018) Epicuticular wax on leaf cuticles does not establish the transpiration barrier, which is essentially formed by intracuticular wax. *J. Plant Physiol.* **227**, 66–74.

Zhang H., Hartmann H., Gleixner G., Thoma M. and Schwab V. F. (2019) Carbon isotope fractionation including photosynthetic and post-photosynthetic processes in C3 plants: Low [CO_2] matters. *Geochim. Cosmochim. Acta* **245**, 1–15.

Zhang Y., Du Z., Han Y., Chen X., Kong X., Sun W., Chen C. and Chen M. (2021) Plasticity of the Cuticular Transpiration Barrier in Response to Water Shortage and Resupply in Camellia sinensis: A Role of Cuticular Waxes. *Front. Plant Sci.* **11**, 1–17.

Zhang Y. G., Henderiks J. and Liu X. (2020) Refining the alkenone-pCO_2 method II: Towards resolving the physiological parameter 'b.' *Geochim. Cosmochim. Acta* **281**, 118–134.

Zhang Y. G., Pagani M., Liu Z., Bohaty S. M. and Deconto R. M. (2013) A 40-million-year history of atmospheric CO_2. *Philos. Trans. R. Soc.* **371**.

Zhang Y. G., Pearson A., Benthien A., Dong L., Huybers P., Liu X. and Pagani M. (2019) Refining the alkenone-pCO_2 method I: Lessons from the Quaternary glacial cycles. *Geochim. Cosmochim. Acta* **260**, 177–191.

Zhou Y., Grice K., Stuart-Williams H., Farquhar G. D., Hocart C. H., Lu H. and Liu W. (2010) Biosynthetic origin of the saw-toothed profile in δ13C and δ2H of n-alkanes and systematic isotopic differences between n-, iso- and anteiso-alkanes in leaf waxes of land plants. *Phytochemistry* **71**, 388–403.

Zhou Y., Stuart-Williams H., Grice K., Kayler Z. E., Zavadlav S., Vogts A., Rommerskirchen F., Farquhar G. D. and Gessler A. (2015) Allocate carbon for a reason: Priorities are reflected in the 13C/12C ratios of plant lipids synthesized via three independent biosynthetic pathways. *Phytochemistry* **111**, 14–20.

Zhu Z., Piao S., Myneni R. B., Huang M., Zeng Z., Canadell J. G., Ciais P., Sitch S., Friedlingstein P., Arneth A., Cao C., Cheng L., Kato E., Koven C., Li Y., Lian X., Liu Y., Liu R., Mao J., Pan Y., Peng S., Peñuelas J., Poulter B., Pugh T. A. M., Stocker B. D.,

Viovy N., Wang X., Wang Y., Xiao Z., Yang H., Zaehle S. and Zeng N. (2016) Greening of the Earth and its drivers. *Nat. Clim. Change* **6**, 791–795.

Appendix

Data, including *n*-alkane concentrations and isotopic composition, and parameters used for TEX_{86} and alkenone-based pCO_2 reconstruction, are available in full at https://www.dropbox.com/scl/fo/5yqliqnv1r972eyqzmu2i/h?dl=0&rlkey=ljzbl3gcyqir1tnoo5ngw27cf

Table A1: *n*-Alkane analysis metadata

Sample code	Species	Array	Date collected	CO2	Concentration of GC-FID (µl)	Run notes	GC-IRMS run location
2849	Sycamore	1	08/06/2018	e	500		Bristol
2850	Sycamore	2	08/06/2018	a	500		Bristol
2851	Sycamore	3	08/06/2018	a	500		Bristol
2852	Sycamore	4	08/06/2018	e	500		Bristol
2853	Sycamore	5	08/06/2018	a	500		Bristol
2854	Sycamore	6	08/06/2018	e	500		Bristol
2861	Hazel	1	08/06/2018	e	500		Bristol
2862	Hazel	2	08/06/2018	a	100	IRMS run failure	Bristol
2863	Hazel	3	08/06/2018	a	500		Bristol
2864	Hazel	4	08/06/2018	e	500		Bristol
2865	Hazel	5	08/06/2018	a	500		Bristol
2866	Hazel	6	08/06/2018	e	500		Bristol
2855	Sycamore	1	03/07/2018	e	500		Hokkaido
2856	Sycamore	2	03/07/2018	a	500		Hokkaido
2857	Sycamore	3	03/07/2018	a	500		Hokkaido
2858	Sycamore	4	03/07/2018	e	500		Hokkaido
2859	Sycamore	5	03/07/2018	a	500		Hokkaido
2860	Sycamore	6	03/07/2018	e	500		Hokkaido
2867	Hazel	1	03/07/2018	e	500		Hokkaido

2868	Hazel	2	03/07/2018	a	500		Hokkaido
2869	Hazel	3	03/07/2018	a	500		Hokkaido
2870	Hazel	4	03/07/2018	e	500		Hokkaido
2871	Hazel	5	03/07/2018	a	500		Hokkaido
2872	Hazel	6	03/07/2018	e	500		Hokkaido
2873	Sycamore	1	03/08/2018	e	500		Bristol
2874	Sycamore	2	03/08/2018	a	500		Bristol
2875	Sycamore	3	03/08/2018	a	500		Bristol
2876	Sycamore	4	03/08/2018	e	500		Bristol
2877	Sycamore	5	03/08/2018	a	500		Bristol
2878	Sycamore	6	03/08/2018	e	500		Bristol
2885	Hazel	1	03/08/2018	e	500		Bristol
2886	Hazel	2	03/08/2018	a	500		Bristol
2887	Hazel	3	03/08/2018	a	500		Bristol
2888	Hazel	4	03/08/2018	e	500		Bristol
2889	Hazel	5	03/08/2018	a	500		Bristol
2890	Hazel	6	03/08/2018	e	500		Bristol
2879	Sycamore	1	31/08/2018	e	500		Bristol
2880	Sycamore	2	31/08/2018	a	500		Bristol
2881	Sycamore	3	31/08/2018	a	500		Bristol
2882	Sycamore	4	31/08/2018	e	500		Bristol
2883	Sycamore	5	31/08/2018	a	500		Bristol
2884	Sycamore	6	31/08/2018	e	500		Bristol
2891	Hazel	1	31/08/2018	e	500		Bristol
2892	Hazel	2	31/08/2018	a	500		Bristol
2893	Hazel	3	31/08/2018	a	500		Bristol
2894	Hazel	4	31/08/2018	e	500	IRMS run failure	Bristol

2895	Hazel	5	31/08/2018	a	500		Bristol
2896	Hazel	6	31/08/2018	e	100		Bristol
2897	Sycamore	1	24/05/2019	e	500		Hokkaido
2898	Sycamore	2	24/05/2019	a	500		Hokkaido
2899	Sycamore	3	24/05/2019	a	500	Run fail: contaminated	Hokkaido
2900	Sycamore	4	24/05/2019	e	500		Hokkaido
2901	Sycamore	5	24/05/2019	a	500		Hokkaido
2902	Sycamore	6	24/05/2019	e	100		Hokkaido
2903	Hazel	1	24/05/2019	e	100		Hokkaido
2904	Hazel	2	24/05/2019	a	100		Hokkaido
2905	Hazel	3	24/05/2019	a	100		Hokkaido
2906	Hazel	4	24/05/2019	e	500		Hokkaido
2907	Hazel	5	24/05/2019	a	500		Hokkaido
2908	Hazel	6	24/05/2019	e	500		Hokkaido
2981	Sycamore	1	04/07/2019	e	500		Hokkaido
2982	Sycamore	2	04/07/2019	a	500		Hokkaido
2983	Sycamore	3	04/07/2019	a	500		Hokkaido
2984	Sycamore	4	04/07/2019	e	500		Hokkaido
2985	Sycamore	5	04/07/2019	a	500		Hokkaido
2986	Sycamore	6	04/07/2019	e	500		Hokkaido
2987	Hazel	1	04/07/2019	e	500		Hokkaido
2988	Hazel	2	04/07/2019	a	500		Hokkaido
2989	Hazel	3	04/07/2019	a	500		Hokkaido
2990	Hazel	4	04/07/2019	e	500		Hokkaido
2991	Hazel	5	04/07/2019	a	500		Hokkaido
2992	Hazel	6	04/07/2019	e	500		Hokkaido
2969	Sycamore	1	29/07/2019	e	500		Bristol

2970	Sycamore	2	29/07/2019	a	500		Bristol
2971	Sycamore	3	29/07/2019	a	500		Bristol
2972	Sycamore	4	29/07/2019	e	500		Bristol
2973	Sycamore	5	29/07/2019	a	500		Bristol
2974	Sycamore	6	29/07/2019	e	500		Bristol
2975	Hazel	1	29/07/2019	e	500		Bristol
2976	Hazel	2	29/07/2019	a	500		Bristol
2977	Hazel	3	29/07/2019	a	500		Bristol
2978	Hazel	4	29/07/2019	e	500		Bristol
2979	Hazel	5	29/07/2019	a	500		Bristol
2980	Hazel	6	29/07/2019	e	500		Bristol
2957	Sycamore	1	23/08/2019	e	500		Hokkaido
2958	Sycamore	2	23/08/2019	a	500		Hokkaido
2959	Sycamore	3	23/08/2019	a	500		Hokkaido
2960	Sycamore	4	23/08/2019	e	500		Hokkaido
2961	Sycamore	5	23/08/2019	a	500		Hokkaido
2962	Sycamore	6	23/08/2019	e	500		Hokkaido
2963	Hazel	1	23/08/2019	e	100		Hokkaido
2964	Hazel	2	23/08/2019	a	500		Hokkaido
2965	Hazel	3	23/08/2019	a	100		Hokkaido
2966	Hazel	4	23/08/2019	e	500		Hokkaido
2967	Hazel	5	23/08/2019	a	100		Hokkaido
2968	Hazel	6	23/08/2019	e	500		Hokkaido
3699	Sycamore	1	27/09/2019	e	500		Hokkaido
3700	Sycamore	2	27/09/2019	a	500		Hokkaido
3701	Sycamore	3	27/09/2019	a	500		Hokkaido
3702	Sycamore	4	27/09/2019	e	500		Hokkaido

3703	Sycamore	5	27/09/2019	a	500		Hokkaido
3704	Sycamore	6	27/09/2019	e	500		Hokkaido
3705	Hazel	1	27/09/2019	e	500		Hokkaido
3706	Hazel	2	27/09/2019	a	500		Hokkaido
3707	Hazel	3	27/09/2019	a	500		Hokkaido
3708	Hazel	4	27/09/2019	e	500		Hokkaido
3709	Hazel	5	27/09/2019	a	500		Hokkaido
3710	Hazel	6	27/09/2019	e	500		Hokkaido
3527	Hazel	1	20/10/2019	e	500		Hokkaido
3528	Hazel	2	20/10/2019	a	500		Hokkaido
3529	Hazel	3	20/10/2019	a	500		Hokkaido
3530	Hazel	4	20/10/2019	e	500		Hokkaido
3531	Hazel	5	20/10/2019	a	500		Hokkaido
3532	Hazel	6	20/10/2019	e	500		Hokkaido
2993	Sycamore	1	30/04/2020	e	500		Hokkaido
2994	Sycamore	2	30/04/2020	a	500		Hokkaido
2995	Sycamore	3	30/04/2020	a	500		Hokkaido
2996	Sycamore	4	30/04/2020	e	500		Hokkaido
2997	Sycamore	5	30/04/2020	a	500		Hokkaido
2998	Sycamore	6	30/04/2020	e	500		Hokkaido
2999	Hazel	1	30/04/2020	e	500		Hokkaido
3000	Hazel	2	30/04/2020	a	100		Hokkaido
3001	Hazel	3	30/04/2020	a	500		Hokkaido
3002	Hazel	4	30/04/2020	e	100		Hokkaido
3003	Hazel	5	30/04/2020	a	500		Hokkaido
3004	Hazel	6	30/04/2020	e	500		Hokkaido
2921	Sycamore	1	28/05/2020	e	500		Bristol

2922	Sycamore	2	28/05/2020	a	500		Bristol
2923	Sycamore	3	28/05/2020	a	500		Bristol
2924	Sycamore	4	28/05/2020	e	500		Bristol
2925	Sycamore	5	28/05/2020	a	500		Bristol
2926	Sycamore	6	28/05/2020	e	500		Bristol
2927	Hazel	1	28/05/2020	e	500	IRMS run failure	Bristol
2928	Hazel	2	28/05/2020	a	500		Bristol
2929	Hazel	3	28/05/2020	a	500		Bristol
2930	Hazel	4	28/05/2020	e	500		Bristol
2931	Hazel	5	28/05/2020	a	500		Bristol
2932	Hazel	6	28/05/2020	e	500		Bristol
2945	Sycamore	1	03/07/2020	e	500		Hokkaido
2946	Sycamore	2	03/07/2020	a	500		Hokkaido
2947	Sycamore	3	03/07/2020	a	500		Hokkaido
2948	Sycamore	4	03/07/2020	e	500		Hokkaido
2949	Sycamore	5	03/07/2020	a	500		Hokkaido
2950	Sycamore	6	03/07/2020	e	500		Hokkaido
2951	Hazel	1	03/07/2020	e	500		Hokkaido
2952	Hazel	2	03/07/2020	a	500		Hokkaido
2953	Hazel	3	03/07/2020	a	500		Hokkaido
2954	Hazel	4	03/07/2020	e	500		Hokkaido
2955	Hazel	5	03/07/2020	a	500		Hokkaido
2956	Hazel	6	03/07/2020	e	500		Hokkaido
2933	Sycamore	1	03/08/2020	e	500		Bristol
2934	Sycamore	2	03/08/2020	a	500		Bristol
2935	Sycamore	3	03/08/2020	a	500		Bristol
2936	Sycamore	4	03/08/2020	e	500		Bristol

2937	Sycamore	5	03/08/2020	a	500		Bristol
2938	Sycamore	6	03/08/2020	e	500		Bristol
2939	Hazel	1	03/08/2020	e	100		Bristol
2940	Hazel	2	03/08/2020	a	100		Bristol
2941	Hazel	3	03/08/2020	a	100		Bristol
2942	Hazel	4	03/08/2020	e	100		Bristol
2943	Hazel	5	03/08/2020	a	100		Bristol
2944	Hazel	6	03/08/2020	e	500		Bristol
3025	Sycamore	1	28/08/2020	e	500		Hokkaido
3026	Sycamore	2	28/08/2020	a	500		Hokkaido
3027	Sycamore	3	28/08/2020	a	500		Hokkaido
3028	Sycamore	4	28/08/2020	e	500		Hokkaido
3029	Sycamore	5	28/08/2020	a	500		Hokkaido
3030	Sycamore	6	28/08/2020	e	500		Hokkaido
3031	Hazel	1	28/08/2020	e	500		Hokkaido
3032	Hazel	2	28/08/2020	a	500		Hokkaido
3033	Hazel	3	28/08/2020	a	500		Hokkaido
3034	Hazel	4	28/08/2020	e	500		Hokkaido
3035	Hazel	5	28/08/2020	a	100		Hokkaido
3036	Hazel	6	28/08/2020	e	500		Hokkaido
3141	Sycamore	1	23/09/2020	e	500		Hokkaido
3142	Sycamore	2	23/09/2020	a	500		Hokkaido
3143	Sycamore	3	23/09/2020	a	500		Hokkaido
3144	Sycamore	4	23/09/2020	e	500		Hokkaido
3145	Sycamore	5	23/09/2020	a	500		Hokkaido
3146	Sycamore	6	23/09/2020	e	500		Hokkaido
3147	Hazel	1	23/09/2020	e	100		Hokkaido

3148	Hazel	2	23/09/2020	a	500		Hokkaido
3149	Hazel	3	23/09/2020	a	100		Hokkaido
3150	Hazel	4	23/09/2020	e	100		Hokkaido
3151	Hazel	5	23/09/2020	a	100		Hokkaido
3152	Hazel	6	23/09/2020	e	100		Hokkaido
3557	Sycamore	1	20/10/2020	e	500		Hokkaido
3558	Sycamore	2	20/10/2020	a	500		Hokkaido
3559	Sycamore	3	20/10/2020	a	500		Hokkaido
3560	Sycamore	4	20/10/2020	e	500		Hokkaido
3561	Sycamore	5	20/10/2020	a	500		Hokkaido
3563	Sycamore	6	20/10/2020	e	500		Hokkaido
3611	Hazel	1	20/10/2020	e	500		Hokkaido
3612	Hazel	2	20/10/2020	a	500		Hokkaido
3613	Hazel	3	20/10/2020	a	500		Hokkaido
3614	Hazel	4	20/10/2020	e	500		Hokkaido
3615	Hazel	5	20/10/2020	a	500		Hokkaido
3318	Sycamore	1	25/05/2021	e	500		Bristol
3319	Sycamore	2	25/05/2021	a	500		Bristol
3320	Sycamore	3	25/05/2021	a	500		Bristol
3321	Sycamore	4	25/05/2021	e	500		Bristol
3322	Sycamore	5	25/05/2021	a	500		Bristol
3323	Sycamore	6	25/05/2021	e	500		Bristol
3324	Hazel	1	25/05/2021	e	100		Bristol
3325	Hazel	2	25/05/2021	a	100		Bristol
3326	Hazel	3	25/05/2021	a	100		Bristol
3327	Hazel	4	25/05/2021	e	100		Bristol
3328	Hazel	5	25/05/2021	a	100	IRMS run failure	Bristol

3329	Hazel	6	25/05/2021	e	100		Bristol
3384	Sycamore	1	09/06/2021	e	500		Hokkaido
3385	Sycamore	2	09/06/2021	a		Run fail: contaminated	
3386	Sycamore	3	09/06/2021	a	500		Hokkaido
3387	Sycamore	4	09/06/2021	e	500		Hokkaido
3388	Sycamore	5	09/06/2021	a	500		Hokkaido
3389	Sycamore	6	09/06/2021	e	500		Hokkaido
3390	Hazel	1	09/06/2021	e	100		Hokkaido
3391	Hazel	2	09/06/2021	a	100		Hokkaido
3392	Hazel	3	09/06/2021	a	100		Hokkaido
3393	Hazel	4	09/06/2021	e	100	Run fail: contaminated	Hokkaido
3394	Hazel	5	09/06/2021	a	100		Hokkaido
3395	Hazel	6	09/06/2021	e	500		Hokkaido
3515	Sycamore	1	15/07/2021	e	500		Bristol
3516	Sycamore	2	15/07/2021	a	500		Bristol
3517	Sycamore	3	15/07/2021	a	500		Bristol
3518	Sycamore	4	15/07/2021	e	500		Bristol
3519	Sycamore	5	15/07/2021	a	500		Bristol
3520	Sycamore	6	15/07/2021	e	500		Bristol
3521	Hazel	1	15/07/2021	e	500		Bristol
3522	Hazel	2	15/07/2021	a	500		Bristol
3523	Hazel	3	15/07/2021	a	500		Bristol
3524	Hazel	4	15/07/2021	e	500		Bristol
3525	Hazel	5	15/07/2021	a	500		Bristol
3526	Hazel	6	15/07/2021	e	500		Bristol
3533	Sycamore	1	23/08/2021	e	500		Bristol
3534	Sycamore	2	23/08/2021	a	500		Bristol

3535	Sycamore	3	23/08/2021	a	500		Bristol
3536	Sycamore	4	23/08/2021	e	500		Bristol
3537	Sycamore	5	23/08/2021	a	500		Bristol
3538	Sycamore	6	23/08/2021	e	500		Bristol
3539	Hazel	1	23/08/2021	e	500		Bristol
3540	Hazel	2	23/08/2021	a	500		Bristol
3541	Hazel	3	23/08/2021	a	500		Bristol
3542	Hazel	4	23/08/2021	e	500		Bristol
3543	Hazel	5	23/08/2021	a	500		Bristol
3544	Hazel	6	23/08/2021	e	500		Bristol
3545	Sycamore	1	27/09/2021	e	500		Hokkaido
3546	Sycamore	2	27/09/2021	a	500		Hokkaido
3547	Sycamore	3	27/09/2021	a	500		Hokkaido
3548	Sycamore	4	27/09/2021	e	500		Hokkaido
3549	Sycamore	5	27/09/2021	a	500		Hokkaido
3550	Sycamore	6	27/09/2021	e	500		Hokkaido
3551	Hazel	1	27/09/2021	e	500		Hokkaido
3552	Hazel	2	27/09/2021	a	500		Hokkaido
3553	Hazel	3	27/09/2021	a	500		Hokkaido
3554	Hazel	4	27/09/2021	e	500		Hokkaido
3555	Hazel	5	27/09/2021	a	500		Hokkaido
3556	Hazel	6	27/09/2021	e	500		Hokkaido
3711	Sycamore	1	25/10/2021	e	500		Hokkaido
3712	Sycamore	2	25/10/2021	a	500		Hokkaido
3713	Sycamore	3	25/10/2021	a	500		Hokkaido
3714	Sycamore	4	25/10/2021	e	500		Hokkaido
3715	Sycamore	5	25/10/2021	a	500		Hokkaido

3716	Sycamore	6	25/10/2021	e	500		Hokkaido
3717	Hazel	1	25/10/2021	e	500		Hokkaido
3718	Hazel	2	25/10/2021	a	500		Hokkaido
3719	Hazel	3	25/10/2021	a	500		Hokkaido
3720	Hazel	4	25/10/2021	e	500		Hokkaido
3721	Hazel	5	25/10/2021	a	500		Hokkaido
3722	Hazel	6	25/10/2021	e	500		Hokkaido
3952	Hazel	1	29/07/2022	e	500	Run FID only	
3953	Hazel	1	29/07/2022	e	500	Run FID only	
3954	Hazel	1	29/07/2022	e	500	Run FID only	
3955	Hazel	1	29/07/2022	e	500	Run FID only	
3956	Hazel	1	29/07/2022	e	500	Run FID only	
3957	Hazel	1	29/07/2022	e	500	Run FID only	
3958	Hazel	2	29/07/2022	a		sample lost	
3959	Hazel	2	29/07/2022	a		sample lost	
3960	Hazel	2	29/07/2022	a		sample lost	
3961	Hazel	2	29/07/2022	a		sample lost	
3962	Hazel	2	29/07/2022	a		sample lost	
3963	Hazel	3	29/07/2022	a	500	Run FID only	
3964	Hazel	3	29/07/2022	a	500	Run FID only	
3965	Hazel	3	29/07/2022	a	500	Run FID only	
3966	Hazel	3	29/07/2022	a	500	Run FID only	
3967	Hazel	3	29/07/2022	a	500	Run FID only	
3968	Hazel	3	29/07/2022	a	500	Run FID only	
3969	Hazel	3	29/07/2022	a	500	Run FID only	
3970	Hazel	4	29/07/2022	e	500	Run FID only	
3971	Hazel	4	29/07/2022	e	500	Run FID only	

3972	Hazel	4	29/07/2022	e	500	Run FID only	
3973	Hazel	4	29/07/2022	e	500	Run FID only	
3976	Hazel	5	29/07/2022	a	500	Run FID only	
3977	Hazel	5	29/07/2022	a	500	Run FID only	
3978	Hazel	5	29/07/2022	a	500	Run FID only	
3979	Hazel	5	29/07/2022	a	500	Run FID only	
3980	Hazel	5	29/07/2022	a	500	Run FID only	
3981	Hazel	5	29/07/2022	a	500	Run FID only	
3982	Hazel	6	29/07/2022	e	500	Run FID only	
3983	Hazel	6	29/07/2022	e	500	Run FID only	
3984	Hazel	6	29/07/2022	e	500	Run FID only	
3985	Hazel	6	29/07/2022	e	500	Run FID only	
3986	Hazel	6	29/07/2022	e	500	Run FID only	
3987	Hazel	6	29/07/2022	e	500	Run FID only	

Table A2: EA-IRMS analysis metadata

Sample code	Species	Array	Date collected	CO2	Bulk isotope run location	Run notes	Birmingham replicates	Hokkaido replicates
2849	Sycamore	1	08/06/2018	e	Birmingham	fail	1	
2850	Sycamore	2	08/06/2018	a	Birmingham	fail	1	
2851	Sycamore	3	08/06/2018	a	Birmingham	fail	1	
2852	Sycamore	4	08/06/2018	e	Birmingham	fail	2	
2853	Sycamore	5	08/06/2018	a	Birmingham		1	
2854	Sycamore	6	08/06/2018	e	Birmingham		1	
2861	Hazel	1	08/06/2018	e	Birmingham, Hokkaido		1	3

2862	Hazel	2	08/06/2018	a	Birmingham, Hokkaido		1	3
2863	Hazel	3	08/06/2018	a	Birmingham, Hokkaido		1	3
2864	Hazel	4	08/06/2018	e	Hokkaido			3
2865	Hazel	5	08/06/2018	a	Hokkaido			3
2866	Hazel	6	08/06/2018	e	Hokkaido			3
2855	Sycamore	1	03/07/2018	e	Hokkaido			3
2856	Sycamore	2	03/07/2018	a	Hokkaido			3
2857	Sycamore	3	03/07/2018	a	Birmingham, Hokkaido		1	2
2858	Sycamore	4	03/07/2018	e	Birmingham, Hokkaido		1	3
2859	Sycamore	5	03/07/2018	a	Birmingham, Hokkaido		1	3
2860	Sycamore	6	03/07/2018	e	Birmingham, Hokkaido		1	3
2867	Hazel	1	03/07/2018	e	Birmingham		1	
2868	Hazel	2	03/07/2018	a	Birmingham		1	
2869	Hazel	3	03/07/2018	a	Birmingham		1	
2870	Hazel	4	03/07/2018	e	Birmingham		2	
2871	Hazel	5	03/07/2018	a	Birmingham		1	
2872	Hazel	6	03/07/2018	e	Birmingham		1	
2873	Sycamore	1	03/08/2018	e	Birmingham, Hokkaido		3	3
2874	Sycamore	2	03/08/2018	a	Birmingham, Hokkaido		3	3
2875	Sycamore	3	03/08/2018	a	Birmingham, Hokkaido		3	3

2876	Sycamore	4	03/08/2018	e	Birmingham, Hokkaido		3	3
2877	Sycamore	5	03/08/2018	a	Birmingham, Hokkaido		3	3
2878	Sycamore	6	03/08/2018	e	Birmingham, Hokkaido		3	3
2885	Hazel	1	03/08/2018	e	Hokkaido			3
2886	Hazel	2	03/08/2018	a	Hokkaido			3
2887	Hazel	3	03/08/2018	a	Hokkaido			3
2888	Hazel	4	03/08/2018	e	Hokkaido			3
2889	Hazel	5	03/08/2018	a	Hokkaido			3
2890	Hazel	6	03/08/2018	e	Hokkaido			3
2879	Sycamore	1	31/08/2018	e	Hokkaido			3
2880	Sycamore	2	31/08/2018	a	Hokkaido			3
2881	Sycamore	3	31/08/2018	a	Hokkaido			3
2882	Sycamore	4	31/08/2018	e	Hokkaido			3
2883	Sycamore	5	31/08/2018	a	Hokkaido			3
2884	Sycamore	6	31/08/2018	e	Hokkaido			3
2891	Hazel	1	31/08/2018	e	Birmingham, Hokkaido		1	2
2892	Hazel	2	31/08/2018	a	Birmingham, Hokkaido		1	3
2893	Hazel	3	31/08/2018	a	Birmingham, Hokkaido		1	3
2894	Hazel	4	31/08/2018	e	Birmingham, Hokkaido		1	3
2895	Hazel	5	31/08/2018	a	Birmingham, Hokkaido		1	3

2896	Hazel	6	31/08/2018	e	Birmingham, Hokkaido		1	3
2897	Sycamore	1	24/05/2019	e	Birmingham		1	
2898	Sycamore	2	24/05/2019	a	Birmingham		1	
2899	Sycamore	3	24/05/2019	a	Birmingham		1	
2900	Sycamore	4	24/05/2019	e	Birmingham		1	
2901	Sycamore	5	24/05/2019	a	Birmingham		1	
2902	Sycamore	6	24/05/2019	e	Birmingham		1	
2903	Hazel	1	24/05/2019	e	Birmingham		1	
2904	Hazel	2	24/05/2019	a	Birmingham		1	
2905	Hazel	3	24/05/2019	a	Birmingham		1	
2906	Hazel	4	24/05/2019	e	Birmingham		1	
2907	Hazel	5	24/05/2019	a		Not run - not enough material		
2908	Hazel	6	24/05/2019	e		Not run - not enough material		
2981	Sycamore	1	04/07/2019	e	Birmingham, Hokkaido		2	3
2982	Sycamore	2	04/07/2019	a	Birmingham, Hokkaido		1	3
2983	Sycamore	3	04/07/2019	a	Birmingham, Hokkaido		1	3
2984	Sycamore	4	04/07/2019	e	Birmingham, Hokkaido		1	3

2985	Sycamore	5	04/07/2019	a	Birmingham, Hokkaido		1	2
2986	Sycamore	6	04/07/2019	e	Birmingham, Hokkaido		1	3
2987	Hazel	1	04/07/2019	e	Birmingham		1	
2988	Hazel	2	04/07/2019	a	Birmingham		1	
2989	Hazel	3	04/07/2019	a	Birmingham		1	
2990	Hazel	4	04/07/2019	e	Birmingham		1	
2991	Hazel	5	04/07/2019	a	Birmingham		1	
2992	Hazel	6	04/07/2019	e	Birmingham		1	
2969	Sycamore	1	29/07/2019	e	Birmingham		2	
2970	Sycamore	2	29/07/2019	a	Birmingham		1	
2971	Sycamore	3	29/07/2019	a	Birmingham		1	
2972	Sycamore	4	29/07/2019	e	Birmingham		1	
2973	Sycamore	5	29/07/2019	a	Birmingham		2	
2974	Sycamore	6	29/07/2019	e	Birmingham		1	
2975	Hazel	1	29/07/2019	e	Birmingham		1	
2976	Hazel	2	29/07/2019	a	Birmingham		1	
2977	Hazel	3	29/07/2019	a	Birmingham		1	
2978	Hazel	4	29/07/2019	e	Birmingham		1	
2979	Hazel	5	29/07/2019	a	Birmingham		1	
2980	Hazel	6	29/07/2019	e	Birmingham		1	
2957	Sycamore	1	23/08/2019	e	Birmingham		1	
2958	Sycamore	2	23/08/2019	a	Birmingham		1	
2959	Sycamore	3	23/08/2019	a	Birmingham		1	
2960	Sycamore	4	23/08/2019	e	Birmingham		1	
2961	Sycamore	5	23/08/2019	a	Birmingham		1	

2962	Sycamore	6	23/08/2019	e	Birmingham		1	
2963	Hazel	1	23/08/2019	e	Birmingham		1	
2964	Hazel	2	23/08/2019	a	Birmingham		1	
2965	Hazel	3	23/08/2019	a	Birmingham		1	
2966	Hazel	4	23/08/2019	e	Birmingham		1	
2967	Hazel	5	23/08/2019	a	Birmingham		1	
2968	Hazel	6	23/08/2019	e	Birmingham		1	
3699	Sycamore	1	27/09/2019	e	Birmingham		2	
3700	Sycamore	2	27/09/2019	a	Birmingham		2	
3701	Sycamore	3	27/09/2019	a	Birmingham		2	
3702	Sycamore	4	27/09/2019	e	Birmingham		2	
3703	Sycamore	5	27/09/2019	a	Birmingham		1	
3704	Sycamore	6	27/09/2019	e	Birmingham		2	
3705	Hazel	1	27/09/2019	e	Birmingham		2	
3706	Hazel	2	27/09/2019	a	Birmingham		2	
3707	Hazel	3	27/09/2019	a	Birmingham		1	
3708	Hazel	4	27/09/2019	e	Birmingham		2	
3709	Hazel	5	27/09/2019	a	Birmingham		2	
3710	Hazel	6	27/09/2019	e	Birmingham		2	
3527	Hazel	1	20/10/2019	e		Not run		
3528	Hazel	2	20/10/2019	a		Not run		
3529	Hazel	3	20/10/2019	a		Not run		
3530	Hazel	4	20/10/2019	e		Not run		
3531	Hazel	5	20/10/2019	a		Not run		
3532	Hazel	6	20/10/2019	e		Not run		
2993	Sycamore	1	30/04/2020	e	Birmingham		1	
2994	Sycamore	2	30/04/2020	a	Birmingham		1	

2995	Sycamore	3	30/04/2020	a	Birmingham		1	
2996	Sycamore	4	30/04/2020	e	Birmingham		1	
2997	Sycamore	5	30/04/2020	a	Birmingham		1	
2998	Sycamore	6	30/04/2020	e	Birmingham		1	
2999	Hazel	1	30/04/2020	e	Birmingham		1	
3000	Hazel	2	30/04/2020	a	Birmingham		1	
3001	Hazel	3	30/04/2020	a	Birmingham		1	
3002	Hazel	4	30/04/2020	e	Birmingham		1	
3003	Hazel	5	30/04/2020	a	Birmingham		1	
3004	Hazel	6	30/04/2020	e	Birmingham		1	
2921	Sycamore	1	28/05/2020	e	Hokkaido			3
2922	Sycamore	2	28/05/2020	a	Hokkaido			3
2923	Sycamore	3	28/05/2020	a	Hokkaido			3
2924	Sycamore	4	28/05/2020	e	Hokkaido			2
2925	Sycamore	5	28/05/2020	a	Hokkaido			3
2926	Sycamore	6	28/05/2020	e	Hokkaido			3
2927	Hazel	1	28/05/2020	e	Hokkaido			3
2928	Hazel	2	28/05/2020	a	Hokkaido			3
2929	Hazel	3	28/05/2020	a	Hokkaido			3
2930	Hazel	4	28/05/2020	e	Hokkaido			3
2931	Hazel	5	28/05/2020	a	Hokkaido			3
2932	Hazel	6	28/05/2020	e	Hokkaido			3
2945	Sycamore	1	03/07/2020	e	Birmingham		1	
2946	Sycamore	2	03/07/2020	a	Birmingham		1	
2947	Sycamore	3	03/07/2020	a	Birmingham		1	
2948	Sycamore	4	03/07/2020	e	Birmingham		1	
2949	Sycamore	5	03/07/2020	a	Birmingham		1	

2950	Sycamore	6	03/07/2020	e	Birmingham		1	
2951	Hazel	1	03/07/2020	e	Hokkaido			3
2952	Hazel	2	03/07/2020	a	Hokkaido			3
2953	Hazel	3	03/07/2020	a	Hokkaido			3
2954	Hazel	4	03/07/2020	e	Hokkaido			3
2955	Hazel	5	03/07/2020	a	Hokkaido			3
2956	Hazel	6	03/07/2020	e	Hokkaido			3
2933	Sycamore	1	03/08/2020	e	Birmingham		1	
2934	Sycamore	2	03/08/2020	a	Birmingham		1	
2935	Sycamore	3	03/08/2020	a	Birmingham		1	
2936	Sycamore	4	03/08/2020	e	Birmingham		1	
2937	Sycamore	5	03/08/2020	a	Birmingham		1	
2938	Sycamore	6	03/08/2020	e	Birmingham		1	
2939	Hazel	1	03/08/2020	e	Birmingham		1	
2940	Hazel	2	03/08/2020	a	Hokkaido			3
2941	Hazel	3	03/08/2020	a	Hokkaido			3
2942	Hazel	4	03/08/2020	e	Hokkaido			3
2943	Hazel	5	03/08/2020	a	Hokkaido			3
2944	Hazel	6	03/08/2020	e	Hokkaido			3
3025	Sycamore	1	28/08/2020	e	Birmingham		1	
3026	Sycamore	2	28/08/2020	a	Birmingham		1	
3027	Sycamore	3	28/08/2020	a	Birmingham		1	
3028	Sycamore	4	28/08/2020	e	Birmingham		1	
3029	Sycamore	5	28/08/2020	a	Birmingham		1	
3030	Sycamore	6	28/08/2020	e	Birmingham		1	
3031	Hazel	1	28/08/2020	e	Hokkaido			3
3032	Hazel	2	28/08/2020	a	Hokkaido			3

3033	Hazel	3	28/08/2020	a	Birmingham		1	
3034	Hazel	4	28/08/2020	e	Birmingham		1	
3035	Hazel	5	28/08/2020	a	Birmingham		1	
3036	Hazel	6	28/08/2020	e	Birmingham		1	
3141	Sycamore	1	23/09/2020	e	Birmingham		1	
3142	Sycamore	2	23/09/2020	a	Birmingham		1	
3143	Sycamore	3	23/09/2020	a	Birmingham		2	
3144	Sycamore	4	23/09/2020	e	Birmingham		2	
3145	Sycamore	5	23/09/2020	a	Birmingham		1	
3146	Sycamore	6	23/09/2020	e	Birmingham		1	
3147	Hazel	1	23/09/2020	e	Birmingham		1	
3148	Hazel	2	23/09/2020	a	Birmingham		1	
3149	Hazel	3	23/09/2020	a	Birmingham		1	
3150	Hazel	4	23/09/2020	e	Birmingham		1	
3151	Hazel	5	23/09/2020	a	Birmingham		1	
3152	Hazel	6	23/09/2020	e	Birmingham		1	
3557	Sycamore	1	20/10/2020	e	Birmingham		1	
3558	Sycamore	2	20/10/2020	a	Birmingham		1	
3559	Sycamore	3	20/10/2020	a	Birmingham		1	
3560	Sycamore	4	20/10/2020	e	Birmingham		1	
3561	Sycamore	5	20/10/2020	a	Birmingham		1	
3563	Sycamore	6	20/10/2020	e	Birmingham		1	
3611	Hazel	1	20/10/2020	e		Not run		
3612	Hazel	2	20/10/2020	a		Not run		
3613	Hazel	3	20/10/2020	a		Not run		
3614	Hazel	4	20/10/2020	e		Not run		
3615	Hazel	5	20/10/2020	a		Not run		

3318	Sycamore	1	25/05/2021	e	Birmingham		3	
3319	Sycamore	2	25/05/2021	a	Birmingham		3	
3320	Sycamore	3	25/05/2021	a	Birmingham		1	
3321	Sycamore	4	25/05/2021	e	Birmingham		1	
3322	Sycamore	5	25/05/2021	a	Birmingham		1	
3323	Sycamore	6	25/05/2021	e	Birmingham		1	
3324	Hazel	1	25/05/2021	e	Birmingham		1	
3325	Hazel	2	25/05/2021	a	Birmingham		1	
3326	Hazel	3	25/05/2021	a	Birmingham		1	
3327	Hazel	4	25/05/2021	e	Birmingham		1	
3328	Hazel	5	25/05/2021	a	Birmingham		1	
3329	Hazel	6	25/05/2021	e	Birmingham		1	
3384	Sycamore	1	09/06/2021	e	Birmingham		1	
3385	Sycamore	2	09/06/2021	a			1	
3386	Sycamore	3	09/06/2021	a	Birmingham		1	
3387	Sycamore	4	09/06/2021	e	Birmingham		1	
3388	Sycamore	5	09/06/2021	a	Birmingham		1	
3389	Sycamore	6	09/06/2021	e	Birmingham		1	
3390	Hazel	1	09/06/2021	e	Birmingham		1	
3391	Hazel	2	09/06/2021	a	Birmingham		1	
3392	Hazel	3	09/06/2021	a	Birmingham		1	
3393	Hazel	4	09/06/2021	e	Birmingham		1	
3394	Hazel	5	09/06/2021	a	Birmingham		1	
3395	Hazel	6	09/06/2021	e	Birmingham		1	

3515	Sycamore	1	15/07/2021	e	Birmingham		4	
3516	Sycamore	2	15/07/2021	a	Birmingham		4	
3517	Sycamore	3	15/07/2021	a	Birmingham		4	
3518	Sycamore	4	15/07/2021	e	Birmingham		4	
3519	Sycamore	5	15/07/2021	a	Birmingham		4	
3520	Sycamore	6	15/07/2021	e	Birmingham		1	
3521	Hazel	1	15/07/2021	e	Birmingham		1	
3522	Hazel	2	15/07/2021	a	Birmingham		1	
3523	Hazel	3	15/07/2021	a	Birmingham		1	
3524	Hazel	4	15/07/2021	e	Birmingham		1	
3525	Hazel	5	15/07/2021	a	Birmingham		1	
3526	Hazel	6	15/07/2021	e	Birmingham		1	
3533	Sycamore	1	23/08/2021	e	Birmingham		3	
3534	Sycamore	2	23/08/2021	a	Birmingham		3	
3535	Sycamore	3	23/08/2021	a	Birmingham		1	
3536	Sycamore	4	23/08/2021	e	Birmingham		3	
3537	Sycamore	5	23/08/2021	a	Birmingham		3	
3538	Sycamore	6	23/08/2021	e	Birmingham		1	
3539	Hazel	1	23/08/2021	e	Birmingham		2	
3540	Hazel	2	23/08/2021	a	Birmingham		2	
3541	Hazel	3	23/08/2021	a	Birmingham		2	
3542	Hazel	4	23/08/2021	e	Birmingham		1	
3543	Hazel	5	23/08/2021	a	Birmingham		1	
3544	Hazel	6	23/08/2021	e	Birmingham		1	
3545	Sycamore	1	27/09/2021	e	Birmingham		1	
3546	Sycamore	2	27/09/2021	a	Birmingham		1	
3547	Sycamore	3	27/09/2021	a	Birmingham		1	

3548	Sycamore	4	27/09/2021	e	Birmingham		1	
3549	Sycamore	5	27/09/2021	a	Birmingham		1	
3550	Sycamore	6	27/09/2021	e	Birmingham		1	
3551	Hazel	1	27/09/2021	e	Birmingham		1	
3552	Hazel	2	27/09/2021	a	Birmingham		1	
3553	Hazel	3	27/09/2021	a	Birmingham		1	
3554	Hazel	4	27/09/2021	e	Birmingham		1	
3555	Hazel	5	27/09/2021	a	Birmingham		1	
3556	Hazel	6	27/09/2021	e	Birmingham		1	
3711	Sycamore	1	25/10/2021	e		Not run		
3712	Sycamore	2	25/10/2021	a		Not run		
3713	Sycamore	3	25/10/2021	a		Not run		
3714	Sycamore	4	25/10/2021	e		Not run		
3715	Sycamore	5	25/10/2021	a		Not run		
3716	Sycamore	6	25/10/2021	e		Not run		
3717	Hazel	1	25/10/2021	e	Birmingham		1	
3718	Hazel	2	25/10/2021	a	Birmingham		1	
3719	Hazel	3	25/10/2021	a	Birmingham		1	
3720	Hazel	4	25/10/2021	e	Birmingham		1	
3721	Hazel	5	25/10/2021	a	Birmingham		1	
3722	Hazel	6	25/10/2021	e	Birmingham		1	

Table A3: Summary statistics for *n*-alkane chemistry and carbon isotopes

Species	Sample date	ACL		CPI		Dispersion		Concentration		ɛlipid WMA	
		aCO$_2$	e CO$_2$	a CO$_2$	e CO$_2$	a CO$_2$	e CO$_2$	a CO$_2$	e CO$_2$	a CO$_2$	e CO$_2$
Hazel	08/06/2018	28.02	27.66	7.47	7.73	7.10	7.75	66.98	69.11	-5.66	-6.40

Hazel	03/07/2018	28.65	28.93	9.22	9.00	4.80	4.94	126.07	159.40	-5.77	-5.25
Hazel	03/08/2018	28.56	28.71	8.64	9.26	4.44	4.53	450.82	160.01	-6.99	-4.30
Hazel	31/08/2018	28.71	28.46	6.31	6.63	3.39	3.95	109.71	232.00	-4.55	-0.69
Hazel	24/05/2019	27.98	28.36	8.52	8.70	5.93	6.21	115.98	75.61	-5.56	-6.82
Hazel	04/07/2019	28.11	27.80	8.83	9.20	5.86	6.47	61.35	48.73	-5.24	-2.99
Hazel	29/07/2019	28.44	28.75	7.51	8.08	4.45	3.42	88.20	175.25	-5.52	-3.73
Hazel	23/08/2019	28.72	28.61	6.46	6.55	3.96	5.32	80.05	34.77	-4.89	-0.41
Hazel	27/09/2019	28.62	28.06	4.75	3.86	4.23	6.14	104.97	45.11		
Hazel	20/10/2019	28.78	28.87	7.77	8.14	3.58	4.07	54.25	70.05		
Hazel	30/04/2020	27.76	26.90	9.67	7.50	6.52	6.32	92.70	75.41	-6.89	-6.16
Hazel	28/05/2020	28.64	28.09	10.48	9.47	4.51	6.16	133.91	231.70	-6.10	-4.44
Hazel	03/07/2020	28.75	28.19	8.39	9.20	4.79	6.20	208.30	96.38	-6.57	-4.13
Hazel	03/08/2020	28.85	28.34	8.25	8.41	4.18	4.40	184.68	66.15	-7.06	-6.02
Hazel	28/08/2020	28.84	28.51	8.92	8.54	3.92	4.53	128.60	53.37	-5.22	-4.22
Hazel	23/09/2020	28.22	27.89	8.60	6.99	4.91	5.04	65.29	60.65	-5.93	-2.48
Hazel	20/10/2020	28.75	28.79	7.17	5.64	3.52	3.24	102.45	106.62		
Hazel	25/05/2021	26.45	26.20	6.28	4.86	7.23	6.99	101.79	76.33	-6.22	-6.78
Hazel	09/06/2021	28.26	28.06	8.05	10.85	6.12	5.95	141.20	95.24	-3.99	0.58
Hazel	15/07/2021	28.71	28.32	9.33	9.36	4.55	5.71	111.12	68.24	-5.50	-4.04
Hazel	23/08/2021	28.96	28.63	8.47	7.40	3.44	4.05	132.39	94.58	-5.25	-2.51
Hazel	27/09/2021	28.63	27.80	6.46	5.43	4.41	5.33	95.40	36.00		
Hazel	25/10/2021	27.66	26.84	1.49	1.07	6.45	7.43	116.21	70.82		
Sycamore	08/06/2018	29.07	29.14	19.24	19.52	4.61	4.18	190.14	272.65	-4.66	-7.01
Sycamore	03/07/2018	28.89	29.03	15.24	14.80	3.89	4.05	203.98	242.61	-5.54	-4.05
Sycamore	03/08/2018	28.76	29.04	12.97	12.15	4.63	4.20	370.62	580.30	-4.98	-4.72
Sycamore	31/08/2018	29.57	29.00	10.04	8.96	3.21	3.03	318.62	831.52	-6.44	-5.20
Sycamore	24/05/2019	28.90	29.03	18.10	11.66	4.98	4.55	214.42	186.08	-4.32	-3.45

Sycamore	04/07/2019	29.02	28.90	15.54	13.58	4.60	5.08	287.91	347.77	-3.55	-1.91
Sycamore	29/07/2019	28.86	28.68	12.77	12.36	4.41	4.31	231.83	284.14	-3.49	-3.35
Sycamore	23/08/2019	29.14	28.83	13.55	12.17	4.13	3.98	278.71	259.32	-3.10	-3.34
Sycamore	27/09/2019	28.67	28.59	5.28	6.80	4.17	3.93	268.86	222.16		
Sycamore	30/04/2020	29.04	29.04	14.80	10.38	5.05	5.08	424.10	352.67	-4.03	-4.59
Sycamore	28/05/2020	28.99	29.22	18.09	16.63	4.57	4.22	402.20	331.75	-4.64	-4.60
Sycamore	03/07/2020	29.07	29.01	14.97	14.72	3.99	4.05	425.63	402.06	-4.56	-3.76
Sycamore	03/08/2020	29.08	29.19	16.30	15.08	4.19	4.07	236.49	242.63		-4.74
Sycamore	28/08/2020	29.07	29.08	13.94	13.55	4.05	3.80	263.21	242.37	-3.70	-2.64
Sycamore	23/09/2020	29.08	29.07	11.71	11.25	3.91	3.55	278.80	293.36	-2.31	-2.65
Sycamore	20/10/2020	28.55	28.83	7.94	9.26	7.97	6.83	331.75	412.43		
Sycamore	25/05/2021	28.72	28.86	15.27	20.86	5.56	5.07	452.71	286.80	-5.54	-4.91
Sycamore	09/06/2021	28.81	28.68	16.26	17.62	4.83	5.20	372.10	458.59	-4.29	-3.37
Sycamore	15/07/2021	28.67	28.61	15.21	15.02	4.76	4.85	206.06	192.54	-3.51	-2.83
Sycamore	23/08/2021	28.93	29.02	13.90	13.24	4.26	4.05	283.12	279.17	-4.02	-3.12
Sycamore	27/09/2021	28.80	28.94	9.12	8.44	4.20	3.80	282.67	390.56		
Sycamore	25/10/2021	28.48	28.53	2.89	3.32	4.18	4.13	241.15	320.43		
Hazel	29/07/2022	30.58	29.96	7.99	7.34	5.65	4.16	113.73	55.39		

Table A4: Ambient bulk oak $\delta^{13}C$ (July 2020). Samples were not homogenised, and were processed as described in chapter 2. Three replicates were taken from the canopy of 2 trees (*Quercus robur*) in arrays 2 and 3.

Array	$\delta^{13}C$		
2	-29.769	-29.7865	-29.025
2	-29.6244	-30.2897	-30.4966
3	-30.2349	-30.0173	-29.8247
3	-28.358	-28.3831	-28.614

Table A5: GDGT -based temperature reconstructions for core 16/28-sb01

Sample code	mid depth (m)	Age	GDGT-0	GDGT-1	GDG-T2	GDGT-3	Crenarchaeol	Cren'	TEX_{86}	Bayspar 5th (°C)	SST Bayspar (°C)	Bayspar 95th (°C)
903	43.51	44.97										
904	53.5	45.33	125431	28039	44155	14736	375145	57459	0.81	27.10	31.97	37.17
905	60.6	45.58	22608	7631	5127	906	47109	6713	0.63	17.27	22.60	27.36
906	68.5	45.86	20872	1541	2995	0	15897	690	0.71	21.78	26.82	31.63
909	80.01	46.26	248866	54073	62686	21424	385843	39785	0.70	21.21	26.26	31.06
910	81	46.15	1022512	146744	199700	37365	476757	40602	0.65	18.92	24.05	28.80
913	82.41	46.33	158179	0	14397	0	84462	7743				
914	82.91	46.37	60709	14674	19221	3855	141075	11092	0.70	21.43	26.44	31.20
915	83.41	49.23	22937657	4049312	4790456	1106554	16418403	2163531	0.67	19.60	24.63	29.50
917	88.4	49.27	2843951	1099078	1317535	503674	6670182	958228	0.72	22.34	27.35	32.17
919	89.26	49.30	21859990	4558343	2651799	1413517	22465236	3257493	0.62	16.87	22.08	26.89
921	89.71	49.32	16573207	3455770	4773396	1086928	18543156	2611737	0.71	21.89	26.99	31.86
922	90.21	49.34	456763	99551	149969	19808	948899	112700	0.74	23.57	28.52	33.59
923	90.81	49.37	3739000	569830	656683	204381	3669778	573105	0.72	22.29	27.29	32.24
924	91.31	49.39	3033920	745225	986933	210573	5207248	662385	0.71	22.24	27.21	32.08
925	91.81	49.41	3739428	875835	1100059	269114	5576436	742305	0.71	21.87	26.81	31.74
926	93.71	49.50	14908710	3910708	5087005	887173	21576938	2894438	0.69	21.13	26.15	31.03
928	94.56	49.54	2079844	376501	692380	207929	2366008	347398	0.77	25.15	30.09	35.00
929	94.81	49.55	11302669	2260431	3182555	829853	11962470	2235578	0.73	23.30	28.27	33.14
931	95.71	49.58	798462	173726	173726	33555	1336641	157333	0.68	20.21	25.29	30.12
932	96.81	49.62	16611278	3803688	5280167	1301177	20321597	3671982	0.73	23.08	28.03	33.01
933	97.41	49.64	4817210	1232508	1863061	421777	7243093	1257343	0.74	23.70	28.70	33.67
934	97.81	49.66	1617070	443827	624928	125501	2848561	359556	0.71	22.24	27.22	32.11

935	105.31	49.93	19425327	4657427	6476108	1872074	24598667	3078968	0.71	22.05	27.03	31.87
936	105.71	49.94	817498	188791	254751	68671	1415475	182273	0.73	22.97	27.90	32.90
937	106.01	49.95	9101119	1930802	2902599	744149	12384106	1586254	0.73	23.16	28.10	33.03
938	106.52	49.97	4823533	1380744	1746053	533112	9671175	1257406	0.72	22.47	27.50	32.38
939	107.46	50.01	15882169	4667070	7249946	1694774	21098425	3991984	0.73	23.35	28.31	33.20
940	107.885	50.04	694029	175271	256786	67661	1189039	209605	0.75	24.23	29.23	34.21
941	108.33	50.06	17688512	4459950	6503209	1878621	22604611	4069822	0.74	23.43	28.38	33.33
942	108.71	50.09	24572120	5756934	8316402	2038640	21343098	4088480	0.72	22.30	27.29	32.10
943	109.21	50.12	10155385	792869	1256908	348673	5316940	737824	0.75	24.01	28.91	34.00
944	109.61	50.15	1968488	371996	449373	106287	1877375	347660	0.71	21.92	26.92	31.70
945	110.21	50.19	15630795	4011271	5035242	1359751	15149956	2933971	0.70	21.44	26.42	31.19
946	110.69	50.21	7909076	2152907	3095768	719606	10565515	1249323	0.70	21.54	26.60	31.33
947	111.11	50.23	15383033	3875437	4258124	1428965	18869000	3085347	0.69	21.12	26.14	31.00
948	111.56	50.24	12520152	3111652	3150780	977944	14087808	1815212	0.66	18.98	24.19	28.93
950	112.365	50.27	20245217	4777050	5957461	1438803	24084766	3204079	0.69	20.88	25.92	30.67
951	112.81	50.29	18771561	4818006	6201041	1547734	19144837	2813378	0.69	20.74	25.79	30.53
952	113.31	50.30	11868149	2923320	3492519	1138984	16497717	2587712	0.71	22.18	27.08	31.94
953	113.98	50.33	1538147	380736	418886	118889	2043229	240583	0.67	19.88	24.99	29.82
954	116.81	50.42	10783421	2459989	3541085	916296	13924685	2384858	0.74	23.33	28.33	33.20
955	118.11	50.46	10535110	2317903	2620472	618799	12305127	1446128	0.67	19.84	24.95	29.64
956	118.61	50.47	715888	151060	208205	43758	1247349	141166	0.72	22.67	27.64	32.46
957	119.01	50.48	3801418	978041	1281571	348013	7604524	926655	0.72	22.80	27.68	32.60
958	119.39	50.49	2069380	487230	604853	156755	3308595	429088	0.71	21.96	26.95	31.87
959	119.81	50.50	7729201	1322544	2198100	483141	7788093	781140	0.72	22.66	27.69	32.58
960	120.31	50.51	6341603	1485424	1843194	557388	8899621	984693	0.70	21.24	26.25	31.11
961	122.31	50.56	11383333	2902207	3900600	1030338	13509402	2370713	0.72	22.29	27.26	32.15
962	122.71	50.57	1059919	300472	360141	92237	1709380	271864	0.71	21.86	26.80	31.68

963	123.19	50.58	16300773	3471054	5084944	1590023	16940578	3454665	0.74	23.85	28.84	33.82
964	123.61	50.59	11686412	2450452	3284476	1047506	14953310	1950430	0.72	22.49	27.49	32.38
965	124.01	50.59	15322813	4462016	5917508	1742766	23640536	3634301	0.72	22.45	27.37	32.14
966	124.41	50.60	641218	150797	231381	70759	944913	159494	0.75	24.39	29.30	34.20
967	124.82	50.61	24205891	6122766	7245845	2167909	34058564	4440437	0.69	21.06	26.15	30.96
968	125.72	50.63	14610820	3609253	5344581	1561630	18498295	3662238	0.75	23.94	28.81	33.78
969	126.11	50.64	20318040	6170589	8569523	2353948	32967078	5696516	0.73	23.07	27.98	32.88
970	126.61	50.65	17383665	4356250	5550151	1704385	29254157	5282239	0.74	23.71	28.67	33.62
971	126.99	50.66	8530227	2455426	3830085	905037	13640224	2366586	0.74	23.68	28.68	33.73
972	127.61	50.68	15425126	4222930	5251087	1436096	22619754	4364801	0.72	22.72	27.72	32.59
973	128.01	50.69	7716645	3707543	5724869	1614907	21391632	4154397	0.76	24.41	29.39	34.40
974	128.41	50.70	12078987	3192109	5173421	1444956	18046667	2789841	0.75	23.95	28.84	33.84
975	128.91	50.71	6078809	1657812	2097620	597245	8966162	1723415	0.73	22.86	27.89	32.84
976	129.31	50.72	2814017	815565	1174517	361335	5550044	1032102	0.76	24.71	29.53	34.63
1682	129.84	50.73	3242596	791115	1309029	399578	6012519	1009086	0.77	25.48	30.34	35.44
977	129.86	50.73	21837741	5543939	7027679	2265913	24213190	4657478	0.72	22.31	27.30	32.22
1683	129.89	50.73	5780830	1386624	2222745	498276	9016828	1562326	0.76	24.42	29.36	34.33
978	130.21	50.73	16881534	5496510	7306225	2081944	24843501	3981362	0.71	21.92	26.90	31.73
1689	135.25	50.79	1061099	354498	407959	139962	1969552	308860	0.71	21.84	26.90	31.71
979	135.86	50.80	16647500	4518360	5398338	1594415	20117609	3000171	0.69	20.83	25.89	30.74
980	136.36	50.81	3479491	909444	1298745	353035	6815473	924010	0.74	23.56	28.49	33.41
981	136.86	50.81	11827	1617	3588	634	29072	4140	0.84	28.70	33.65	38.99
982	137.21	50.82	3120502	778646	1242884	377439	5147141	751921	0.75	24.20	29.19	34.18
1700	137.24	50.82	4108653	1030993	1462492	386164	7213699	1197569	0.75	24.07	28.93	33.88
1701	137.31	50.82	1340081	298030	356857	100107	1612721	242952	0.70	21.52	26.55	31.36
983	137.71	50.82	727654	164532	248237	68266	1491287	188595	0.75	24.52	29.31	34.30
984	144.21	52.66	793875	81430	113557	24847	478203	56789	0.71	21.76	26.76	31.57

1708	144.74	52.68	3717670	1165946	1931235	613585	7118590	1395123	0.77	25.26	30.20	35.34

Table A6: Alkenone-based temperature reconstructions from core 16/28-sb01

Sample code	mid depth (m)	Age (Ma)	373 alkenone	372 alkenone	Bayspline 5th (°C)	SST Bayspline (°C)	Bayspline 95th (°C)
903	43.51	44.97	0.34	0.66	15.24	17.96	20.70
904	53.5	45.33	0.37	0.63	14.31	17.01	19.76
905	60.6	45.58	0.37	0.63	14.22	17.00	19.77
906	68.5	45.86	0.32	0.68	15.80	18.52	21.27
909	80.01	46.26	0.34	0.66	15.24	17.99	20.72
910	81	46.15	0.53	0.47	9.60	12.32	15.05
915	83.41	49.23	0.25	0.75	17.75	20.53	23.29
923	90.81	49.37	0.05	0.95	24.33	28.28	34.33
924	91.31	49.39	0.03	0.97	25.11	29.26	35.56
925	91.81	49.41	0.06	0.94	23.80	27.44	33.45
926	93.71	49.50	0.01	0.99	25.62	30.02	36.41
927	94	49.52	0.02	0.98	25.31	29.64	35.93
928	94.56	49.54	0.02	0.98	25.26	29.56	35.94
929	94.81	49.55	0.02	0.98	25.10	29.32	35.54
932	96.81	49.62	0.02	0.98	25.34	29.61	35.93
934	97.81	49.66	0.02	0.98	25.37	29.68	36.10
935	105.31	49.93	0.01	0.99	25.59	29.98	36.44
937	106.01	49.95	0.41	0.59	13.25	15.98	18.73
938	106.52	49.97	0.03	0.97	24.97	29.12	35.28
939	107.46	50.01	0.03	0.97	25.06	29.21	35.41
941	108.33	50.06	0.28	0.72	17.04	19.77	22.58

942	108.71	50.09	0.07	0.93	23.57	27.08	32.76
943	109.21	50.12	0.02	0.98	25.21	29.48	35.82
944	109.61	50.15	0.02	0.98	25.35	29.65	36.06
945	110.21	50.19	0.02	0.98	25.24	29.47	35.82
946	110.69	50.21	0.03	0.97	24.81	28.90	35.19
947	111.11	50.23	0.02	0.98	25.37	29.67	36.01
948	111.56	50.24	0.02	0.98	25.18	29.43	35.75
949	111.91	50.26	0.01	0.99	25.45	29.79	36.22
950	112.365	50.27	0.03	0.97	25.05	29.19	35.52
951	112.81	50.29	0.06	0.94	23.96	27.62	33.55
952	113.31	50.30	0.28	0.72	16.95	19.76	22.61
953	113.98	50.33	0.04	0.96	24.68	28.71	34.87
955	118.11	50.46	0.04	0.96	24.62	28.59	34.69
957	119.01	50.48	0.02	0.98	25.42	29.78	36.08
958	119.39	50.49	0.09	0.91	23.01	26.32	31.76
959	119.81	50.50	0.01	0.99	25.53	29.93	36.30
960	120.31	50.51	0.04	0.96	24.54	28.50	34.66
961	122.31	50.56	0.04	0.96	24.43	28.32	34.40
962	122.71	50.57	0.20	0.80	19.44	22.25	25.34
963	123.19	50.58	0.02	0.98	25.25	29.50	35.83
964	123.61	50.59	0.06	0.94	23.79	27.40	33.21
967	124.82	50.61	0.03	0.97	25.09	29.28	35.53
969	126.11	50.64	0.06	0.94	23.85	27.51	33.48
972	127.61	50.68	0.13	0.87	21.77	24.77	29.33
973	128.01	50.69	0.07	0.93	23.42	26.89	32.66
975	128.91	50.71	0.05	0.95	24.39	28.26	34.38
979	135.86	50.80	0.02	0.98	25.17	29.36	35.65

980	136.36	50.81	0.01	0.99	25.51	29.91	36.27
982	137.21	50.82	0.03	0.97	24.90	29.06	35.28
983	137.71	50.82	0.08	0.92	23.29	26.66	32.33

Table A7: Details of parameters used for CO_2 reconstruction in core 16/28-sb01.

Sample	mid depth	age	Alkenone $\delta^{13}C$	Calcite $\delta^{13}C$*	UK'37 temperature (°C)	TEX temperature (°C)	Lith size*	εp
208	41.01	44.64	-33.17	**2.32600**	18.40151	26.68969	3.80	21.75156
214	52.51	45.95342	-33.88	**2.32600**	21.44807	25.83316	3.66	23.55724
217	87.91	49.24891	-34.06	**3.58882**	24.62021	22.08171	3.89	24.97998
919	89.26	49.30374	-32.90	**3.58882**	29.46262	28.09701	3.89	23.60177
213	96.31	49.6	-36.48	**3.58882**	29.61044	28.03117	**4.11**	27.40058
932	96.81	49.62048	-32.07	**3.58882**	29.98293	27.02657	4.33	22.79478
935	105.31	49.92894	-32.49	**3.58882**	29.12152	27.50089	**5.21**	23.56991
938	106.52	49.97285	-29.88	**3.58882**	29.16754	27.90807	6.09	20.5065
215	107.01	49.99064	-33.96	**3.58882**	29.47508	28.90962	**5.92**	24.89845
943	109.21	50.12057	-33.12	**3.58882**	29.65411	26.91678	5.75	24.03496
944	109.61	50.14639	-30.22	**3.58882**	29.4703	26.41944	6.39	20.77796
945	110.21	50.18513	-33.82	**3.58882**	29.79452	24.94877	6.69	24.84359
949	111.91	50.25531	-31.96	**3.58882**	28.60664	24.94582	6.25	22.95166
218	117.21	50.43807	-33.33	**3.58882**	28.58655	24.94598	**5.59**	23.99197
955	118.11	50.46047	-32.11	**3.58882**	26.32123	26.94646	4.94	23.10157
958	119.39	50.48963	-30.04	**3.58882**	29.92716	27.6857	**4.67**	20.67861
959	119.81	50.4992	-33.93	**3.58882**	28.44937	26.53937	4.41	25.22617
212	120.89	50.52381	-33.76	**3.58882**	22.24512	26.80081	4.17	24.82764
962	122.71	50.56527	-32.66	**3.58882**	29.49526	28.84105	**4.10**	23.39215
963	123.19	50.57621	-32.44	**3.58882**	29.27917	26.15383	**4.10**	23.21584

967	124.82	50.61335	-31.28	**3.58882**	28.73627	27.32203	4.03	22.14317
216	125.21	50.62223	-33.48	**3.58882**	24.76719	27.71945	4.17	24.39354
972	127.61	50.67691	-32.88	**3.58882**	26.89406	29.38885	3.81	23.51884
973	128.01	50.68602	-32.25	**3.58882**	28.25831	27.8863	4.09	22.91904
975	128.91	50.70653	-32.18	**3.58882**	29.28964	26.70234	3.80	22.7886
209	135.36	50.79537	-33.25	**3.58882**	29.35533	25.89058	4.62	24.09263
979	135.86	50.80132	-32.34	**3.58882**	29.9126	28.48686	4.44	23.33833
980	136.26	50.80564	-31.78	**3.58882**	29.05833	29.19292	4.33	22.46326
982	137.21	50.81532	-32.96	**3.58882**	26.66477	29.31054	**4.49**	23.84745
983	137.71	50.82041	-31.45	**3.58882**			4.66	22.02887

Table A8: Monte Carlo CO_2 reconstruction for core 16/28-sb01

Sample	mid depth (m)	Age (Ma)	Temperature	εf=25 PO4=0.4		εf=25 PO4=0.8		εf=25 PO4=0.4		εf=25 PO4=0.4	
				Mean	Standard deviation	Mean	Standard deviation	Mean	Standard deviation	Mean	Standard deviation
208	41.01	44.64									
214	52.51	45.95342	18.40151	1936.903	971.6481	2680.453	2069.193	899.9908	484.0805	1185.053	629.3258
217	87.91	49.24891	21.44807	3635.549	14882.48	5007.227	13419.75	1047.119	560.2774	1381.677	759.7874
919	89.26	49.30374	24.62021	1089.846	355.4514	1463.842	468.4845	685.2706	349.4073	901.8462	456.2199
213	96.31	49.6	29.46262	51384.84	599917.8	80892.98	502015.9	1858.193	1218.563	2475.417	1656.994
932	96.81	49.62048	29.61044	1550.626	517.5177	2121.525	705.4147	918.8315	433.1591	1216.161	567.8333
935	105.31	49.92894	29.98293	1911.953	646.5309	2594.957	874.878	1083.242	471.8377	1438.821	620.9696
938	106.52	49.97285	29.12152	1038.834	218.3552	1412.025	289.7294	847.5198	308.1185	1118.225	400.243
215	107.01	49.99064	29.16754	9550.088	96919.08	13253.57	196196.9	1693.2	792.6379	2233.642	1032.97
943	109.21	50.12057	29.47508	3098.448	1988.423	4274.643	2807.091	1417.081	612.2149	1869.114	798.8432
944	109.61	50.14639	29.65411	1075.431	220.5619	1473.389	295.9704	879.1548	309.3179	1157.383	402.0382

945	110.21	50.18513	29.4703	8474.356	160436.7	13305.28	246871.7	1755.59	771.1499	2316.733	1019.763
949	111.91	50.25531	29.79452	1550.262	397.5679	2117.506	542.7342	1051.41	401.5368	1385.51	527.46
218	117.21	50.43807	28.60664	2888.142	1818.192	3943.413	2362.064	1267.473	564.3223	1676.294	738.0387
955	118.11	50.46047	28.58655	1615.306	529.586	2197.072	719.7551	957.0245	419.2941	1268.57	557.1143
958	119.39	50.48963	26.32123	872.8271	210.7854	1186.109	277.7109	693.852	290.5026	914.1904	384.037
959	119.81	50.4992	29.92716	12851.76	182193.1	15885.15	142545.6	1386.477	745.7322	1835.554	960.8078
212	120.89	50.52381	28.44937	4873.45	26524.37	7030.492	61425.4	1170.402	628.7402	1544.857	813.9913
962	122.71	50.56527	22.24512	2093.673	1317.467	2849.542	2479.071	973.8283	492.0116	1290.285	649.7011
963	123.19	50.57621	29.49526	2236.896	1544.616	2996.937	1481.912	1031.374	516.518	1359.169	680.859
967	124.82	50.61335	29.27917	1055.739	309.6234	1434.533	421.644	721.9636	346.3092	953.9734	454.8808
216	125.21	50.62223	28.73627	6531.446	30989.38	19576.43	956477.9	1247.994	666.5461	1648.233	885.8712
972	127.61	50.67691	24.76719	1386.895	502.1978	1874.979	661.0783	811.4196	407.6573	1071.863	529.9887
973	128.01	50.68602	26.89406	1291.421	397.3972	1746.659	524.5202	829.848	391.5564	1101.963	517.5069
975	128.91	50.70653	28.25831	1192.11	374.8097	1636.582	514.5788	767.2437	378.4124	1010.089	498.9012
209	135.36	50.79537	29.28964	2796.379	9163.41	3615.718	3777.129	1126.98	549.423	1491.264	709.249
979	135.86	50.80132	29.35533	1424.109	455.1393	1941.604	617.2071	867.6767	404.1107	1142.867	528.3037
980	136.26	50.80564	29.9126	1345.136	406.7244	1846.852	554.6318	866.1404	399.3917	1146.321	523.4178
982	137.21	50.81532	29.05833	4350.391	77621.81	5383.424	68511.69	1221.705	596.6151	1612.483	789.5187
983	137.71	50.82041	26.66477	1176.257	307.84	1612.581	419.4989	842.4224	361.8866	1115.316	477.4599
214*	52.51	45.95342	18.40151	943.5571	315.1796	1302.055	455.8185	590.7811	155.3598	782.5942	204.0584

*Sample used BAYSPLINE temperature. All others used BAYSPAR.